

On the spectral emission of impurity species for diagnostic application to magnetically confined fusion plasmas

A THESIS SUBMITTED TO THE DEPARTMENT OF PHYSICS
OF THE UNIVERSITY OF STRATHCLYDE
FOR THE DEGREE OF DOCTOR OF PHILOSOPHY.

Allan D Whiteford

September 2004

© Copyright 2004

The copyright of this thesis belongs to the author under the terms of the United Kingdom Copyright Acts as qualified by University of Strathclyde Regulation 3.49. Due acknowledgement must always be made of the use of any material contained in, or derived from, this thesis.

Abstract

This thesis addresses the use of impurity species in a fusion plasma as they are applied to diagnostics to interpret the behaviour of the plasma. The work gives a brief overview of the interpretation of emission coming from light species, with particular attention paid to the modelling and fundamental atomic data entering the analysis of soft x-ray helium-like spectra.

A framework for the modelling of heavy species (e.g. tungsten) is presented with comment made on the quality of atomic data, models and what parts of the light-element problem do not scale sufficiently to heavy species.

The application of atomic modelling to fusion plasmas is treated in detail; discussing the use of diagnostics measuring line-radiation, quasi-continuum-radiation and radiated power. Particular emphasis is given as to how valid interpretations from spectral emission are in the determination of impurity transport.

Extract from 'A glossary for research reports', Graham (1957)¹:

The W–Pb system was chosen as especially suitable to show the predicted behaviour...

The fellow in the next lab had some already made up.

Extract from section 2.2.4 on page 17:

In order to study the behaviour and emission of heavy metals in ITER relevant conditions, laser ablation experiments were performed at JET with a number of sources such as tungsten, hafnium, bismuth and lead.

¹C D Graham, Jr 1957 *Metal Progress* **71** 75

Contents

List of Figures	iv
List of Tables	vii
Acknowledgements	viii
1 Introduction	1
2 Interpretation and modelling of line radiation	12
2.1 Introduction	12
2.2 Examples of spectroscopic measurements	13
2.2.1 VUV spectroscopy of neon near the plasma edge	13
2.2.2 Molecular emission from BeD and BeT	15
2.2.3 Helium-like satellite line region	16
2.2.4 Emission from heavy metals in the core plasma	17
2.3 Population and emission modelling	18
2.3.1 Diagnostically useful deliverables	18
2.3.2 Population structure	24
2.3.3 Ionisation balance	27
2.3.4 Fundamental atomic data	31
2.4 Special feature analysis of helium- and lithium-like systems	39
2.4.1 Introduction	39
2.4.2 Overview of the spectral emission	43
2.4.3 Theory of the satellite line special feature	44
2.4.4 The population calculations	47
2.4.5 The background continuum	51
2.4.6 Representing and fitting the spectral interval	52
2.4.7 Illustrative results	55
2.5 Electron-impact excitation of helium- and lithium-like systems	55
2.5.1 Introduction	57
2.5.2 Calculations and results	60

2.5.3	Application of fundamental data	73
3	Interpretation and modelling of quasi-continuum radiation	83
3.1	Introduction	83
3.2	Modelling a quasi-continuum spectrum	84
3.2.1	Feature photon emissivity coefficients	84
3.2.2	Promotional strategy	86
3.3	Fundamental atomic data for very large systems	88
3.3.1	Mixing data of varying quality	88
3.3.2	Baseline quality electron-impact excitation	89
3.3.3	Baseline quality ionisation and recombination	90
3.3.4	Intermediate quality electron-impact excitation	96
3.3.5	Intermediate quality ionisation and recombination	97
3.4	Data reduction	101
3.4.1	Need for data reduction and superstages	101
3.4.2	Flexible partitioning methodology	102
3.4.3	Flexible partitioning implementation and example	105
3.5	Atomic data for tungsten	107
3.5.1	Excitation data	107
3.5.2	Recombination data	108
3.5.3	Ionisation data	110
3.5.4	Equilibrium ionisation balance	112
3.5.5	Feature photon emissivity coefficients	114
4	Application to fusion plasmas and the analysis environment	119
4.1	Introduction	119
4.2	Spectroscopic comparison of high- Z emission	120
4.3	Radiated power	120
4.3.1	Recombination and bremsstrahlung	122
4.3.2	Line radiated power	122
4.3.3	Soft x-ray filters	123
4.3.4	Data for tungsten	126
4.4	Impurity transport modelling	129
4.5	Measurement of transport coefficients from diagnostic data	131
4.5.1	The fitting and error analysis methodology	131
4.5.2	Constructing a model plasma	135
4.5.3	Calculation of uncertainties in the free parameters	140
4.5.4	Identification of covariances	140
4.5.5	Diagnostic effects	142
4.6	Application to heavy elements	149
4.7	Tritium transport modelling and neutron emission	150

4.7.1	Background	150
4.7.2	Influx and plasma profiles	150
4.7.3	Modelling neutron emission	152
4.7.4	Forward modelling of the diagnostic system	153
4.7.5	Results	155
5	Conclusions	162
	References	164
A	Fusion experiments	178
B	Computational details	180

List of Figures

1.1	Radiation loss function for xenon	3
1.2	Spectra from tungsten ablation into JET	5
1.3	Spectra from tungsten/hafnium composite ablation into JET	6
1.4	Coronal, CR and LTE regimes of C^{3+}	8
2.1	VUV spectrum between 740Å and 790Å	14
2.2	Ne^{7+} VUV emission as a function of time	15
2.3	Emission from BeD and BeT during JET shot 60433	16
2.4	Helium-like resonance region of Ar^{16+} measured on TEXTOR	17
2.5	Helium-like resonance region of Ti^{18+} measured on Tore-Supra	18
2.6	Spectra from tungsten ablation into JET	19
2.7	Spectra from hafnium ablation into JET	19
2.8	Spectra from tungsten/hafnium composite ablation into JET	20
2.9	Spectra from tungsten/hafnium alloy ablation into JET	20
2.10	Collision strengths versus cross-sections when comparing data	34
2.11	He-like spectra of varying resolution	42
2.12	Fit to helium-like argon spectrum from TEXTOR	56
2.13	Fit to helium-like titanium spectrum from Tore-Supra	56
2.14	Fit to helium-like iron spectrum from TEXTOR	57
2.15	Reduced electron-impact excitation collision strengths for the $1s^2\ ^1S_0 - 1s2p\ ^1P_1$ transition in Fe^{24+}	69
2.16	Electron-impact excitation collision strengths for the $1s2s\ ^1,^3S_{0,1} -$ $1s4f\ ^3F_3$ transitions in Fe^{24+} with infinite energy limit points	70
2.17	Electron-impact excitation collision strengths for the $1s^2\ ^1S_0 -$ $1s3s\ ^1S_0$ transition in Ar^{16+} and Fe^{24+} showing damped and un- damped results	71
2.18	Reduced electron-impact excitation collision strengths for the $1s^22s\ ^2S - 1s^22p\ ^2P$ transition in Ar^{15+}	72
2.19	Electron-impact excitation collision strengths for the $1s^22s\ ^2S_{\frac{1}{2}} -$ $1s2s^2\ ^2S_{\frac{1}{2}}$ transition in Fe^{23+}	73

2.20	Effective collision strengths for the electron-impact excitation of the $1s2p\ ^1P_1 - 1s3s\ ^1S_0$ transition in Ar^{16+} showing effects of resonances and radiation damping	74
2.21	Effective collision strengths for the electron-impact excitation of the $1s^{21}S_0 - 1s3p\ ^1P_1$ transition and the $1s^{21}S_0 - 1s2s^3S_1$ transition in Fe^{24+}	76
2.22	Effective collision strengths for the $1s^22p\ ^2P_{\frac{1}{2}} - 1s^22p\ ^2P_{\frac{3}{2}}$ transition of Fe^{23+}	77
2.23	Effective collision strengths for the $1s^22s^2S_{\frac{1}{2}} - 1s2s^2S_{\frac{1}{2}}$ transition of Fe^{23+}	78
2.24	Effective collision strengths for the electron-impact excitation of the $1s2s\ ^3S_1 - 1s5p\ ^3P_1$ transition in Fe^{24+}	80
3.1	Comparison between configuration-average distorted-wave (CADW) and R -matrix collision strengths	96
3.2	CADW ionisation cross-sections for Kr^{20+}	98
3.3	CADW ionisation rate coefficients for Kr^{20+}	99
3.4	DR rate coefficients for beryllium-like krypton	100
3.5	Fractional change in ionisation potential of krypton	106
3.6	Ionisation balance of krypton in coronal equilibrium	107
3.7	Partitioned ionisation balance of krypton in coronal equilibrium	108
3.8	Number of levels included in tungsten excitation calculations	109
3.9	Number of transitions included in tungsten excitation calculations	109
3.10	Effective recombination rate coefficients for all ionisation stages of tungsten	110
3.11	Ionisation cross-sections for W^{4+}	111
3.12	Effective ionisation rate coefficients for all ionisation stages of tungsten	111
3.13	Effective ionisation rate coefficients for W^{24+}	113
3.14	Equilibrium ionisation balance for tungsten.	113
3.15	Temperature of peak abundance for tungsten	114
3.16	Density dependence of the emission of W^{30+} between $40 - 80\ \text{\AA}$	116
3.17	Low temperature dependence of the emission of W^{30+} between $40 - 80\ \text{\AA}$	117
3.18	Temperature dependence of the emission of W^{30+} between $46 - 54\ \text{\AA}$	118
4.1	Emission from W^{46+} in ASDEX-U	121
4.2	Response function for the JT60-U SXR detector	125
4.3	Theoretical radiated power from krypton with and without a SXR filter	126

4.4	Radiated power for tungsten, splitting the different contributions	127
4.5	Radiated power for tungsten compared with other work	128
4.6	Radiated power for tungsten as a function of density	129
4.7	Temperature and density profiles for simulated plasma	137
4.8	Reference D and v profiles	138
4.9	Reference influx	139
4.10	Chord positions of simulated CXRS system	142
4.11	Error in D_0 as a function of number of CXRS chords	144
4.12	Covariance between v/D_4 and v/D_6 as a function of number of CXRS chords	145
4.13	Covariance between v/D_6 and IM_1 as a function of number of CXRS chords	145
4.14	Error in D_0 as a function of the timebase of the CXRS system	146
4.15	Line of sight of the simulated VUV instrument	147
4.16	Modelled VUV emission	149
4.17	Tritium influx for shot 61097	151
4.18	Electron temperature profile for shot 61097	151
4.19	Electron density profile for shot 61097	152
4.20	Lines of sight of the JET neutron profile monitor	153
4.21	Deduced D profile for JET shot 61097	156
4.22	Deduced v profile for JET shot 61097	156
4.23	Global 14MeV neutron yield for JET shot 61097	158
4.24	D–D neutron counts for JET shot 61097	159
4.25	D–T neutron counts for JET shot 61097	160

List of Tables

2.1	Cross-section determination techniques	36
2.2	Summary of important lines for helium-like argon soft x-ray spectra	44
2.3	Energy levels of Ar^{16+} and Fe^{24+}	62
2.4	Energy levels of Ar^{15+} and Fe^{23+}	63
2.5	Effects of Auger damping on effective collision strengths	79
2.6	Uncertainties of level populations in Ar^{16+} and Fe^{24+}	82
3.1	Shell ionisation potentials of W^{24+}	112
4.1	Reference transport parameters	136
4.2	Radial position of charge exchange measurements	139
4.3	Errors in the fit parameters of the reference model	140
4.4	Covariances in the reference model	141
4.5	Chord positions of simulated CXRS system	143
4.6	Covariances with the addition of a VUV signal	148
4.7	Errors with the addition of a VUV signal	148
4.8	χ^2 breakdown for the fit to shot 61097	157
4.9	Values and propagated errors in fit parameters for shot 61097 . . .	157
4.10	Covariances in fit parameters for shot 61097	158

Acknowledgements

Acknowledgement is due first and foremost to my supervisor, Hugh Summers, who has always been supportive of my work and whose wealth of knowledge and experience in the field has been invaluable. In addition, his training and guidance in scientific rigour and the importance of honest, high quality work focused on application has been key to everything I have done.

Thanks also goes to Martin O'Mullane who has served as a scientific role model for me in terms of his approach to atomic physics, computational physics, plasma modelling and the scientific method in general; it is Martin whom I have aspired to most.

On the fundamental atomic physics, I am indebted to Nigel Badnell for all of his help with atomic structure and fundamental atomic processes. Thanks is also given for his insight into surviving in the world of academic publishing. And, of course, for his guidance on my first publication.

Thanks go to Klaus-Dieter Zastrow for many (patient) hours discussing plasma physics (particularly impurity transport modelling) and how it should be approached along with passing on physical insight into how a fusion plasma behaves. Klaus-Dieter has also been key to training me in the application of statistics to experimental data and the assessment of covariances in models. This has been invaluable for me in performing quantitative analysis.

Stuart Loch is acknowledged for help, encouragement and patience at the start of my career and also for continuing collaboration on atomic modelling and ionisation theory. Connor Ballance is also thanked for a great deal of help at the start of my studies and continuing collaboration on R -matrix work.

Gordon Fischbacher and Harvey Anderson provided a great deal of help towards the start of my career. Gordon in particular, whose realistic approach to science and life in general is something I have always admired. Even though he has left the field, I would still turn to Gordon for help and support with the broader aspects of my work and career.

Andy Meigs is thanked for many discussions about the scientific method, statistics, plasma physics, data visualisation and computer programming and allowing me access to his extensive knowledge of these areas. Carine Giroud is also acknowledged for her ongoing collaboration working on impurity transport and for providing a testbed for UTC. Her explanations of spectroscopy, charge exchange and transport have proved invaluable to my work.

Thanks goes to Paul Bryans, Iain Paton and Martin Torney for giving me a sounding board (often one which spoke back with clarity and new ideas) for my work. Particular thanks goes to Paul for detailed discussions about mathematics, non-Maxwellians and the consumption of alcohol! All of the members of staff in the Department of Physics at the University of Strathclyde are also acknowledged

for their direct or indirect support of my work. In particular Steve Barnett, Ricky Martin and Robbie Stewart.

During my time working at the National Institute for Fusion Science (NIFS) in Japan I had the pleasure of working with many people, including Kato-san, Murakami-san, Richard More and Andrey Starostin. Thanks is given to Kato-san and Murakami-san for their help with my work and the collaboration which we set up. Thanks also goes to Dick and Andrey for the detailed work we did on thermodynamics, while it doesn't form part of this thesis it was eye-opening to work with them and something I am pleased to have done. Thanks also goes to Dick for a very detailed discussion about my career. A great deal of appreciation goes to everyone in the Data and Planning Center for helping me to survive in Japan for three months.

During my brief visit to JT60-U I had the pleasure of working with Kubo-san and Nakano-san. They were excellent hosts and have continued to be supportive of my work.

Thomas Pütterich is acknowledged and thanked for his long running collaboration on the spectral emission of tungsten. His patience is to be highly commended and he has always proved a pleasure to work with, talk to and, occasionally, to drink with.

Particular thanks goes (again) to Nigel Badnell, Paul Bryans and Martin O'Mullane for taking the time to check this thesis from cover to cover and for providing useful feedback. Thanks also goes to my internal examiner, Gian-Luca Oppo for guiding me through the examination process and for providing helpful feedback on this thesis. I would particularly like to thank my external examiner, Kurt Behringer, for taking the time to read my thesis in detail and for travelling from Germany to examine me.

Thanks also goes to the following people whom I have worked for, worked with and learned from: Robin Barnsley, Bob Bingham, Ivor Coffey, James Colgan, Sean Conroy, Ralph Dux, Geoff Duxbury, Don Griffin, Lorne Horton, Thomas Krücken, Jim Lang, Kerry Lawson, Oleksander Marchuk, Mitch Pindzola, Elisabeth Rachlew, Alex Thomas, Paul Thomas, Manfred von-Hellerman and Alexei Zabolotsky .

My career thus far has also allowed me to meet people which I would otherwise not have been able to do, these people include Zikri Altun, Kate Bell & family, Keith Berrington, Guenter Bertschinger, Marco Bigi, Mathias Brix, Dave Cowan, Amelis Daras, Ursel Fantz, Adam Foster, Awi Gondelakar, Tom Gorczyca, Rémy Guirlet, Kato Daiji-san, Kato Masatoshi-san, Mattias Kuldkepp, Axel Larson, Alessandro Lanzafame, Peter Lindner, Ian Linnington, Iain Loch, Sheena Menmuir, Darren McDonald, Brendan McLaughlin, Peter McWhirter, Philip Mertens, Barbara Mroz, Clive Negus, Terry O'Neil, Byron Peterson, Francis Robicheaux, Béatrix Schunke, Dave Shultz, Randall Smith, Anna Stork,

Derek Stork, Sofia Sundstrom, Oleg Tolstikhin, David Tskhakaya, Susan Turnbull, Michael Witthoef, Donald Wilson, Peter Young and Zou-san. And, in particular, Vladimir Gligorov, Robin Sangar and Amanda Wright.

Personal acknowledgement also goes to some colleagues listed above, namely Andy Meigs, Sean Conroy and Misha Beldishevski for putting up with me as a housemate during my time working at JET. In particular to Andy for his firm friendship and to both Sean and Andy for showing me that there are things too hot for me to eat, and many many things I shouldn't drink.

My close family are acknowledged and thanked for their support during the course of my work and the writing of this thesis. This work would not have been possible without the support of my parents, David & Marjorie Whiteford and without the enthusiasm of my sister, Lynda Whiteford, who seldom failed to ask what I had 'discovered today' or what sort of 'sums' I had been doing. Thank you, Lynda.

The personal friendships with James Myles and John Redgate are particularly appreciated, without them I am almost certain I would not be in a position to write this thesis.

Past and present members of the 113th (Burnside) Glasgow scout group are thanked for their support over the years, in particular for the many character-building experiences I have taken part in. Particular thanks goes to Kenny Barr, Richard Easton, H Stewart Graham, Nigel Macdonald and Carolyn Ritchie.

Finally, the support of my girlfriend, Helen Flockhart, has been invaluable to me in the writing of this thesis, her support and love is appreciated and reciprocated in a way which cannot be expressed here in words by me.

— Allan D Whiteford
September 2004

Chapter 1

Introduction

The spectral emission from light impurities within a fusion plasma has, for many years, been promoted as a key diagnostic to temperature, density and transport characteristics of the plasma. In actuality, the diagnostic results obtained from such analysis are not always as successful as one could hope for, or expect.

Key deficiencies are often present in the analysis procedure. The cornerstone of these deficiencies is usually a lack of highly specialised knowledge of each of the aspects, and their linkage, which make up the problem as a whole. For instance, plasma physicists, usually attached to labs, are non-expert in the sources of fundamental atomic data while fundamental atomic data producers, usually attached to universities, are non-expert in the eventual application of their work. Exceptions do exist, of course.

The present work seeks to address this problem in general and at a high level of detail for specific problems (namely helium- and lithium-like systems and the diagnostic potential of heavy species). The gap is bridged between fundamental atomic data production using a state of the art method (i.e. *R*-matrix) and modelling the transport characteristics of a fusion plasma. These two topics are of great scientific interest in themselves but between them there is a great deal of work which is often dismissed as trivial. Knowledge of both extreme ends of the production and use of atomic data allows for a greater appreciation of, and hence greater success in, the task to provide **useful** atomic data to plasma physicists.

For diagnostic purposes, cross-sections are not of themselves useful atomic

data for plasma analysis, they must first be processed before they can be considered usable in direct application to experiment. This highlights a key problem in many atomic databases — they archive cross-sections. More useful quantities to archive for diagnostic purposes are direct indications of emission (see sections 2.3.1.1 and 2.3.1.2), ionisation and recombination (see section 2.3.1.3).

Another key problem in the diagnosis of fusion plasmas is over-interpretation of the measured data; often not enough is recorded to tie down all of the unknowns. This leads to a situation where differences between measurement and theory is simply put down to something immeasurable, such as transport. There exists a real need for a rigorous treatment of theoretical, experimental and propagated uncertainties to underpin analysis. For instance, of the more than one hundred submissions from JET to the 2001 European Physical Society plasma physics conference, fewer than ten contained error bars (Cordey 2001). It is insufficient to draw two curves which are close, label them ‘model’ and ‘measurement’ and because they are close say they match or, because they disagree, to blame a single effect and claim measurement of that effect. Covariances must be obtained between free parameters to provide a true indication of what can and cannot be measured. For example, the covariance between a simple influx model and edge diffusion coefficient in a fusion plasma can be greater than 99% if only charge exchange measurements are used (see section 4.5.4). If an edge spectrometer is added to the suite of diagnostics then the covariance drops significantly (see section 4.5.5.2).

Turning to impurity species in a burning plasma, it was widely held as necessary to minimise these impurities since the resultant radiative power loss can easily quench the fusion reaction, e.g. 0.1% of molybdenum will easily quench a fusion reaction (Summers and McWhirter 1979). However, impurities have been shown as having key diagnostic and controlment roles.

For the purposes of controlling a fusion plasma noble gases are often used — see, e.g., Higashijima *et al* (2003) where argon was used to control the heat flux to the divertor in JT60-U, and Kubo *et al* (2003) where the impurity accumulation via an internal transport barrier (ITB) and subsequent radiation enhancement were studied. Such gases also include krypton and xenon — much heavier elements than those which are routinely used for diagnostic purposes in a fusion plasma.

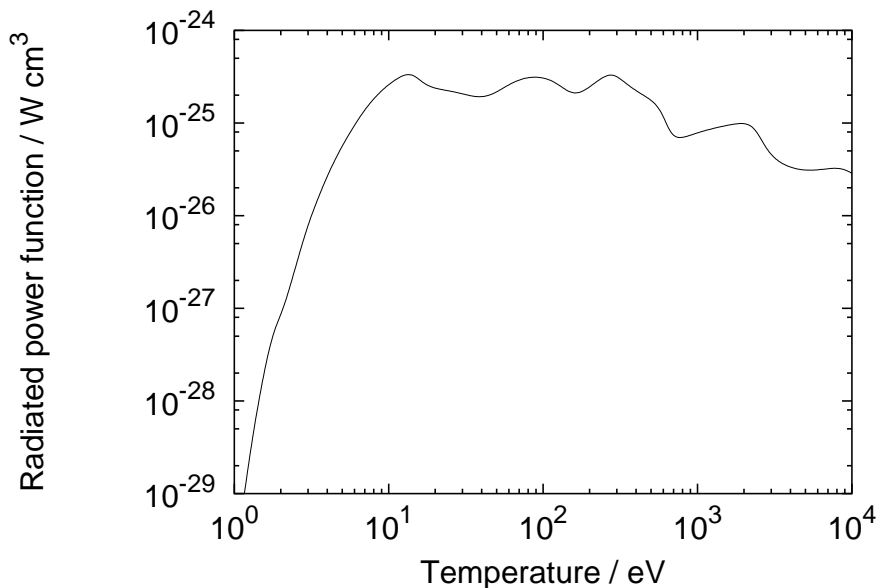


Figure 1.1: Radiative cooling curve for xenon in equilibrium at an electron density of 10^{13}cm^{-3} . The ‘bumps’ are features of the line emission from key ionisation stages contributing heavily to the radiated power in the temperature range where these stages are particularly abundant.

It is also important to obtain an estimate of the radiative cooling an element such as xenon will produce when introduced to a plasma. Recent experiments with krypton and xenon have been performed at JT60-U and the analysis of the results falls within the scope of the present work. A typical radiative loss function for xenon as a function of temperature is shown in figure 1.1 (see section 4.3 for more details).

On the control function of heavy impurities in radiated power loss, it is noted that the radiative power loss also has an intrinsic use, as touched on above. We now turn to this in greater detail. The majority of heat flux will go to the divertor in a modern tokamak (e.g. JET, ASDEX-U, JT60-U) (see Appendix A for a summary of the character of these machines). For the next generation of fusion devices (specifically ITER¹) and, indeed future burning plasmas, this heat flux will be much larger than previously attained. Impurity seeding into the scrape off layer

¹see ITER Physics team, (1999a-f).

(SOL) as a way to cool the plasma before it reaches the divertor (thus reducing the heat flux to the wall) has been proposed for ITER (Mandrekas and Stacey 1995, Mandrekas *et al* 1996) following the (non-ITER specific) work of Lackner *et al* (1984) and Neuhauser (1992). General studies on impurity seeding have recently been performed on JET (Maddison *et al* 2003) while Kukushkin *et al* (2002) recently studied the impurity seeding need for ITER. They showed that, while the radiative cooling itself is important, the impurity causing this cooling will not significantly affect divertor performance.

Even with impurity seeding, the heat flux to the divertor will still be large. To this end, tungsten has been proposed as an alternative to lighter materials as a first wall material for the ITER divertor because of its low sputtering yield (due to a higher sputtering threshold energy (Eckstein *et al* 1993)). Such low sputtering yields are necessary to cope with the predicted power flow onto plasma facing wall, $\sim 20 \text{ MWm}^{-2}$ being a maximum but $< 10 \text{ MWm}^{-2}$ being desirable (ITER team 2000). However, the radiative losses from tungsten are far higher than from lighter materials. For a burning plasma the concentration must stay below a limit of around 0.0002%, as opposed to the permissible 1% allowed for lighter species (Peacock *et al* 1996).

The first wall on ASDEX-U has recently been replaced by tungsten walls in order to simulate such a scenario following a lot of preparatory work, notably Naujoks *et al* (1996). These experiments have been successful and details can be found in Neu *et al* (1996, 1997, 2001, 2002, 2003a, 2003b) and Neu (2003). Investigations into the power deposition have been performed recently by Herrmann *et al* (2003) and the subsequent erosion, deposition and transport in the SOL have been studied by Geier *et al* (2003).

A novel proposal is to use heavy species such as tantalum in fusion plasmas (specifically ITER) for the purposes of monitoring wall erosion. Such elements would be embedded into the first wall material and be revealed to the plasma as, and when, the wall is sufficiently eroded. Released into the plasma, these would be spectroscopically detected and identified, making a tangible measurement of wall erosion possible whilst the plasma is running. It would be necessary to detect a marker species, such as tantalum, against a 'natural' (possibly tungsten) background. Experiments have been performed at JET by laser ablating heavy metals

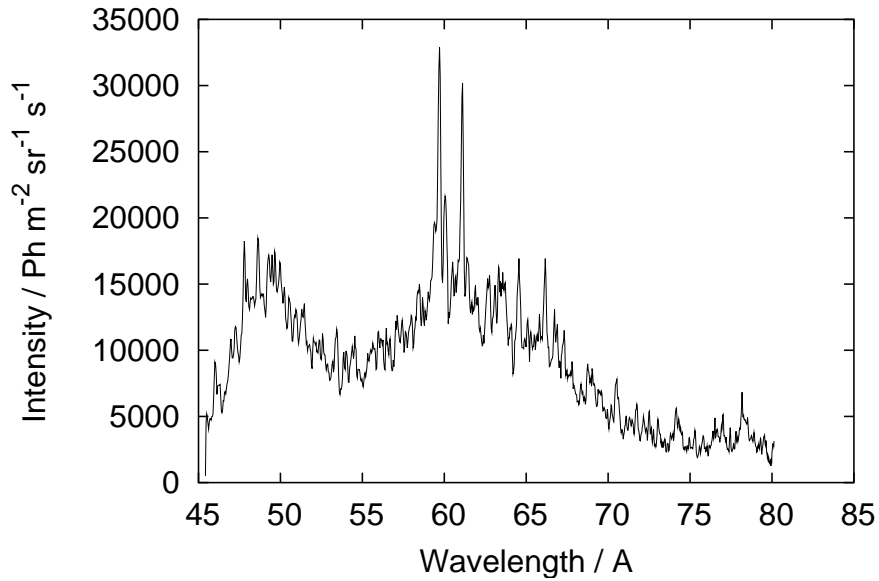


Figure 1.2: Spectra recorded from ablation of a tungsten tile into JET using a grazing incidence spectrometer for shot 55155.

into the plasma (O’Mullane *et al* 2002). The key importance of using JET, as opposed to other current devices, is that JET can typically attain a much higher temperature than other machines. These experiments are interesting in that more than one impurity is ablated at the same time, giving an opportunity to detect, e.g., tantalum in the presence of tungsten and, indeed, see if they can be distinguished. An example of a recorded spectrum from ablation of a tungsten tile is shown in figure 1.2 and one from a mixture of tungsten/hafnium in figure 1.3. More examples are given in section 2.2.4. A first attempt at modelling this emission was performed by Loch *et al* (2002a) and O’Mullane *et al* (2002). The work presented in this thesis can be seen both as an integral part of that work and also as an extension to it.

The recent studies by Ohgo *et al* (2003) on tungsten and tantalum test limiters in TEXTOR are also noted. They used the work of Post *et al* (1977) to calculate radiation losses to analyse the results.

The most comprehensive work to date on radiation losses from fusion plasmas is that of Post *et al* (1977) mentioned above. The average-ion model (Strömngren

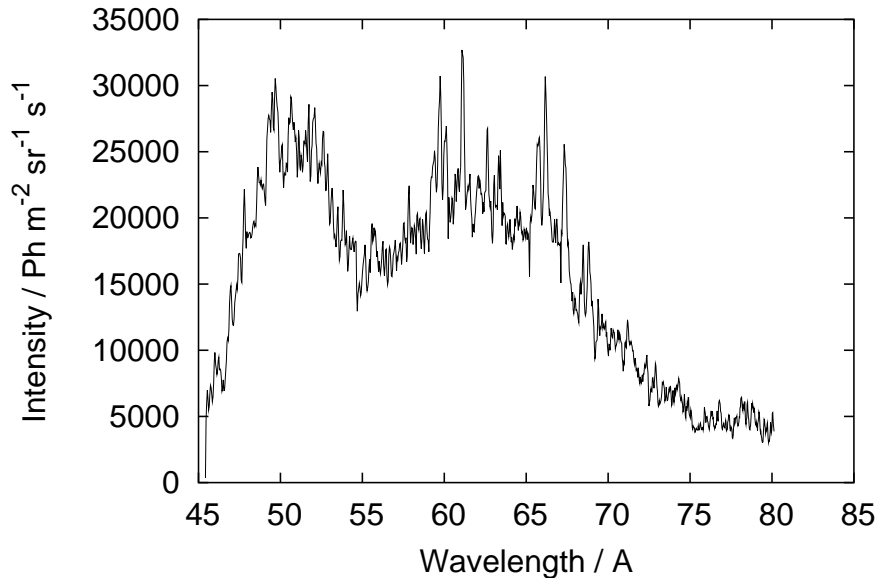


Figure 1.3: Spectra recorded from ablation of a tungsten/hafnium composite tile into JET using a grazing incidence spectrometer for shot 55159.

1932) was used to construct radiative cooling curves for ions in equilibrium. We compare the work presented in this thesis to that of Post *et al* (1977) in section 4.3.4. Limited work was done by other authors before that of Post *et al* (1977), we make particular note of Gervids and Kogan (1975) who calculated radiative cooling data for tungsten.

More advanced ways to calculate radiative power and spectral emission now exist. Underpinning these calculations are fundamental data which can come from a number of different sources. A lot of work was done by Sampson and co-workers (e.g. Sampson (1986) and references therein) to systematically produce rate coefficients for many applications. This work was extensive in that it generally covered a wide range of elements but the methods (although not the comprehensive data coverage) have since been superseded by more modern techniques. Partly, this thesis seeks to address the lack of data coverage by creating a scheme to automate the production of atomic data. Other techniques to calculate fundamental data include *R*-matrix (Burke and Berrington (1993), and discussed in detail in section 2.5) and HULLAC (Bar-Shalom *et al* (1988), and discussed in section 3.3.4).

For fusion plasma analysis, these fundamental data feed into a collisional–radiative model. This was first put forward by Bates *et al* (1962) and then extended by many people — notably, for this work, Summers (1999).

The need for collisional–radiative modelling is best illustrated by a specific case. In figure 1.4 the three main (electron-impact dominated) population structure regimes in an optically thin plasma are shown for the case of C^{3+} . At very low densities, the regime is that of coronal equilibrium where each level is only effectively populated (internal to the ion) from the ground state before spontaneously decaying back to the ground state, either directly or indirectly, and emitting radiation; no cross-coupling between levels is observed due to the low number of electron-impact events. Given a population, the probability of a specific level emitting a given spectral line is described by a branching ratio. This branching ratio is only dependent upon spontaneous emission coefficients and is, hence, temperature independent. One important consequence of this is that, in the coronal regime, the only temperature dependent process within a given ion (i.e. neglecting ionisation and recombination) is that of direct collisional excitation. Thus the atomic physics going into the analysis of such a coronal regime plasma is much more straightforward than for a plasma in the collisional–radiative regime. The coronal model is still in extensive use at the time of writing despite it being shown that it is invalid at moderate densities — this is an unacceptable way to analyse many fusion plasma regimes.

The other extreme, at very high densities, is that of local thermodynamic equilibrium (LTE), where the population of each level is given by Boltzmann statistics. Once this regime has been reached, the dependence on electron density is removed, in contrast to the coronal regime. When a plasma is in LTE the relative intensity of spectral lines are given only by the relative values of spontaneous emission coefficients with no dependence on electron-impact rate coefficients, provided the plasma remains optically thin. This is a strong qualification in dense plasmas. The densities required for LTE are not normally reached within current magnetically confined fusion plasmas; such densities typically exist in the core of the sun and in laser induced plasmas.

The region bridging between coronal and LTE is known as the collisional–

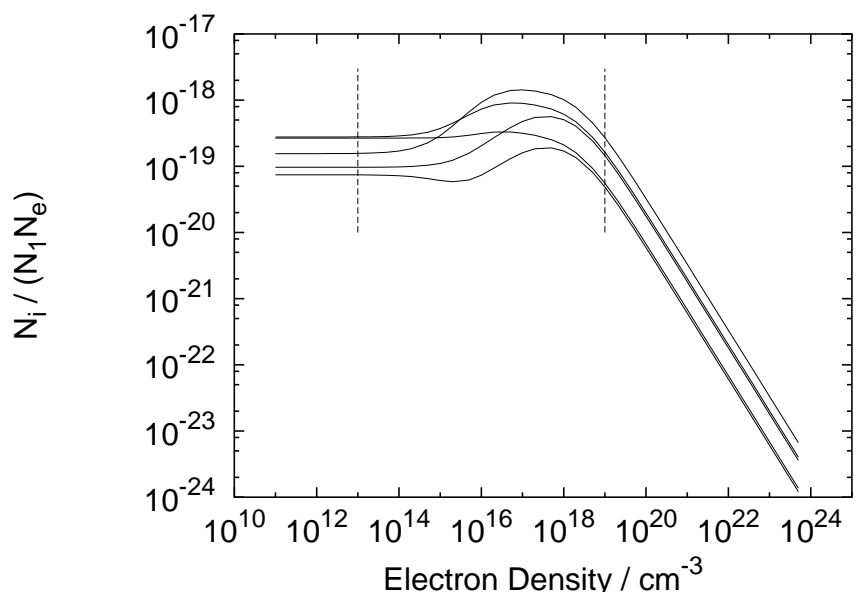


Figure 1.4: Population relative to ground of five lowest excited levels of C^{3+} as a function of density illustrating (from low density to high density) the coronal, CR and LTE regimes, approximate boundaries are marked with dashed lines. Note that the plotted quantity is normalised to the ground population and not to the total population of the ion.

radiative (CR) regime². For many important ions, this regime occurs at densities typical of those found in magnetically confined fusion devices. The basic theory underpinning CR modelling was first proposed by Bates *et al* (1962) and has been extensively developed by Summers and co-workers (1999) with a recent review by Summers *et al* (2002) (and references therein).

In the CR regime, it is necessary to consider the cross-coupling between levels using explicit collision rates (from cross-sections). In the simplest case, for optically thin plasmas (usually a valid assumption in current magnetically confined fusion devices) these rates will be electron-impact excitation and de-excitation along with spontaneous emission rates.

At the present time, the most sophisticated method of handling the CR regime is called generalised collisional radiative (GCR) modelling. Attention is drawn to two projects which this thesis is closely linked with, namely the DR project (Badnell *et al* 2003) and the GCR project (O’Mullane and Summers, unpublished). The DR project is a programme for the assembly of a comprehensive dielectronic recombination (DR) database in order to supply the necessary rates to model fully plasmas within the generalised-collisional-radiative (GCR) framework. The dielectronic recombination data produced by the DR project is usable at finite densities (i.e. valid for the CR regime as outlined above) as opposed to much of the earlier data as summarised by Mazzotta *et al* (1998). At the present time the O-like (Zatsarinny *et al* 2003) and Li-like (Colgan *et al* 2003) DR sequences have been presented in the literature with another six papers in the publication process. The GCR project is discussed in detail in section 2.3.1.5.

On non-plasma studies of heavy species, attention is drawn to extensive measurements of ionised tungsten in electron-beam ion-trap (EBIT) experiments, specifically those at IPP-Berlin. From the perspective of the fusion program, these experiments provide a key insight in to how tungsten will behave in a fusion plasma. A great deal of atomic modelling has also taken place to support and explain these experiments (e.g. Radtke *et al* 2001). Comparison with these data should be seen as a rigorous test of the current work. We also note the ionisation cross-section measurements of Stenke *et al* (1995) for near-neutrals of tung-

²Note that the CR description implicitly encompasses and describes both extremes; it moves smoothly between the coronal and LTE limit.

sten (up to W^{10+}) and the calculations of Pindzola and Griffin (1997) to describe the measured data. Earlier measurements were also performed for singly ionised tungsten by Montague and Harrison (1984).

The work presented here deals firstly with the problem of light impurities, specifically those where individual spectral lines can be easily distinguished and analysed with respect to other spectral lines — most often in the same spectral region. A re-working of the specific problem of the helium-like emission spectrum along with its associated lithium-like satellite lines is performed, based on the R -matrix method for excitation cross sections. This highlights new refinements of the cross-section calculations which can significantly alter results. Such methods for few-electron systems are typical of those used for light elements.

The techniques developed for light elements are then reviewed, expanded and modified so as to be able to address very heavy species, such as tungsten. Consideration is given as to what part of the analysis procedure from light ions can be retained and what parts need a complete or partial re-working. In particular, the fact that the emission lines merge into an effective quasi-continuum necessitates the replacement of individual line emissivities with ones which describe a group of many (blended) lines. Special attention is given to the size and complexity of the problem with the specific view of generating a framework for arbitrarily complex systems which provides diagnostically useful atomic data for fusion experiments.

An analysis environment for using this data is then presented. The main novel issue in this analysis system is the extended use of quantitative data and, specifically, error analysis and propagation. Particular attention has been given to correlations in measurable quantities so as to give a proper indication of what can and cannot be measured and derived given the experimental data available.

The work presented here is driven by application rather than utilisation of fundamental data. Rather than generating fundamental data (such as cross-sections) and then seeking an application, the approach taken here is to identify what is required for plasma diagnostics. Then a prescription may be laid out on the basis of which appropriate theory and tailored data may be prepared. While this approach may seem natural and more useful it is often the case that fundamental data is generated and then an application sought. Thus, the structure of the chapters are such that diagnostic needs are first outlined, and then met using atomic physics. In

section 2.2, for example, we give examples of spectroscopic measurements from fusion plasmas, identifying ones which lead to different types of analysis. To analyse these examples, we identify diagnostically useful deliverables (section 2.3.1), subsequently explain how collisional–radiative modelling can provide these data (sections 2.3.2 and 2.3.3) and finally (section 2.3.4) go into the details of the data which feed into the collisional–radiative model. This presentation does not have the elegance of starting from *ab initio* calculations and showing how they are built up to plasma diagnostics but rather it shows how a diagnostic need is identified, researched, developed and met — this is a more accurate portrayal of the modern analysis environment.

Chapter 2

Interpretation and modelling of line radiation

2.1 Introduction

The modelling of line radiation has been the basis of most atomic physics, going back to the fundamental work of modelling the line emission of hydrogen in a discharge lamp and the resultant quantum mechanical description which is still in use today. It also has a long history in astrophysics where it has been used both to describe the evolution of plasmas, often very active plasmas such as solar flares and also for more fundamental measurements such as the first proper experimental evidence for the existence of helium. This chapter discusses in detail how line emission is currently modelled for application to a magnetically confined fusion device using explicit excitation, recombination and ionisation rates to determine a population structure which gives rise to line emission.

The techniques used to combine all of this atomic data as well as the sources of fundamental data are discussed. Emphasis is then given to a particular spectral region, namely the soft x-ray emission of helium-like systems along with its associated lithium-like satellite lines. This is given as an example of how diagnostically useful the information given by spectra can be and a re-working is given to the modelling of these spectra, a necessary improvement on earlier work in light of recent spectroscopic measurements and available atomic data generation

techniques.

Atomic data is then generated for helium- and lithium-like systems using the R -matrix method, a (state of the art) technique used here to generate excitation and de-excitation rates. Attention is given to the validity of this data as a function of temperature, as well as the energetic behaviour of the fundamental collision strengths at both low and high energy.

2.2 Examples of spectroscopic measurements

We present here a number of examples of spectroscopic measurements from fusion devices to highlight and justify the approach to atomic physics used and developed in this thesis. Each of these measurements is unique and merits a particular type of analysis. In section 2.2.1 we give an example of a VUV measurement where individual spectral lines can be readily observed and hence only requires modelling of a single transition, without any spectral resolution. In section 2.2.2 we give an example of molecular emission where single lines cannot be resolved and thus a complex feature must be built up to model the spectrum. In section 2.2.3 we expand on the need for modelling of special features by showing soft x-ray measurements from TEXTOR and Tore-Supra, the modelling and precise description is later discussed in section 2.4. Finally, in section 2.2.4 we show examples of laser ablation of heavy elements into JET — a problem which requires spectroscopic resolution and also the handling of a large amount of atomic data. The theoretical techniques to describe these spectra are given throughout chapter 3.

2.2.1 VUV spectroscopy of neon near the plasma edge

During a series of neon and argon gas-puff experiments at JET (Giroud *et al* 2004), VUV spectroscopy was performed on Ne^{7+} and Ar^{15+} . We take the neon as an example here as observed in shot 60933. Spectra were recorded throughout the experiment in the VUV region, the spectral interval where the $1s^2 2p^2 P_{\frac{3}{2}} - 1s^2 2s^2 S_{\frac{1}{2}}$ and $1s^2 2p^2 P_{\frac{1}{2}} - 1s^2 2s^2 S_{\frac{1}{2}}$ transitions occur are shown in figure 2.1. Immediately before the puff, the lines are very weak but following the puff the lines become

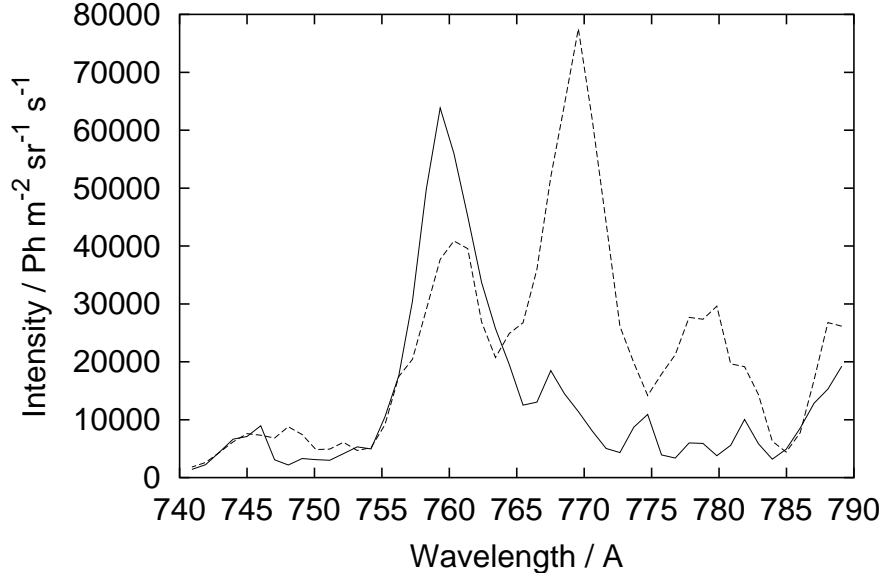


Figure 2.1: VUV spectrum as recorded during a neon gas puff experiments in JET shot 60933. The solid line denotes the signal before the gas puff and the dashed line the signal just after. The VUV lines of Ne^{7+} at 770\AA and 780\AA , corresponding to the $1s^2 2p\ ^2P_{3/2} - 1s^2 2s\ ^2S_{1/2}$ and $1s^2 2p\ ^2P_{1/2} - 1s^2 2s\ ^2S_{1/2}$ transitions respectively, can be seen after the puff.

much stronger as the neon enters the plasma. Since Ne^{7+} only occurs at the edge of JET (typically $r/a \gtrsim 0.8$ with peak abundance around $r/a \sim 0.95$) the emission is seen almost immediately. Fits were performed to these two lines and their brightness summed as a function of time. This time trace can be seen in figure 2.2. Qualitatively, the neon can be seen entering the plasma rapidly then coming back out with an exponential decay.

Atomic data for a number of processes is required in order to model the VUV emission. If one knows the abundance of Ne^{7+} then a local emissivity is required (which will be a function of temperature and density). Such an emissivity, called a \mathcal{PEC} , is introduced in section 2.3.1.1. However, if the abundance of Ne^{7+} is also to be determined in order to calculate the emission then effective ionisation and recombination coefficients are required (see section 2.3.1.3) to enter an impurity transport model (see section 4.4).

Modelling of VUV emission at the edge of a fusion plasma in this way is often

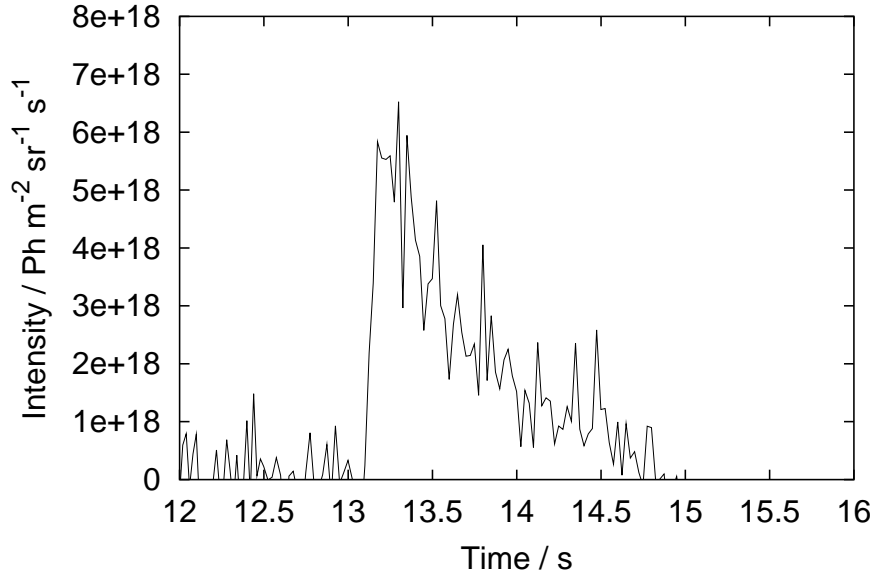


Figure 2.2: Ne^{7+} VUV emission for a summation of fits to the emission from the $1s^2 2p^2 P_{3/2} - 1s^2 2s^2 S_{1/2}$ and $1s^2 2p^2 P_{1/2} - 1s^2 2s^2 S_{1/2}$ transitions in JET shot 60933.

used to determine the influx of impurities into the core, this is discussed in detail in section 4.4 and demonstrated to be useful in determining plasma behaviour (i.e. transport coefficients) at the edge in section 4.5.5.2.

2.2.2 Molecular emission from BeD and BeT

During the JET trace tritium campaign, experiments were performed attempting to distinguish different isotopes of beryllium hydrides — the theoretical work performed was successful but the detectability of different isotopes was difficult to observe due to the low tritium concentrations in the experiments. During the discharges, visible spectra of the divertor region were recorded. One such spectrum recorded from JET shot 60433 is shown in figure 2.3 (Meigs, 2003).

This type of spectra clearly needs a different sort of analysis from the far simpler line spectra given in section 2.2.1. Modelling by fitting lines on purely mathematical models (e.g. Gaussian curves) cannot be performed whilst retaining all of the diagnostic information contained within the spectrum. Instead a ‘spe-

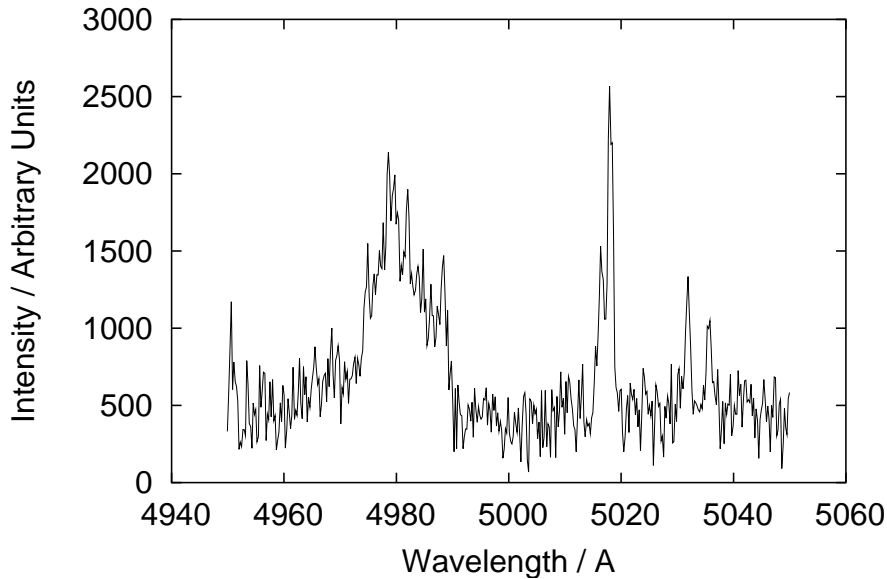


Figure 2.3: Emission from BeD and BeT during JET shot 60433, the A-X transition array is observed.

cial feature’ is created, which is a collection of simulated spectra parametrised according to physically meaningful quantities such as temperature and density. These features still model local emission so line integration at each wavelength point (corresponding to a pixel on a spectrometer) must still be performed. See Duxbury *et al* (2004) for details of this analysis, it is noted that the spectrum shown here is of only moderate resolution.

Special feature analysis forms a major part of this thesis and is introduced in section 2.3.1.4.

2.2.3 Helium-like satellite line region

Soft x-ray helium-like spectra near the resonance line have been used for a great many years in astrophysical and laboratory diagnostics. Previous analysis centred around taking various line ratios, such as the (temperature dependent) G-ratio (Gabriel 1972). The preferred analysis procedure is now to use special feature analysis to fit spectra based on physical parameters such as electron temperature and density. Such a method allows a much better use of the high quality atomic

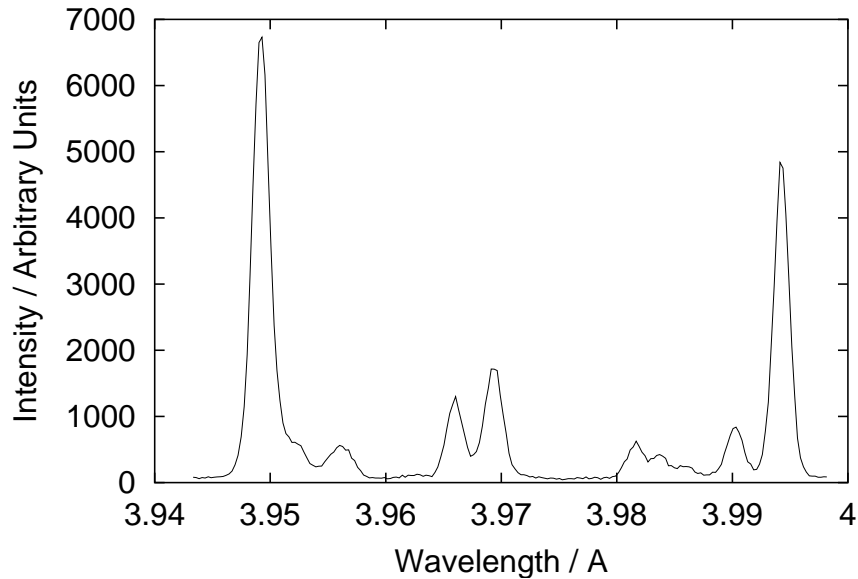


Figure 2.4: Helium-like resonance region of Ar^{16+} measured on TEXTOR in shot 88710 between $t = 3700\text{ms}$ and $t = 4700\text{ms}$.

models and data available.

A spectrum of Ar^{16+} recorded on the TEXTOR tokamak is shown in figure 2.4 and a similar spectrum from Ti^{18+} recorded on Tore-Supra is shown in figure 2.5 (Marchuk *et al* 2003, Marchuk 2004).

The special feature analysis of the helium-like resonance region is discussed in detail in section 2.4. A complete model is produced and discussed and examples of experimental comparisons are presented which used the models (section 2.4) and data (section 2.5) given in this thesis.

2.2.4 Emission from heavy metals in the core plasma

In order to study the behaviour and emission of heavy metals in ITER relevant conditions, laser ablation experiments were performed at JET with a number of sources such as tungsten, hafnium, bismuth and lead. A tungsten spectrum is shown from JET shot 55155 in figure 2.6 and a hafnium spectrum is shown from shot 55154 in figure 2.7. These spectra are interesting in isolation but if ITER has tungsten plasma facing components and, say, hafnium doped tiles to measure wall

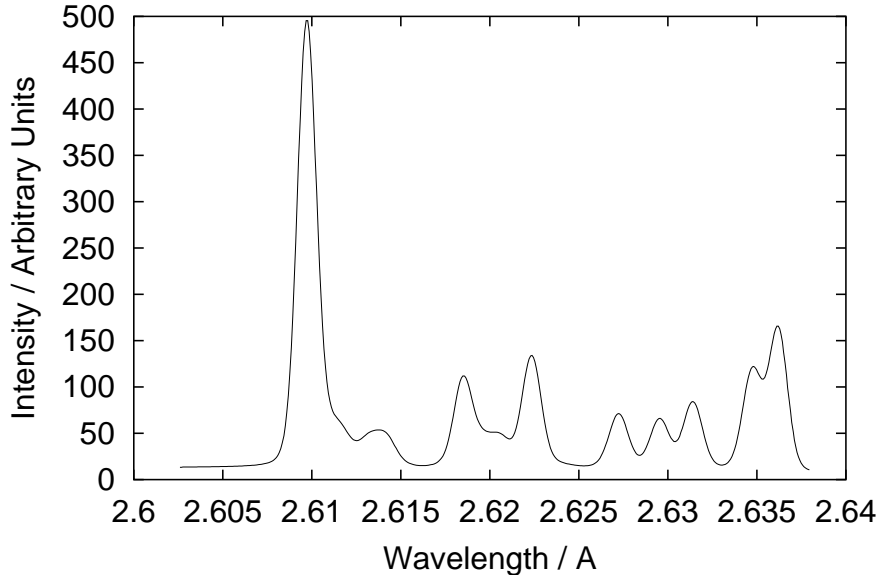


Figure 2.5: Helium-like resonance region of Ti^{18+} measured on Tore-Supra in discharge 23706 between $t = 4620\text{ms}$ and $t = 5040\text{ms}$.

erosion then it will be necessary to detect and distinguish both species simultaneously. Figures 2.8 and 2.9 show such a mixture of tungsten and hafnium. The former figure, from shot 55159, is a composite tile for the laser ablation and the latter, from shot 55153, is an alloy tile.

The special feature analysis of high- Z impurities is discussed in detail in section 4.2. As in the case of the helium-like region spectral analysis, complete forward modelling is presented along with examples of experimental comparisons performed using the atomic data and models presented here.

2.3 Population and emission modelling

2.3.1 Diagnostically useful deliverables

For analysis of the emission and transport of impurity species in a fusion plasma there exist a number of useful atomic deliverables — exactly the sort of deliverables which would be used to confront the example spectra given above in section

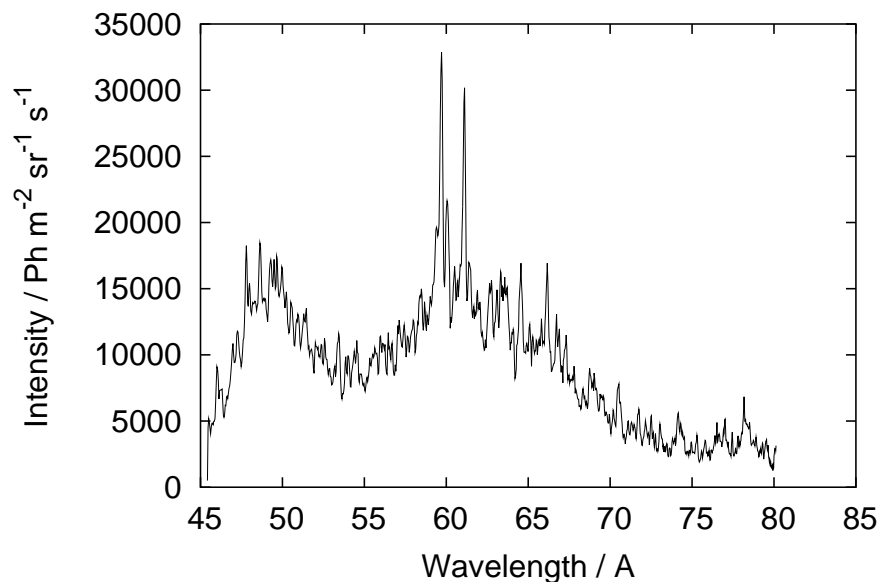


Figure 2.6: Spectra recorded from ablation of a tungsten tile into JET during shot 55155.

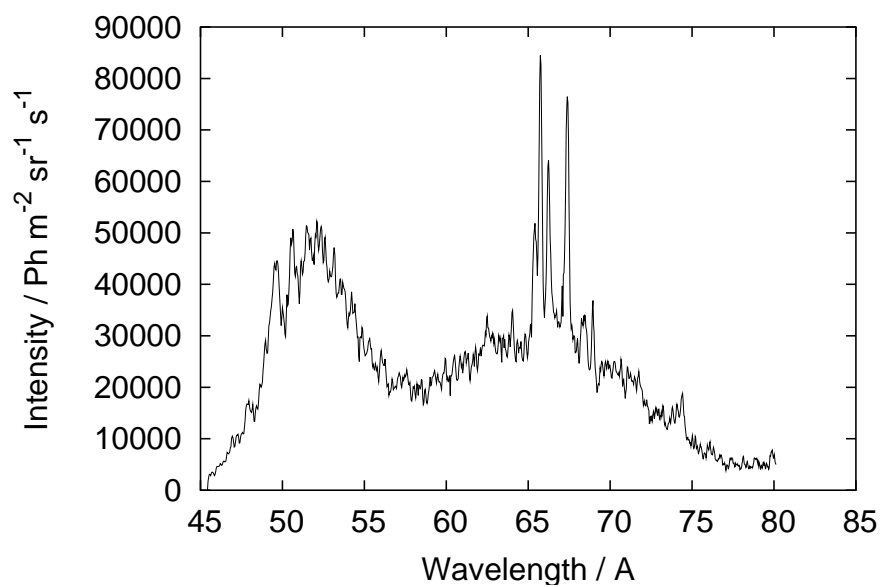


Figure 2.7: Spectra recorded from ablation of a hafnium tile into JET during shot 55154.

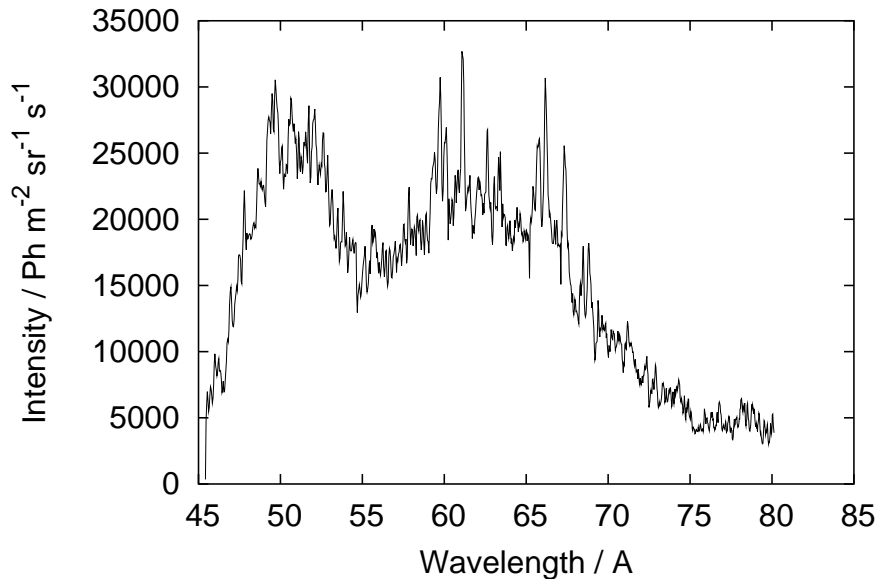


Figure 2.8: Spectra recorded from ablation of a tungsten/hafnium composite tile into JET during shot 55159.

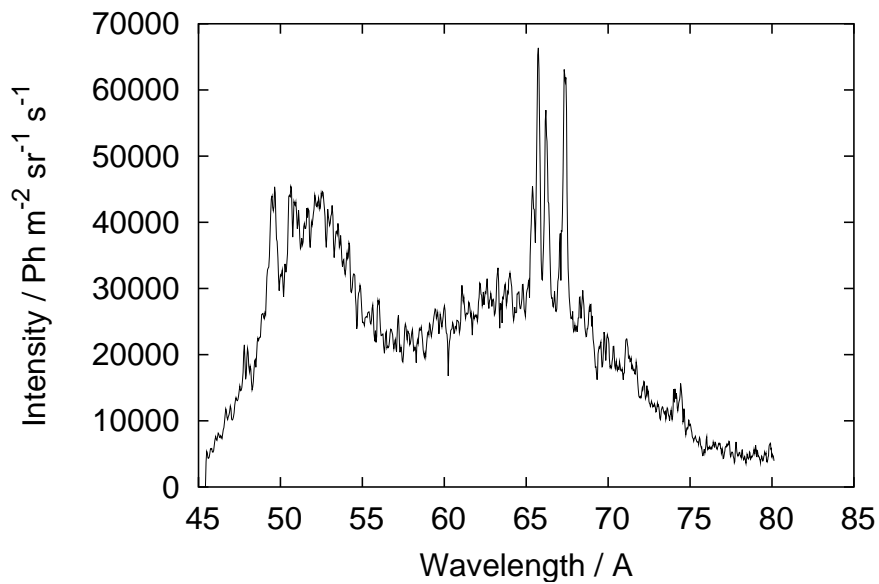


Figure 2.9: Spectra recorded from ablation of a tungsten/hafnium alloy tile into JET during shot 55153.

2.2. These quantities can be applied directly to spectroscopic measurements without unnecessary complications. It has been the trend in ‘atomic data centres’ (e.g. IAEA¹ and NIFS²) to collect, archive and validate cross-sections. While cross-sections are valid quantities to collate, they are not immediately useful to a fusion plasma diagnostician studying trace impurity species, in contrast to claims often made by such data centres. Within the Atomic Data and Analysis Structure (ADAS) database (Summers 1999) a number of different types of atomic data are archived, many of which are directly applicable to fusion plasmas. In particular, photon emissivity coefficients, photon efficiencies, total ionisation and recombination rates and radiated power coefficients. These quantities are calculated with highly complex atomic modelling and often underpinned with high quality cross-sections but the values themselves are presented in a simple form for a diagnostician to use.

2.3.1.1 Photon emissivity coefficients

For an ion, X^{z+} , within a plasma at local temperature and density of T_e and N_e respectively, it is useful (for spectroscopy) to know how many photons that ion will emit for a given transition, $j \rightarrow k$. We call such a quantity a photon emissivity coefficient ($\mathcal{P}\mathcal{E}\mathcal{C}_{z,j \rightarrow k}(T_e, N_e)$). If we know the electron temperature, electron density and ion density profiles, $T_e(l)$, $N_e(l)$ and $n_z(l)$ we can obtain a line integrated emission along a line of sight, l (from $l = 0$ to $l = L$) from,

$$\int_0^L \mathcal{P}\mathcal{E}\mathcal{C}_{z,j \rightarrow k}(T_e(l), N_e(l)) N_e(l) n_z(l) dl. \quad (2.1)$$

In reality, the $\mathcal{P}\mathcal{E}\mathcal{C}$ s are more complicated: there is an excitation and recombination part, but the basic principle remains the same. There is a diagnostic need for a quantity which gives photons emitted per second as a function of electron temperature and density, as was highlighted with the VUV analysis in section 2.2.1. $\mathcal{P}\mathcal{E}\mathcal{C}$ s are used, and developed, throughout this thesis and are defined in section 2.3.2.

¹<http://www-amdis.iaea.org/>

²<http://dbshino.nifs.ac.jp/>

2.3.1.2 Photon efficiencies

The photon efficiencies, or ionisations per photon, are often used to determine influx from measured line intensities. The number used is termed S/\mathcal{XB} which is the ionisation rate, S , divided by the excitation rate, X , and the branching ratio, B . These are functions of temperature and density and are defined in section 2.3.2.

Early work using this technique was done by Stamp *et al* (1987) and Behringer (1987b) with a review by Behringer *et al* (1989). Recent studies of carbon influx from the walls of ASDEX-U have also been successfully performed by Pütterich *et al* (2003a) using this method. S/\mathcal{XB} s are not utilised in this thesis but have been included here for completeness as one of the three main types of deliverable data (\mathcal{PEC} s, S/\mathcal{XB} s and effective ionisation & recombination coefficients).

2.3.1.3 Total ionisation and recombination rates

In order to determine a dynamic ionisation balance inside a tokamak plasma, or, indeed many other types of laboratory or astrophysical plasmas it is normal to use a temporal and spatial model commonly referred to as a transport model (or impurity transport model to distinguish it from, e.g., an energy transport model or majority species plasma transport model). This type of modelling typically involves solving a set of equations of the form:

$$\frac{\partial n_z}{\partial t} = -\frac{1}{r} \frac{\partial}{\partial r} (r\Gamma_z) + \text{Sources} - \text{Sinks} \quad (2.2)$$

where n_z is the density of ionisation stage z of a particular species. The sources and sinks include:

- electron-impact ionisation from lower charge states,
- electron recombination from higher charge states,
- charge exchange recombination with neutrals.

The particle flux, Γ_z , is described by either a plasma model or it can be ‘measured’ by least-squares fitting based on forward modelling (see section 4.4).

To describe the ionisation and recombination from and to a given ionisation state, it is necessary to build up an atomic model to give effective ionisation

and recombination coefficients. The highest quality coefficients come from a collisional–radiative model. The procedure for the determination of these coefficients is detailed in section 2.3.3 and the calculation of these data for heavy species (e.g. tungsten) is one of the main outputs of the present work, as discussed in chapter 3.

2.3.1.4 Spectral features

We define a spectral feature (i.e. special feature) to be a group of connected lines from a collisional–radiative model parameterised according to physical parameters, typically those which would be used in a fitting procedure. The justification for these features was given in sections 2.2.2, 2.2.3 and 2.2.4. All of these examples contained interconnected lines which must be treated together in order to perform self-consistent modelling or multi-parameter fits.

A special feature is general in that it may retain information about the origins of individual lines (i.e. the transitions they correspond to) or the lines may be bundled together. This definition also allows special features to describe both quasi-continuum (see chapter 3) and true-continuum radiation. Two special features in particular are developed in this thesis, one for the modelling of soft x-ray helium-like emission is developed in section 2.4 and one more suited to the modelling of heavy species in section 3.2.1.

2.3.1.5 Metastable-resolution

The GCR project calculates and provides self consistent atomic data primarily for the fusion community (Summers 1999), but is also useful to the astrophysical community. It builds upon the generalised collisional–radiative (GCR) (Summers and Hooper 1983) picture. In this level of approximation, metastable (long lived) states are assumed to evolve on the same timescales as the plasma evolves. Metastable states have lifetimes of (Summers 1999)

$$\tau_m \sim \frac{10}{Z^8} \text{ s.} \quad (2.3)$$

Excited states, on the other hand, are very short lived and have lifetimes typically of

$$\tau_{ex} \sim \frac{10^{-8}}{Z^4} \text{ s.} \quad (2.4)$$

There also exists a decay time for doubly-excited (autoionising) states which scales as

$$\tau_{auto} \sim \frac{10^7}{N_e} (Z + 1)^2 \left(\frac{I_H}{kT_e} \right)^{\frac{1}{2}} \exp \left(\frac{E_I}{kT_e} \right) \text{ s.} \quad (2.5)$$

The different timescales are ranked as follows,

$$\tau_p \sim \tau_m \gg \tau_{ex} \gg \tau_{auto}, \quad (2.6)$$

where τ_p is the timescale at which the plasma evolves³.

Thus, for application to many aspects of the spectral emission from fusion plasmas, the derived atomic data provided must be metastable-resolved. This means that ionisation and recombination rates must be from metastable to metastable (for the purposes of modelling, we refer to a ground state as simply being one of the metastable states) and the emission coefficients for radiation emitted from the plasma must be based on metastable, and not ionic, densities. The metastable-resolved coefficients described here are the main outputs of the GCR project (O’Mullane and Summers, unpublished).

GCR-modelling is the theoretical cornerstone of the present work in terms of the calculation of data to enter the GCR-model, the modelling itself and the application of the models to experiment.

2.3.2 Population structure

Consider an ion, X^{z+} , of the element X with adjacent ionisation stages $X^{(z+1)+}$ and $X^{(z-1)+}$. We separate the levels within the ion X^{z+} into

- metastable levels — long-lived levels (including the ground state) indexed by Greek indices and denoted as X_ρ^{z+} , X_σ^{z+} etc.

³For non-fusion plasmas the plasma timescales can be much slower or faster than the rate at which the metastables evolve.

- ordinary levels — short-lived levels indexed by Roman indices and denoted as X_i^{z+} , X_j^{z+} etc.

We denote the population densities of an ordinary level by N_i , a metastable level by N_ρ and a metastable level of the parent ion (i.e. $X^{(z+1)+}$) by N_ρ^+ . It is assumed that the populations of the metastable levels are known. These would typically come from a transport model (see section 4.4) or an ionisation balance calculation (see section 2.3.3). We also assume that the free electron density, N_e , the proton density, N_p , and the neutral hydrogen density, N_H , are all known. These are considered inputs to the collisional–radiative model. Of course, in practice, these can be free parameters and varied in a fitting procedure should one wish to determine, e.g., the electron density.

Let M denote the number of metastables, O the number of ordinary levels and M^+ the number of metastable levels in the parent ion. The statistical balance equations then take the form

$$\sum_{j=1}^O C_{ij} N_j = - \sum_{\sigma=1}^M C_{i\sigma} N_\sigma + \sum_{\rho=1}^{M^+} N_e N_\rho^+ r_{\rho \rightarrow i} + \sum_{\rho=1}^{M^+} N_H N_\rho^+ q_i^{(\text{CX})} \quad i \in [1, O]. \quad (2.7)$$

C_{ij} and $C_{i\sigma}$ are elements of the collisional–radiative matrix, $r_{\rho \rightarrow i}$ is the free electron recombination directly to the level i from the parent metastable ρ and $q_i^{(\text{CX})}$ is the charge exchange (CX) recombination coefficient from neutral hydrogen directly to level i . The element C_{ij} of the collisional–radiative matrix is composed as

$$C_{ij} = -A_{j \rightarrow i} - N_e q_{j \rightarrow i}^{(e)} - N_p q_{j \rightarrow i}^{(p)} \quad i \neq j \quad (2.8)$$

where $A_{j \rightarrow i}$ is the radiative rate (see section 2.3.4.2) and $q_{j \rightarrow i}^{(e)}$ and $q_{j \rightarrow i}^{(p)}$ are the rate coefficients for electron (e) and proton (p) induced transitions (see section 2.3.4.3). The diagonal elements of the collisional–radiative matrix (C_{ii}) are composed differently:

$$C_{ii} = \sum_{j < i} A_{i \rightarrow j} + N_e \sum_{j \neq i} q_{i \rightarrow j}^{(e)} + N_p \sum_{j \neq i} q_{i \rightarrow j}^{(p)} + N_e q_i^{(I)} \quad (2.9)$$

this term represents the total loss rate from level i with $q_i^{(I)}$ the electron-impact ionisation rate coefficient. The solution for an ordinary level, j , is then,

$$\begin{aligned}
N_j &= - \sum_{i=1}^O C_{ji}^{-1} \sum_{\sigma=1}^M C_{i\sigma} N_\sigma + \sum_{i=1}^O C_{ji}^{-1} \sum_{\sigma=1}^{M^+} r_{\sigma \rightarrow i} N_e N_\sigma^+ \\
&\quad + \sum_{i=1}^O C_{ji}^{-1} \sum_{\sigma=1}^{M^+} q_{\sigma \rightarrow i}^{(\text{CX})} N_{\text{H}} N_\sigma^+ \\
&\equiv \sum_{\sigma=1}^M \mathcal{F}_{j\sigma}^{(\text{exc})} N_e N_\sigma + \sum_{\sigma=1}^M \mathcal{F}_{j\sigma}^{(\text{rec})} N_e N_\sigma^+ + \sum_{\sigma=1}^M \mathcal{F}_{j\sigma}^{(\text{CX})} N_{\text{H}} N_\sigma^+
\end{aligned} \tag{2.10}$$

where the $\mathcal{F}_{j\sigma}^{(\text{exc})}$, $\mathcal{F}_{j\sigma}^{(\text{rec})}$ and $\mathcal{F}_{j\sigma}^{(\text{CX})}$ are, respectively, the effective contributions to the excited populations from excitation from the metastables, from free electron capture from the parent metastables and from charge exchange recombination from neutral hydrogen onto the parent metastables. All of these coefficients depend on both density and temperature and the actual populations of an ordinary level may be obtained if the dominant population densities are given.

For transition $j \rightarrow k$, the emissivity, $\epsilon_{j \rightarrow k}$, of the spectral line is then given by,

$$\begin{aligned}
\epsilon_{j \rightarrow k} &= A_{j \rightarrow k} \sum_{\sigma=1}^M \mathcal{F}_{j\sigma}^{(\text{exc})} N_e N_\sigma + A_{j \rightarrow k} \sum_{\sigma=1}^{M^+} \mathcal{F}_{j\sigma}^{(\text{rec})} N_e N_\sigma^+ \\
&\quad + A_{j \rightarrow k} \sum_{\sigma=1}^{M^+} \mathcal{F}_{j\sigma}^{(\text{CX})} N_{\text{H}} N_\sigma^+.
\end{aligned} \tag{2.11}$$

It can be seen that the photon emissivity coefficients as outlined in section 2.3.1.1, can then be simply extracted according to,

$$\mathcal{P}\mathcal{E}\mathcal{C}_{\sigma, j \rightarrow k}^{(\text{exc})} = A_{j \rightarrow k} \mathcal{F}_{j\sigma}^{(\text{exc})}, \tag{2.12}$$

$$\mathcal{P}\mathcal{E}\mathcal{C}_{\sigma, j \rightarrow k}^{(\text{rec})} = A_{j \rightarrow k} \mathcal{F}_{j\sigma}^{(\text{rec})}, \tag{2.13}$$

$$\mathcal{P}\mathcal{E}\mathcal{C}_{\sigma, j \rightarrow k}^{(\text{CX})} = A_{j \rightarrow k} \mathcal{F}_{j\sigma}^{(\text{CX})}. \tag{2.14}$$

The \mathcal{S}/\mathcal{XB} s (i.e. reciprocal photon efficiencies), as described in section 2.3.1.2, can also be extracted according to

$$\mathcal{S}/\mathcal{XB}_{\sigma,j \rightarrow k} = \frac{1}{A_{j \rightarrow k} \mathcal{F}_{j\sigma}^{(\text{exc})}} \sum_{\rho=1}^{M^+} S_{\text{CD},\sigma \rightarrow \rho}, \quad (2.15)$$

where $S_{\text{CD},\sigma \rightarrow \rho}$ is the collisional ionisation rate from metastable σ of X^{z^+} to the metastable parent, ρ , of $X^{(z+1)^+}$.

2.3.3 Ionisation balance

Starting with the collisional–radiative formalism, it is possible to obtain effective ionisation and recombination rate coefficients in finite density plasmas. This was first established by Bates *et al* (1962). It is possible to perform this analysis in keeping with the metastable-resolved picture as used in section 2.3.2. However, since the application of metastable-resolved ionisation balance data does not play a major role in this thesis we choose to present the details assuming only the ground state is significantly populated. We discuss briefly at the end of this section the implications of applying metastable-resolution.

As in section 2.3.2, an ion in a plasma is viewed as being composed of a complete set of levels indexed by i and j and a set of radiative and collisional couplings between them denoted by C_{ij} to which are added direct ionisations from each level of the ion to the next ionisation stage (coefficient $q_i^{(I)}$) and direct recombinations to each level of the ion from the next ionisation stage (coefficient r_i). Without loss of generality, we can ignore other ionisation stages, provided that couplings to and from them are only via ground states. For each level there is a total loss rate coefficient for its population denoted by

$$-C_{ii} = \sum_{j \neq i} C_{ji} + N_e q_i^{(I)}. \quad (2.16)$$

The population of any level is determined by the balance of processes populating and depopulating it, as described in detail in section 2.3.2. Suppose the dominant populations are a recombined ion ground state ($i = 1$) and a recom-

binion ion ground state denoted by +. These two states alone are assumed to be significantly populated (compared to the excited level populations) from the point of view of the ionisation balance problem. With this assumption, all excited levels are relaxed and so the quasi-equilibrium statistical balance is,

$$\frac{dN_1}{dt} = \sum_{j \neq 1} C_{1j} N_j + C_{11} N_1 + N_e N_+ r_1, \quad (2.17)$$

$$0 = \sum_{j \neq 1} C_{ij} N_j + C_{i1} N_1 + N_e N_+ r_i. \quad (2.18)$$

In matrix form these become

$$\begin{bmatrix} \frac{d}{dt} N_1 \\ 0 \end{bmatrix} = \begin{bmatrix} C_{11} & C_{1j} \\ C_{i1} & C_{ij} \end{bmatrix} \begin{bmatrix} N_1 \\ N_j \end{bmatrix} + N_e N_+ \begin{bmatrix} r_1 \\ r_i \end{bmatrix}, \quad (2.19)$$

where C_{i1} is a column vector, C_{1j} is a row vector, and C_{ij} is a matrix.

From section 2.3.2 we know that the populations of the excited levels in quasi-equilibrium, N_j^{eq} , are given by,

$$N_j^{\text{eq}} = -N_e N_+ \sum_{i \neq 1} C_{ji}^{-1} r_i - \sum_{i \neq 1} C_{ji}^{-1} C_{i1} N_1. \quad (2.20)$$

Substitution of 2.20 into 2.19 allows identification of an effective ionisation coefficient, S_{CD} , given by

$$S_{CD} = C_{11} - \sum_{j \neq 1} \sum_{i \neq 1} C_{1j} C_{i1}^{-1} C_{ij} \quad (2.21)$$

and an effective recombination coefficient, α_{CD} , given by

$$\alpha_{CD} = r_1 - \sum_{j \neq 1} \sum_{i \neq 1} C_{1j} C_{ji}^{-1} r_i, \quad (2.22)$$

where the CD denotes ‘collisional-dielectronic’ to indicate that the coefficients include collisional effects and recombination/ionisation processes (including dielectronic recombination), these are the coefficients whose use was described in section 2.3.1.3 and the S_{CD} is the coefficient required in the definition of an \mathcal{S}/\mathcal{XB}

(equation 2.15).

From an application viewpoint, the coefficients given above specify the contributions to the effective growth rates for the ground state population due to recombination from, and ionisation to, the state $+$, so that the time dependent equation for N_1 becomes

$$\frac{dN_1}{dt} = -N_e S_{CD} N_1 + N_e \alpha_{CD} N_+. \quad (2.23)$$

In a finite density plasma, the populations of metastables can be significant, as discussed in section 2.3.1.5 and 2.3.2. Some extension is required to the above equations to treat this correctly. We use the term ‘metastable’ to refer to both ground and metastable states and index them by ρ for the recombined ion and ν for the recombining ion. Therefore, the ion of charge state z has metastable populations N_ρ^{z+} and the recombining ion metastable populations are $N_\nu^{(z+1)+}$. It is common to call the recombining ion metastable states ‘parent’ states. Generalised collisional–radiative theory provides effective coefficients which are the metastable-resolved analogues of the ones derived above, viz.

- the ionisation coefficients — $S_{CD,\rho \rightarrow \nu}$,
- the free electron recombination coefficients — $\alpha_{CD,\nu \rightarrow \rho}$,
- the charge exchange recombination coefficients — $C_{CD,\nu \rightarrow \rho}$,
- the metastable cross-coupling coefficients — $Q_{CD,\nu' \rightarrow \nu}$,
- the parent metastable cross-coupling coefficients — $X_{CD,\rho' \rightarrow \rho}$.

Note that the latter two are only present for the case of metastable-resolution. The $Q_{CD,\rho' \rightarrow \rho}$ couples two metastable levels of the same ionisation stage together via excitation within the ionisation stage while the $X_{CD,\nu' \rightarrow \nu}$ couples them by a transition occurring via the adjacent ionisation stage, e.g., ionisation to an excited (i.e. non-metastable) level of the next ionisation stage and then recombination back to a metastable of the original ionisation stage.

The ionisation, recombination and cross-coupling coefficients are what typically enter an impurity transport model, as described in section 2.3.1.3 and discussed in detail in section 4.4. In practice, transport modelling of the core plasma

is often not done at metastable-resolution so cross-coupling coefficients are not required.

In the astrophysical domain, it is common to establish an ionisation balance equilibrium. That is, the state which a system at a given temperature and density will eventually converge upon with no transport. It is often instructive in the fusion regime to consider ionisation equilibrium where insufficient transport information exists and/or to give a first estimate of an ionisation stage distribution without the need for detailed plasma modelling. An analytical solution exists for this problem, bypassing the need to propagate a set of equations until equilibrium is reached. For brevity, the solution for the non-metastable-resolved case is given here. See Summers (1999) for more details.

Consider the evolution of populations of ions of an element in a plasma. For an element X of nuclear charge z_0 , the populations of the ionisation stages are denoted by

$$N^{(z)} : z = 0, \dots, z_0. \quad (2.24)$$

The time-dependence of the ionisation stage populations is given by the equations

$$\begin{aligned} \frac{dN^{(z)}}{dt} = & N_e S_{CD}^{(z-1 \rightarrow z)} N^{(z-1)} \\ & - \left(N_e S_{CD}^{(z \rightarrow z+1)} + N_e \alpha_{CD}^{(z \rightarrow z-1)} + N_H C_{CD, \rho \rightarrow \rho'}^{(z \rightarrow z-1)} \right) N^{(z)} \\ & + N_e \alpha_{CD}^{(z+1 \rightarrow z)} N^{(z+1)} + N_H C_{CD}^{(z+1 \rightarrow z)} N^{(z+1)}. \end{aligned} \quad (2.25)$$

This is called an unresolved or stage-to-stage picture. The coefficients are the (ordinary) collisional–radiative coefficients. In equilibrium ionisation balance, the time derivatives are set to zero and the stage populations are the solutions of the matrix equation

$$N_e \begin{bmatrix} -S_{CD}^{(0 \rightarrow 1)} & \alpha_{CD}^{1 \rightarrow 0} + (N_H/N_e) C_{CD}^{1 \rightarrow 0} & 0 & 0 \\ S_{CD}^{(0 \rightarrow 1)} & - \left(S_{CD}^{(1 \rightarrow 2)} + \alpha_{CD}^{1 \rightarrow 0} + (N_H/N_e) C_{CD}^{1 \rightarrow 0} \right) & \alpha_{CD}^{(1 \rightarrow 0)} & 0 \\ 0 & S_{CD}^{(1 \rightarrow 2)} & \cdot & \cdot \\ 0 & 0 & \cdot & \cdot \end{bmatrix} \begin{bmatrix} N^{(0)} \\ N^{(1)} \\ N^{(2)} \\ \cdot \end{bmatrix} = 0 \quad (2.26)$$

subject to the normalisation condition

$$N_{tot} = \sum_{z=0}^{z_0} N^{(z)}, \quad (2.27)$$

where N_{tot} is the number density of ions of element X in any ionisation stage. The equilibrium fractional abundances $N^{(z)}/N_{tot}$ at a set of temperatures and densities are then available for application to plasmas considered (or approximated) to be in equilibrium.

2.3.4 Fundamental atomic data

A large amount of fundamental atomic data is necessary to model a given species in typical fusion plasma conditions. Key types of data are outlined here along with explanations and discussion of how they are obtained, compared and validated, along with the applicability of different approaches.

2.3.4.1 Energy levels and wavelengths

Accurate energy levels (hence wavelengths) have been tabulated for many species, most notably in the work of Kelly (1987) and the NIST database⁴. It is noted that a lot of the data contained in the NIST database originates from Kelly (1987).

While it is possible to calculate wavelengths (see, e.g., Eissner *et al* (1974)), it tends to be the case that they are best measured. See Kelly (1987) for more details of the sources. However, for many systems the number of observed energy levels is too small or non-existent, in this case the energy levels must be calculated. Measurements for other (similar) systems are then used to benchmark the techniques.

2.3.4.2 Radiative Data

Radiative data, in the context of this thesis, is referring to anything which is a function of the N electron system and independent of external influences such as radiation fields and electron collisions. The most common form of radiative

⁴<http://physics.nist.gov/>

data is the A-value or ‘radiative rate’, denoted $A_{j \rightarrow i}$ which is the probability of an electron in a state j going to a lower (in absolute energy) state i by emitting a photon.

Transitions are categorised into different multipole types, only the lowest of which are relevant for this work, labelled:

- E0 — electric monopole⁵,
- E1 — electric dipole,
- E2 — electric quadrupole,
- M1 — magnetic Dipole.

See Eissner *et al* (1974) and Cowan (1981) for more details and expressions used in the calculation of radiative data. We note that the Cowan (Cowan 1981), SUPERSTRUCTURE (Eissner *et al* 1974) and AUTOSTRUCTURE (Badnell 1997) codes can calculate data for higher multipole transitions besides these.

These same data can be expressed in a number of equivalent ways, namely A-values, oscillator strengths and line strengths. Care has to be taken when converting between them but no further data needs to be calculated, see Eissner *et al* (1974) for details.

2.3.4.3 Excitation and de-excitation rates

Consider the electron-impact excitation ($i < j$) (or de-excitation ($i > j$)) reaction denoted by

$$X_i^{z+}(E_i) + e(\epsilon_i) \rightarrow X_j^{z+}(E_j) + e(\epsilon_j), \quad (2.28)$$

with $\epsilon_i + E_i = \epsilon_j + E_j$, where E_i is the excitation energy of the state i denoted by X_i^{z+} relative to the lowest level of the ion X^{z+} , similarly for j . Without loss of generality we assume that state j is higher in energy (i.e. closer to the continuum) than state i giving rise to $E_i < E_j$; ϵ_i is the energy of the incident electron and ϵ_j the energy of the scattered electron. The reaction can be described by a cross-section denoted by $\sigma_{i \rightarrow j}(\epsilon_i)$. Energetically, this reaction requires that

⁵We note that an electric monopole A-value is zero but the same nomenclature is also used for excitation transitions where the cross-sections are finite.

$\epsilon_i \geq \Delta E_{ij} = E_j - E_i$. The de-excitation cross-section is denoted by $\sigma_{j \rightarrow i}(\epsilon_j)$. It is preferable to use a dimensionless quantity which is symmetric between excitation and de-excitation reactions for a given i and j . This quantity, called the collision strength (introduced by Hebb and Menzel (1940) and named/used by Seaton (1953b,1955)), is denoted by $\Omega_{ij}(\epsilon)$ ⁶. As well as being symmetric, it also has the advantage that it is typically slowly-varying in energy. It is connected to the excitation and de-excitation cross-section via,

$$\Omega_{ij}(\epsilon) = \omega_i \left(\frac{\epsilon_i}{I_H} \right) \left(\frac{\sigma_{i \rightarrow j}(\epsilon_i)}{\pi a_0^2} \right) = \omega_j \left(\frac{\epsilon_j}{I_H} \right) \left(\frac{\sigma_{j \rightarrow i}(\epsilon_j)}{\pi a_0^2} \right) \quad (2.29)$$

where I_H is the ionisation potential of hydrogen, ω_i is the statistical weight of the lower level, ω_j is the statistical weight of the upper level and a_0 is the Bohr radius. Since the collision strength is slowly varying with energy, it is a more useful quantity to analyse qualitatively and compare quantitatively. Figure 2.10 indicates how differences are highlighted in plots much more easily when comparing collision strengths as opposed to cross-sections, particularly at high energies. The two pieces of data are for the $1s2s \ ^3S_1 - 1s2p \ ^1P_1$ transition in Ar^{16+} , the data are from R -matrix calculations (see section 2.5) with one set of data including a contribution from ‘top-up’ (contributions to the process from high angular momenta — see section 2.5.2.4) and the other not including this contribution. It can be seen that a comparison using collision strengths lends itself to distinguishing differences and behaviour (hence potential errors) across all energy ranges.

For a thermal plasma, i.e. one where the electrons have a Maxwellian distribution, it is useful to convolute the collision strength with an electron distribution for a temperature, T_e . The resultant quantity is then a slowly-varying function of temperature, denoted by Υ_{ij} , and defined by

$$\Upsilon_{ij} = \int_0^\infty \Omega_{ij}(\epsilon) e^{-\epsilon/kT_e} d \left(\frac{\epsilon}{kT_e} \right). \quad (2.30)$$

Υ_{ij} is then related to the excitation rate coefficient $q_{i \rightarrow j}(T_e)$ and de-excitation rate coefficient $q_{j \rightarrow i}(T_e)$ as required for the population modelling described previously

⁶The distinction between ϵ being the incident or ejected energy is sometimes ambiguous in the literature.

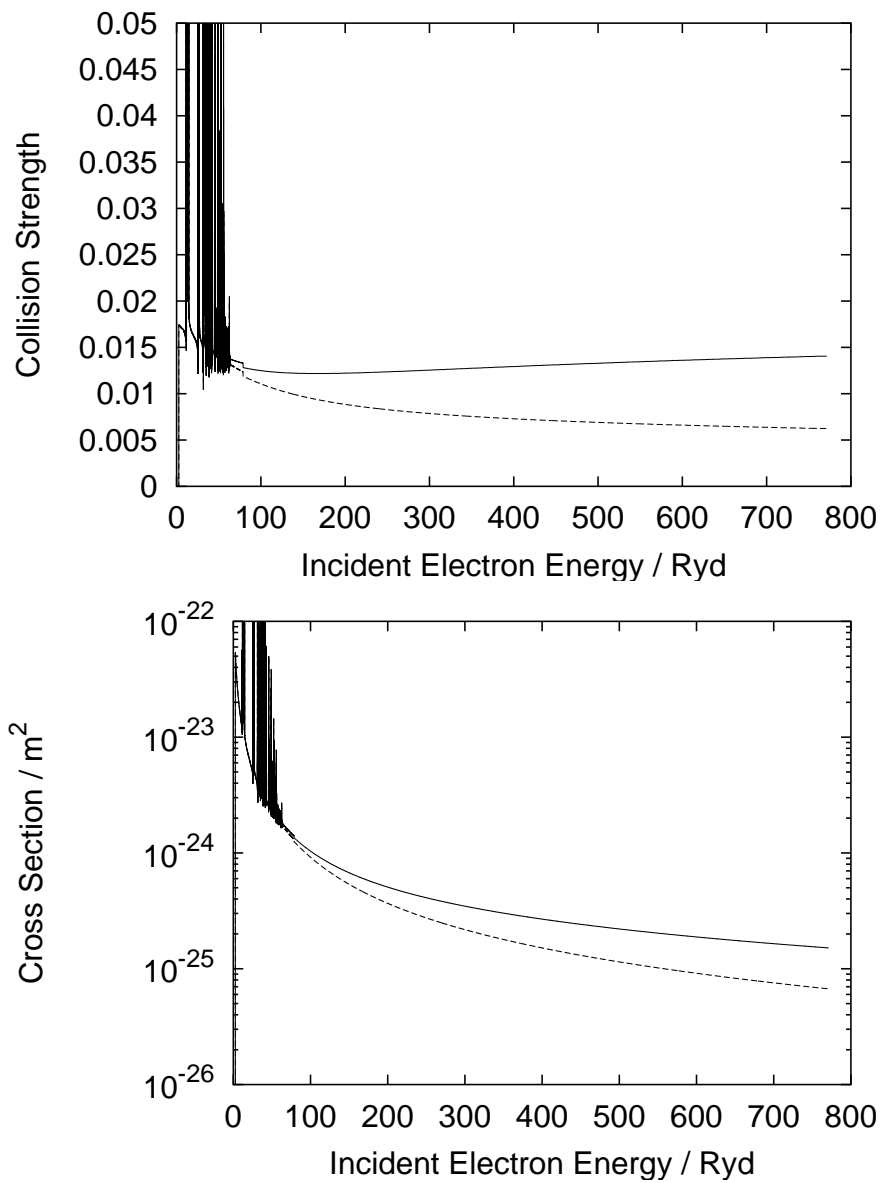


Figure 2.10: Two plots of the $1s2s^3S_1 - 1s2p^1P_1$ transition in Ar^{16+} , the upper plot shows this comparison using collision-strengths while the lower plot shows the same data compared using cross-sections. The solid curves include a contribution from ‘top-up’ from high angular momenta while the dashed curves do not.

in section 2.3.2 by

$$q_{i \rightarrow j}(T_e) = 2\sqrt{\pi}\alpha c a_0^2 \frac{1}{\omega_i} e^{-\Delta E_{ij}/kT_e} \left(\frac{I_H}{kT_e}\right)^{\frac{1}{2}} \Upsilon_{ij} \quad (2.31)$$

and

$$q_{j \rightarrow i}(T_e) = 2\sqrt{\pi}\alpha c a_0^2 \frac{1}{\omega_j} \left(\frac{I_H}{kT_e}\right)^{\frac{1}{2}} \Upsilon_{ij} \quad (2.32)$$

where α is the fine structure constant and c is the speed of light. Note these equations satisfy the relationship

$$q_{j \rightarrow i}(T_e) = \frac{\omega_i}{\omega_j} e^{\Delta E_{ij}/kT_e} q_{i \rightarrow j}(T_e). \quad (2.33)$$

Burgess and Tully (1992) introduced the ‘C-plot’ which maps the whole collision strength or effective collision strength onto a finite range of $[0, 1]$ corresponding to the physical range of $[0, \infty)$. Designed to reveal both the low energy and high energy behaviour in a balanced way, the mapping is dependant on the type of transition. It is also numerically and computationally more efficient and accurate to perform interpolations and integrations on reduced energy grids of this type. For more details see Burgess and Tully (1992), or see section 2.5 where use is made of these plots.

The collision strengths (or cross-sections) as described above can come for a variety of different sources, these are summarised along with advantages and disadvantages in table 2.1.

There exist a number of key physical processes affecting collision strengths (and hence effective collision strengths) which have been developed as part of the present work. Analysis and discussion is given in section 2.5. It is, however, worthwhile to highlight here the importance of resonances and the damping (radiation and Auger) of these resonances.

Consider an electron impacting a helium-like ion. During the process of excitation, the system will become lithium-like as it captures the incoming electron. If the energy of the total system (i.e. electron and helium-like system) corresponds to an allowed energy level in the intermediate lithium-like system then a resonance will occur. This is observed as a sharp increase in cross-section at the given

Type	Advantages	Disadvantages
Measurement	Real Results	Restricted energy ranges
Plane Wave Born	Quick to perform	Baseline quality results
Unitarised Born	Quick to perform	Baseline quality results
Distorted-Wave	Fairly quick	No resonances
CCC ^a	Valid at all energies	Slow resonance resolution
<i>R</i> -matrix	Rapid resonance resolution	Not valid at all energies
TDSE ^b	Very accurate	Very slow

^a — Convergent Close Coupling

^b — Time Dependant Schrödinger Equation

Table 2.1: Summary of main cross-section determination techniques along with the major advantages and disadvantages

incoming electron energy.

The effect of this resonance can be reduced if the intermediate lithium-like state has branches other than re-ejection of an electron to remain excited (i.e. Auger breakup). The most usual other process is for the lithium-like system to undergo a radiative transition (i.e. we have a DR process, not an excitation process). This ‘damps’ the effect of the resonance by an amount given by:

$$\text{Damping} = \frac{A_a}{A_r + A_a} \quad (2.34)$$

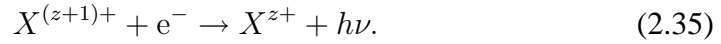
where A_r is the radiative probability (i.e. damping) and A_a is the Auger probability (i.e. the excitation reaction takes place). This was first implemented within the *R*-matrix framework by Robicheaux *et al* (1995) and was numerically refined as part of the present work⁷.

Another damping process is Auger damping (see Gorczyca and Robicheaux (1999)), which is discussed in detail in section 2.5.2.3. This had not previously been included in an *R*-matrix excitation calculation. Subsequent work by Bautista *et al* (2003) confirms the work presented in this thesis (also published in Whiteford *et al* (2002)) on the Auger damping process.

⁷See <http://amdpp.phys.strath.ac.uk/rmatrix/serial/UPDATES>, update dated 07/02/02.

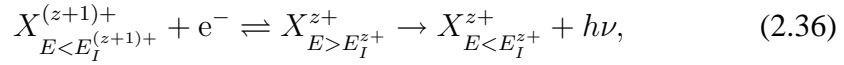
2.3.4.4 Recombination rates

The recombination of an ion $X^{(z+1)+}$ to ionisation state X^{z+} can be achieved by a number of different physical processes. Key in a fusion plasma environment are radiative recombination and dielectronic recombination. Radiative recombination is the simplest, occurring when an electron ‘falls’ into the potential well created by the target ion and emits a photon,



These rates can be calculated by a number of approximations, see section 3.3.3.2 for more details.

Dielectronic recombination is often the dominant recombination process in plasmas. It is a two stage process starting with resonance capture then radiative stabilisation. The overall rate is reduced by Auger decay occurring before the radiative stabilisation can occur. It can be described schematically by

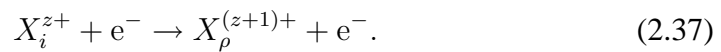


where the intermediate state ($X_{E > E_I^{z+}}^{(z+1)+}$) is autoionising.

Detailed calculations of these rates are given in sections 3.3.3.2 and 3.3.5, with application to tungsten discussed in section 3.5.2.

2.3.4.5 Ionisation rates

The ionisation of an ion X^{z+} to ionisation state $X^{(z+1)+}$ can be achieved by a number of different physical processes such as ion collision, electron collision and photo-ionisation. The main one of interest in the fusion regime is electron-impact ionisation. This process can be subdivided further into direct ionisation and stepwise ionisation along with excitation–autoionisation (EA). Direct ionisation occurs when an incoming electron has enough energy to ionise the target ion. It can be represented thus,



This is the simplest form of ionisation. There also exists the possibility that an ion is excited into a higher state and then another electron impact completes the ionisation process, this is known as stepwise ionisation. The second electron impact has to compete with the radiative decay of the excited ion, leading to the effect only being important at higher densities. Since the process can also occur with less energetic electrons than the direct ionisation it is often the dominant process at low temperatures.

Excitation–autoionisation (EA) is where the electron-impact excites the ion into a state from which it can autoionise (i.e. Auger decay), this autoionisation rate competes with a radiative stabilisation rate. The intermediate state of this process is identical to the intermediate state found in the DR process as described in section 2.3.4.4.

Techniques to calculate ionisation rates based on electron impact can be logically divided into three groups, namely semi-empirical, perturbative and non-perturbative methods.

Semi-empirical ones include Lotz (Lotz 1968), ECIP (Burgess *et al* 1977), Burgess-Chidichimo (Burgess and Chidichimo 1983) and BEB (Kim and Rudd 1994; Kim 2001). The Burgess-Chidichimo approximation includes the effects of EA. The BEB method also includes EA, the implementation is to use Born excitation rates as discussed in Kim (2001).

Perturbative techniques are usually based on a distorted-wave (DW) type approach as recently used by Loch *et al* (2002b) to calculate the ionisation rates of every stage of krypton. They used a configuration-average distorted-wave (CADW) approach and generated term and level resolved data using the angular splitting techniques as given by Sampson (1986). A more detailed discussion of these calculations (which form part of the present work) along with illustrative results can be found in section 3.3.5.

Non perturbative theories include R -matrix with pseudo-states (RMPS) as originally formulated by Bartschat *et al* (1996)⁸, convergent close coupling (CCC) (Bray 1993) and time dependent close coupling (Pindzola and Robicheaux 1996). For neutrals and near neutrals it is generally necessary to use one of these non-perturbative approaches to obtain acceptable precision. However, it is often the

⁸We note that this formulation was incomplete — see Badnell and Gorczyca (1997).

case that for these complex systems the ECIP approach is in surprising agreement with non-perturbative theories — in the case of neutral lithium, ECIP is within 40% of CCC whereas DW is significantly worse (Loch, 2003), this level of agreement should not be extrapolated or relied upon, however.

2.3.4.6 Radiation driven processes

Radiation driven processes, namely stimulated emission, photo-excitation and photo-ionisation are usually negligible for fusion application in the core plasma. A recent study was carried out by Reiter *et al* (2002), confirming that opacity effects could be important in the divertor, where the density is greater. Work in a similar area was performed by Behringer (1998) who used escape factor methods to model opacity. The latter modelling was used by Loch (2001) and implemented within the ADAS Project (Summers 1999). The primary optically thick lines (i.e. lines where re-absorption is important) in the magnetically confined fusion regime are those of the Lyman series of hydrogen. Opacity is far more important in astrophysics and laser induced plasmas. Detailed analysis of the upper solar atmosphere can be found in Brooks *et al* (2000) and Fischbacher *et al* (2000, 2002).

2.4 Special feature analysis of helium- and lithium-like systems

2.4.1 Introduction

The spectral emission of highly-charged helium-like ions has been used heavily in the diagnostic analysis of solar coronal and laboratory plasmas since the 1960s (Gabriel 1972). Its value stems from the fact that the ionisation equilibrium fractional abundance of the helium-like ionisation stage has an extended temperature range. This leads to large spectral intensities in temperature-stratified plasmas such as the chromosphere and corona. Thus, collectively, the helium-like ionisation stages of elements span virtually all temperature regimes of a plasma. Hence, a particular zone of a plasma may be studied by the emission lines of the helium-like ion which exists there. In recognition of this, soft x-ray instruments such as

the bent-crystal spectrometer (BCS) on the *SMM* satellite were targeted on these lines. This practice which has continued to the present with satellites such as *YOHKOH* for solar studies and *Chandra & XMM-Newton* for deep-space observations. Using these instruments, soft x-ray emission from cosmological objects is now observed with unprecedented resolution. Astrophysical phenomena such as galactic cooling flows and accretion columns around black holes show soft x-ray emission of iron, but often in contrasting excitation conditions.

In view of these new high-quality observations, it is timely to re-appraise the atomic data and modelling entering the interpretation of helium-like systems. The differences between low density photoionised environments and the higher density collisionally ionised environments warrant the incorporation of more sophisticated data.

Argon and iron have been chosen for this work, partly because of their importance in fusion and astrophysical plasmas, but also because they display the range of more complex collisional aspects now recognised as necessary to obtain high-precision cross-sections.

In magnetic confinement fusion, argon is a species of choice for the modification of edge conditions by radiative cooling (see chapter 1) and this has led to the decision to establish argon as a reference species. Diagnostic experiments are planned at the EFDA-JET facility to compare and evaluate measured argon spectra against modelled emission. Also, the International Atomic Energy Agency (IAEA) has established a diagnostics collaborative research proposal (CRP), of which the assembly of argon electron-impact data (as presented in this thesis) is a part. Spectroscopic deduction of argon concentrations uses core observations of the helium- and lithium-like ionisation stages. Such deduction exploits the soft x-ray along with visible lines of charge exchange spectroscopy. The high-quality atomic data presented here is part of the theoretical input to these activities.

High-resolution soft x-ray spectra of both argon and iron are measured at the TEXTOR tokamak (Marchuk *et al* 2003, Marchuk 2004). A significant concentration of thermal neutral hydrogen can penetrate to the core of the plasma in this device. The familiar helium-like resonance line spectral vicinities show small modifications of relative intensities, as discussed in the case of argon by Rosmej *et al* (1999). These modifications are believed to be due to the disturbing effect of

charge exchange from the thermal neutral hydrogen on the conventional electron-impact driven emission. The separation of these effects places a high demand for accuracy on the electron-impact collision cross-section calculations.

The data and GCR calculations described in this thesis allow, in principle, prediction of the complete spectrum in wavelength or pixel space as observed by a spectrometer. This ‘forward modelling’ is our preferred route for application in the fusion plasma regime and for handling widely varying spectral resolutions as illustrated in figure 2.11. We use certain terminologies. A connected group of spectrum lines is called a feature primitive, feature or super-feature depending upon whether the connections are via pure branching ratios, via an excited level population balance or via an ionisation balance. The generic name ‘feature’ is used for all three types of connection. Ionisation balance in this context may include transport and/or transient influences and reflect the geometry of the plasma. The feature is a local quantity but the super-feature is non-local. It is super-features which are observed along a line of sight through the plasma and which we seek to predict. In the present situation, we have two super-features, namely the satellite line and continuum special features. Each of these are functions of plasma parameters. In spectral measurements on real plasmas, additional unconnected spectrum lines (called ordinary lines) from different ions or elements may lie in the observed spectral segment possibly overlaying the connected group. Special spectral feature fitting distinguishes the ordinary lines and background from the special features and conducts a non-linear search for the parameters of both simultaneously. Our assembly of data, which is designed to allow rapid creation of the superfeatures, follows the prescriptions of the ADAS Project (Summers, 1999).

The plan for the remainder of this section is as follows: in section 2.4.2 an overview is given of the main transitions making up the satellite line special feature and some qualitative discussion is presented. In section 2.4.3 we describe the generalised collisional–radiative approach to obtaining the satellite line feature, which allows us to extend the region of validity of the work to high densities. This section is much more rigorous than that qualitative arguments presented in section 2.4.2. In section 2.4.4 we focus on the population calculation and in section 2.4.5 we briefly describe the corresponding calculation of the continuum

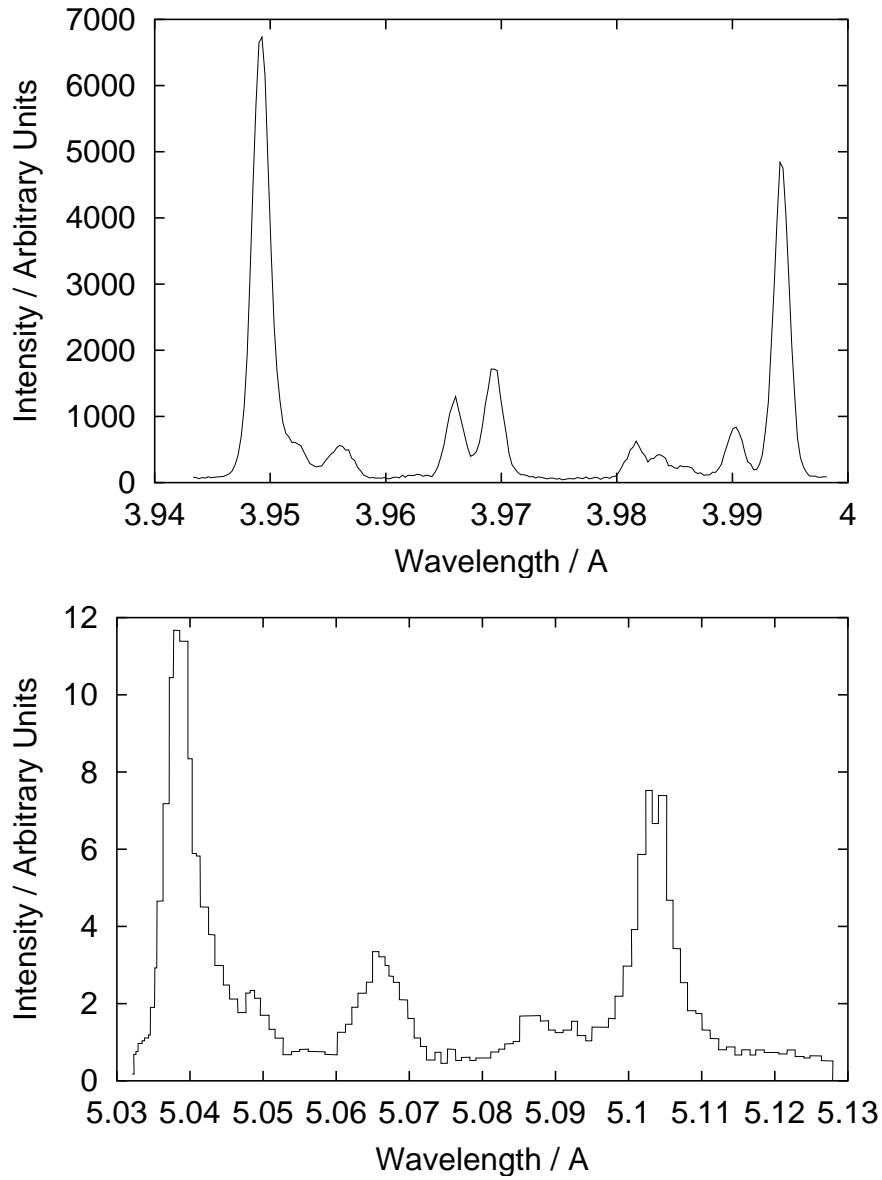


Figure 2.11: He-like spectra of different resolution, the lower plot shows spectra recorded by the YOHKOH spacecraft of S^{14+} with a poor resolution and the upper plot argon spectra from the TEXTOR tokamak at a much higher resolution

feature. Fundamental atomic data is then discussed in section 2.5, in keeping with the application-driven presentation used in this thesis. In these sections, we assess in some detail the components and behaviours of satellite feature populations and emission and the progress in precision of the new study in comparison with earlier work. In section 2.4.6 we address the full creation of the spectral interval and its fitting to observation. Section 2.4.7 gives some examples of fits to measured spectra.

2.4.2 Overview of the spectral emission

The transitions giving rise to the helium-like spectral interval emission are four transitions from the helium-like system itself and further transitions from the lithium-like system. Important transitions for the helium- and lithium-like systems are presented in table 2.2, following the notation of Gabriel (1972) for the labelling of each line, along with data for Ar¹⁵⁺ and Ar¹⁶⁺.

Note that the q and s lines have the same upper and lower levels in table 2.2. The difference is in the parentage of the upper level, the q line comes from a (¹P)²P term while the s lines comes from a (³P)²P term, similarly (and respectively) for the r and t lines. See also section 2.5.2.2 and Whiteford *et al* (2002) for a discussion of this point.

As an example, we consider the *w* and *z* line. The radiative rate of the *w* line is far higher than that of the *z* line so one would, naively, expect greater emission (which would be true if the populations of the upper levels were the same). The *z* line has a branching ratio of exactly 1⁹ (since no levels lie below it) so, in the absence of any other processes (i.e. at low density), any population in the 1s2s³S₁ will result in emission no matter what the radiative rate — see chapter 1 for the discussion of the low density coronal approximation where the line emission is only dependent on the excitation rate and the branching ratio. Within the ion, the depopulation of the 1s2s³S₁ level is given by

$$\frac{dN}{dt} = A_{1s2s^3S_1 \rightarrow 1s^2^1S_0} + N_e \sum_{i \neq 1s2s^3S_1} q_{1s2s^3S_1 \rightarrow i}. \quad (2.38)$$

⁹We note that the *w* line also has a branching ratio of approximately 1.

Line	Ion	Transition	$\lambda_{ij} / \text{\AA}$	A_{ij}^r / s^{-1}	A_{ij}^a / s^{-1}
w	Ar ¹⁶⁺	1s2p ¹ P ₁ – 1s ² ¹ S ₀	3.9492	1.08×10^{14}	—
x	Ar ¹⁶⁺	1s2p ³ P ₂ – 1s ² ¹ S ₀	3.9660	4.04×10^8	—
y	Ar ¹⁶⁺	1s2p ³ P ₁ – 1s ² ¹ S ₀	3.9695	1.82×10^{12}	—
z	Ar ¹⁶⁺	1s2s ³ S ₁ – 1s ² ¹ S ₀	3.9943	4.80×10^6	—
a	Ar ¹⁵⁺	1s2p ² ² P _{$\frac{3}{2}$} – 1s ² 2p ² P _{$\frac{3}{2}$}	3.9852	1.42×10^{14}	1.04×10^{13}
j	Ar ¹⁵⁺	1s2p ² ² D _{$\frac{5}{2}$} – 1s ² 2p ² P _{$\frac{3}{2}$}	3.9941	1.53×10^{14}	2.28×10^{14}
k	Ar ¹⁵⁺	1s2p ² ² D _{$\frac{3}{2}$} – 1s ² 2p ² P _{$\frac{1}{2}$}	3.9900	1.44×10^{14}	1.67×10^{14}
q	Ar ¹⁵⁺	1s2s2p ² P _{$\frac{3}{2}$} – 1s ² 2s ² S _{$\frac{1}{2}$}	3.9815	9.91×10^{13}	3.24×10^{12}
r	Ar ¹⁵⁺	1s2s2p ² P _{$\frac{1}{2}$} – 1s ² 2s ² S _{$\frac{1}{2}$}	3.9836	8.29×10^{13}	1.60×10^{13}
s	Ar ¹⁵⁺	1s2s2p ² P _{$\frac{3}{2}$} – 1s ² 2s ² S _{$\frac{1}{2}$}	3.9678	8.07×10^{12}	9.41×10^{13}
t	Ar ¹⁵⁺	1s2s2p ² P _{$\frac{1}{2}$} – 1s ² 2s ² S _{$\frac{1}{2}$}	3.9687	2.43×10^{13}	8.18×10^{13}

Table 2.2: Summary of important lines for helium-like argon soft x-ray spectra, along with the corresponding transition. Data for argon are also included, namely, the wavelength of each transition λ_{ij} , their radiative rate, A_{ij}^r , and the Auger rate, A_{ij}^a , for the doubly excited states. The entries at the top of the table correspond to emission from the helium-like system and at the bottom emission from the lithium-like system.

Inspection of this equation shows that, at low density, the main depopulating process is line emission and, as the electron density increases, the line emission will fall off as the excitation/de-excitation becomes significant. The ratio of the w to z line is a good density diagnostic for this reason.

2.4.3 Theory of the satellite line special feature

The dielectronic satellite line special feature is the connected set of spectrum lines composed of: the manifold of dielectronic recombination stabilisation photons $\lambda_{\sigma,nl \rightarrow \sigma',nl}$ occurring in the recombination of the ion A_{ρ}^{+z} via the parent excited state A_{σ}^{+z} with different spectators nl ; a similar manifold $\lambda_{\sigma,nl \rightarrow \sigma',nl}$ associated with the radiative decay of resonances $A_{\sigma,nl}^{+z-1}$ formed by inner-shell excitation of an ion A_{ρ}^{+z-1} ; and the manifold of photons $\lambda_{\sigma J \rightarrow \rho' J'}$ associated with transitions between the A_{σ}^{+z} and $A_{\rho'}^{+z}$ complexes induced by electron-impact excitation of A_{ρ}^{+z} or recombination of the ion A_{ρ}^{+z+1} . We broadly adopt the notation that σ refers to excited parents in doubly-excited recombined systems and to excited

recombining systems, ρ refers to ground or metastable parents in singly-excited recombined systems and to ground or metastable recombining systems.

The present study spans from light ions of low charge-state to heavy ions of high charge-state and are conducted in intermediate coupling (IC). It will be convenient to identify levels with both $J_p j$ and LS nomenclatures. We use the notation $A_{\sigma, nlJ}^{+z-1}$ for a resolved level of distinguishable parent in either scheme for the general development. Using equation 2.10, the population of the level $A_{\sigma, nlJ}^{+z-1}$ may then be written as

$$N_{\sigma, nlJ}^{+z-1} = \sum_{\rho=1}^{M^{(z-1)}} \mathcal{F}_{\sigma, nlJ; \rho}^{(exc)} N_e N_{\rho}^{+z-1} + \sum_{\rho=1}^{M^{(z)}} \mathcal{F}_{\sigma, nlJ; \rho}^{(rec)} N_e N_{\rho}^{+z} \quad (2.39)$$

and that of the level A_{σ}^{+z} may be written as

$$N_{\sigma}^{+z} = \sum_{\rho=1}^{M^{(z)}} \mathcal{F}_{\sigma; \rho}^{(exc)} N_e N_{\rho}^{+z} + \sum_{\rho=1}^{M^{(z+1)}} \mathcal{F}_{\sigma; \rho}^{(rec)} N_e N_{\rho}^{+z+1} \quad (2.40)$$

where the factors $\mathcal{F}_{\sigma, nlJ; \rho}^{(exc)} N_e N_{\rho}^{+z-1}$, $\mathcal{F}_{\sigma, nlJ; \rho}^{(rec)} N_e N_{\rho}^{+z}$ are the contributions from inner shell excitation and dielectronic recombination for the $z - 1$ times ionised ion, and the factors $\mathcal{F}_{\sigma; \rho}^{(exc)} N_e N_{\rho}^{+z}$, $\mathcal{F}_{\sigma; \rho}^{(rec)} N_e N_{\rho}^{+z+1}$ are the contributions from excitation and recombination for a z times ionised ion. The sums are over the dominant driver populations (ground and metastables) of each ionisation state, such as $M^{(z)}$

of stage z . The emissivity function of a satellite line may be written as

$$\begin{aligned} \frac{G_{\sigma, nlJ \rightarrow \rho', nlJ'}}{N_e N^{tot}} &= \left(\frac{N_1^{+z}}{N_e N^{tot}} \right) \left(\sum_{\rho=1}^{M^{(z-1)}} [A_{\sigma, nlJ \rightarrow \rho', nlJ} \mathcal{F}_{\sigma, nlJ; \rho}^{(exc)}] \frac{N_\rho^{+z-1}}{N_1^{+z}} \right. \\ &\quad \left. + \sum_{\rho=1}^{M^{(z)}} [A_{\sigma, nlJ \rightarrow \rho', nlJ'} \mathcal{F}_{\sigma, nlJ; \rho}^{(rec)}] \frac{N_\rho^{+z}}{N_1^{+z}} \right) \end{aligned} \quad (2.41)$$

$$\begin{aligned} &= \left(\frac{N_1^{+z}}{N_e N^{tot}} \right) \left(\sum_{\rho=1}^{M^{(z-1)}} \mathcal{E}_{\sigma, nlJ \rightarrow \rho', nlJ'; \rho}^{(exc)} R_{1; \rho}^{(z-1)} \mathcal{A}_{\rho, 1}^{(z-1, z)} \right. \\ &\quad \left. + \sum_{\rho=1}^{M^{(z)}} \mathcal{E}_{\sigma, nlJ \rightarrow \rho', nlJ'; \rho}^{(rec)} R_{1; \rho}^{(z)} \mathcal{A}_{\rho, 1}^{(z, z)} \right) \end{aligned} \quad (2.42)$$

where $\mathcal{E}_{\sigma, nlJ \rightarrow \rho', nlJ'; \rho}^{(exc)}(T_e, N_e)$ is the excitation emissivity coefficient, $\mathcal{E}_{\sigma, nlJ \rightarrow \rho', nlJ'; \rho}^{(rec)}(T_e, N_e)$ is the dielectronic recombination emissivity coefficient and $N^{tot} = \sum_{z, \rho} N_\rho^{+z}$. $R_{1; \rho}^{(z-1)}$ and $R_{1; \rho}^{(z)}$ measure the dis-equilibrium in the ionisation balance and

$$\mathcal{A}_{\rho, 1}^{(z-1, z)} = \frac{N_\rho^{+z-1}}{N_1^{+z}}|_{eq} \quad \text{and} \quad \mathcal{A}_{\rho, 1}^{(z, z)} = \frac{N_\rho^{+z}}{N_1^{+z}}|_{eq} \quad (2.43)$$

measure the metastable abundances in ionisation equilibrium relative to the z -times ionised ion ground state. In most fusion and astrophysical plasma conditions, metastable populations of a given ionisation stage are close to quasi-static equilibrium with the ground so that $R_{1; \rho}^{(z-1)} = R_1^{(z-1)}$ independent of ρ and $R_{1; \rho}^{(z)} = 1$. Thus, the emissivity function is a function of the three parameters $R_1^{(z-1)}$, T_e and N_e principally, although there is a weaker Z_{eff} and T_i dependence at high density (see section 2.4.4 below).

In like manner, the emissivity function of an associated line of the recombining

ion may be written as

$$\begin{aligned} \frac{G_{\sigma \rightarrow \rho'}}{N_e N^{tot}} &= \left(\frac{N_1^{+z}}{N_e N^{tot}} \right) \left(\sum_{\rho=1}^{M^{(z)}} [A_{\sigma \rightarrow \rho'} \mathcal{F}_{\sigma; \rho}^{(exc)}] \frac{N_\rho^{+z}}{N_1^{+z}} \right. \\ &\quad \left. + \sum_{\rho=1}^{M^{(z+1)}} [A_{\sigma \rightarrow \rho'} \mathcal{F}_{\sigma; \rho}^{(rec)}] \frac{N_\rho^{+z+1}}{N_1^{+z}} \right) \end{aligned} \quad (2.44)$$

$$\begin{aligned} &= \left(\frac{N_1^{+z}}{N_e N^{tot}} \right) \left(\sum_{\rho=1}^{M^{(z)}} \mathcal{E}_{\sigma \rightarrow \rho'; \rho}^{(exc)} R_{1; \rho}^{(z)} \mathcal{A}_{\rho, 1}^{(z, z)} \right. \\ &\quad \left. + \sum_{\rho=1}^{M^{(z+1)}} \mathcal{E}_{\sigma \rightarrow \rho'; \rho}^{(rec)} R_{1; \rho}^{(z+1)} \mathcal{A}_{\rho, 1}^{(z+1, z)} \right) \end{aligned} \quad (2.45)$$

where $\mathcal{E}_{\sigma \rightarrow \rho'; \rho}^{(exc)}(T_e, N_e)$ is the excitation emissivity coefficient, $\mathcal{E}_{\sigma \rightarrow \rho'; \rho}^{(rec)}(T_e, N_e)$ is the radiative (including dielectronic) recombination emissivity coefficient. $R_{1; \rho}^{(z)}$ and $R_{1; \rho}^{(z+1)}$ measure the dis-equilibrium in the ionisation balance, with the same simplification above so that $R_{1; \rho}^{(z)} = 1$ and $R_{1; \rho}^{(z+1)} = R_1^{(z+1)}$ independent of ρ .

$$\mathcal{A}_{\rho, 1}^{(z+1, z)} = \frac{N_\rho^{+z+1}}{N_1^{+z}} |_{eq} \quad (2.46)$$

measures the ionisation equilibrium relative metastable abundances for the $z + 1$ -times ionised ion. Again, the emissivity function is a function principally of the three parameters $R_1^{(z+1)}$, T_e and N_e . Thus, the theoretical local emissivity of the combined satellite lines and associated resonance line feature is functionally dependent on four parameters, $R_1^{(z-1)}$, $R_1^{(z+1)}$, T_e and N_e . These parameters are used in a least-squares fit as described in section 2.4.6.2.

2.4.4 The population calculations

Conventional population modelling in generalised collisional-radiative theory addresses ‘singly-excited’ states built on ground and metastable parents. Efficiency of computation is achieved by handling the two-step dielectronic process as a single effective process populating these singly excited states (Badnell *et al* 2003).

To model the satellite line feature on the other hand, the dielectronic process must be separated out in the population structure — at least for the resolved satellite lines with low-lying ($n \lesssim 4$) spectators. Spectrally unresolved satellite lines with higher-lying spectators provide a second order supplementation of the parent ion lines. Also, the associated upper level populations of these satellite lines give a contribution to the observed satellite line intensities via cascades of the spectators. It is valid to bundle over outer quantum numbers for such populations and to adopt some of the techniques of Badnell *et al* (2003) for their evaluation in finite density plasma, although care is required to avoid double counting.

For the ion A^{+z-1} , we introduce principal quantum numbers n_0 , n_1 and n_2 . n_0 is the principal quantum shell of the ground state valence shell. The range $n_0 \leq n \leq n_1$ spans the spectator shells for which the individual satellite lines are distinguished in the calculations. The range $n_1 < n \leq n_2$ spans spectator shells for which the satellite lines are individually unresolved, with n_2 an upper limit chosen sufficiently large for convergence in the calculation. Typically, in our calculations, we take $n_0 = 2$, $n_1 = 4$ and $n_2 \sim 15$.

2.4.4.1 The unresolved dielectronic part

In the range $n_1 < n \leq n_2$, consider the bundled population (that is summed over substates of an nl - or n -shell), designated by $N_{\sigma,nl}$, built on an excited parent $\sigma \equiv (\gamma_{\sigma} J_{\sigma})$ such that

$$N_{\sigma,nl} = \sum_{j,J} N_{\sigma,nljJ} \quad (2.47)$$

Then, following Badnell *et al* (2003), the populations in a finite density plasma are determined by the equations

$$\begin{aligned}
& - \left(N_e q_{nl-1 \rightarrow nl}^e + N^{z_{\text{eff}}} q_{nl-1 \rightarrow nl}^{z_{\text{eff}}} \right) N_{\sigma, nl-1} \\
& + \left(\sum_{l'=l \pm 1} N_e q_{nl \rightarrow nl'}^e + \sum_{l'=l \pm 1} N^{z_{\text{eff}}} q_{nl \rightarrow nl'}^{z_{\text{eff}}} \right. \\
& + \sum_{\sigma'=1}^{\sigma-1} \sum_{l'=l-1}^{l+1} A_{\sigma, nl \rightarrow \sigma', \kappa l'}^a + \sum_{\sigma'=1}^{\sigma-1} A_{\sigma, nl \rightarrow \sigma', nl}^r \\
& + \left. \sum_{n'=n_1+1}^{n-1} \sum_{l'=l-1}^{l+1} A_{\sigma, nl \rightarrow \sigma'', n' l'}^r + \sum_{n'=n_0}^{n_1} \sum_{l'=l-1}^{l+1} A_{\sigma, nl \rightarrow \sigma, n' l'}^r \right) N_{\sigma, nl} \\
& - \left(N_e q_{nl+1 \rightarrow nl}^e + N^{z_{\text{eff}}} q_{nl+1 \rightarrow nl}^{z_{\text{eff}}} \right) N_{\sigma, nl+1} \\
& = N_e \sum_{\rho=1}^{M^{(z)}} \sum_{l'=l-1}^{l+1} q_{\rho, \kappa l' \rightarrow \sigma, nl}^c N_{\rho} + \sum_{\sigma''=\sigma+1}^{P^{(z)}} A_{\sigma'', nl \rightarrow \sigma, nl}^r N_{\sigma'', nl} \\
& + \sum_{n''=n+1}^{n_2} \sum_{l''=l-1}^{l+1} A_{\sigma, n'' l'' \rightarrow \sigma, nl}^r N_{\sigma, n'' l''} . \tag{2.48}
\end{aligned}$$

Here, $M^{(z)}$ denotes the dominant ground and metastables of the recombining ion, which are the targets for recombination, and $P^{(z)}$ denotes the complete set of active parents so, $M^{(z)} \subset P^{(z)}$.

Both electron and ion dipole-allowed impact collisions are included, but only between l -levels of the same n -shell. It is noted that these have very large cross-sections (since the l -levels are nearly degenerate) and that ion cross-sections are usually larger than those for electrons, and in general have a density dependence. This leads to a non-linear (and therefore not simply scalable) density behaviour of the population equations and influences our method of calculation. Inner-shell excitation from the ground and metastables of the recombined ion is ignored for this high n -part. These equations may be solved recursively downwards through n -shells and parents.

2.4.4.2 The resolved part

The range $n_0 \leq n \leq n_1$ provides the bulk of the dielectronic feature. It includes dielectronic contributions paralleling those of section 2.4.4.1, but also contributions from inner shell excitation from the ground and metastables states of the A^{+z-1} ion. For $n = n_0$, with equivalent electrons in the shell, parentage is not in general well specified and so it is convenient to divide the resolved level population equations into parent-attributable ($\sigma n l J'$) and parent-unattributable ($\gamma n J$) groups. This takes the form, for a doubly-excited parent-attributable level, of

$$\begin{aligned}
& - \sum_{\gamma', n', J'} N_e q_{\gamma' n' J' \rightarrow \sigma'' n l J}^e N_{\gamma', n' J'} \\
& - \sum_{\substack{\sigma', n', l', J' \\ E' < E}} N_e q_{\sigma' n' l' J' \rightarrow \sigma'' n l J}^e N_{\sigma', n' l' J'} \\
& + \left(\sum_{l'=l\pm 1} N_e q_{n l \rightarrow n l'}^e + \sum_{l'=l\pm 1} N^{z_{\text{eff}}} q_{n l \rightarrow n l'}^{z_{\text{eff}}} \right. \\
& + \sum_{\sigma=1}^{\sigma''-1} \sum_{l'=l-1}^{l+1} A_{\sigma'', n l \rightarrow \sigma, \kappa l'}^a + \sum_{\sigma'=1}^{\sigma''-1} A_{\sigma'', n l \rightarrow \sigma', n l}^r \\
& + \left. \sum_{n'=n_1+1}^{n-1} \sum_{l'=l-1}^{l+1} A_{\sigma'', n l \rightarrow \sigma'', n' l'}^r + \sum_{n'=n_0}^{n_1} \sum_{l'=l-1}^{l+1} A_{\sigma'', n l \rightarrow \sigma'', n' l'}^r \right) N_{\sigma'', n l} \\
& - \sum_{\substack{\sigma', n', l', J' \\ E' > E}} \left(N_e q_{\sigma' n' l' J' \rightarrow \sigma'' n l J}^e + A_{\sigma', n' l' J' \rightarrow \sigma'', n l J}^r \right) N_{\sigma', n' l' J'} \\
& = N_e \sum_{\sigma=1}^{M(z)} \sum_{l', J'} q_{\sigma, \kappa l' J' \rightarrow \sigma'', n l J}^c N_{\sigma} + \sum_{n'=n_1+1}^{n_2} \sum_{l'} A_{\sigma', n' l' \rightarrow \sigma'', n l J}^r N_{\sigma', n l},
\end{aligned} \tag{2.49}$$

with similar forms for parent-unattributable levels and single excited levels. There are equivalent sets of equations to equations 2.48 and 2.49 for the ion A^{+z} . Note the spectator electron cascade contribution from unresolved levels — the last term of equation 2.49. In this formulation, the helium-like lines are envelopes of the true helium-like line, and the satellite lines with spectator $n > n_1$, so that the spectral emissivity coefficient for a helium-like line $\sigma \rightarrow \sigma'$, driven by metastable

ρ , is given by

$$\begin{aligned}
\epsilon_{\sigma \rightarrow \sigma'; \rho}^{\text{eff}}(\nu) &= \epsilon_{\sigma \rightarrow \sigma'; \rho} + \sum_{n, l; n > n_1} \epsilon_{\sigma nl \rightarrow \sigma' nl; \rho} \\
&= (A_{\sigma \rightarrow \sigma'}^r \phi(\nu) N_{\sigma} + \sum_{n, l; n > n_1} A_{\sigma nl \rightarrow \sigma' nl}^r \times \\
&\quad \phi(\nu - \Delta\nu_{nl}) N_{\sigma nl}) / N_e N_{\rho},
\end{aligned} \tag{2.50}$$

where $\phi(\nu)$ is the line broadening function. We are only concerned with the case of $\sigma' = \rho$ for the present helium-like system.

In spite of the apparent simplicity of the one-, two- and three-electron systems considered here, the quality of excitation cross-sections, especially the excitations from the ground states of the ions by promotion of a 1s electron, has been a limiting factor on the precision to which analysis can be performed. In preparing the population models above we have substituted high precision data for all transitions between all singly and doubly excited states of the helium- and lithium-like system of the form $1s_1^q 2l_2^q$, $1s^{q_1-1} 2l^{q_2-1} 2l' n l''$ with $n \leq 4$. The calculation of these new data has been a substantial part of the work and are discussed in detail in section 2.5 and in Whiteford *et al* (2001,2002).

2.4.5 The background continuum

The background continuum underlying the satellite line special feature in actual spectral observations can be instrumental in origin, but in many cases it is a true plasma-sourced free-free (bremsstrahlung) + free-bound continuum. In that case, we call it the continuum special feature. A theoretical representation, as a parametric feature, can be assembled for contributing ions in a local plasma modelling environment following the methods of Burgess and Summers (1987). As such, it can be viewed as a second basis function to associate with the satellite line special feature in analysis of the spectral interval, but usually with a different emission measure. For this work, the continuum is treated as a simple (up to quadratic) mathematical form to be fitted along with the ordinary lines (see section 2.4.6 below).

2.4.6 Representing and fitting the spectral interval

2.4.6.1 Line broadening and calibration

Forward modelling to the observed spectrum must address the issues of intrinsic (to the plasma) broadening and instrumental broadening. Semi-analytic physical or mathematical forms (usually Doppler or Gaussian) represent the intrinsic line broadening. Instrumental effects on an individual line are described by a predetermined superposition of the original form but at specified displacements and relative amplitudes to it. For example, the post-loss instrumental profile for the CDS-NIS1 spectrometer on the SOHO spacecraft is represented (Thompson 1999) as the triplet of Gaussian components $(A'_i, \lambda', \sigma'_i) \sim (1.0, 0.0, 1.0), (0.2, 0.002, 1.0), (0.3, -0.002, 1.0)$, where the primed quantities are relative amplitude, wavelength and variance relative to the mathematical line. The final step is then a simple convolution with our mathematical form in pixel space but, as it is system specific, not addressed further here.

Concerning wavelength calibration, it is recognised that the *ab initio* prediction of energy levels of the methods of this thesis are expected to be accurate only to within $\sim 0.5\%$, see section 2.3.4.1. Because of the variation with atomic level of self-screening for the $n = 2$ shell (that is when the spectator electron is in the $n = 2$ shell), helium- and lithium-like ($n = 2$ spectator) lines must be adjusted individually to observed wavelengths for the most exact work.

2.4.6.2 Fitting methodology

Mathematically, the ordinary lines and background are represented as several Gaussian shaped lines together with a constant, linear or quadratic background, as given by Brooks (1997). That is

$$I_k^O = b_0 + b_1 x_k + b_2 x_k^2 + \sum_{i=1}^L h_i^O \exp\left(\left((x_k - x_i^O)/w_i^O\right)^2\right), \quad (2.51)$$

here, L is the number of ordinary lines in the spectrum, such that the i th line has central amplitude h_i^O , pixel position x_i^O at the centre of the line and half-width w_i^O . x_k is the detector pixel number, indexed by k over the spectral segment

distinguished for analysis.

Introduce a spectral profile for each line of the satellite line special feature, indexed by c of natural wavelength, λ_c , of the form $\psi_{\lambda-\lambda_c-\Delta\lambda}(T_i, b)$. T_i is the ion temperature and b is a second parameter of the profile shape. $\Delta\lambda$ is a further parameter which is displacement of lines driven from the lithium-like ground state from those driven from the helium-like ground state. Thus $\Delta\lambda$ is zero for lines driven from the helium-like stage ground state. Thus the theoretical count rate at detector pixel position x_k is

$$I_k^F = h \sum_c \mathcal{E}_c(R_1, R_2, T_e, N_e) \psi_{\lambda-\lambda_c-\Delta\lambda}(T_i, b) \quad (2.52)$$

where \mathcal{E} denotes a generic emissivity functional from the equations in previous sections. The observed data are then fitted to the equation

$$I_k = I_k^O + I_k^F \quad (2.53)$$

where I_k is the observed count rate at a particular detector pixel position, x_k . I_k^O represents the ordinary line & background and the special feature part is represented by I_k^F . Statistical variation in I_k is assumed to have the normal form, with variance proportional to the mean value of I_k . Hence

$$\sigma_k^2 = \text{var} I_k = \sigma^2 E(I_k) \quad k = 1, 2, \dots, P \quad (2.54)$$

where σ^2 is an unknown constant of proportionality, P is the number of pixel positions and E denotes the expectation value. Under these conditions, the likelihood function can be formed and values which maximise it also maximise its (natural) logarithm. Thus, to maximise the (logarithm of the) likelihood in order to estimate the N variables $b_0, b_1, b_2, \{h_i^O, x_i^O, w_i^O\}, R_1, R_2, T_e, N_e, \lambda_c, \Delta\lambda, T_i, b$, the need is to minimise the function

$$\sum_{k=1}^P \left(\frac{I_k}{\sigma_k^2} - \frac{1}{\sigma_k^2} (I_k^O + I_k^F) \right). \quad (2.55)$$

The σ_k^2 are unknown. Assuming however that the counts per sampling interval

follow the Poisson distribution, the σ_k^2 are equal to the true unknown mean count per sampling interval divided by the number of sampling intervals. If the unknown mean count rate is estimated by I_k , then an estimate of σ_k^2 follows, namely I_k divided by the number of intervals where the number of intervals is the dwell time in seconds. A standard numerical routine will find the unconstrained minimum of the function, i.e. minimise

$$F(x) = \sum_{i=1}^P (f_i(x))^2. \quad (2.56)$$

The functions $f_i(x)$ (the residuals), their first derivatives and a starting point must be supplied. The starting point was obtained from the observed spectrum by indicating the number of lines to be fitted and estimating their peak positions and full-width half-maxima. The background was also obtained from the spectrum and estimates of b_0, b_1, b_2 made. Once estimates of b_0, b_1, \dots (denoted by $\hat{b}_0, \hat{b}_1, \dots$) have been found, a second routine is used to find the diagonal elements of the covariance matrix C . In the routine, it is assumed (see below) that the Hessian (i.e. matrix of second partial derivatives) of $F(x)$ at the solution can be approximated adequately by $2J^T J$ where J is the Jacobian (i.e. matrix of first partial derivatives) of $F(x)$ at the solution. C is then given by

$$C = \hat{\sigma}^2 (J^T J)^{-1}, \quad (2.57)$$

for $J^T J$ non-singular, where $\hat{\sigma}^2$ is the estimated variance of the residual at the solution ($\vec{x} = \hat{b}_0, \hat{b}_1, \dots$) and is given by

$$\hat{\sigma}^2 = F \left(\frac{\hat{x}}{P - N} \right) \quad (2.58)$$

The square root of the diagonal elements of C give the estimated standard errors of the corresponding elements of \hat{x} . A 95% confidence interval for each of the elements of \hat{x} is obtained using $\hat{x}_j \pm t_{P-N;97.5} (C_{jj})^{1/2}$ where $t_{P-N;97.5}$ denotes the upper 97.5% point of Student's t distribution with $P - N$ degrees of freedom. Note that the approximation of the Hessian by $2J^T J$ is justified as follows: the

Hessian matrix $G(x)$ is of the form

$$G(x) = 2[J^T(x)J(x) + \sum_{i=1}^P f_i(x)G_i(x)] \quad (2.59)$$

where $G_i(x)$ is the Hessian matrix of $F(x)$. In the neighbourhood of the solution $\|f(x)\|$ is often small compared to $\|J^T(x)J(x)\|$, for example when $f_i(x)$ represents the goodness of fit of a non-linear model to observed data. In such cases $2J^T(x)J(x)$ may be an adequate approximation to $G(x)$. This avoids the need to compute or approximate second derivatives of the $f_i(x)$.

2.4.7 Illustrative results

Illustrative results of fits to experimental data are shown for helium-like argon in figure 2.12, helium-like titanium in figure 2.13 and helium-like iron in figure 2.14. These spectra correspond to the same ones as shown in figures 2.4 and 2.5 in section 2.2.3.

The plasma analysis based on these fits is presented in Marchuk *et al* (2003) and Marchuk (2004); they are only here for illustration.

2.5 Electron-impact excitation of helium- and lithium-like systems

Electron-impact excitation collision strengths for transitions between all singly-excited levels up to the $n = 4$ shell of helium-like argon and the $n = 4$ and $n = 5$ shells of helium-like iron have been calculated using a radiation damped, intermediate coupling frame transformation, R -matrix approach (Whiteford *et al* 2001). In addition, collision strengths for transitions among doubly-excited levels up to the $n = 3$ shell (excluding the $1s3l3l'$ configurations) of lithium-like argon and iron have been calculated using a radiation and Auger damped, intermediate coupling frame transformation, R -matrix approach. Collision strengths have also been calculated for transitions between all singly-excited levels up to the $n = 5$ shell for the same lithium-like systems (Whiteford *et al* 2002).

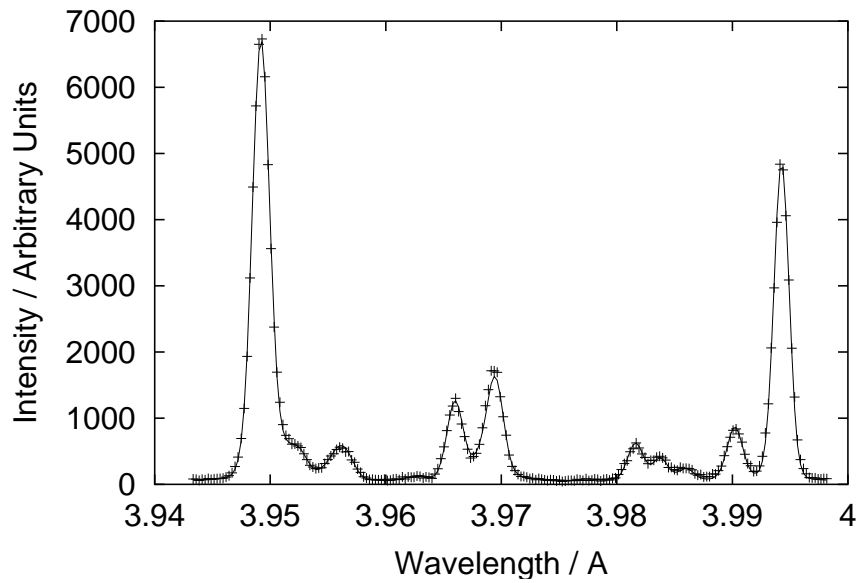


Figure 2.12: Helium-like argon spectrum (crosses) plus fitted model (solid curve) of a recorded spectrum taken on the TEXTOR tokamak during shot 88710.

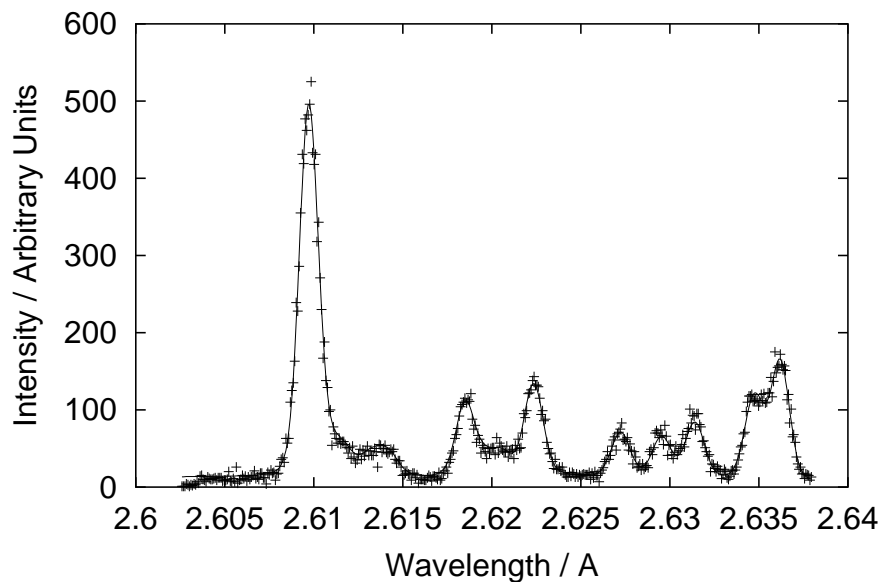


Figure 2.13: Helium-like titanium spectrum (crosses) plus fitted model (solid curve) of a recorded spectrum taken on Tore-Supra during shot 23706. Note that the crosses are not indicating an error bar.

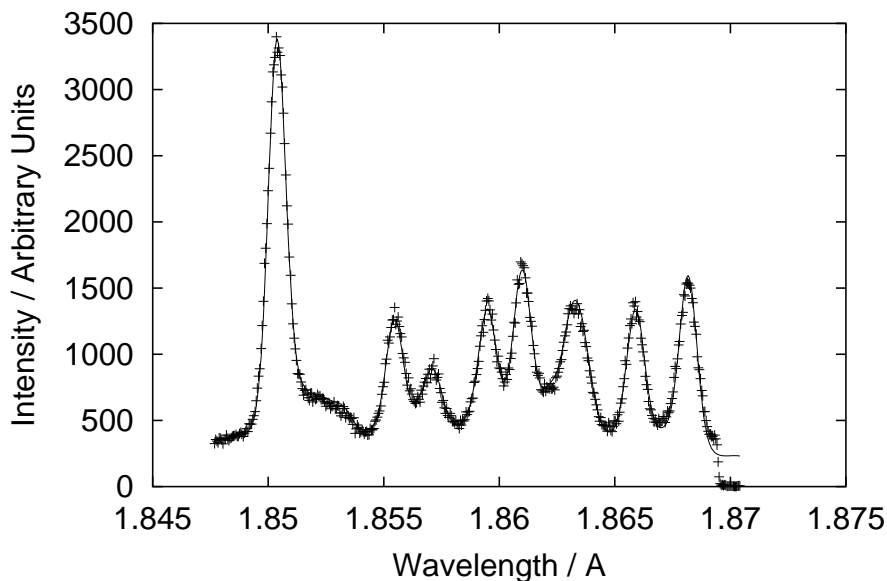


Figure 2.14: Helium-like iron spectrum (crosses) plus fitted model (solid curve) of a recorded spectrum taken on the TEXTOR tokamak during shot 15721. Note that the crosses are not indicating an error bar.

The theoretical collision strengths have been examined and associated with their infinite-energy limit values to allow the preparation of Maxwell-averaged effective collision strengths. These are conservatively considered to be accurate to within 20% at all temperatures, $3 \times 10^5 - 3 \times 10^8$ K for Ar^{16+} , $10^6 - 10^9$ K for Fe^{24+} , $5 \times 10^4 - 5 \times 10^8$ K for Ar^{15+} and $10^5 - 10^9$ K for Fe^{23+} . They have been compared with the results of previous studies, where possible, and we find a broad accord.

2.5.1 Introduction

The simple Van Regemorter (1962) P-factor¹⁰ approach to the rate coefficients used by Gabriel (1972) was replaced by the results of distorted-wave calculations for a number of astrophysically important elements by Jones (1974), along with additional distorted-wave work by a number of authors, of which Bhatia and Tempkin (1977) is representative. These calculations were restricted to levels with

¹⁰The Maxwell-averaged \bar{g} -factor.

$n \leq 2$. Sampson *et al* (1983) extended them, from $n = 1$ and 2, to all levels up to $n = 5$. All of these calculations ignored resonances.

The effect of resonances in helium-like ions was considered by Pradhan (1983a,b). He used multi-channel quantum defect theory (MQDT) and a combined close-coupling and distorted-wave approach to examine the effect on the effective collision strengths of resonances (including damping) converging on the $n = 2$ and $n = 3$ thresholds. For Fe^{24+} , he found almost a factor of 2 resonant enhancement for the forbidden transition $1s^2\ ^1S_0 - 1s2s\ ^3S_1$ and $\sim 10\%$ reduction due to damping, both at a temperature of $\sim 10^7\text{K}$. The peak coronal abundance of Fe^{24+} lies at about $3 \times 10^7\text{K}$. Effective collision strengths, including resonances and damping, were presented by Pradhan (1985) for 78 transitions between the lowest 13 levels (i.e., up to the $1s3p\ ^3P_2$ level) of Ca^{18+} and Fe^{24+} .

Also for helium-like ions, Zhang and Sampson (1987) used a distorted-wave method along with a perturbative approach to resonances and their damping. They allowed for resonances converging on the $n = 3$ thresholds only. This should suffice for highly-charged ions. They presented effective collision strengths for the 21 transitions between the lowest 7 levels (i.e., up to the $1s2p\ ^1P_1$ level) for 18 ions spanning $Z = 8 - 74$.

Limited R -matrix calculations have been carried-out for O^{6+} and Mg^{10+} by Tayal and Kingston (1984, 1985). More recently, Kimura *et al* (2000) have carried-out 31-level (i.e., up to $n = 4$) Dirac–Fock R -matrix calculations so as to generate effective collision strengths for three helium-like ions, including Fe^{24+} . Results were obtained only for the 16 transitions from the ground-level up to the $n = 2$ and $n = 3$ levels. They did not allow for radiation damping. Present computing resources indicate that a state-of-the-art R -matrix calculation is possible for helium-like ions, including radiation damping, extending to all 1176 transitions that arise between singly-excited levels up to $n = 5$ in an intermediate coupling picture.

We note that Wong *et al* (1995) have measured electron-impact excitation cross-sections for the w, x, y and z lines in Fe^{24+} , just above the $n = 2$ thresholds, using an electron-beam ion-trap. Given the experimental uncertainties and the need to correct for cascades, they found broad accord with the results of several theoretical groups, including those of an R -matrix calculation by Zhang and

Pradhan (1995). Only the non-resonant background cross-section was measured though. However, Chantrenne *et al* (1992) carried-out a similar measurement for the helium-like ion Ti^{20+} but were able to span a wider range of energies above the $n = 2$ thresholds and presented results that included the KMn resonances. These results are in broad accord with the radiation damped R -matrix results of Gorczyca *et al* (1995).

Recent work by Ballance *et al* (2001) addressed the key problematic issues of highly charged lithium-like ions. The importance of inner-shell processes of Fe^{23+} using the R -matrix method was appraised and special consideration was given to radiation damping for the doubly-excited transitions. Following this pilot study by Ballance *et al* (2001), and in light of present computing power, it is appropriate to address a complete calculation for lithium-like ions. The present calculations include radiation and Auger damping (Auger damping was not considered by Ballance *et al* (2001)) and extend to all 4005 transitions that arise between doubly-excited levels up to the $n = 3$ shell (excluding $1s3l3l'$ levels) in an intermediate coupling picture. They also encompass the 276 transitions between all singly-excited levels up to the $n = 5$ shell. The inclusion of Auger damping for doubly excited transitions gives a significant difference from the work of Ballance *et al* (2001) for a number of transitions.

The effects of Auger damping have been studied extensively for electron-impact ionisation of lithium-like ions by a number of authors including Tayal and Henry (1991) and Chen and Reed (1992). Badnell and Pindzola (1993) studied the electron impact excitation of few-electron highly charged ions and discussed Auger breakup and its effect on resonance contributions.

Merts *et al* (1980) presented (unreferenced) excitation data for a number of ions including data by Mann, Younger and Sampson for Ar^{15+} and data by Mann, Eissner, Hummer, Pindzola and Dufton for Fe^{23+} . However, these data were only presented in LS coupling, i.e. the transitions were between terms and not levels.

Goett and Sampson (1983) calculated collision strengths for the $1s^22l - 1s2l'2l''$ transitions for all ions with $6 \leq Z \leq 74$ using a distorted-wave approach, this was an extension of their work (Goett *et al* 1984) which calculated data for the same transitions for only lithium-like Si, Ca, Fe, Kr and Gd ions¹¹.

¹¹The publication (Goett *et al* 1984) focusing only on limited ions was published after the

Sampson *et al* (1985a,b) went on to calculate core-excited distorted-wave collision strengths for the $1s^22l - 1s2l2l'$ (1985a) and the $1s^23l - 1s2l'3l''$ (1985b) transitions, of all ions with $6 \leq Z \leq 74$, with Zhang *et al* (1986) producing data for all transitions occurring within the levels of the $1s^22l2l'$ configurations of the same ions.

Zhang *et al* (1990) published data using a distorted-wave approach for all ions with $8 \leq Z \leq 92$ and calculated outer-shell electron-impact collision strengths between the levels of the $n = 2$ shell and from these levels up to the $n = 5$ shell. Transitions between excited states of the $n = 3, 4, 5$ shell were not calculated, resonances were neglected and effective collision strengths were not generated.

Berrington and Tully (1997) performed calculations for the outer-shell excitation rates up to the $n = 4$ shell of Fe^{23+} using an R -matrix approach as part of the Iron Project (Hummer *et al* 1993). They published effective collision strengths between $1.6 \times 10^6\text{K}$ and 10^8K , highlighting the importance of the resonance contribution (particularly in the $1s^22p^2P_{\frac{1}{2}} - 1s^22p^2P_{\frac{3}{2}}$ transition) by comparing with the earlier distorted-wave work of Zhang *et al* (1990). They only presented data for transitions which included levels within the ground configuration.

2.5.2 Calculations and results

2.5.2.1 Methodology

Our approach to the determination of radiation damped collision strengths is to use the R -matrix method (Burke and Berrington 1993) in conjunction with the intermediate coupling frame transformation (ICFT) method (Griffin *et al* 1998) and the optical potential approach to damping (Robicheaux *et al* 1995, Gorczyca and Badnell 1996). A complete solution, in terms of reactance or scattering (collision) matrices is obtained firstly in LS -coupling. In particular, use is made of multi-channel quantum defect theory to obtain ‘unphysical’ collision matrices (as implemented by Gorczyca and Badnell (2000)). These are then transformed, first, algebraically to jK -coupling and then, via the use of the term-coupling coefficients, to intermediate coupling. The key advantages of using this method versus the equiv-

publication (Goett and Sampson 1983) on all ions with $6 \leq Z \leq 72$ even though the latter was based on the methodology of the former.

alent full Breit–Pauli R -matrix approach, as well as some of the computational issues, are outlined by Badnell and Griffin (2001). Suffice to say, at this time, the ICFT method is computationally less demanding than the full Breit–Pauli approach but does not suffer the inaccuracies associated with the term-coupling of physical collision matrices. Finally, we note that the use of the optical potential modifies the usual (i.e. undamped) expressions for the R -matrix, unphysical collision matrices and MQDT closure relations by making them complex — see Robicieux *et al* (1995) for details.

Use is made of multi-channel quantum defect theory (MQDT) to obtain ‘unphysical’ collision matrices (as implemented by Gorczyca and Badnell (2000)). The outer region solutions include the long-range coupling potentials as a perturbation still within the MQDT framework (see Gorczyca *et al* 1996, Badnell and Seaton 1999).

Our approach to the inner- and outer-shell data for the lithium-like systems is to perform the calculations independently and later merge the effective collision strengths back together into a single dataset because this cuts down on the size of Hamiltonians to diagonalise and the number of transitions to process.

2.5.2.2 Atomic structure calculation details

We used AUTOSTRUCTURE (Badnell 1997) to calculate the atomic structure and, hence, to generate radial wavefunctions for the collision calculation. Table 2.3 summarises the energy-level results of the two helium-like systems in comparison with those of NIST (2001). Agreement is very good (within 0.13% for Ar^{16+} and 0.17% for Fe^{24+}) with the $1s2s\ ^1S_0$ level being the worst case. For dipole-allowed transitions, the length and velocity forms of the oscillator strengths agreed to within 3% (Ar^{16+}) and 4% (Fe^{24+}) for the $1s^2\ ^1S - 1snp\ ^1P$ series, to within 5% (Ar^{16+}) and 6% (Fe^{24+}) for the $1s2s\ ^3S_1 - 1s3p\ ^3P_{0,1,2}$ transitions and to within 11% (Ar^{16+}) and 14% (Fe^{24+}) for the $1s2s\ ^3S_1 - 1s4p\ ^3P_{0,1,2}$ transitions.

The variation between the length and velocity forms is much larger for the $1s2s\ ^3S_1 - 1s2p\ ^3P_{0,1,2}$ transitions due to the long-range radial overlaps. The length form is to be preferred and this is the relevant form for assessing the accuracy of the resultant collision strengths. In the case of Fe^{24+} , the present A-values for

Level	Ar ¹⁶⁺		Fe ²⁴⁺	
	Present	NIST ^a	Present	NIST
1s ² ¹ S ₀	0	0	0	0
1s2s ³ S ₁	25 061 788	25 036 585	53 608 482	53 527 090
1s2s ¹ S ₀	25 227 719	25 200 958	53 858 375	53 781 300
1s2p ³ P ₀	25 207 029	25 187 783	53 822 873	53 760 280
1s2p ³ P ₁	25 216 430	25 192 896	53 853 844	53 779 140
1s2p ³ P ₂	25 240 697	25 215 174	53 976 753	53 895 550
1s2p ¹ P ₁	25 354 018	25 322 193	54 129 514	54 040 000
1s3s ³ S ₁	29 661 294	29 633 330	63 507 258	63 421 610
1s3s ¹ S ₀	29 703 843	29 676 817	63 570 330	63 488 390
1s3p ³ P ₀	29 701 043	29 674 992	63 565 901	63 486 290
1s3p ³ P ₁	29 703 670	29 676 554	63 574 243	63 490 690
1s3p ³ P ₂	29 710 675	29 683 166	63 609 903	63 525 620
1s3p ¹ P ₁	29 740 741	29 712 200	63 649 896	63 565 470
1s3d ³ D ₁	29 733 631	—	63 643 861	—
1s3d ³ D ₂	29 734 111	—	63 644 768	—
1s3d ³ D ₃	29 736 831	—	63 658 602	—
1s3d ¹ D ₂	29 737 983	—	63 660 201	—
1s4s ³ S ₁	31 248 528	31 219 900	66 933 257	66 847 000
1s4s ¹ S ₀	31 265 381	31 238 100	66 957 978	66 874 060
1s4p ³ P ₀	31 264 789	31 273 331	66 957 245	66 873 940
1s4p ³ P ₁	31 265 847	31 238 000	66 960 570	66 875 780
1s4p ³ P ₂	31 268 713	31 240 787	66 975 228	66 890 550
1s4p ¹ P ₁	31 280 856	31 253 100	66 991 257	66 906 790
1s4d ³ D ₁	31 278 006	—	66 988 969	—
1s4d ³ D ₂	31 278 242	—	66 989 436	—
1s4d ³ D ₃	31 279 348	—	66 995 140	—
1s4d ¹ D ₂	31 279 983	—	66 996 006	—
1s4f ³ F ₂	31 279 887	—	66 995 877	—
1s4f ³ F ₃	31 279 892	—	66 995 886	—
1s4f ³ F ₄	31 280 560	—	66 998 975	—
1s4f ¹ F ₃	31 280 567	—	66 998 986	—

^a — NIST database (<http://physics.nist.gov/>).

Table 2.3: Energy levels (cm⁻¹) of Ar¹⁶⁺ and Fe²⁴⁺, up to $n = 4$.

Level	Ar ¹⁵⁺		Fe ²³⁺	
	Present	NIST ^a	Present	NIST
1s ² 2s ² S _{1/2}	0	0	0	0
1s ² 2p ² P _{1/2}	257 755	257 026	392 591	392 000
1s ² 2p ² P _{3/2}	283 159	282 603	520 041	520 720
1s ² 3s ² S _{1/2}	4 177 981	4 176 030	9 276 233	9 272 400
1s ² 3p ² P _{1/2}	4 249 034	4 246 460	9 384 701	9 378 000
1s ² 3p ² P _{3/2}	4 256 554	4 254 050	9 421 775	9 417 000
1s ² 3d ² D _{3/2}	4 284 176	4 281 170	9 465 645	9 459 000
1s ² 3d ² D _{5/2}	4 286 540	4 283 560	9 477 659	9 472 000
1s ² 4s ² S _{1/2}	5 608 169	5 605 740	12 469 633	12 464 000
1s ² 5s ² S _{1/2}	6 262 964	6 259 500	13 935 076	—
1s2s ² ² S _{1/2}	24 879 049	24 834 000	53 340 361	—
(1s2s ³ S) 2p ² P _{1/2}	25 148 657	31 333 000 ^b	53 757 894	53 657 000
(1s2s ³ S) 2p ² P _{3/2}	25 161 992	31 342 000 ^b	53 834 716	53 752 000

^a — NIST database (<http://physics.nist.gov/>).

^b — We believe these values to be incorrect — see text for details.

Table 2.4: Energy levels (cm⁻¹) of Ar¹⁵⁺ and Fe²³⁺, up to $n = 3$ for all singly-excited levels and selected (representative) levels from higher singly- and doubly-excited states.

these transitions agree with those of NIST (2001) to within 4%, 27% and 14% for $J = 0, 1, 2$, respectively. For transitions between excited levels with $n > 2$, agreement was to within $\sim 20\%$ for most transitions.

The energy-level results in comparison with those of NIST (2001) for the two lithium-like systems are summarised in table 2.4 . The energies given for the (1s2s ³S) 2p ²S_{1/2, 3/2} levels should not be confused with the results of Ballance *et al* (2001) (Table 1) as they presented energies for the (1s2s ³S) 2p ⁴S_{1/2, 3/2} levels but they did not specify the term or parentage in their table¹².

Note that we show a strong disagreement with NIST for the 1s2s2p ²S_{1/2, 3/2} levels of Ar¹⁵⁺ we find disagreements of a similar magnitude between the present work and NIST for all doubly-excited energy levels of Ar¹⁵⁺ with the exception of the

¹²It is noted that term and parentage assignment is breaking down and the *LS* coupled labelling scheme is used as a convenience.

$1s2s^2\ ^2S_{\frac{1}{2}}$ level. The energy of the $(1s2s\ ^3S)2p\ ^2P_{\frac{1}{2}}$ level as given by Goett and Sampson (1983) is $25\ 116\ 613\ \text{cm}^{-1}$ which is in much closer agreement with the present work than with NIST. We note that the NIST data disagrees with the data of Kelly (1987) which is the publication NIST references for its Argon data. We conclude that the NIST energy levels for doubly-excited states of Ar^{15+} are in error¹³.

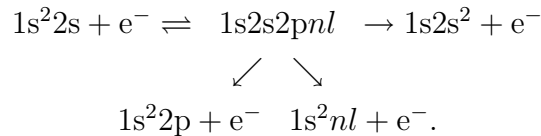
The Auger widths of the target levels were calculated using AUTOSTRUCTURE for Auger breakup routes which are not implicitly dealt with by the R -matrix method.

These results were deemed satisfactory for continuation within the collision calculation and it was verified that re-generation of the energy levels within the R -matrix calculations was accurate to within 10^{-7} Rydbergs and, as such, no re-ordering took place.

2.5.2.3 Auger damping

The damping of resonances due to Auger breakup is dealt with in two distinct cases. The first case is for the Auger breakup to states included explicitly in the calculation, this case is dealt with within the R -matrix approach intrinsically. The second case is for Auger breakup to states not included in the close-coupling expansion. In this latter case, we use AUTOSTRUCTURE to calculate Auger widths for the core re-arrangement of each target level and include them in the optical potential in our outer-region calculation.

As an example, consider the $1s^22s\ ^2S_{\frac{1}{2}} - 1s2s^2\ ^2S_{\frac{1}{2}}$ transition. This will have near-threshold resonances corresponding to $1s2s2pnl$ states. The core re-arrangement Auger damping of such intermediate states to $1s^2nl + e^-$ for $n > 3$ (in our case) is not included explicitly in the R -matrix calculation. We can represent this schematically by



¹³We also note that the energies NIST quote for Ar^{15+} are very close to the energies of the corresponding states in (lithium-like) Ca^{17+} .

The \leftarrow and \swarrow Auger pathways scale as n^{-3} while the \searrow route is independent of n and thus dominates for sufficiently high n .

To calculate the Auger width of such a process we consider the Auger breakup of the three electron system going from $1s2s2p$ to $1s^2 + e^-$. This neglects the effect of the spectator nl electron on the core N -electron Auger breakup. We then incorporate the Auger width into the optical potential approach to damping as discussed by Gorczyca and Robicieux (1999) for the case of Auger damping following photoexcitation.

For the case of the $1s^22s\ ^2S_{\frac{1}{2}} - 1s2s^2\ ^2S_{\frac{1}{2}}$ transition in Fe^{23+} , only resonances with $n \geq 10$ are above threshold (Chen and Reed 1992) and so none of these would be (core re-arrangement) Auger damped in a standard R -matrix calculation. Analysis of the effects of such Auger damping on the $1s^22s\ ^2S_{\frac{1}{2}} - 1s2s^2\ ^2S_{\frac{1}{2}}$ transition is presented when we discuss our effective collision strengths.

2.5.2.4 Collisional calculation details

The inner-region solutions were obtained using R -matrix codes which are based upon the published exchange codes of Berrington *et al* (1995) and the non-exchange codes of Burke *et al* (1992). The outer-region solutions, including radiation damping, were obtained in an LS -coupling scheme using the code STGF-DAMP and the intermediate coupling frame transformation was applied using the code STGICFDAMP which, for the lithium-like systems, included the effect of Auger damping not already included implicitly by the R -matrix method. At high angular momenta and/or energies, no resonances are resolved and/or present and it is more efficient to use the undamped versions of these codes, viz. STGF and STGICF.

We used 40 continuum basis orbitals per angular momentum within the exchange R -matrix codes for the two helium-like systems. The non-exchange R -matrix codes reduce this number progressively as the continuum orbital angular momentum increases. Accurate collision strengths can be generated for electron energies up to about half of the smallest maximum basis-orbital energy. This corresponds to ~ 1000 Rydbergs in the case of Ar^{16+} and ~ 1500 Rydbergs in the case of Fe^{24+} ($n = 4$ calculation). In the case of the (Fe^{24+}) $n = 5$ calculation,

one should increase the number of basis orbitals or reduce the maximum scattering energy. We used 50 basis orbitals in the $n = 5$ case. This leads to a smallest maximum basis-orbital energy of ~ 1500 Rydbergs (at $l = 5$). However, we still computed collision strengths up to 1500 Rydbergs. Past experience tells us that a severe deterioration in accuracy does not occur until after 1500 Rydbergs. The maximum basis orbital energy is significantly larger than this for most angular momenta. The results for the forbidden transitions are most sensitive to such an approach as they are dominated by contributions from low angular momenta. We can assess the accuracy of this approach by comparing our effective collision strengths with those determined via our $n = 4$ calculation.

For the inner-shell calculations of the two lithium-like systems, we used 30 continuum basis orbitals per angular momentum within the exchange R -matrix codes. The non-exchange R -matrix codes reduce this number progressively as the continuum orbital angular momentum increases. Accurate collision strengths can be generated for electron energies up to between half and three-quarters of the smallest maximum basis-orbital energy. The smallest maximum basis orbital energy corresponds to ~ 1116 Rydbergs in the case of Ar^{15+} and ~ 2445 Rydbergs in the case of Fe^{23+} , the smallest maximum basis orbital occurred for the $l = 3$ partial wave in both ions. For the outer-shell calculation, we used 80 continuum basis orbitals per angular momentum within the exchange R -matrix codes which gave smallest maximum basis orbital energies of ~ 1567 for Ar^{15+} and ~ 3515 in the case of Fe^{23+} . Both of these minima occurred for the $l = 5$ partial wave.

For the helium-like systems, the exchange calculation was performed up to $J = 10.5$ and the non-exchange calculation up to $J = 58.5$ while for the lithium-like systems, the exchange calculation was performed up to $J = 10$ and the non-exchange calculation up to $J = 58$. After that, ‘top-up’ was used to complete the partial collision strength sum over higher-values of J .

The top-up for non-dipole transitions was calculated by assuming a geometric series in energy, but taking care to switch-over smoothly to the degenerate-energy limiting case (Burgess *et al* 1970). The top-up for dipole transitions was computed using the Burgess (1974) sum rule — a discussion of the stability of this method, and our implementation of it, is in Badnell and Griffin (2001).

In all of the considered systems, we used an energy mesh of $1 \times 10^{-5} z^2$ Ry-

dbergs (z being the ionic charge) wherever resonances were present and a mesh of $1 \times 10^{-3} z^2$ Rydbergs in regions where resonances were not present. This energy mesh resolves the primary resonance structure in the detail necessary for the application to the analysis of plasmas. We note that the incorporation of radiation and Auger damping at the centre of our approach both reduces and broadens the resonances that we need to resolve. Hence, our effective resolution is greater than that of an, initially, undamped calculation that uses an equivalent energy mesh, as is done in the resonance-fitting approach to the damping of low- n resonances (Sakimoto *et al* 1990).

For the lithium-like systems, we follow closely the methodology used by Ballance *et al* (2001) but we perform the calculation with the express intention of making it directly applicable to experimental analysis. Ballance *et al* (2001) used a combination of Breit–Pauli (BP) (up to $J = 4$) and ICFT (from $J = 5$ to $J = 28$) and then used top-up to complete their calculation. We instead choose to perform an exclusively ICFT exchange calculation up to $J = 10$ and then use it with the non-exchange codes of Burke *et al* (1992) from $J = 11$ to $J = 58$ in order to increase efficiency for the intermediate partial waves (i.e. $J = 11$ to $J = 28$) and also to give a higher quality cross-section for the higher partial waves (i.e. $J = 29$ to $J = 58$). We choose to use more continuum basis orbitals so that we can produce more accurate collision strengths at higher energies and we have also used a four times finer energy mesh so that we can be confident the resonances are sufficiently resolved for the integration to produce effective collision strengths. Ballance *et al* (2001) neglected the effects of Auger damping, which we show here to be important for low temperature effective collision strengths.

2.5.2.5 Results illustrating key issues

Our $n = 5$ calculation for Fe^{24+} yields effective collision strengths for 1176 transitions and, for the lithium-like systems, our inner-shell calculations yield effective collision strengths for 4005 transitions and the outer shell calculations yield effective collision strengths for 276 transitions (with 28 transitions overlapping between the two cases) and so only illustrative results are presented here.

Results for all the considered systems, for energy levels, dipole radiative rates,

infinite-energy Born collision strengths and Maxwell-averaged effective collision strengths have been compiled¹⁴ according to the requirements of the ADAS Project (Summers 1999). on the tabulated temperature ranges of $3 \times 10^5 - 3 \times 10^8$ K for Ar^{16+} , $10^6 - 10^9$ K for Fe^{24+} , $5 \times 10^4 - 5 \times 10^8$ K for Ar^{15+} and $10^5 - 10^9$ K for Fe^{23+} .

The data format used¹⁵ is a compact and useful way of archiving the present data so that it can be directly applied to plasma analysis with little inconvenience on the part of the modeller. Care has been taken to ensure the dataset is complete including, e.g. non-dipole radiative rates which are often not generated. For the case of a dataset containing 4253 transitions, it is non-trivial for a modeller to separately obtain or calculate radiative rates and insert them into the dataset since even a very slightly different structure will cause the re-ordering of levels. For the case of Ar^{15+} , 1968 non-dipole (M1/E2) radiative rates were included.

Of interest is the quality of data at medium-to-high energies and particular care was taken to check that our results were consistent with the expected infinite-energy limits. We use the ‘C-plot’ method of Burgess and Tully (1992) to plot a reduced collision strength (Ω_r) against reduced energy (E_r). Here,

$$\Omega_r(E_r) = \frac{\Omega(E_j)}{\ln(E_j/E_{ij} + e)}, \quad (2.60)$$

for a dipole transition, where E_j is the scattered energy and E_{ij} is the excitation energy, for a transition $i \rightarrow j$. e is simply the base of natural logarithms (2.71828...). The reduced energy is given by

$$E_r = 1 - \frac{\ln(C)}{\ln(E_j/E_{ij} + C)} \quad (2.61)$$

where C is a constant chosen to weight how much of the plot is given to the high energy part, and how much given to the low energy part. Typically C is chosen between 1 and 5. An example of a ‘C-plot’ is given in figure 2.15 for the $1s^2 \ ^1S_0 - 1s2p \ ^1P_1$ transition in Fe^{24+} . This demonstrates the approach of the

¹⁴Available from the Oak Ridge Controlled Fusion Atomic Data Center, USA — http://www-cfadc.phy.ornl.gov/data_and_codes/.

¹⁵ADF04 — see Summers (1999).

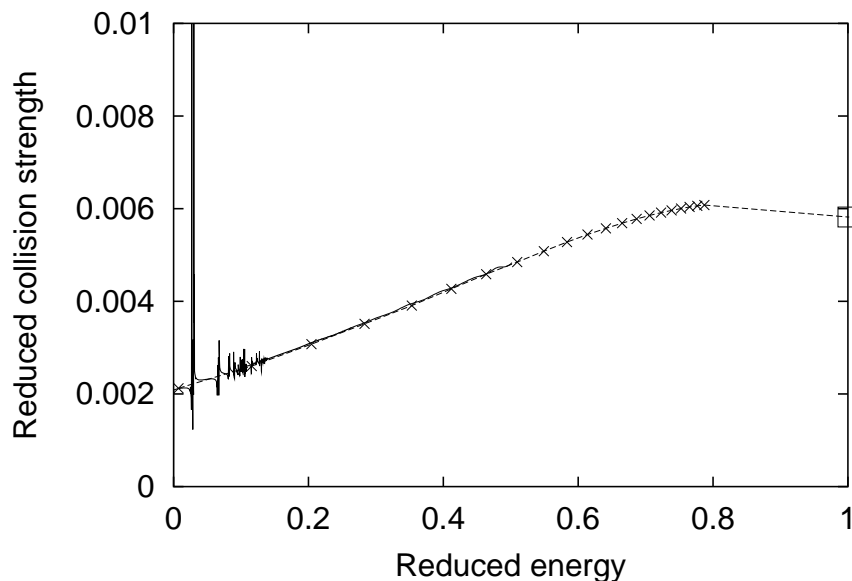


Figure 2.15: Reduced electron-impact excitation collision strengths for the $1s^2\ ^1S_0 - 1s2p\ ^1P_1$ transition in Fe^{24+} obtained using a reduced-energy parameter of $C = 2$ (see text for details). The solid curve denotes the present results and shows the detailed resonance structure. The dashed curve and crosses denote the distorted-wave results of Mann (1983). The straight line between the last point of Mann and the infinite-energy limit point (square box) shows the approach to the limit point.

reduced collision strength to the infinite-energy limit point (at $E_r = 1$), given by $\Omega_r(1) = 4S/3$, where S is the line strength. Also shown are the results of Mann (1983) which substantiate the present work closely in the high-energy region and clarify the approach to the infinite-energy limit point.

For non-dipole allowed transitions, we make use the infinite-energy Born limit (Burgess *et al* 1997). In figure 2.16, we show the collision strength ($\Omega_r = \Omega$) versus reduced energy (E_r) for the $1s2s\ ^1,^3S_{0,1} - 1s4f\ ^3F_3$ transitions in Fe^{24+} . (Now, $E_r = (E_j/E_{ij})/(E_j/E_{ij}+C)$.) Again, we note the approach of the collision strengths to the infinite-energy limit points at $E_r = 1$. It should be noted that the $1s2s\ ^1S_0 - 1s4f\ ^3F_3$ transition is forbidden by the LS -coupling selection rules but spin-orbit mixing with the $1s4f\ ^1F_3$ level gives rise to a non-vanishing Born limit. This type of transition is sometimes described as ‘semi-forbidden’. However,

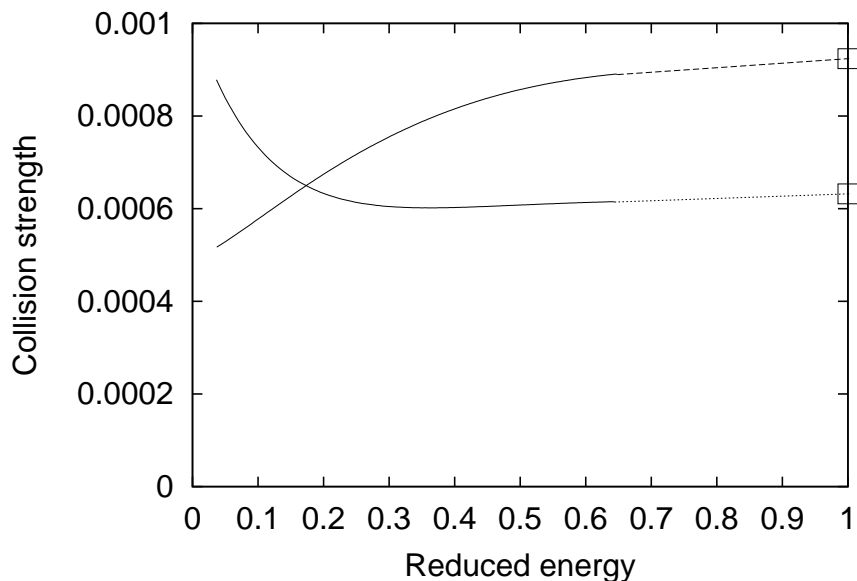


Figure 2.16: Electron-impact excitation collision strengths for the $1s2s\ ^1\text{S}_{0,1} - 1s4f\ ^3\text{F}_3$ transitions in Fe^{24+} , obtained using a reduced-energy parameter of $C = 4$ (see text for details). The solid lines denote calculated values and the dotted and dashed lines link them to their infinite-energy limit points (square boxes), for the $1s2s\ ^1\text{S}_0$ and $1s2s\ ^3\text{S}_1$ initial states, respectively.

from an automated analysis point of view, we classify all transitions with a non-vanishing dipole line-strength as dipole, all those with a non-vanishing Born limit as (non-dipole) allowed and all those with a vanishingly small, or zero, limit-value as forbidden. The interpolation or extrapolation of the (reduced) collision strengths as a function of (reduced) energy thus follows types 1, 2 and 3 of Burgess and Tully (1992). The issue of a precise definition of ‘vanishingly small’ only arises for low-charge ions, which is not the case here — this is the Burgess and Tully (1992) type 4 transition.

The effect of radiation damping is also important and an analysis of its effect was performed for both Ar^{16+} and Fe^{24+} . An illustration is shown in figure 2.17 for the $1s^2\ ^1\text{S}_0 - 1s3s\ ^1\text{S}_0$ transition. This clearly shows the effect of damping on the lowest-energy resonance group.

Figure 2.18 shows a comparison of a dipole transition, $1s^22s\ ^2\text{S} - 1s^22p\ ^2\text{P}$ in Ar^{15+} with the data presented by Merts *et al* (1980). The plot is presented in the

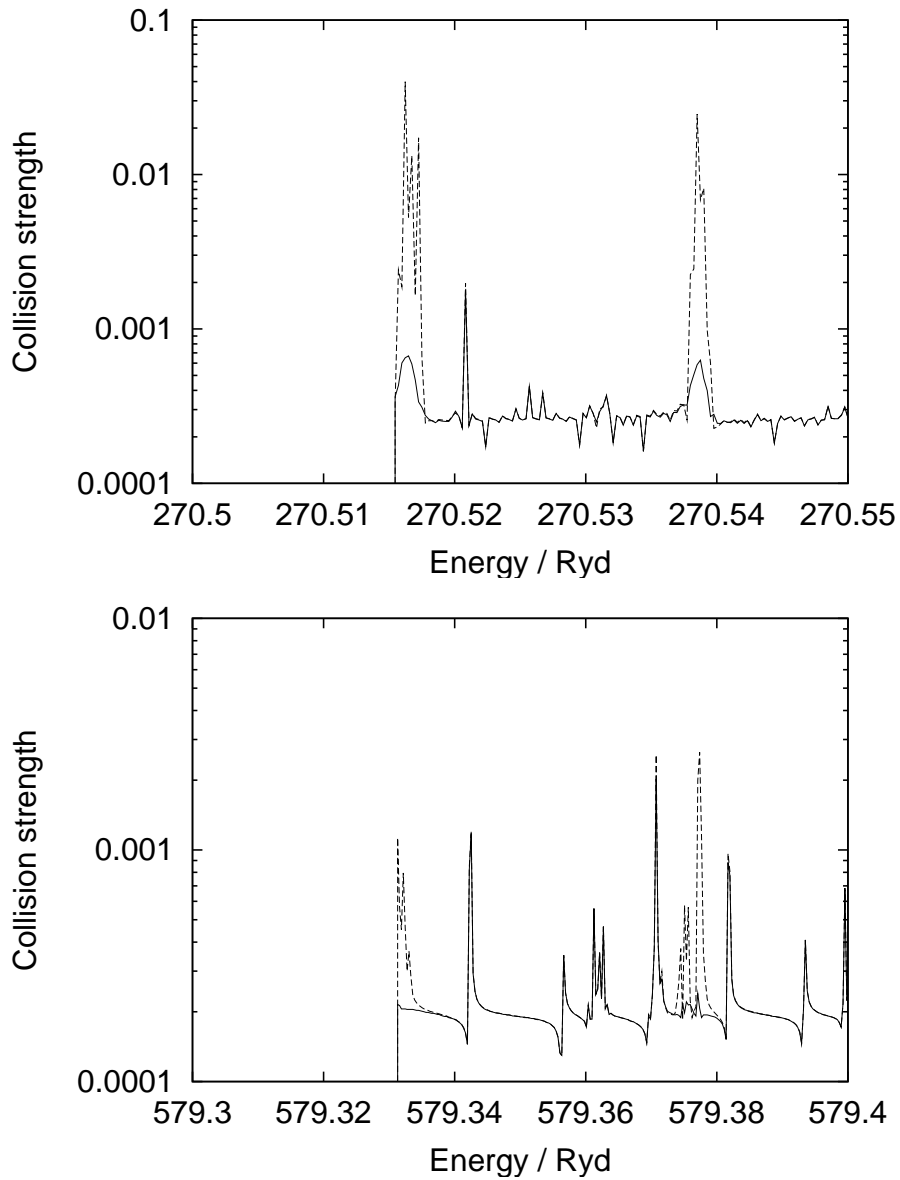


Figure 2.17: Electron-impact excitation collision strengths for the $1s^2 \ ^1S_0 - 1s3s \ ^1S_0$ transition in Ar^{16+} (upper) and Fe^{24+} (lower) illustrating a limited energy-range of the resonant region near threshold. The solid curves denote the damped results and the dashed curves denote the undamped results.

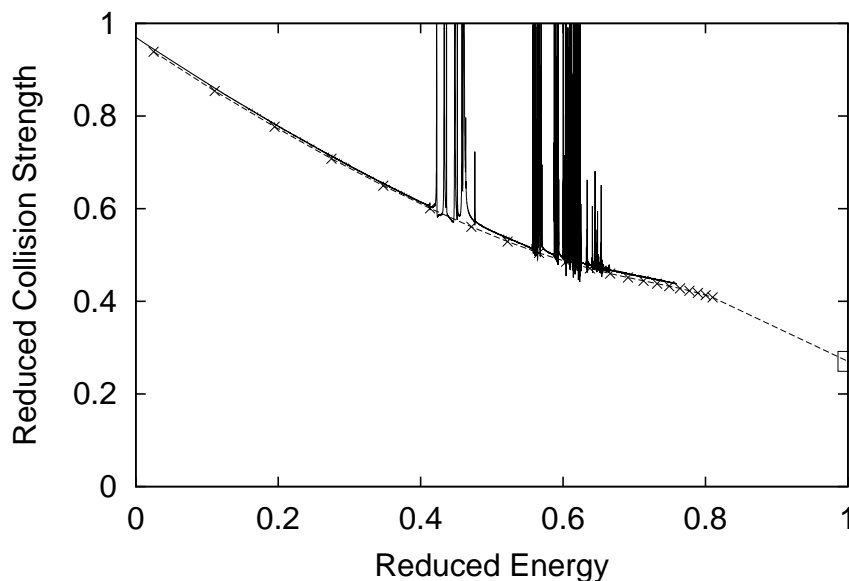


Figure 2.18: Reduced electron-impact excitation collision strengths for the $1s^2 2s^2 S - 1s^2 2p^2 P$ transition in Ar^{15+} obtained using a reduced-energy parameter of $C = 3$. The solid curve denotes the present results and shows the detailed resonance structure. The dashed curve and crosses denote the distorted-wave results presented by Merts *et al* (1980). The straight line between the last point of Merts and the infinite-energy limit point (square box) shows the approach to the limit point.

‘C-plot’ of Burgess and Tully (1992). Note that in order to make the comparison we show our LS coupled results before they were transformed to IC using the ICFT approach.

Figure 2.19 shows a comparison between the current work and the work of Ballance *et al* (2001) in the $1s^2 2s^2 \ ^2S_{\frac{1}{2}} - 1s 2s^2 \ ^2S_{\frac{1}{2}}$ transition of Fe^{23+} . Note the shallow oscillations in the background collision strength (well outside of the resonance region) in the work of Ballance *et al* (2001) since they used fewer basis orbitals than the present work. It can be seen, however, that the collision strengths of Ballance *et al* (2001) are oscillating around the collision strengths of the present work. Upon integration to form effective collision strengths the over- and under-estimations will tend to cancel each other out, but such a cancellation is best avoided if possible.

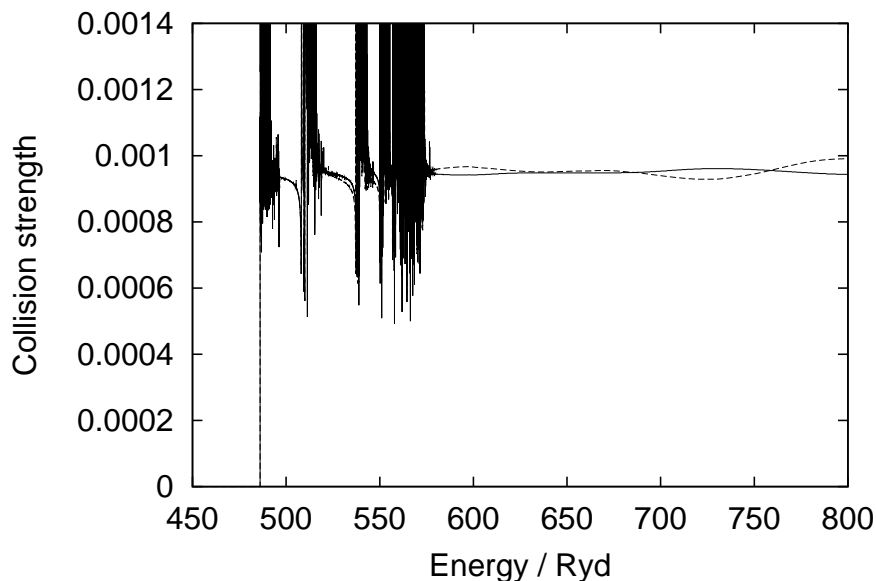


Figure 2.19: Electron-impact excitation collision strengths for the $1s^2 2s^2 \ ^2S_{\frac{1}{2}} - 1s 2s^2 \ ^2S_{\frac{1}{2}}$ transition in Fe^{23+} . The solid line denotes the present work and the dashed lines the work of Ballance *et al* (2001).

2.5.3 Application of fundamental data

2.5.3.1 Calculation of effective collision strengths

The collision strengths calculated above were Maxwell-averaged, using the approach of Burgess *et al* (1997), to generate effective collision strengths for spectral analysis and modelling. The collision strengths for allowed transitions were interpolated at higher energies using the infinite-energy limit points in the ‘C-plot’ picture. This gives a more accurate integrand at higher energies and so improves the precision of the effective collision strengths at higher temperatures. In particular, although we only calculated collision strengths up to a scattered (final) energy of ~ 900 Rydbergs for Fe^{24+} , we can now tabulate effective collision strengths up to 10^9K . By looking at the sensitivity to the high-energy interpolation, we estimate the effective collision strengths for the allowed transitions to be accurate to within $\sim 10\%$ at 10^9K .

The collision strengths for forbidden transitions were extrapolated by assum-

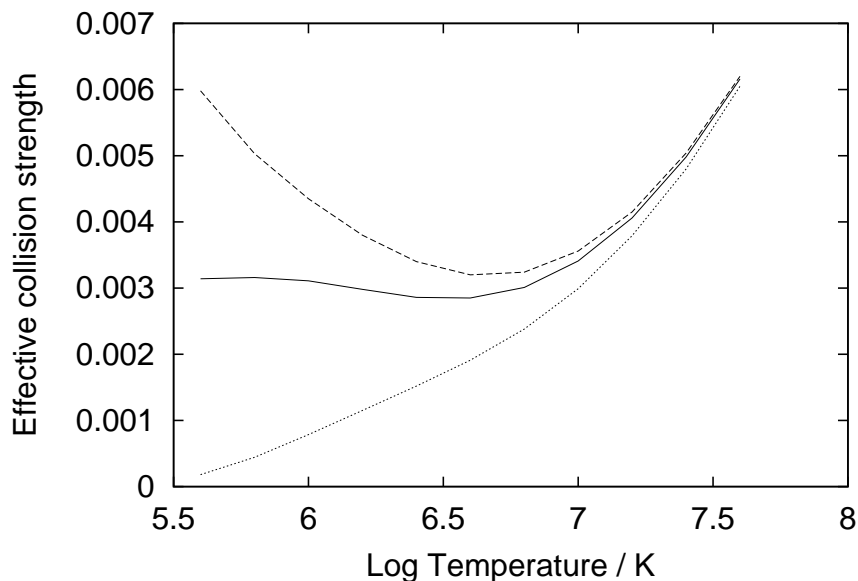


Figure 2.20: Effective collision strengths for the electron-impact excitation of the $1s2p^1P_1 - 1s3s^1S_0$ transition in Ar^{16+} . The solid curve denotes results that include the radiation damping of resonances. The dashed curve denotes results that omit the radiation damping of resonances. The dotted curve denotes results for the underlying (non-resonant) background only.

ing an $E^{-\alpha}$ energy dependence, with $\alpha = [1, 2]$. Formally (Burgess and Tully 1992), an E^{-2} energy dependence is expected asymptotically. However, some forbidden transitions are enhanced by coupling via allowed transitions and so fall-off more slowly with energy, and do not approach their asymptotic limit within our range of calculated energies. The accuracy of the effective collision strengths for forbidden transitions is estimated to be at worst $\sim 20\%$ at 10^9K . Here, they are even weaker, relatively speaking, than at lower temperatures and are relatively unimportant. Furthermore, the results from our $n = 5$ calculation for Fe^{24+} differ by less than 20% from our $n = 4$ results, at 10^9K .

Figure 2.20 illustrates the influence of damping and resonances on the effective collision strength for the $1s2p^1P_1 - 1s3s^1S_0$ transition in Ar^{16+} . We see that it is important to allow for both effects at lower temperatures.

We have compared our effective collision strengths for Fe^{24+} with those of Kimura *et al* (2000) (for the sixteen transitions out of our 1176 for which they ob-

tained results) and we find a broad agreement (to within $\sim 20\%$) for all transitions at 10^7K . Two such comparisons are illustrated in figure 2.21. Very good agreement is found with them for the $1s^2\ ^1S_0 - 1s3p\ ^1P_1$ dipole transition and also with that of Pradhan (1985). The agreement is not so good for the resonance-dominated $1s^2\ ^1S_0 - 1s2s\ ^3S_1$ forbidden transition, although that with Pradhan (1985) is much better. Pradhan (1983b) quoted a 9% reduction of the effective collision strength due to radiation damping for this transition, at a temperature of $2 \times 10^7\text{K}$. This is consistent with the results of Kimura *et al* (2000) being higher than ours since they do not allow for radiation damping. There may also be some sensitivity to the resolution of high- n resonances converging-on higher $n = 2$ thresholds. We find that the sensitivity to both resonance resolution and to the use of observed versus calculated target-level energies gives rise to a less than 2% change in our effective collision strength for this transition at $6.3 \times 10^6\text{K}$, which is where the largest disagreement with Kimura *et al* (2000) is to be found. The results of Zhang and Sampson (1987) are somewhat lower than ours and those of Pradhan (1985) in this case.

In figure 2.22, we display the importance of including enhancement due to resonances attached to levels in the $n = 4$ and $n = 5$ shells in the $1s^22p\ ^2P_{\frac{1}{2}} - 1s^22p\ ^2P_{\frac{3}{2}}$ transition of Fe^{23+} . A comparison with Berrington and Tully (1997), who included the effects of resonances attached to levels up to the $n = 4$ shell, is also shown. While the position of the resonance enhancement of the effective collision strength is at the same place, the results themselves differ somewhat when we include resonances attached to $n = 4$ and $n = 5$ shells. We note that Berrington and Tully (1997) have closer agreement with our results for inclusion of resonances up to the $n = 3$ shell even though they also included resonances attached to the $n = 4$ shell.

In figure 2.23, the effect of Auger damping, not included in a standard R -matrix calculation, is illustrated at low temperatures for the $1s^22s\ ^2S_{\frac{1}{2}} - 1s2s^2\ ^2S_{\frac{1}{2}}$ transition in Fe^{23+} . The effective collision strength at low temperatures is dominated by the resonances corresponding to the $1s2s2pnl$ ($N + 1$)-electron states. Such intermediate states have a high rate of Auger breakup to $1s^2nl + e^-$ and, hence, the resonances are damped almost completely. The breakdown of the contributions to the effective collision strength are given in table 2.5 for a range of

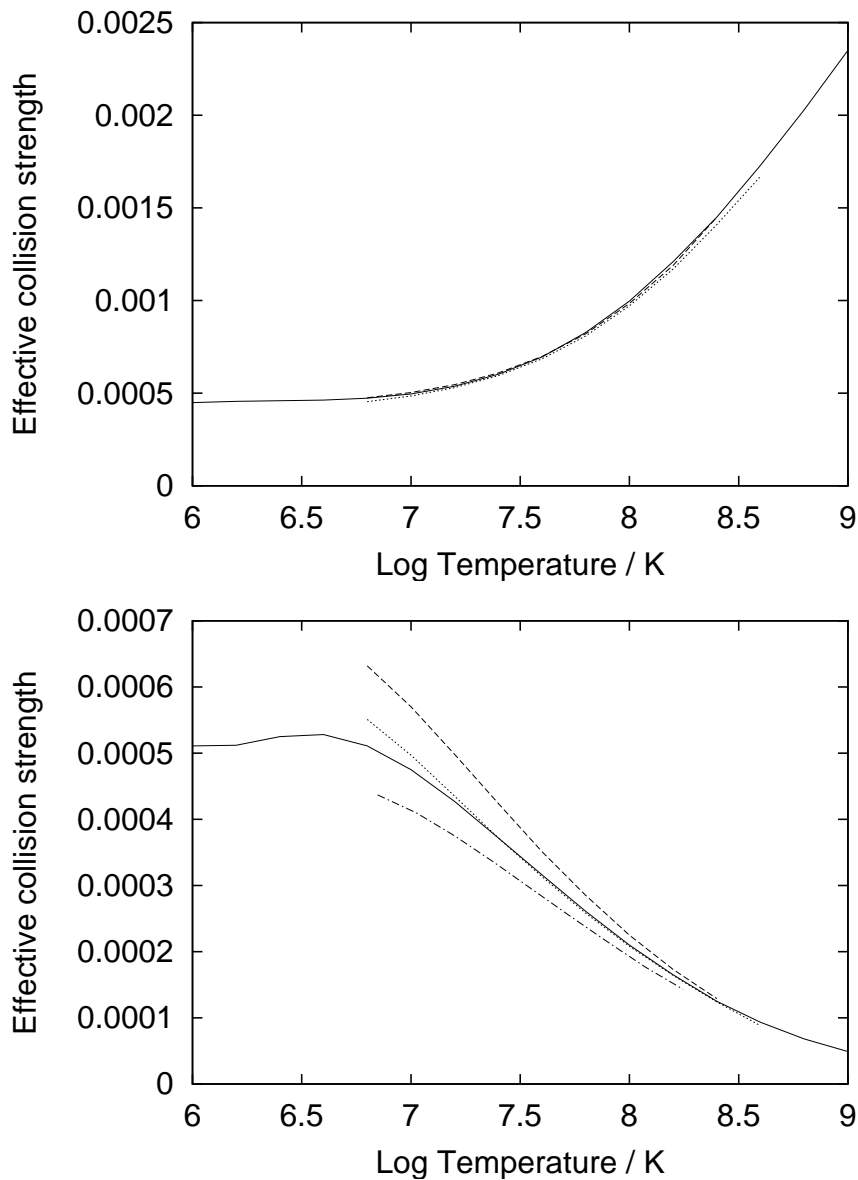


Figure 2.21: Effective collision strengths for the electron-impact excitation of the $1s^2\ ^1S_0 - 1s3p\ ^1P_1$ transition (upper) and the $1s^2\ ^1S_0 - 1s2s\ ^3S_1$ transition (lower) in Fe^{24+} . The solid curve denotes the present results, the dashed curve denotes the results of Kimura *et al* (2000), the dotted curve denotes the results of Pradhan (1985) and the chained curve denotes the results of Zhang and Sampson (1987), lower only.

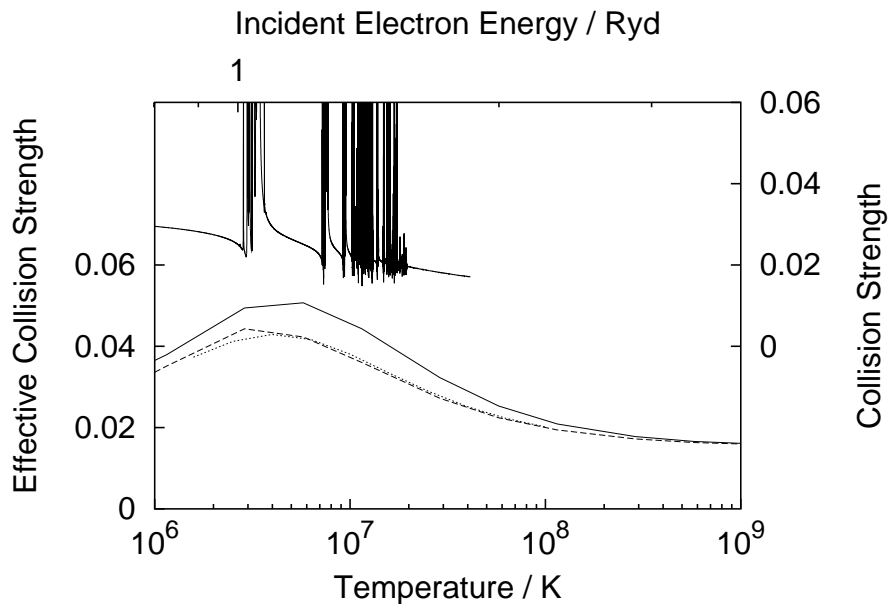


Figure 2.22: Effective collision strengths for the $1s^2 2p^2 P_{\frac{1}{2}} - 1s^2 2p^2 P_{\frac{3}{2}}$ transition of Fe^{23+} . The solid line shows the effective collision strength including resonances attached to $n = 3, 4$ and 5 states, the dashed line shows the results with resonance contribution coming only from resonances attached to $n = 3$ states. Also shown (dotted line) are the results of Berrington and Tully (1997). The solid line above the effective collision strengths is the underlying collision strength. The energy and temperature ordinates are scaled according to $E = kT$.

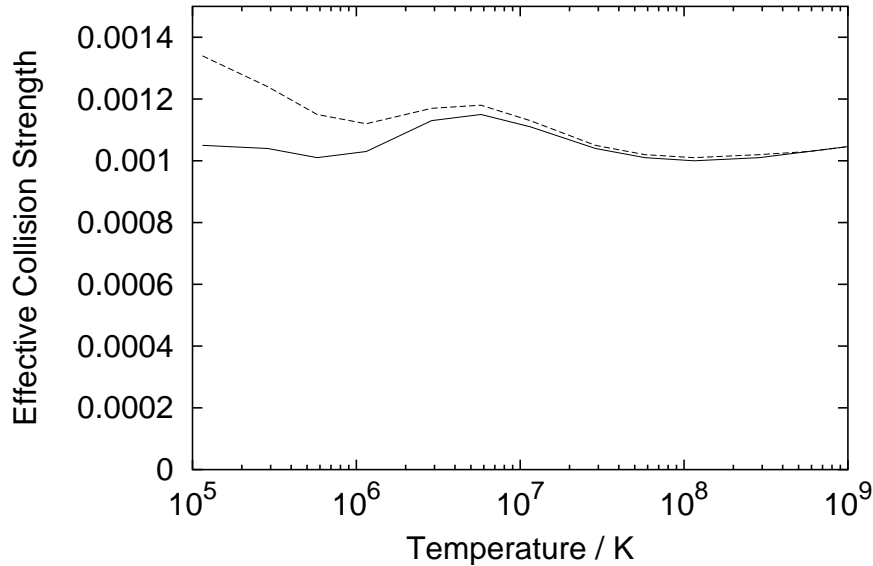


Figure 2.23: Effective collision strengths for the $1s^2 2s \ ^2S_{\frac{1}{2}} - 1s 2s^2 \ ^2S_{\frac{1}{2}}$ transition of Fe^{23+} . The solid line shows the effective collision strength including the effects of Auger damping not included in a standard R -matrix calculation. The dashed line shows the results neglecting the effects of such Auger damping.

different temperatures. As would be expected, the resonance contribution is large at low temperature, but the full inclusion of Auger damping reduces this contribution greatly.

At a temperature of 10^6K in Fe^{23+} , effective collision strengths for ~ 750 transitions are overestimated by $\gtrsim 30\%$ if Auger damping is neglected, with the worst case being a factor of ~ 9 overestimate in the $1s 2s 3s \ ^2S_{\frac{1}{2}} - 1s 2p 3p \ ^2P_{\frac{1}{2}}$ transition.

We find broad accord with the effective collision strengths calculated by Ballance *et al* (2001)¹⁶ for a number of representative transitions and temperature ranges where Auger damping does not have a significant effect.

From the point of view of fundamental excitation-data evaluation, it is unlikely that the extension to significantly higher n -shells ($n > 5$) will be undertaken. Yet, for application in low-to-moderate density plasmas, the populations of levels with

¹⁶We note that table 3 of Ballance *et al* (2001) is in error; we compared with the *adf04* dataset produced by Ballance *et al* (2001) and not to table 3.

Temperature	$3 \times 10^5\text{K}$		$3 \times 10^6\text{K}$		$3 \times 10^7\text{K}$		$3 \times 10^8\text{K}$	
Contribution	ADI	ADE	ADI	ADE	ADI	ADE	ADI	ADE
Background	9.48		9.49		9.51		10.0	
$1s2s2pnl$	0.92	2.92	0.05	0.47	— ^b	—	—	—
$1s2s3l3l'$	—	—	1.41	1.41	0.49	0.49	0.01	0.01
$1s2s3l4l'$	—	—	0.11	0.13	0.20	0.22	0.01	0.01
$1s2s3l5l'$	—	—	0.09	0.09	0.24	0.26	0.01	0.01
$1s2s3lnl'^a$	—	0.11	—	—	0.02	0.69	—	0.01
Total	10.4	12.5	11.1	11.6	10.4	11.2	10.0	10.0

^a $n \geq 6$

^b — denotes a negligible contribution

Table 2.5: Contributions to the effective collision strength (divided by 10^{-4}) of the $1s^22s^2\ ^2S_{\frac{1}{2}} - 1s2s^2\ ^2S_{\frac{1}{2}}$ transition in Fe^{23+} showing contributions with Auger damping not implicitly present in the R -matrix method included (ADI) and such damping excluded (ADE).

$n > 5$ deviate from Saha–Boltzmann and must be modelled with explicit reaction rates. Thus, we have given some attention to the problem of the extrapolation of our results to $n > 5$. The broad scaling of the effective collision strengths is as n^{-3} , but we observe deviations from this behaviour. We have used fits to the present data which indicate that errors which are not worse than 30% can be achieved for the extrapolated data. Figure 2.24 illustrates the result of the extrapolation technique for the $1s2s\ ^3S_1 - 1s5p\ ^3P_1$ transition in Fe^{24+} . The fitting was performed as $\Upsilon' = an^{-b}$ pointwise on a reduced temperature scale. The latter allows the extrapolation to be extended to the threshold region. The parameters a and b were calculated using the $1s2s\ ^3S_1 - 1s3p\ ^3P_1$ and $1s2s\ ^3S_1 - 1s4p\ ^3P_1$ data and then the $1s2s\ ^3S_1 - 1s5p\ ^3P_1$ data was determined and compared to the explicitly calculated effective collision strengths. It should be noted that explicit calculations were performed for all transitions up to $n = 5$ and this extrapolation and comparison is merely to investigate the importance of calculating rates explicitly instead of attempting to obtain them via extrapolation.

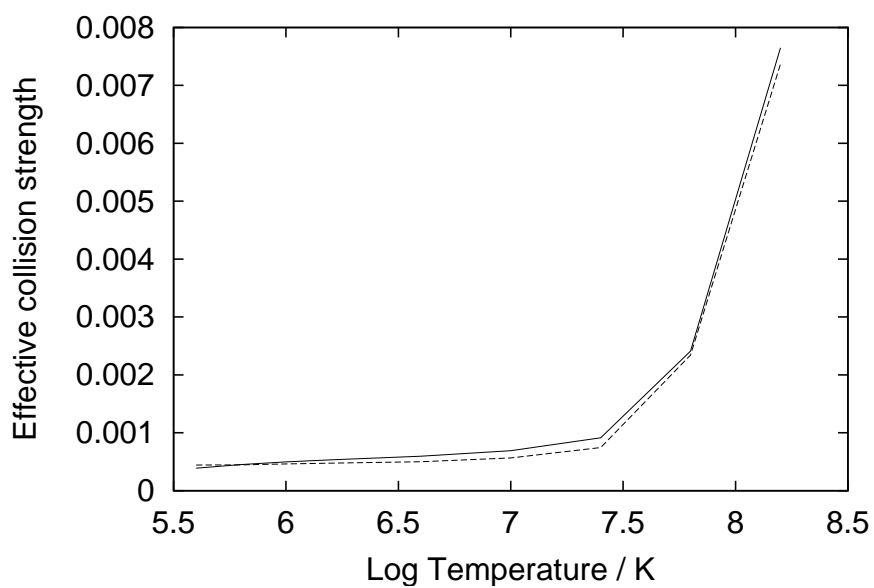


Figure 2.24: Effective collision strengths for the electron-impact excitation of the $1s2s\ ^3S_1 - 1s5p\ ^3P_1$ transition in Fe^{24+} . The solid curve denotes the explicitly calculated results and the dashed curve denotes the results extrapolated from lower n -shells.

2.5.3.2 Calculation of important line ratios

For application, the present resultant rate-coefficients must be incorporated into excited-population models. We are concerned with the impact of both absolute values of the collision data and its uncertainties on populations and consequential line emission — particularly on the familiar diagnostic line-ratios. There are two sources of uncertainty associated with our collision data, namely, the absolute accuracy of rate coefficient evaluation in the R -matrix approach and the uncertainty introduced by our extrapolation procedures for higher quantum-shell rates. It is appropriate also to assess the actual contribution of excitation to higher quantum-shells to the populating of lower (especially $n = 2$) levels by cascading and, hence, the contribution to diagnostic line ratios. For this assessment, we adopt a collisional–radiative model that is restricted to levels up to some quantum shell, n_0 . All electron-impact collisional and radiative processes are included between these levels, but all other processes, including recombination, are excluded. Thus, it is strictly the excitation driven part of the population structure which is examined.

The completeness of the R -matrix calculations performed here suggests that the absolute error of the rate coefficients should approach the limiting accuracy of the method. We take this to be 10%, as representative of the dominant transitions, for every explicit (non-extrapolated in n) rate coefficient, at all temperatures, and 30% for extrapolated rate coefficients. Also, it is assumed that the error in each rate coefficient can be treated as independent from each other and with a Gaussian distribution of half-width equal to the absolute error. On this basis, a statistical error on each population was computed by Monte Carlo random sampling of the errors in every rate coefficient using the code ADAS216 (Summers 1999). After sufficient samples, the set of results for each population delimits a Gaussian whose half-width is the statistical error in the population, for a given temperature and density.

We found that the error propagated to the populations was less than 10%. Table 2.6 shows the statistical uncertainties for the excited-level populations which give rise directly to the x/y-ratio and the G-ratio $((w+x+y)/z)$, at a representative temperature and density for both ions. The results isolate the effects of including

Fe²⁴⁺

Level	Line	Ar ¹⁶⁺	Fe ²⁴⁺		
			$n = 4$	$n = 5$	$n = 5^a$
1s2p ¹ P ₁	w	9.7%	8.3%	8.2%	9.7%
1s2p ³ P ₁	x	4.3%	8.2%	8.1%	9.8%
1s2p ³ P ₂	y	4.7%	9.4%	9.8%	9.3%
1s2s ³ S ₁	z	4.9%	5.1%	5.1%	8.1%

^a — Extrapolated.

Table 2.6: Propagated uncertainty in the populations of the levels responsible for the transitions leading to the x/y-ratio and G-ratio at an electron temperature of 1.58×10^7 K and density of 10^{13}cm^{-3} (Ar¹⁶⁺) and an electron temperature of 3.98×10^7 K and density of 10^{14}cm^{-3} (Fe²⁴⁺, for several models — see text).

higher n -shells, using both exact and extrapolated data, with their associated errors. We are able to resolve the contribution from any given rate coefficient to the population of any level. This shows that the uncertainty of the 1s2s ³S₁ population is most affected by the uncertainties in the higher-level fundamental rates (see table 2.6). Note that the 1s2s ³S₁ level is long-lived and has a weak radiative rate, thus, excitation to higher levels and de-excitation to the ground is more influential than in other levels — see section 2.4.2 for a discussion of this point.

Chapter 3

Interpretation and modelling of quasi-continuum radiation

3.1 Introduction

In this chapter we will develop and extend the concepts given in chapter 2 for application to quasi-continuum radiation — specifically to radiation emitted by very heavy species (e.g. tungsten) in the core plasma, as exemplified in section 2.2.4. These examples show that most individual lines cannot be distinguished since they blend together into a spectral envelope. Measurements and predictions typically involve thousands of lines and their indistinguishability arises from both broadening mechanisms within the plasma and from the wavelength resolution of the detection system. It is noted that some lines do stand out in isolation.

As in chapter 2, we still require diagnostically useful deliverables (section 2.3.1), a population structure via a collisional–radiative model (section 2.3.2) and atomic data to enter the model (section 2.3.4). Care must now be taken, however, as to how deliverables are calculated, handled and presented, given the size of the problem.

In section 3.2, we will discuss how to model a quasi-continuum spectrum, largely a refinement of the $\mathcal{P}\mathcal{E}\mathcal{C}$ s defined in section 2.3.1.1. The fundamental atomic data required and, perhaps more importantly, possible to calculate for the problem will be discussed at length with specific examples from heavy species (in

particular krypton) in section 3.3.

The reduction of the atomic data delivered to plasma modellers and how, for example, the total ionisation & recombination coefficients would enter a transport calculation differently from the lighter species (see section 2.3.1.3) is discussed in section 3.4 where the concept of flexible partitioning is developed.

Finally, tungsten is taken as an example case in section 3.5, where an overview of the atomic data produced for tungsten as part of this thesis is given.

3.2 Modelling a quasi-continuum spectrum

An important difference in modelling a quasi-continuum spectrum as opposed to, e.g., a low to medium weight helium-like spectrum (discussed in section 2.4) is the number of lines emitted and their diagnostic indistinguishability. Refinement has to be made as to the prescription of the problem and the deliverables as outlined in section 2.3.1; namely, \mathcal{PEC} s, S/\mathcal{XB} s and total ionisation & recombination coefficients. In section 3.2.1 we describe an $\mathcal{F-PEC}$, that is the extension of the \mathcal{PEC} as defined in section 2.3.1.1. A well defined ‘promotional strategy’ must also be implemented to keep the size of the problem manageable — this is discussed in section 3.2.2. Due to the number of transitions typically under consideration, the $\mathcal{F-PEC}$ is a special feature which does not retain information on its constituent transitions, but rather tabulates spectra as a function of temperature, density and wavelength (the distinction between this and the helium-like special feature is described in section 2.3.1.4).

3.2.1 Feature photon emissivity coefficients

An envelope feature photon emissivity coefficient, denoted by $\mathcal{F-PEC}$, is defined on a wavelength interval and is a composite feature arising from very many lines from a single ionisation (or metastable) stage. The $\mathcal{F-PEC}$ is suitable when the individual component lines are unresolved or only partly resolved. This situation occurs with very complex heavy element ions — it becomes economical to handle the envelope feature rather than the individual line emissivity coefficients (\mathcal{PEC} s) defined in section 2.3.1.1 and derived in section 2.3.2.

Consider the spectral interval, $[\Lambda_0, \Lambda_1]$, subdivided into N_{pix} intervals as

$$\lambda_i^{[0,1]} = \left[\Lambda_0 + i \frac{\Lambda_1 - \Lambda_0}{N_{\text{pix}}}, \Lambda_0 + (i + 1) \frac{\Lambda_1 - \Lambda_0}{N_{\text{pix}}} \right] \quad i = 0, \dots, N_{\text{pix}} - 1. \quad (3.1)$$

Note, this implies $\lambda_i^1 = \lambda_{i+1}^0$.

Also suppose that the spectrum line $j \rightarrow k$ has a normalised emission profile $\phi_{j \rightarrow k}(\lambda)$. Typically, such a profile is a convolution of Doppler and instrumental functions. Then, the envelope feature photon emissivity coefficient vector is defined as

$$\mathcal{F}\text{-}\mathcal{P}\mathcal{E}\mathcal{C}_{\sigma,i}^{[0,1]} = \sum_{j \rightarrow k} \mathcal{P}\mathcal{E}\mathcal{C}_{\sigma,j \rightarrow k} \int_{\lambda_i^0}^{\lambda_i^1} \phi_{j \rightarrow k}(\lambda) d\lambda, \quad (3.2)$$

$\lambda_{j \rightarrow k}$ is the natural wavelength of the $j \rightarrow k$ spectrum line¹. The default broadening assumed is Doppler, with a Maxwellian distribution for the emitting ion at temperature, T_{ion} , equal to the electron temperature, T_e , used in the collisional-radiative modelling of the $\mathcal{F}\text{-}\mathcal{P}\mathcal{E}\mathcal{C}$. This constitutes a minimum broadening resulting in spectra which may be further broadened for instrumental effects or if $T_e > T_{\text{ion}}$. The integral in equation 3.2 is then expressible in terms of error functions as

$$\mathcal{F}\text{-}\mathcal{P}\mathcal{E}\mathcal{C}_{\sigma,i}^{[0,1]} = \sum_{j \rightarrow k} \mathcal{P}\mathcal{E}\mathcal{C}_{\sigma,j \rightarrow k} \frac{1}{2} \left(\text{erfc} \left(\frac{\lambda_i^0 - \lambda_{j \rightarrow k}}{W} \right) - \text{erfc} \left(\frac{\lambda_i^1 - \lambda_{j \rightarrow k}}{W} \right) \right), \quad (3.3)$$

where, for Doppler broadening

$$W = \lambda_{j \rightarrow k} \alpha \left(\frac{k T_{\text{ion}} m_e}{I_{\text{H}} m_x} \right)^{\frac{1}{2}}, \quad (3.4)$$

and m_x is the emitting ion mass. Note we have used W rather than σ for the width of the line here to avoid confusion with the metastable state denoted by σ .

In principle, the Doppler broadened $\mathcal{F}\text{-}\mathcal{P}\mathcal{E}\mathcal{C}$ s can be convolved with effective instrument functions and/or representations of wavelength dependent filters. The $\mathcal{F}\text{-}\mathcal{P}\mathcal{E}\mathcal{C}$ s are archived at the minimal broadening expected in the experimental

¹This definition is valid for excitation, recombination and charge exchange $\mathcal{P}\mathcal{E}\mathcal{C}$ s, where σ must be appropriately defined as either the emitting or parent metastable.

spectra.

We can use an equilibrium ionisation balance with \mathcal{F} - \mathcal{PEC} s by introducing the equilibrium ionisation balance fractional abundances, $N_\sigma^{z+}/N_{\text{tot}}$, so that

$$N_\sigma \equiv N_\sigma^{z+} = \frac{N_\sigma^{z+}}{N_{\text{tot}}} \frac{N_{\text{tot}}}{N_e} N_e, \quad (3.5)$$

where the ratio $N_\sigma^{z+}/N_{\text{tot}}$ is evaluated in equilibrium at the local temperature and density. Then,

$$A_{j \rightarrow k} N_j = \frac{N_{\text{tot}}}{N_e} N_e^2 \mathcal{GTN}_{j \rightarrow k}(T_e, N_e), \quad (3.6)$$

where the definition of \mathcal{GTN} is given by using the expression for N_j given in equation 2.10;

$$\mathcal{GTN}_{j \rightarrow k}(T_e, N_e) = A_{j \rightarrow k} \left(\sum_{\sigma=1}^{M_z} \mathcal{F}_{j\sigma}^{(\text{exc})} \frac{N_\sigma^{z+}}{N_{\text{tot}}} + \sum_{\nu=1}^{M_z} \mathcal{F}_{j\nu}^{(\text{rec})} \frac{N_\nu^{(z+1)+}}{N_{\text{tot}}} \right) \quad (3.7)$$

is called the generalised contribution function or photon emissivity function. This is a density-dependent extension of the $G(T_e)$ function used in the astrophysical community.

For the spectral interval, $[\Lambda_0, \Lambda_1]$ as used to define an \mathcal{F} - \mathcal{PEC} , the envelope feature photon emissivity function vector is defined as

$$\mathcal{F}\text{-}\mathcal{GTN}_i^{[0,1]} = \sum_{j \rightarrow k} \mathcal{GTN}_{j \rightarrow k} \int_{\lambda_i^0}^{\lambda_i^1} \phi_{j \rightarrow k}(\lambda) d\lambda, \quad (3.8)$$

which can also be expressed using error functions as in equation 3.3.

Like the \mathcal{F} - \mathcal{PEC} s, the \mathcal{F} - \mathcal{GTN} s can be convoluted with effective instrument functions and/or representations of wavelength dependent filters.

3.2.2 Promotional strategy

For each ion whose structure is required, we must establish a working set of configurations, which includes the ground configuration and a number of excited configurations. The excited configurations to be included (from the infinite set available) are determined by criteria of relevance to observed spectrum lines, sufficient

precision in calculated energy levels & A-values (i.e. via configuration interaction) and computational resources. For the baseline calculations we use a promotional strategy to generate configurations automatically and this is focused on a set of ions of an element. Consider a group of ions $\{X^{z+} : z = z_{\min}, \dots, z_{\max}\}$ of the element X . A set of configurations targeted on a structure calculation is established by promoting electrons from the ground configurations of the ions. The criteria for promotion are shell-based and not set up ion-by-ion i.e. they are for the group of ions sharing the same valence shell². By reviewing the ground configurations of the ion group, a list of single valence shells present is identified — likewise for double valence shells and, in principle, on to triple valence shells. The promotional strategy depends on whether there is a single or double valence shell. For complex ions, the number of configurations which satisfy even quite restricted promotional rules can be large and since these configurations often include more than one unfilled shell, the level count for each configuration can be large. Mechanisms beyond the basic promotional rules are required and used to restrict the total level set to match available computer power.

Consider a spectral region of interest $[\Lambda_0, \Lambda_1]$, which may be the range of a particular spectrometer or an interval of special diagnostic value. For two configurations, I and J , we introduce their configuration-average energies, $E_I^{(\text{av})}$ and $E_J^{(\text{av})}$, the transition array average energy can then be defined as

$$\Delta E_{IJ}^{(\text{av})} = E_J^{(\text{av})} - E_I^{(\text{av})} \quad (3.9)$$

and the transition array average wavelength as

$$\lambda_{IJ}^{(\text{av})} = \frac{hc}{|E_J^{(\text{av})} - E_I^{(\text{av})}|} \quad (3.10)$$

Configurations which have a transition wavelength, $\lambda_{IJ}^{(\text{av})} \in [\Lambda_0, \Lambda_1]$, should be handled at high resolution, i.e. level resolved. Configurations such that the transition wavelength $\lambda_{IJ}^{(\text{av})} \notin [\Lambda_0, \Lambda_1]$ may be handled at low resolution, i.e. configuration-average — where the whole configuration is treated as one effective

²It is noted that for complex ions, it is possible to have ground configurations with more than one effective valence shell.

energy level. Section 3.3.1 outlines how data of different resolution and quality may be connected and used together.

3.3 Fundamental atomic data for very large systems

Two levels of data quality are discussed here, namely baseline data in sections 3.3.2 and 3.3.3 and intermediate quality data in sections 3.3.4 and 3.3.5. Whilst some of the intermediate techniques have been developed as part of this thesis, they have not yet been fully utilised for the problem of heavy species.

We define high quality collision data to be that obtained from R -matrix and other close-coupling techniques (see also table 2.1). They are not addressed here but for heavy species, attention is drawn to the DARC codes (Norrington and Grant 1987) which extend the R -matrix method to the fully relativistic regime. The high quality atomic structure problem is very similar to that of the lighter systems (see sections 2.3.4.1 and 2.3.4.2) but with the necessary inclusion of more relativistic effects and in particular the full Dirac code, GRASP (Dyall *et al* 1989).

It should be noted, however, that the framework presented here lends itself to inclusion of very high quality data (such as the above) for targeted ionisation states, or even single transitions; see section 3.3.1 for details.

3.3.1 Mixing data of varying quality

In section 3.2.2 the concept of resolved and unresolved levels was developed, where levels which directly contribute to spectral emission are dealt with at a higher quality from those which only affect population structure. These data have to be combined with one another in order to calculate a population structure.

For example, combining level-resolved data with configuration-average data requires statistical splitting of the excitation and radiative rates between individual and grouped levels (i.e. the configurations). Such splitting for the LS/IC case is discussed in detail in Brooks (1997).

One of the main advantages of the collisional–radiative treatment used in this thesis is that data of varying quality can be mixed without the danger of double counting states and resonances. Other population codes, such as HULLAC

(Bar-Shalom *et al* 1988; see also section 3.3.4), include the autoionising levels in the collisional–radiative matrix as a way of modelling such resonance behaviour. This is in contrast to the ADAS approach where it is assumed that the resonances have been included in the rates which are used as input to the collisional–radiative matrix. This means that the high quality R -matrix calculations which typically resolve resonances from thousands of intermediate states are automatically modelled in the ADAS collisional–radiative model.

The present model is then able to give a complete description of any system using baseline quality atomic data with the facility to selectively improve stages and transitions of interest with more precise data from other techniques, literature or measurements (see table 2.1). Other approaches intrinsically exclude this selective refinement. We note, however, that the fundamental HULLAC atomic collision data (distorted wave) is better than the baseline data used here.

3.3.2 Baseline quality electron-impact excitation

For baseline electron-impact excitation, a plane wave Born (PWB) approach is utilised as implemented within the Cowan code³ (Cowan 1981). Such an approach does not take into account resonance structure (discussed in section 2.3.4.3) but does provide a rapid way of generating baseline data for every ionisation stage of, e.g., tungsten (see section 3.5.1 for such results).

The practical implementation is to take integrals of spherical Bessel functions over the wavefunctions, thus obtaining $\langle i|B(K)|j \rangle$ as a function of momentum transfer, K . Then,

$$gf(K) = \frac{\Delta E}{K^2} |\langle i|B(K)|j \rangle|^2 \quad (3.11)$$

where $f(K)$ is the generalised oscillator strength. Integrations over K are then performed in order to find collision strengths, Ω , as a function of electron energy, ϵ ,

$$\Omega(\epsilon) = \frac{8}{\epsilon} \int_{K_{min}}^{K_{max}} gf(K) d(\ln K) \quad (3.12)$$

³<ftp://aphysics.lanl.gov/pub/cowan/>

where,

$$K_{min} = \epsilon^{\frac{1}{2}} - (\epsilon - \Delta E)^{\frac{1}{2}} \quad (3.13)$$

$$K_{max} = \epsilon^{\frac{1}{2}} + (\epsilon - \Delta E)^{\frac{1}{2}}. \quad (3.14)$$

The method presented here lends itself to calculations using a computer code and is the method implemented in the Cowan code (Cowan 1981)⁴. It has also been recently implemented within AUTOSTRUCTURE (Badnell 1997) as an extension to the infinite energy Born calculations as discussed in section 2.5.2 and Whiteford *et al* (2001).

3.3.3 Baseline quality ionisation and recombination

Baseline quality methods are required to generate arbitrary data without too much time and use of computational resources. This has two main uses, namely, to gain a first-cut appreciation as to how the plasma is behaving without the need for complex calculations and also to fill in gaps in data where the accuracy of the data is not critical for the application, but is nonetheless required. This approach is in keeping with the theme of recognising a problem in analysis of a plasma and then generating appropriate data and models, rather than simply calculating all possible data at the highest level.

The methods described below have been used to generate systematically ionisation and recombination coefficients for many elements in the range $1 \leq Z \leq 82$ (Pb) and automatic procedures exist for the generation of data between $1 \leq Z \leq 92$ (U) as a result of the work presented in this thesis⁵.

The construction of ionisation, recombination and power coefficients has been performed extensively in the past, by exploiting simple parametric forms for key rates, such as the general formula for dielectronic recombination of Burgess (1965), the ionisation formula of Lotz (1968) and the excitation formula of Van Regemorter (1962). Prior to the use of more sophisticated collisional (and gen-

⁴We note that equation 18.157 of Cowan (1981) is incorrect (equation 3.12 here contains the correct expression) but the implementation within the Cowan code is correct.

⁵We note that the Cowan code (Cowan 1981) can calculate data for any element, even ones that don't exist.

eralised collisional) radiative coefficients, impurity transport codes (see sections 2.3.1.3 and 4.4) relied on these formulae, which in turn required only relatively simple parameters such as oscillator strengths, ionisation potentials and excitation energies. Numerical tabulation of data as opposed to simple expressions are necessary when more complex techniques are used. These numerical tabulations are also more suited to the selective data refinement as described in section 3.3.1.

For quick estimates on unfamiliar species, such approximate methods described above are still in use. Within the ADAS Project (Summers 1999), they are made available as ‘Case A’ parameterisations. These parametric forms are of only modest precision in general, depending partly on the quality of the parameters themselves, but are unsafe for medium/heavy species. A more robust parameterisation, called ‘Case B’ was developed for the ADAS Project and it is this which is described here.

3.3.3.1 Ionisation

We consider separately the processes described in section 2.3.4.5 for ionisation, namely direct ionisation and excitation–autoionisation.

The effective ionisation rate coefficient is treated in Case B as the ionisation rate coefficient from the ground state, ignoring stepwise ionisation. This restricts the applicability to scaled electron densities $N_e/z_1^7 < 10^{14} \text{ cm}^{-3}$. It is based on the semi-empirical expression of Burgess and Chidichimo (1983) where $S^{\text{bchid}}(z, \chi, \zeta, T_e)$ is viewed as a formula for the ionisation of an ion of charge z from a quantum shell of ionisation potential χ and with the number of equivalent electrons in the shell being ζ . The expression is

$$S^{\text{bchid}} = 2.17 \times 10^{-8} c \zeta (I_{\text{H}}/\chi)^{3/2} (\chi/kT_e)^{1/2} \times E_1(\chi/kT_e) w \text{ cm}^3 \text{ s}^{-1}, \quad (3.15)$$

where

$$w = \left(\ln \left(1 + \frac{kT_e}{\xi} \right) \right)^{\beta(1+kT_e/\chi)}, \quad (3.16)$$

$$\beta = \frac{1}{4} \left(\left(\frac{100z + 91}{4z + 3} \right)^{1/2} - 5 \right) \quad (3.17)$$

and $E_1(x)$ is the first exponential integral function. Although the expression has similarities to the Lotz (1968) formula, the Burgess and Chidichimo (1983) formula was created with a recognition of the contribution of excitation–autoionisation to net ionisation. With a proper prescription for the inclusion of excitation–autoionisation, as described by Burgess *et al* (1977) and elaborated by Burgess and Chidichimo (1983), the semi-empirical formulae match higher quality results with significantly lower discrepancy. We write

$$S^{(z \rightarrow z+1)} = S_{\text{shd}}^{\text{approx}} + S_{\text{excit}}^{\text{approx}}, \quad (3.18)$$

where

$$S_{\text{shd}}^{\text{approx}} = \sum_I c_I \sum_{i \in I} S^{\text{bchid}}(z, \chi_i, \zeta_i, T_e) \quad (3.19)$$

is called the shell direct (shd) part and the summation is over the set of quantum shells I .

$$S_{\text{excit}}^{\text{approx}} = \sum_R c_R \sum_{r \in R} 1.45 \omega_r(I_H / \Delta E_r) (I_H / \epsilon) \pi a_0^2 \quad (3.20)$$

is the excitation–autoionisation part and the summation is over a set of isolated autoionising resonances R . For the Case B parameterisations, the ionisation potentials (χ_i), shell occupancies (ζ_i) and the division of ionisation between shell-direct and excitation–autoionisation are treated flexibly.

The principles are evident from two examples. Consider an ion, such as W^{12+} , whose ground state has the outer electron configuration $5s^2 5p$. The ionisation potential for the $5p$ electron is denoted by I_{5p} and for a $5s$ electron is denoted by I_{5s} . The initial shell direct equivalent electron assignments are $\zeta_{5p} = 1$ and $\zeta_{5s} = 2$ at these ionisation potentials, respectively. However, autoionising levels of the form $5s 5p n l$ lie densely through the $5s^2$ ionisation threshold and on into the $5s^2 + e^-$ continuum. Excitation of a $5s$ electron to such levels leads to autoionisation into this continuum with almost unit branching probability. The effect can be included in the shell direct part by setting the effective ionisation potential for the $5s$ electron to I_{5p} . Burgess *et al* (1977) called this case (ii). The complete

shell structure is $[\text{Kr}] 4d^{10}4f^{13}5s^25p$. The shell direct part from the inner shells, especially $4f^{13}$ and $4d^{10}$ have a large ζ weighting and must be included. The first auto-ionising configuration from promotion of a 4f electron is $4f^{12}5s^25p^2$ and it is noted that it lies substantially above the $5s^2$ ionisation threshold. It might be appropriate to include such auto-ionisation by reducing the ionisation potential of the 4f electron from I_{4f} to $I_{4f} - I_{5p}$. This is the Burgess *et al* (1977) case (i) situation. On the other hand, ionisation cross-sections are zero at threshold whereas excitation cross-sections (for ions) are finite at threshold. Detailed measured ionisation cross-sections show steps at discrete auto-ionising level energies. For a more precise description within the Case B parameterisation, we include an $S_{\text{excit}}^{\text{approx}}$ contribution from $4f^{13}5s^25p \rightarrow 4f^{12}5s^25p^2$ and then put autoionising configurations $4f^{12}5s^25pnl$ with $n > 5$ into the shell direct part at effective ionisation potential $I_{4f} - I_{6s}$. The complete sets of effective χ s, ζ s, ΔE_r s and ω_r s can be prepared semi-automatically from the results of structure calculations. Available detailed assessments, such as that of Loch *et al* (2003) allow a final adjustment, handled as a scaling and ionisation potential shift, as

$$S^{(z \rightarrow z+1)} = \text{scale } e^{e \text{disp} / kT_e} [S_{\text{shd}}^{\text{approx}} + S_{\text{excit}}^{\text{approx}}]. \quad (3.21)$$

See section 3.5.3 for an example of this method being used on tungsten, specifically W^{24+} .

3.3.3.2 Recombination

Three body recombination is not taken into account for baseline quality recombination data as it is not a significant contributor to recombination in fusion plasmas. It is assumed that radiative recombination and dielectronic recombination are independent processes (see Pindzola *et al* 1992):

$$\alpha^{(z+1 \rightarrow z)} = \alpha_d + \alpha_r. \quad (3.22)$$

Instead of detailed modelling of redistribution and ionisation from excited states (which reduces the effective dielectronic rate coefficient especially in finite den-

sity plasma), a cut-off n -shell, n_t , is introduced (Wilson 1962),

$$n_t = \left(5.57 \times 10^{17} \frac{\text{cm}^{-3}}{N_e} z_1^6 \left(\frac{kT_e}{I_H} \right)^{\frac{1}{2}} \right)^{\frac{1}{7}}. \quad (3.23)$$

Captures to levels below n_t are assumed to populate ultimately the ground level and so contribute to the effective coefficient, whereas captures to levels above n_t do not. n_t depends on electron density and it is this which represents the finite density collisional-radiative effects⁶.

For dielectronic recombination, the termination of the capture sum to higher n -shells is a critical matter for modelling finite density plasmas. On the other hand, the distribution of dielectronic capture with n -shell depends on details of the parent transition — not only on the oscillator strength and transition energy, but also on quality of resonance capture collision strengths and alternative Auger channels. The Burgess general formula (GF) does not allow these latter issues to be addressed directly. By contrast, the Burgess–Bethe general program, BBGP, see Badnell *et al* (2004), does and so is used as the basis of the Case B dielectronic recombination. BBGP evaluates dipole nl -selective resonance capture in the Bethe approximation via a correspondence principle argument. More precisely, introduce

$$cor_l = \frac{\sum_{l'} \Omega((S_p L'_p J'_p) k' l', (S_p L_p J_p) k |_{=0} l)}{\sum_{l'} \Omega^{\text{Bethe}}((S_p L'_p J'_p) k' l', (S_p L_p J_p) k |_{=0} l)}. \quad (3.24)$$

The GF is a functional fit to extensive BBGP calculations at zero-density. The latter used a fixed set of Bethe correction factors based on cross-section data available at the time. Alternative Auger channels open primarily extra loss channels competing with stabilisation. To a good approximation, it can be assumed that once an alternate channel is open then there is unit branching ratio in its favour. Thus an n -shell cut-off, n_{aa} , may be introduced based only on energetics. In practice, the lower of n_t and n_{aa} is applied. All necessary data for the above two

⁶We note that the Wilson cut-off predates DR (discovered in 1964) and works best when DR is ignored.

aspects can be obtained from an atomic structure calculation, as can more precise energies for the lowest n -shell stabilised states which influence the low temperature dependence of dielectronic recombination. Residual error of the Case B approach, in comparison with detailed calculations, comes from non-dipole collisional transitions and specific low-lying resonances. In principle, availability of high quality data, such as that of the DR project (Badnell *et al* 2003; see also section 3.3.5) for a few members of an iso-electronic sequence allows a final adjustment, handled as a scaling and an effective transition energy shift, as

$$\alpha_d = \text{scale}_1 e^{\text{edisp}_1/akT_e} \sum_{i_1 \in \text{grp}_1} \alpha_{i_1}^{BGP} + \text{scale}_2 e^{\text{edisp}_2/akT_e} \sum_{i_2 \in \text{grp}_2} \alpha_{i_2}^{BGP}. \quad (3.25)$$

This is treated as scalings on two parent transition groups corresponding to $\Delta n = 0$ and $\Delta n > 0$.

$$a = 1.0 + 0.015 \left(\frac{z_1^3}{(z_1 + 1)^2} \right) \quad (3.26)$$

is taken from the *GF* specification.

Radiative recombination is assembled as

$$\alpha_r = \text{scale} (z_1^2 I_H / kT_e \nu^2)^{\text{edisp}} \alpha^H(\nu_0) + \sum_{n > n_0}^{n_t} \alpha^H(\nu_n), \quad (3.27)$$

comprising adjusted hydrogenic recombination to the lowest n -shell at the effective principal quantum number ν_0 plus a sum of hydrogenic recombination to higher n -shells at integer values of the principal quantum number — terminated at n_t . The adjustment factors ‘scale’ and ‘edisp’ are obtained from selected fits to higher precision data.

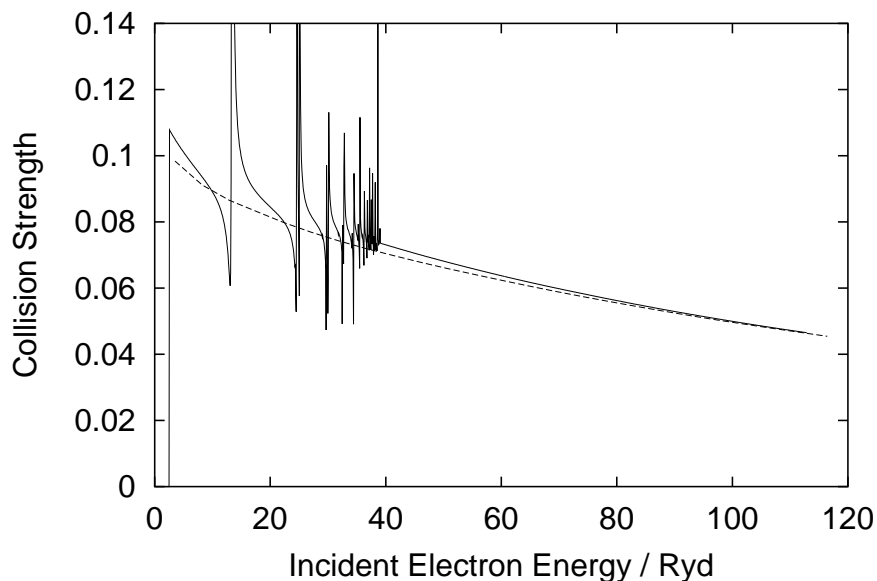


Figure 3.1: Comparison between configuration-average distorted-wave (CADW) and R -matrix collision strengths for the $2s - 2p$ transition in Ar^{15+} for the $l = 4$ partial wave. The dashed line denotes the results of the CADW calculation and the solid line that of the R -matrix calculation.

3.3.4 Intermediate quality electron-impact excitation

The configuration-average distorted-wave (CADW) approximation of Pindzola *et al* (1986a,1986b⁷) can be used for calculating electron-impact excitation cross-sections between configurations of any given system, as well as for ionisation (see section 3.3.5).

In figure 3.1, a comparison is made with R -matrix data as calculated in section 2.5 for one partial wave of the $1s^22s - 1s^22p$ transition in Ar^{15+} . As would be expected, the CADW results trace the background of the R -matrix collision strength but do not include the resonance effects. The CADW method was investigated as part of this thesis but data was not produced in bulk as part of the present work.

The factorised distorted-wave approach (Bar-Shalom *et al* 1988) splits (i.e. factorises) the angular and radial parts of the distorted-wave problem to obtain full

⁷We note the typographical error in equation 4 of Pindzola *et al* (1986b) — the q_3 should be q_2 .

IC semi-relativistic cross-sections. This method is implemented within the HULLAC (Bar-Shalom *et al* 1988) and FAC (Gu 2003) codes. It should be noted that these codes are more than just factorised DW codes and also contain implementations of atomic structure and collisional–radiative modelling techniques. See section 3.3.1 for a discussion of the difference in approach between the collisional–radiative modelling used in these codes and the present work.

3.3.5 Intermediate quality ionisation and recombination

As mentioned in 3.3.4 above, CADW can be used for ionisation as well as excitation. Calculation of the ionisation rates of all stages of krypton forms part of this work and is published in Loch *et al* (2002b).

The threshold energies and the bound radial orbitals for the krypton configurations are calculated using the Cowan code (Cowan 1981). The direct and excitation–autoionisation contributions to electron-impact single ionisation of an atom or ion are calculated in a configuration-average distorted-wave approximation (Pindzola *et al* 1986a, 1986b), which has been successfully employed in the study of many ionised systems (Pindzola *et al* 1987, Pindzola *et al* 1991 and Hathiramani *et al* 1996) and more recently in Colgan *et al* (2000), Shaw *et al* (2001) and Aichele *et al* (2001).

For the more highly-charged ionisation stages, configuration-average radiative and autoionisation rates are evaluated and used to determine the branching ratios needed for contributions from excitation–autoionisation. In this work, we have not included contributions from resonant-excitation double-autoionisation, which are generally small compared to the contribution from excitation–autoionisation.

Configuration-average photoionisation calculations are used to obtain the infinite energy limit point for the direct contributions to electron-impact ionisation. The cross-section contributions from excitation–autoionisation at the higher incident energies are given by extrapolations of fits to the lower energy results. The ionisation cross-sections are then transformed into rate coefficients by integration with a Maxwellian velocity distribution at the appropriate temperature.

Figure 3.2 shows cross sections for the ionisation of Kr^{20+} and figure 3.3 show the corresponding rate coefficients. Data for tungsten, calculated using the

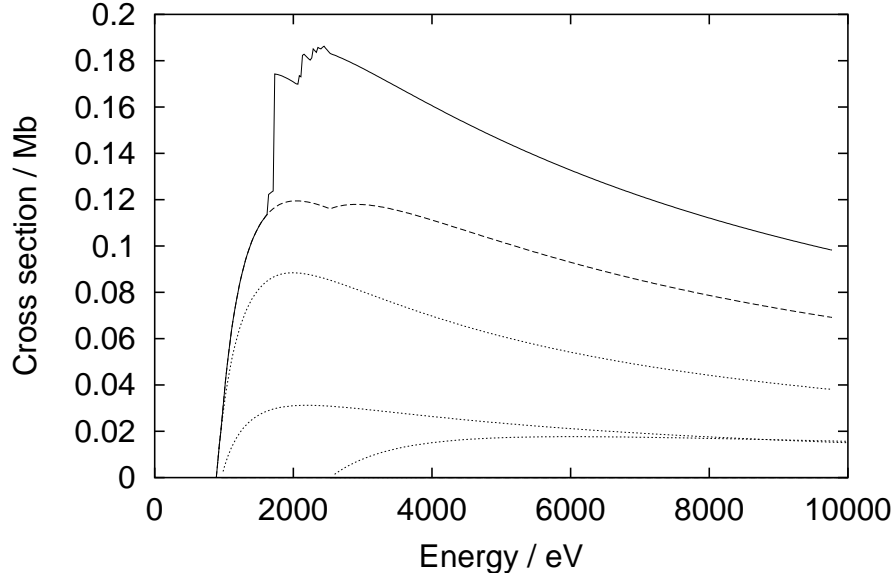


Figure 3.2: CADW cross-sections for Kr^{20+} . The dotted lines denote the contributions from the various direct ionisation routes from the 2p, 3s and 3p sub-shells, along with the total for direct ionisation (dashed line) and the total cross-section including EA (solid line)

methods given above are presented in section 3.5.3.

Intermediate (and also high) quality recombination data is considered to be that of the DR project (Badnell *et al* 2003). This has not yet been extended to very heavy species but does include few electron ions of krypton and xenon. The beryllium-like sequence as calculated by Colgan *et al* (2003) and as part of the present work is discussed here as an example.

For a $\Delta n = 0$ core transition, the DR process for a beryllium-like ion can be represented by,

$$1s^2 2s^2 \ ^1S_0 + e^- \rightarrow 1s^2 2s 2p \ [^3P_{0,1,2}; ^1P_1] \ nl \quad (3.28)$$

$$1s^2 2s^2 \ ^1S_0 + e^- \rightarrow 1s^2 2p^2 \ [^1S_0; ^3P_{0,1,2}; ^1D_2] \ nl \quad (3.29)$$

$$1s^2 2s 2p \ [^3P_{0,1,2}] + e^- \rightarrow 1s^2 2s 2p \ [^3P_{0,1,2}; ^1P_1] \ nl \quad (3.30)$$

$$1s^2 2s 2p \ [^3P_{0,1,2}] + e^- \rightarrow 1s^2 2p^2 \ [^1S_0; ^3P_{0,1,2}; ^1D_2] \ nl \quad (3.31)$$

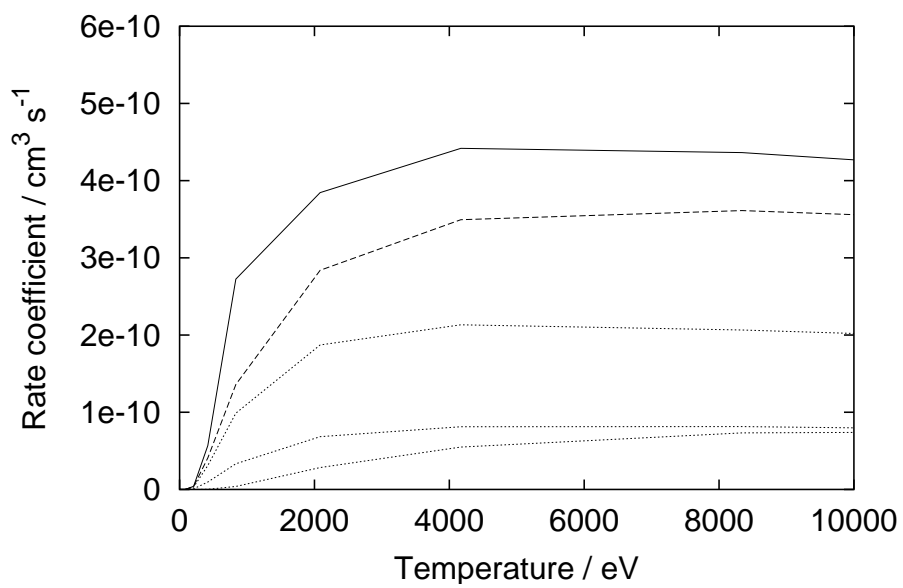


Figure 3.3: CADW rate coefficients for Kr^{20+} . The dotted lines denote the contributions from the various direct ionisation routes from the 2p, 3s and 3p sub-shells along with the total for direct ionisation (dashed line) and the total cross-section including EA (solid line)

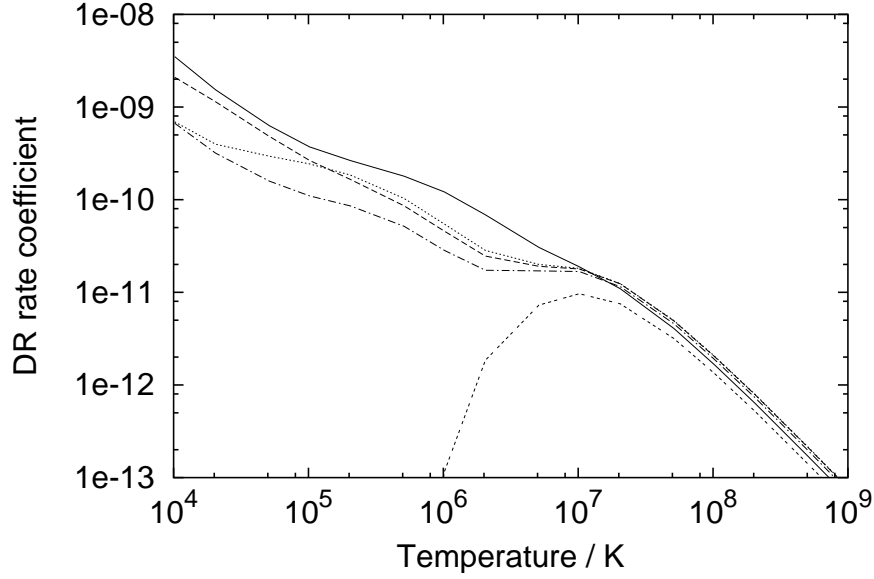
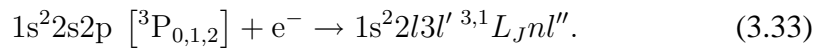
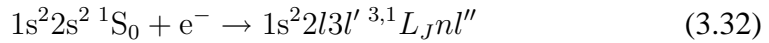


Figure 3.4: Total (i.e. unresolved by final state) DR rate coefficients for beryllium-like krypton going from a $1s^2 2s^2 \ ^1S_0$ parent (solid curve), a $1s^2 2s 2p \ ^3P_0$ parent (dashed curve), a $1s^2 2s 2p \ ^3P_1$ parent (dotted curve) and a $1s^2 2s 2p \ ^3P_2$ parent (chained curve). The dashed-space curve shows the DR rate coefficient from the $1s^2 2s^2 \ ^1S_0$ parent if $\Delta n = 0$ transitions are excluded.

and for a $\Delta n = 1$ core transition by,



In keeping with using krypton as an example, figure 3.4 contains DR totals for beryllium-like krypton illustrating why the $\Delta n = 0$ core transitions are important at low temperature.

3.4 Data reduction

3.4.1 Need for data reduction and superstages

In order for the quantity of atomic data described in this thesis to be usable for plasma modelling, it needs to be presented in a reduced form. The method used here is to bundle ionisation stages together into ‘superstages’. These superstages represent a group of ionisation stages assumed to be in equilibrium within the superstage with an effective ionisation and recombination rate in and out of the superstage. This is analogous (in fact it is simpler) to assuming that ordinary levels of an atom are relaxed and that only the populations of the ground and metastable states change in time. These concepts are expressed more formally below in section 3.4.2.

All of the diagnostic deliverables suited to modelling a fusion plasma can be bundled into superstages by solving for an ionisation balance within the superstage and then summing the deliverables, weighting by the local ionisation balance. These deliverables are:

- effective ionisation coefficient (see section 2.3.1.3),
- effective recombination coefficient (see section 2.3.1.3),
- feature photon emissivity coefficient (see section 3.2.1),
- total radiated power (see section 4.3),
- effective ion charge (see section 4.6).

When modelling transport using, e.g., the JETTO suite of codes (see Parail *et al* 1999, Lönnroth *et al* 2003) a number of quantities are modelled (temporally and spatially) in an integrated and self consistent way. Namely, electron temperature, electron density and the density of each ionisation stage. These are included in an iterative model which uses SANCO (Lauro-Taroni *et al* 1994, see also section 4.4). The time it takes to solve this problem scales as $\sim N^3$ (Parail, 2003). For a species such as neon, $N = 13$ (11 ionisation stages with an addition of electron temperature and density). Going to tungsten, $N = 77$, giving a factor of $\gtrsim 200$

increase in the resources required to solve the problem. Reducing the number of effective ionisation stages to ~ 20 will reduce this factor to just over six.

3.4.2 Flexible partitioning methodology

In the generalised collisional–radiative picture, an element in a plasma is described by the abundances of all the metastables of every ionisation stage, by the effective recombination and ionisation coefficients which link them together and by the emission coefficients which are quasi-static with respect to and driven by these metastables. The complete set of populations which is then (in principle) tracked in dynamic transport modelling is large. However, not all populations are of equal importance and so grouping of populations may be appropriate. This is called a condensation, which converts the situation to tracking the group populations with their equivalent effective recombination and ionisation coefficients and emission coefficients. The specification of a grouping is called a partition. The original complete set of individual metastables is called the root partition and we can envisage a particular partition having parent and grandparent partitions, and on back to the root partition.

Consider the definition of a partition, and the procedure for condensing from the parent partition to it,

$$\{1 \oplus 2 \oplus 3 \oplus \dots \oplus i \oplus \dots \oplus N\} \quad (3.34)$$

where

$$\{1\} \subset \{p_1 \oplus p_2 \oplus \dots \oplus p_{N_1}\}_{\text{prt}} \quad (3.35)$$

$$\{2\} \subset \{p_{N_1+1} \oplus p_{N_1+2} \oplus \dots \oplus p_{N_2}\}_{\text{prt}} \quad (3.36)$$

...

$$\{N\} \subset \{p_{N_{\text{prt}}-1+1} \oplus p_{N_{\text{prt}}-1+2} \oplus \dots \oplus p_{N_{\text{prt}}}\}_{\text{prt}} \quad (3.37)$$

and $P \equiv p_1, \dots, p_{N_{\text{prt}}}$ is a permutation of $1, \dots, N_{\text{prt}}$ and N_{prt} is the number of

groups in the parent partition

$$\{1 \oplus 2 \oplus 3 \oplus \cdots \oplus i \oplus \cdots \oplus N_{\text{prt}}\}_{\text{prt}}. \quad (3.38)$$

Consider next the evolution of populations of members of a partition of an element in a plasma. For an element of nuclear charge z_0 , without loss of generality, consider the partition layer ‘#01’ with members indexed by i and total number of members, $I^{[\#01]}$. The populations of the partition members are denoted by,

$$N_i^{[\#01]} : i = 0, \dots, I^{[\#01]}. \quad (3.39)$$

The time dependence of the partition member populations are then given by the equations,

$$\begin{aligned} \frac{d}{dt} N_i^{[\#01]} &= N_e S_{i-1 \rightarrow i}^{[\#01]} N_{i-1}^{[\#01]} \\ &\quad - \left(N_e S_{i \rightarrow i+1}^{[\#01]} + N_e \alpha_{i \rightarrow i-1}^{[\#01]} \right) N_i^{[\#01]} \\ &\quad + N_e \alpha_{i+1 \rightarrow i}^{[\#01]} N_{i+1}^{[\#01]}, \end{aligned} \quad (3.40)$$

as in section 2.3.3, where the coefficients are the partitioned collisional radiative coefficients.

Consider now the daughter partition layer ‘#02’. Again, without loss of generality, suppose that the members of layer ‘#01’ between index values i_0 and i_1 map into the member p of ‘#02’, so that

$$N_p^{[\#02]} = \sum_{i=i_0}^{i_1} N_i^{[\#01]} \quad (3.41)$$

and, summing the time dependent equations,

$$\begin{aligned} \frac{d}{dt} N_k^{[\#02]} &= N_e S_{i_0-1 \rightarrow i_0}^{[\#01]} N_{i_0-1}^{[\#01]} \\ &\quad - \left(N_e S_{i_1 \rightarrow i_1+1}^{[\#01]} + N_e \alpha_{i_0 \rightarrow i_0-1}^{[\#01]} \right) N_{i_0}^{[\#01]} \\ &\quad + N_e \alpha_{i_1+1 \rightarrow i_1}^{[\#01]} N_{i_1+1}^{[\#01]}. \end{aligned} \quad (3.42)$$

Impose a quasi-static equilibrium for the '#01' partition members of populations i_0 to i_1 so that

$$N_{i_0}^{[#01]} \Big|_{\text{eq}} = \left(\frac{\alpha_{i_0+1 \rightarrow i_0}^{[#01]}}{S_{i_0 \rightarrow i_0+1}^{[#01]}} \right) N_{i_0+1}^{[#01]} \Big|_{\text{eq}} \quad (3.43)$$

$$N_{i_0+1}^{[#01]} \Big|_{\text{eq}} = \left(\frac{\alpha_{i_0+2 \rightarrow i_0+1}^{[#01]}}{S_{i_0+1 \rightarrow i_0+2}^{[#01]}} \right) N_{i_0+2}^{[#01]} \Big|_{\text{eq}} \quad (3.44)$$

...

$$N_{i_1-1}^{[#01]} \Big|_{\text{eq}} = \left(\frac{\alpha_{i_1 \rightarrow i_1-1}^{[#01]}}{S_{i_1-1 \rightarrow i_1}^{[#01]}} \right) N_{i_1}^{[#01]} \Big|_{\text{eq}}, \quad (3.45)$$

still subject to the normalisation

$$N_p^{[#02]} = \sum_{i=i_0}^{i_1} N_i^{[#01]} \Big|_{\text{eq}}. \quad (3.46)$$

Then, finally,

$$\alpha_{p \rightarrow p-1}^{[#02]} = \alpha_{i_0 \rightarrow i_0-1}^{[#01]} N_{i_0}^{[#01]} \Big|_{\text{eq}} \quad (3.47)$$

$$S_{p \rightarrow p+1}^{[#02]} = S_{i_1 \rightarrow i_1+1}^{[#01]} N_{i_1}^{[#01]} \Big|_{\text{eq}}. \quad (3.48)$$

Also, for the equilibrium stage population solution, the radiated power function (see section 4.3) for the daughter partition is $\text{tot}P_p^{[#02]}$ and is calculated as

$$\text{tot}P_p^{[#02]} = \sum_{i=i_0}^{i_1} \text{tot}P_i^{[#01]} \left(\frac{N_i^{[#01]}}{N_p^{[#02]}} \right) \Big|_{\text{eq}} \quad (3.49)$$

$$= \sum_{i=i_0}^{i_1} \left({}_{\text{LT}}P_i^{[#01]} + {}_{\text{RB}}P_i^{[#01]} \right) \left(\frac{N_i^{[#01]}}{N_p^{[#02]}} \right) \Big|_{\text{eq}}, \quad (3.50)$$

with separate radiated power function contributions arising from low level line power, ${}_{\text{LT}}P$, and the recombination-bremsstrahlung-cascade power, ${}_{\text{RB}}P$, usually expressed as P_{LT} and P_{RB} respectively, see sections 4.3.1 and 4.3.2.

For the spectral interval $[\Lambda_0, \Lambda_1]$, the envelope feature photon emissivity coef-

ficients (as originally introduced in its non-condensed form in section 3.2.1) is

$$\mathcal{F}\text{-}\mathcal{P}\mathcal{E}\mathcal{C}_j^{[\#01]} = \sum_{i=i_0}^{i_1} \mathcal{F}\text{-}\mathcal{P}\mathcal{E}\mathcal{C}_{i,j} N_i^{[\#01]}, \quad (3.51)$$

where j is used here to denote the wavelength position of the $\mathcal{F}\text{-}\mathcal{P}\mathcal{E}\mathcal{C}$.

3.4.3 Flexible partitioning implementation and example

As an example of the implementation of flexible partitioning, consider krypton, with 37 ionisation stages, including the fully stripped ion (Kr^{36+}). Neglecting metastables, partition layer 1 is given by

$$\{\text{Kr}^{0+} \oplus \text{Kr}^{1+} \oplus \dots \oplus \text{Kr}^{35+} \oplus \text{Kr}^{36+}\}. \quad (3.52)$$

Figure 3.5 shows the fractional change in ionisation potential as a function of charge. Taking the peaks in this fractional change as an indication of where partition layers should sit, and with a buffer layer of one ion at each layer we form the partitioned set (analogous to equation 3.34),

$$\{1 \oplus 2 \oplus 3 \oplus \dots \oplus i \oplus \dots \oplus N\} \quad N = 16, \quad (3.53)$$

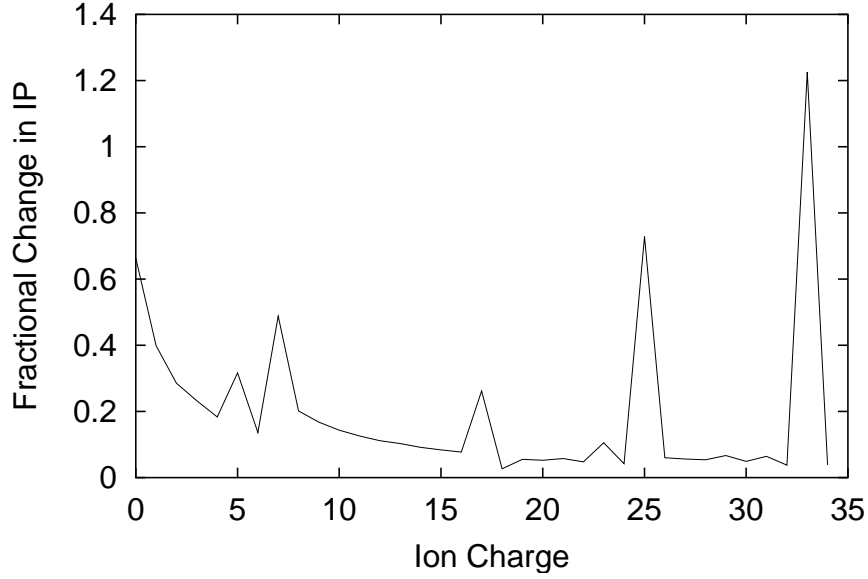


Figure 3.5: Fractional change in the ionisation potential of krypton as a function of charge state. The sharp peaks correspond to shell boundaries and are the natural places to have partition boundaries.

where (analogous to equations 3.35 through 3.37),

$$\{1\} \subset \{\text{Kr}^{0+}\} \quad (3.54)$$

$$\{2\} \subset \{\text{Kr}^{1+}\} \quad (3.55)$$

$$\{3\} \subset \{\text{Kr}^{2+} \oplus \text{Kr}^{3+} \oplus \text{Kr}^{4+} \oplus \text{Kr}^{5+} \oplus \text{Kr}^{6+}\} \quad (3.56)$$

$$\{4\} \subset \{\text{Kr}^{7+}\} \quad (3.57)$$

$$\{5\} \subset \{\text{Kr}^{8+}\} \quad (3.58)$$

$$\{6\} \subset \{\text{Kr}^{9+} \oplus \text{Kr}^{10+} \oplus \text{Kr}^{11+} \oplus \text{Kr}^{12+} \oplus \text{Kr}^{13+} \oplus \text{Kr}^{14+} \oplus \text{Kr}^{15+} \oplus \text{Kr}^{16+}\} \quad (3.59)$$

$$\{7\} \subset \{\text{Kr}^{17+}\} \quad (3.60)$$

$$\{8\} \subset \{\text{Kr}^{18+}\} \quad (3.61)$$

$$\{9\} \subset \{\text{Kr}^{19+} \oplus \text{Kr}^{20+} \oplus \text{Kr}^{21+} \oplus \text{Kr}^{22+} \oplus \text{Kr}^{23+} \oplus \text{Kr}^{24+}\} \quad (3.62)$$

$$\{10\} \subset \{\text{Kr}^{25+}\} \quad (3.63)$$

$$\{11\} \subset \{\text{Kr}^{26+}\} \quad (3.64)$$

$$\{12\} \subset \{\text{Kr}^{27+} \oplus \text{Kr}^{28+} \oplus \text{Kr}^{29+} \oplus \text{Kr}^{30+} \oplus \text{Kr}^{31+} \oplus \text{Kr}^{32+}\} \quad (3.65)$$

$$\{13\} \subset \{\text{Kr}^{33+}\} \quad (3.66)$$

$$\{14\} \subset \{\text{Kr}^{34+}\} \quad (3.67)$$

$$\{15\} \subset \{\text{Kr}^{35+}\} \quad (3.68)$$

$$\{16\} \subset \{\text{Kr}^{36+}\}. \quad (3.69)$$

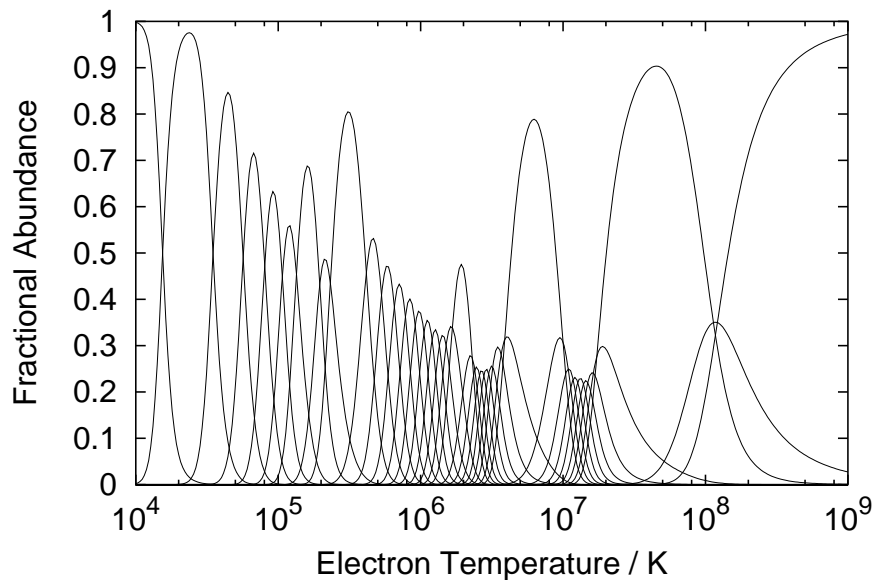


Figure 3.6: Ionisation balance of krypton in coronal equilibrium for all ionisation stages

The ions for partition boundaries can be chosen heuristically using a figure such as figure 3.5 or via a more rigorous, numerical method. In the example above, partition layers were chosen such that the change in peaks were at the 3σ level. We note that the ‘buffer’ layers (at shell boundaries) are also typically the ones which give rise to isolated line emission.

From the partitioned data we can then form a set of partitioned fractional abundances assuming coronal equilibrium. Such a balance is shown in figure 3.6 for no partitioning and in figure 3.7 for the partitions given above.

3.5 Atomic data for tungsten

3.5.1 Excitation data

The excitation data were calculated using the methods described in section 3.3.2.

The number of levels included in each excitation calculation is given in figure 3.8. Note that the number of levels can become very large with just a few configu-

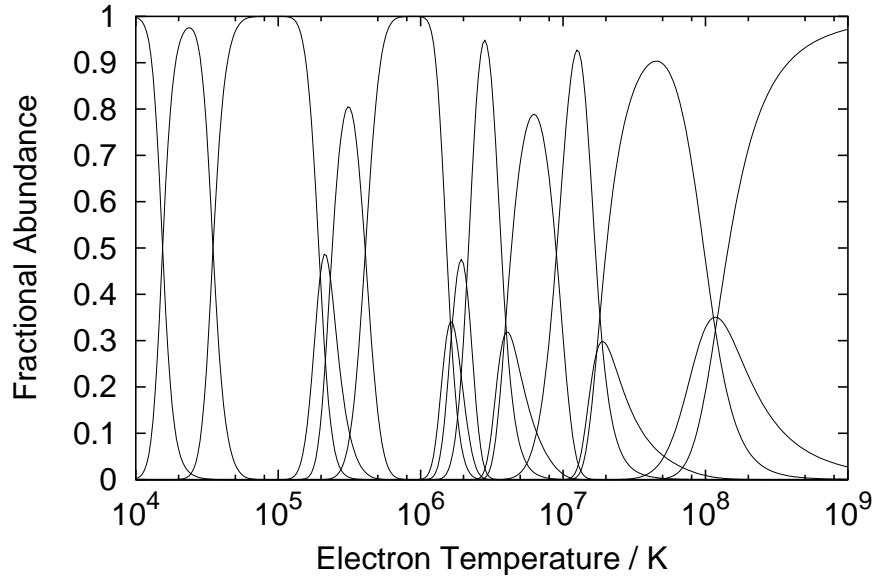


Figure 3.7: Partitioned ionisation balance of krypton in coronal equilibrium with a partitioning applied such that sixteen effective superstages are present

rations. For example, the $[\text{Kr}] 4d^{10}4f^95d$ configuration in W^{18+} gives rise to 1878 J-resolved levels. The number of transitions for each ionisation stage is given in figure 3.9. The total possible number transitions is given by,

$$N_{\text{transitions}} = \frac{N_{\text{levels}} (N_{\text{levels}} - 1)}{2}. \quad (3.70)$$

However, in the PWB method we are using for this data (section 3.3.2), only E0, E1, E2 and M1 transitions (see section 2.3.4.2 for transition categorisation) are calculated so the number of transitions are fewer.

The complete datasets are archived within the ADAS Project (Summers 1999).

3.5.2 Recombination data

The recombination data were calculated using the methods described in section 3.3.3.2.

Effective recombination coefficients for all stages of tungsten are shown in figure 3.10, the DR ‘hump’ can be readily seen in this figure.

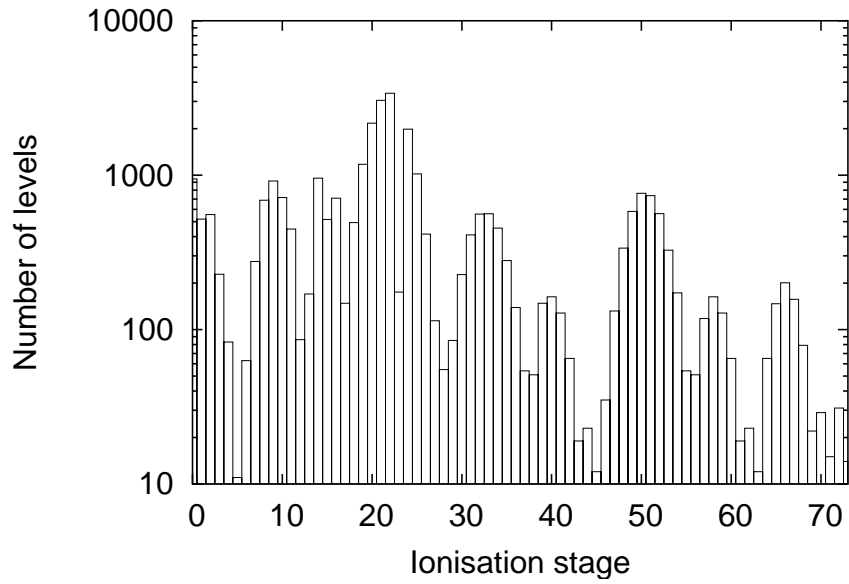


Figure 3.8: Number of levels included in tungsten excitation calculations for each ionisation stage.

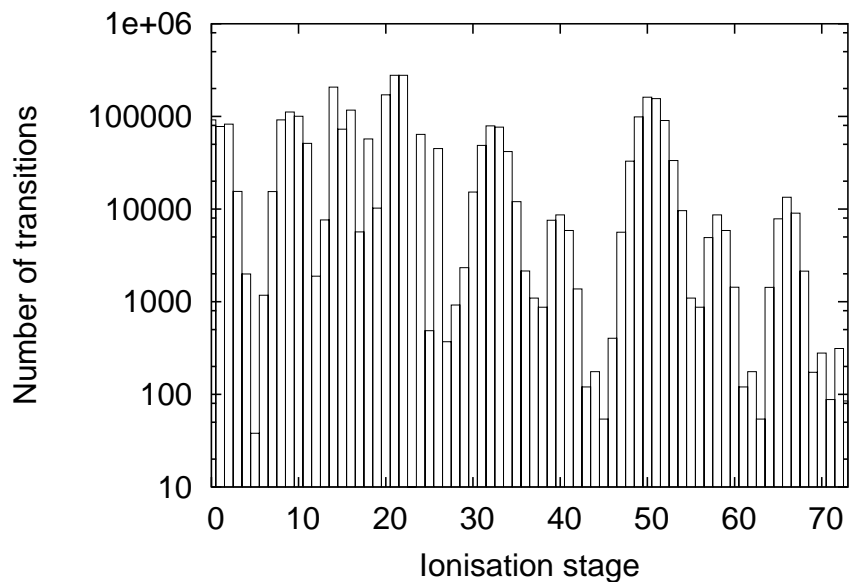


Figure 3.9: Number of transitions included in tungsten excitation calculations for each ionisation stage.

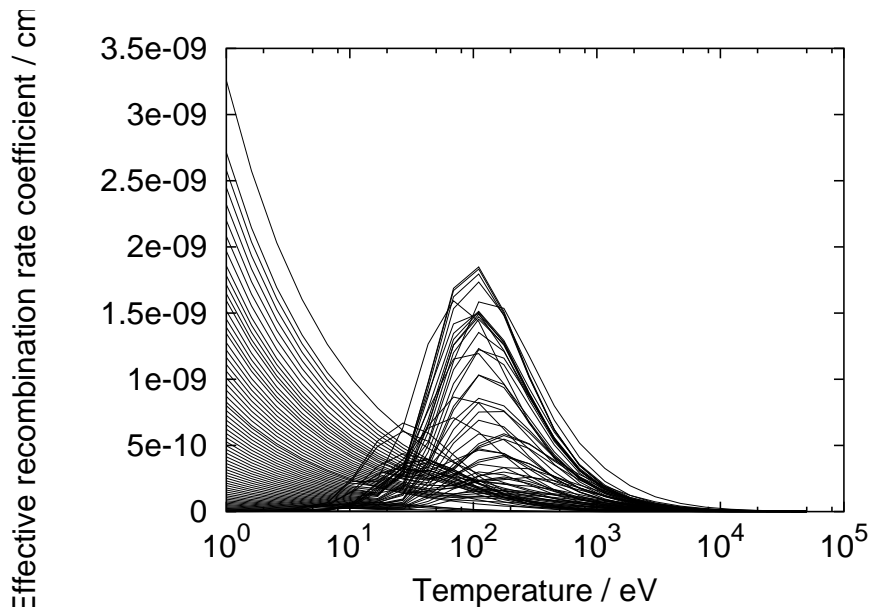


Figure 3.10: Effective recombination rate coefficients for all ionisation stages of tungsten, the DR enhancement at moderate temperatures can be easily seen.

3.5.3 Ionisation data

The ionisation data were calculated using the methods described in section 3.3.3.1.

We note the measurements of Stenke *et al* (1995) and the calculations of Pindzola and Griffin (1997) for the low ionisation stages of tungsten. A comparison for these is shown in figure 3.11.

Effective ionisation coefficients for all stages of tungsten are shown in figure 3.12.

In addition, CADW cross-sections and rate coefficients were calculated for all ionisation stages of tungsten using the same method as used by Pindzola and Griffin (1996), and shown in figure 3.11.

Taking the case of W^{24+} as an example, we can compare approximate forms using the method put forward in section 3.3.3.1 with the CADW results. The ground configuration of W^{24+} is

$$1s^2 2s^2 2p^6 3s^2 3p^6 3d^{10} 4s^2 4p^6 4d^{10} 4f^4 \quad (3.71)$$

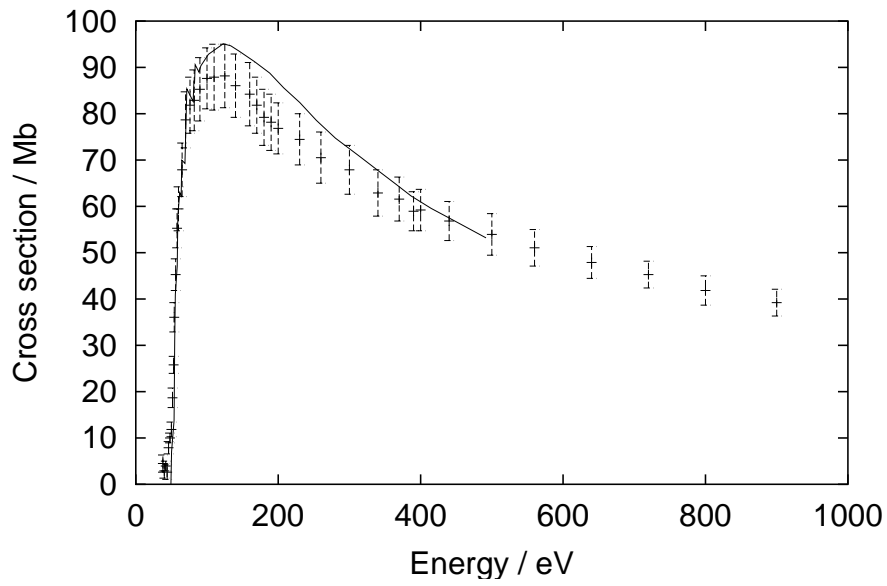


Figure 3.11: Ionisation cross-sections for W^{4+} , the solid curve denotes the CADW work of Pindzola and Griffin (1997) and the points the measurements by Stenke *et al* (1995).

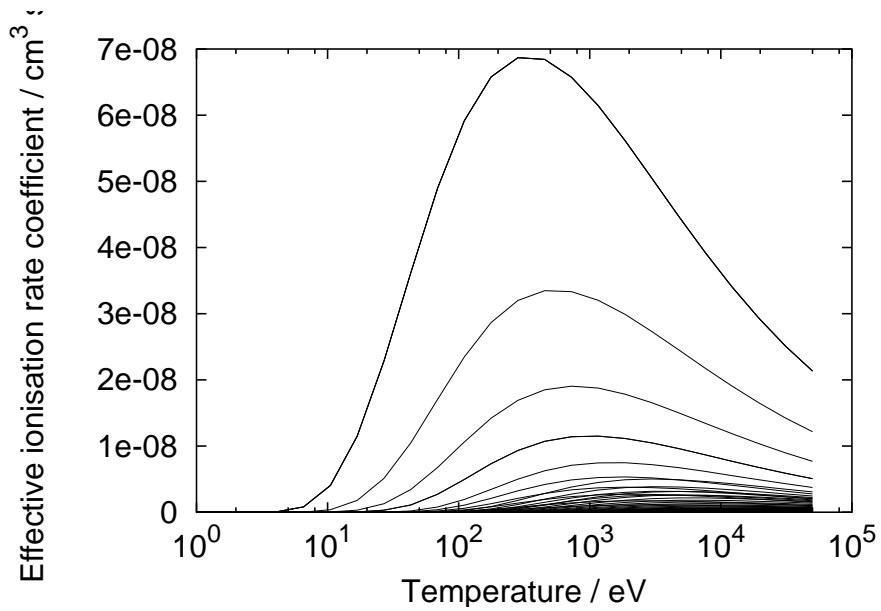


Figure 3.12: Effective ionisation rate coefficients for all ionisation stages of tungsten

Shell	Potential / Ryd (χ_i)	Equivalent electrons (ζ_i)
1s	5185.65	2
2s	952.32	2
2p	844.20	6
3s	266.02	2
3p	233.05	6
3d	193.26	10
4s	96.78	2
4p	85.11	6
4d	69.70	10
4f	53.75	4

Table 3.1: Shell ionisation potentials of W^{24+} as calculated by the Cowan code along with the number of equivalent electrons in each shell when the ion is in its ground configuration. The χ_i and ζ_i refer to the terms entering equation 3.15.

and the shell ionisation potentials (as calculated by the Cowan code) and the number of equivalent electrons are given in table 3.1.

Following the arguments of section 3.3.3.1 we may wish to adjust, say, the χ of the 4d shell to be the same as the 4f shell. Or, equivalently, set ζ_{4d} to zero and ζ_{4f} to fourteen. A comparison between taking these ζ_i s compared with the ζ_i s given in table 3.1 is shown in figure 3.13, along with the CADW results generated as part of this thesis. It can be seen that increasing ζ_{4f} to fourteen gives a better ionisation coefficient but it is still not perfect. A more significant improvement (not shown here) is that the ratio of the CADW result to the $\zeta_{4f} = 14$ result is almost constant compared to the ratio of the CADW result to the $\zeta_{4f} = 4$ result which varies strongly with temperature.

This sort of result can be used to produce the scale parameters which are present in equation 3.21. These scaling parameters could then be used iso-electronically for nearby elements such as tantalum and hafnium.

3.5.4 Equilibrium ionisation balance

Using the above recombination (section 3.5.2) and ionisation (3.5.3) data, an equilibrium ionisation balance can be generated using the techniques outlined in section 2.3.3.

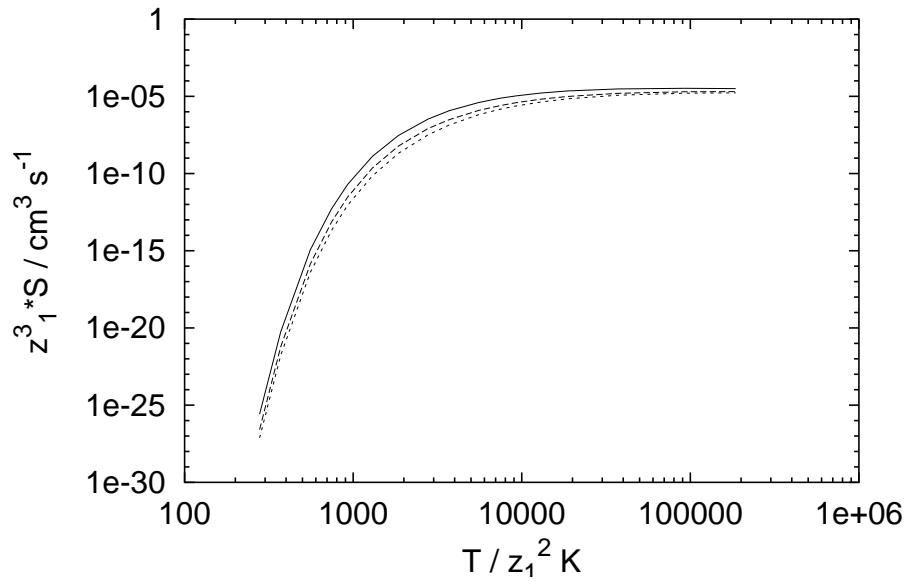


Figure 3.13: Effective ionisation rate coefficients for W^{24+} , the solid curve denotes CADW results, the dashed curve comes from the approximate analytical forms with $\zeta_{4f} = 14$ and the dotted curve corresponds to assuming $\zeta_{4f} = 4$.

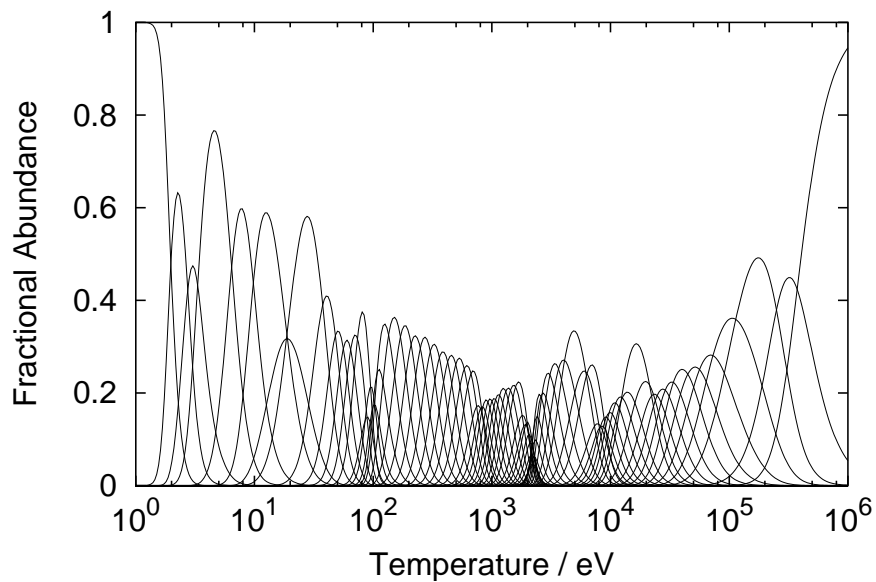


Figure 3.14: Equilibrium ionisation balance for tungsten. Note the complexity at around the 1 – 10keV temperature range, typical of a fusion plasma.

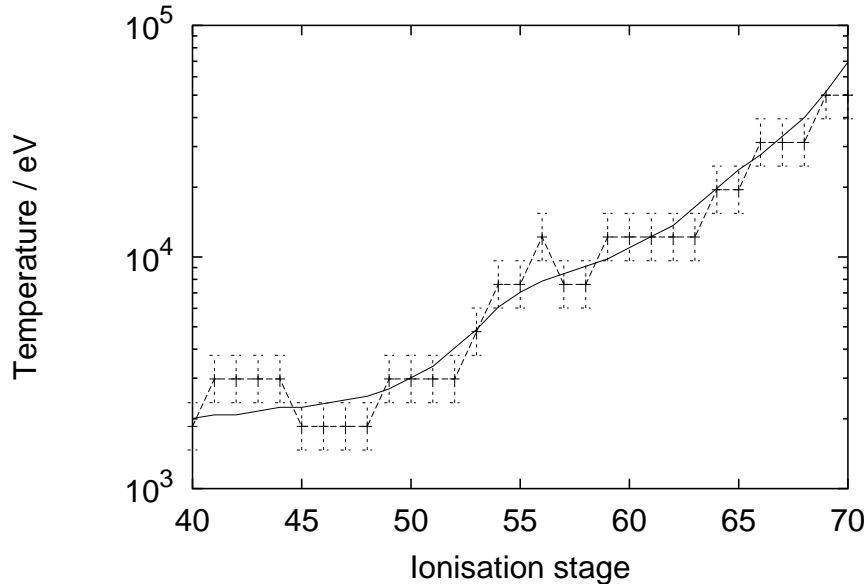


Figure 3.15: Temperature of peak abundance (solid curve) from $z = 40$ to $z = 70$ of tungsten along with temperature at which ionisation and recombination rates are equal (dashed curve), the error bars in the latter data do not show theoretical uncertainties but take account of the data tabulation grid.

Data on radiated power are discussed and given in section 4.3.4 for the above ionisation balance. More complex distributions of ionisation stages due to transport are discussed in detail in section 4.4.

It is illustrative to compare where the ionisation and recombination rate coefficients cross one another (in T_e space) for each ionisation stage and compare this to where the peak abundance lies, such a comparison is made in figure 3.15. Note that the temperature of peak abundance is typically higher than the ionisation potential, this is in contrast to the behavior of lighter species but is expected.

3.5.5 Feature photon emissivity coefficients

\mathcal{F} - $\mathcal{P}\mathcal{E}\mathcal{C}$ s for tungsten can be generated from the data given in section 3.5.1 and the theory given in section 3.2.1.

We take the emission band of W^{30+} in the 40 – 80 Å wavelength region (cor-

responding to the JET KT4 grazing incidence spectrometer⁸) as an example. In figure 3.16 the electron density dependence is shown at a temperature of 828eV⁹. In figure 3.17 the electron temperature dependence is shown at a fixed density of 10^{14}cm^{-3} for low temperatures. Note how the ‘effective’ line ratio of the group of lines at $\sim 50\text{\AA}$ to the group of lines at $\sim 67\text{\AA}$ changes rapidly with temperature. We note that the ionisation potential of W^{30+} is such that emission at these low temperatures is unlikely to be observed in a tokamak. In figure 3.18 the temperature dependence (still for a fixed electron density of 10^{14}cm^{-3}) is shown for higher temperatures, where this ion is more likely to be found in a tokamak.

Application of these $\mathcal{F}\text{-}\mathcal{P}\mathcal{E}\mathcal{C}$ s is given in chapter 4 and in particular section 4.2.

⁸The wavelength range of the KT4 instrument is nominally 10 – 120 \AA but W^{30+} only emits between 40 – 80 \AA .

⁹This value corresponds to $T_e = 1 \times 10^4 z_1^2 \text{K}$ which is why it does not appear as a more rounded value when given in eV.

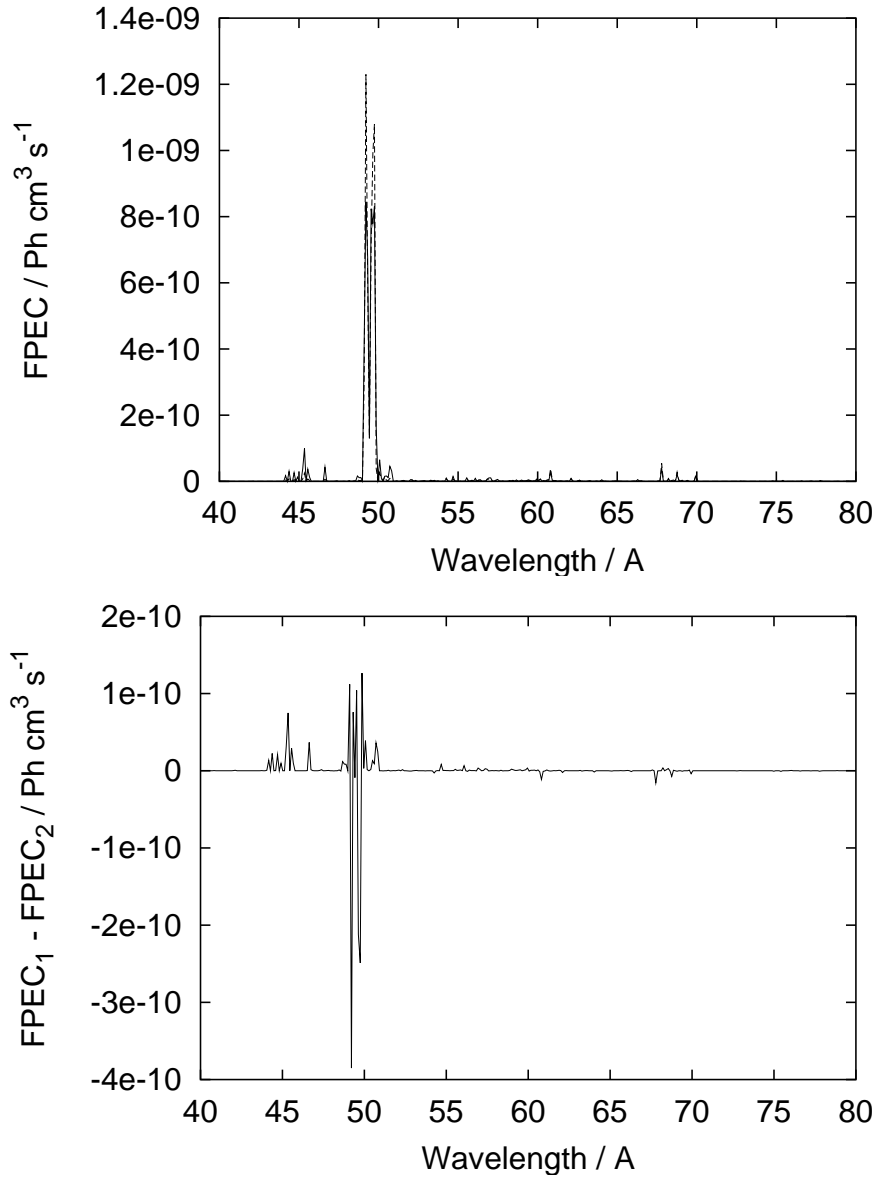


Figure 3.16: Density dependence of the emission of W^{30+} between 40 – 80 Å at a fixed temperature of 828eV. In the upper plot, the emission at a density of 10^{13} cm^{-3} is denoted by a solid line and the dashed line a density of 10^{14} cm^{-3} . The lower plot shows the absolute difference between the two spectra.

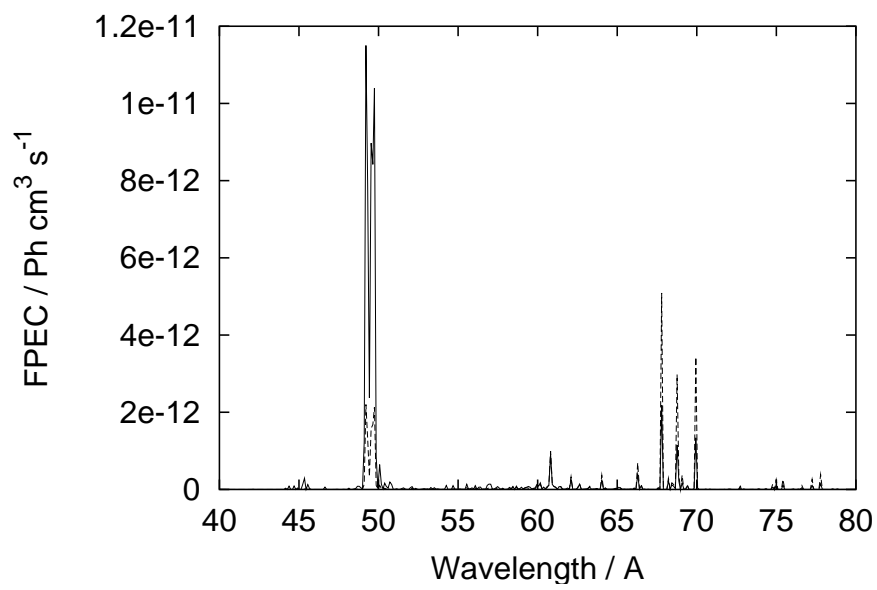


Figure 3.17: Low temperature dependence of the emission of W^{30+} between 40 – 80 Å at a fixed density of 10^{14}cm^{-3} . The emission at a temperature of 41eV is denoted by a solid line and the dashed line a temperature of 16eV (with the data scaled up by a factor of 1×10^3).

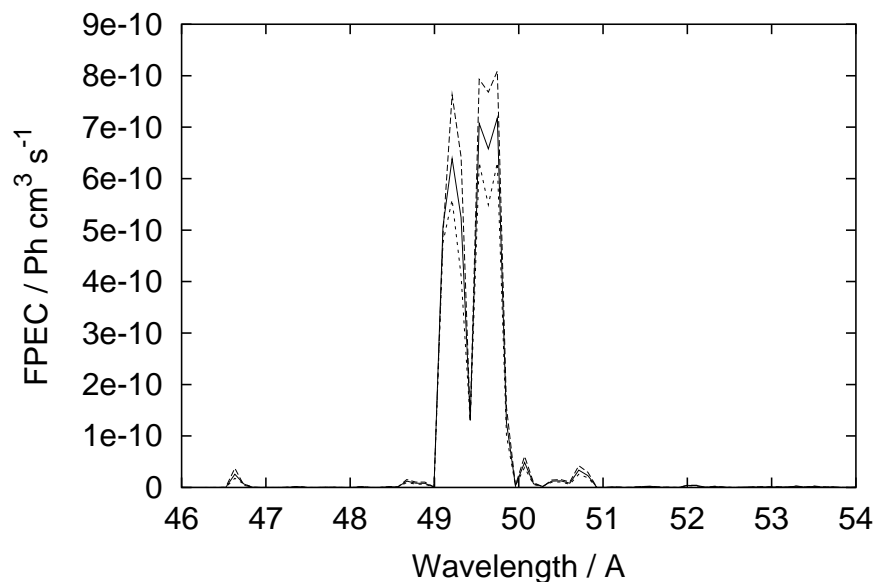


Figure 3.18: Temperature dependence of the emission of W^{30+} between 46 – 54 Å at a fixed density of 10^{14}cm^{-3} . The emission at a temperature of 1660eV is denoted by the solid line, the emission at 4140eV is denoted by the dashed line and the dotted line denotes the emission at a temperature of 8280eV.

Chapter 4

Application to fusion plasmas and the analysis environment

4.1 Introduction

In this chapter we will consider the methodology behind the confrontation of models (using the atomic data discussed in chapters 2 and 3) to fusion experiments.

In section 4.2 the \mathcal{F} - $\mathcal{P}\mathcal{E}\mathcal{C}$ s as defined in section 3.2.1 and calculated for tungsten in section 3.5.5, are compared with measurements from ASDEX-U.

In section 4.3 the radiated power from a fusion plasma is discussed; particular focus is given to soft x-ray filters (section 4.3.3) so that atomic data is provided which can be compared almost directly with bolometer data. The soft x-ray emission in JT60-U is given as a specific example of this application. Comparison with the work of Post *et al* (1977) is also performed for the case of tungsten.

In section 4.4, transport modelling is briefly discussed with an overview of what atomic data can provide: this an expansion of the brief discussion given in section 2.3.1.3. The quantitative aspect of transport analysis is then detailed in section 4.5, where the measurability of transport coefficients from diagnostic data is discussed, with particular emphasis being given to covariances in the transport model.

In section 4.6, we outline briefly how the quantitative transport analysis discussed in section 4.5 can be applied to heavy species (e.g. tungsten).

In section 4.7 the transport of tritium in JET is discussed for a specific shot (61097) this is the most complete demonstration of UTC to date and forms part of a larger piece of analysis currently being performed by Whiteford *et al* (2004) and Zastrow *et al* (2004).

It should be noted that it is not the goal of this thesis to analyse fusion experiments *per se*, but to provide the necessary atomic data, atomic modelling and infrastructure to allow such an analysis to be performed rigorously, quantitatively and with the minimum of specialist (atomic) knowledge by a diagnostician.

4.2 Spectroscopic comparison of high- Z emission

Spectral comparisons (between modelled predictions and measurements) based partly on the work of this thesis have been performed by O’Mullane *et al* (2002) and Pütterich *et al* (2003b); an illustrative examples is given here — see O’Mullane *et al* (2002) and Pütterich *et al* (2003b) for more details of the plasma analysis. The data used here are the \mathcal{F} - $\mathcal{P}\mathcal{E}\mathcal{C}$ s as theoretically described in section 3.2.1 and calculated in section 3.5.5 for tungsten.

In figure 4.1, spectroscopic measurements from ASDEX-U are presented along with a comparison from the emission of W^{46+} . Perfect agreement is not observed since other ionisation stages along the line of sight of the detector are not included, but the key features of the measurement are present in the model.

4.3 Radiated power

The total radiated power from a plasma impurity species is of key importance in determining the behaviour of the plasma. Details are presented here of how such data is calculated, both in equilibrium and non-equilibrium conditions. Radiated power is often measured on tokamak devices using a photodiode that does not have uniform spectroscopic response — see section 4.3.3 for more details on how this is handled and why it is an issue for calculations of the sort presented here.

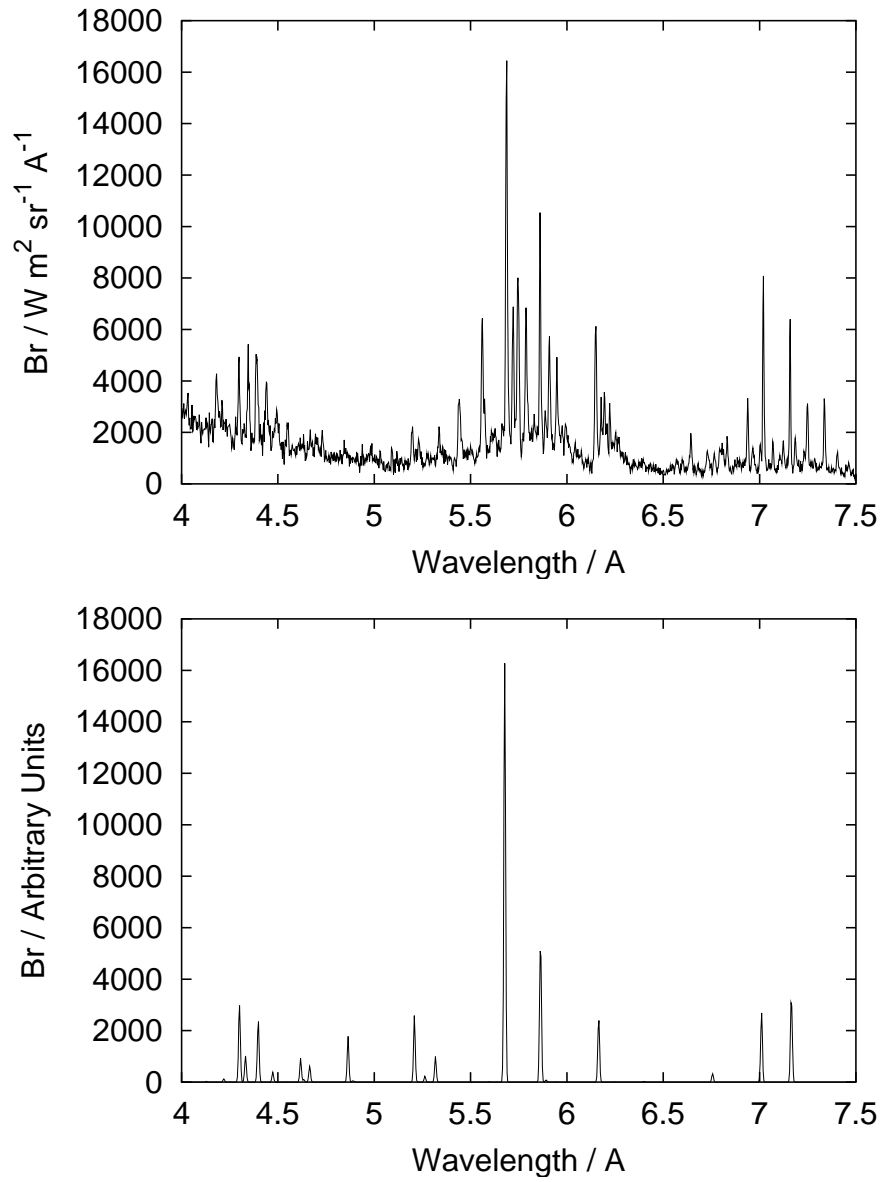


Figure 4.1: Emission from W^{46+} in ASDEX-U, the upper plot shows the measurements and the lower plot the prediction of the emission.

4.3.1 Recombination and bremsstrahlung

A radiative recombination event is assumed to release energy equal to the ground state ionisation energy of the recombined ion. Dielectronic recombination energy loss is summed over a number of transitions and each is assumed to release energy equal to the parent transition energy, together with the ionisation energy of the ground state of the recombined ion. Bremsstrahlung is taken to be hydrogenic. This leads to a total radiated power from recombination and bremsstrahlung to be

$$P_{\text{RB}}^{z+1 \rightarrow z} = 1.6 \times 10^{-19} \left(\alpha_r^{z+1 \rightarrow z} \chi + \sum_{j=1}^2 (\alpha_d^{z+1 \rightarrow z} (\Delta E_j + \chi)) \right) + 1.54 \times 10^{-32} z_1^2 \sqrt{T_e} \langle g_{f-f} \rangle \text{ Wcm}^3 \quad (4.1)$$

where the α_r comes from equation 3.27 and the α_d from equation 3.25. $\langle g_{f-f} \rangle$ is the Maxwell-averaged Gaunt factor (see Burgess (1974)).

4.3.2 Line radiated power

The power emitted by a spectral line is equal to the energy of the photon emitted (defined by its wavelength) and the number of transitions per second. These data are calculated by a collisional–radiative model. For the case of quasi-continuum spectra, the output goes into \mathcal{F} – $\mathcal{P}\mathcal{E}\mathcal{C}$ s as defined in section 3.2.1.

In the case of no broadening, the total emitted power by line radiation is simply a summation of $\mathcal{P}\mathcal{E}\mathcal{C}$ s weighted by photon energy over every transition. In the case of a broadening function, we need to integrate under an \mathcal{F} – $\mathcal{P}\mathcal{E}\mathcal{C}$. From conservation of energy grounds, this should be the same as the simple summation; it can be shown that this is indeed the case analytically.

Let ϵ be the emitted energy by integrating under a broadened emission line; E_0 the central energy of this line and the broadening, defined by a function $f(x)$ be even about $x = 0$, taking the argument $E - E_0$ (or $\nu - \nu_0$) and normalised such that

$$\int_{-\infty}^{\infty} f(x) dx = 1. \quad (4.2)$$

The above broadening properties hold true for broadening mechanism such as

Doppler, Voigt etc. The emitted energy is then,

$$\epsilon = \int_{-\infty}^{\infty} E f(E - E_0) dE. \quad (4.3)$$

Taking,

$$x = E - E_0, \quad (4.4)$$

$$E = x + E_0, \quad (4.5)$$

we get,

$$\begin{aligned} \epsilon &= \int_{-\infty}^{\infty} (x + E_0) f(x) dx \\ &= E_0 \int_{-\infty}^{\infty} f(x) dx + \int_{-\infty}^{\infty} x f(x) dx \\ &= E_0 + 0 \end{aligned} \quad (4.6)$$

where the second integral goes to zero since the integrand is an odd function in x . So the integral remains a summation of each emitted line as expected from physical grounds.

Radiated power data due to line emission calculated using this method, as opposed to simple parametric methods, have the advantage of being correctly density dependent. It is shown in section 4.3.4 that the density effects of the line emission are significant enough to require their inclusion so as to predict radiated power from a fusion plasma.

4.3.3 Soft x-ray filters

4.3.3.1 Background theory

Photodiode detectors with their glass covering removed are in general use for measurement of the radiated power from a high temperature plasma. Such diagnostics are typically a silicon diode with a transmission window between it and the source (the radiating plasma). Neither the efficiency of the detector or the transmission of the window is 100%: both have a wavelength dependence.

The instrument response must be convoluted with the spectral emission to produce radiated power predictions that can be compared to experiment. This

means that the ‘filtering’ needs to be done as the radiated power is computed, and not after it has been summed over all wavelengths.

The spectral absorption characteristics of all elements ($Z = 1, \dots, 92$) between 30eV and 50,000eV have been calculated and tabulated by Henke *et al* (1993). It is these data which are used here.

If the frequency-dependent absorption cross-section of a thin layer of element X , at a given frequency ν , is a_ν^X , then the intensity variation at a given frequency (still ν) through this layer is

$$\frac{dI_\nu}{dl} = -N^X a_\nu^X I_\nu, \quad (4.7)$$

where N^X is the number density of the element X in the layer. After passage through a set (I) of different layers, indexed by i , made up of elements X_i , with thickness d^{X_i} , the intensity is given by

$$I_\nu = I_n u^0 \exp \left(- \sum_{i=1}^I N^{X_i} a_\nu^{X_i} d^{X_i} \right), \quad (4.8)$$

so the transmission is trivially

$$T_\nu = \exp \left(- \sum_{i=1}^I N^{X_i} a_\nu^{X_i} d^{X_i} \right). \quad (4.9)$$

For absorption by the (typically silicon) diode, denoted by Y , with number density N^Y , thickness D^Y , and absorption cross-section a_ν^Y , the absorption factor is

$$A_\nu = 1 - \exp \left(-N^Y a_\nu^Y D^Y \right). \quad (4.10)$$

The final factor, as a function of frequency, is then

$$F_\nu = A_\nu T_\nu \quad (4.11)$$

so,

$$F_\nu = \left(1 - \exp \left(-N^Y a_\nu^Y D^Y \right) \right) \exp \left(- \sum_{i=1}^I N^{X_i} a_\nu^{X_i} d^{X_i} \right). \quad (4.12)$$

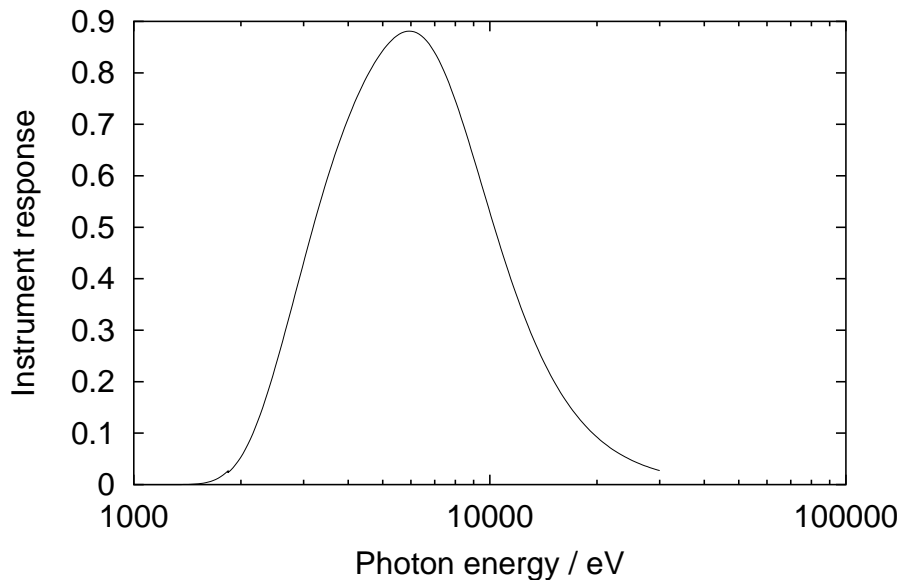


Figure 4.2: Response function for the JT60-U SXR detector, including effects of the beryllium/silicon window.

4.3.3.2 Implementation on JT60-U

The methodology given above in section 4.3.3.1 was used in the determination of filtered power for the SXR detector on JT60-U. The system comprises of a window with 200μ of beryllium and 0.2μ of silicon along with a 100μ silicon detector. The response function for this system is shown in figure 4.2.

Using the above filter, radiative power was generated using the techniques described in sections 4.3.1 and 4.3.2 and then convoluted with the response function. These coefficients are given stage-resolved as a function of temperature and density. Assuming equilibrium conditions, figure 4.3 shows the radiated power coefficient, along with the corresponding filtered coefficient for all ionisation stages. This shows that the emission seen is predominantly continuum and only the very high ionisation stages contribute to the observed line emission.

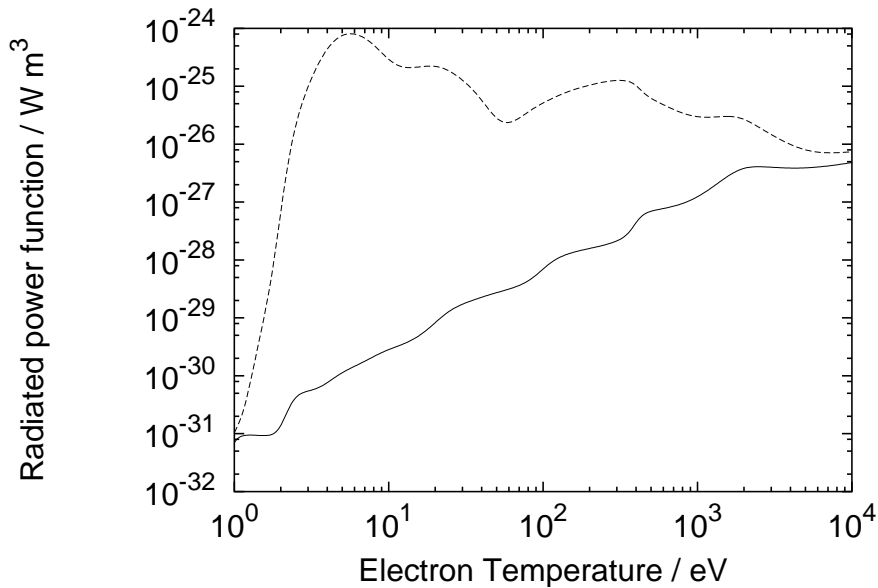


Figure 4.3: Comparison of filtered (solid curve) and unfiltered (dashed curve) radiated power from krypton using the JT60-U SXR filter transmission function.

4.3.4 Data for tungsten

Radiated power for tungsten has been calculated by a summation of $\mathcal{P}\mathcal{E}\mathcal{C}$ s along with a contribution from bremsstrahlung, as given in sections 4.3.2 and 4.3.1. Figure 4.4 shows how the bremsstrahlung (section 4.3.1) and line emission (section 4.3.2) contribute to the radiated power in equilibrium (see sections 2.3.3 and 3.5.4).

A comparison with the total radiated power as function of temperature (for two representative densities) between the present work and the results of Post *et al* (1977) and Gervids and Kogan (1975) is shown in figure 4.5. It can be seen that while the results agree in form, the absolute magnitudes are different. The method used here for calculating the emitted power is, in principle, better than the method used by Post *et al* (1977) and the (similar zero-density) method employed by Gervids and Kogan (1975). A density dependence can also be seen between $N_e = 10^8 \text{cm}^{-3}$ and $N_e = 10^{13} \text{cm}^{-3}$ in figure 4.6 for the present work. We also note the more recent work of Post *et al* (1995) where radiative cooling for ITER is specifically discussed.

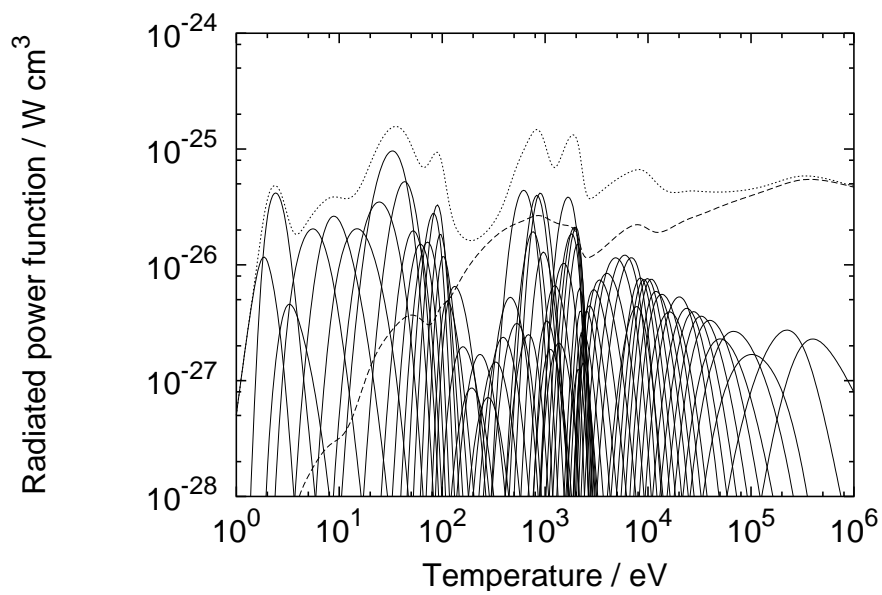


Figure 4.4: Radiated power for tungsten as a function of temperature at $N_e = 10^{13} \text{cm}^{-3}$. The solid curves denotes the line power contribution from each ionisation stage, the dashed line from continuum radiation and the dotted curve the total radiated power function.

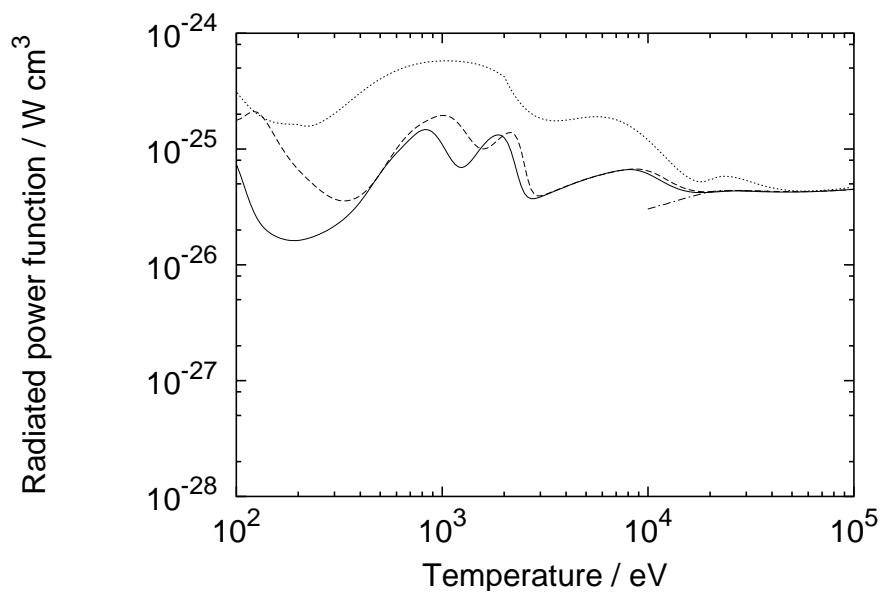


Figure 4.5: Radiated power for tungsten as a function of temperature. The solid curve denotes the present work at a density of $N_e = 10^{13}\text{cm}^{-3}$, the dashed curve at a density of $N_e = 10^8\text{cm}^{-3}$; the dotted curve, the (zero-density) work of Post *et al* (1977); and the chained curve, the work of Gervids and Kogan (1975).

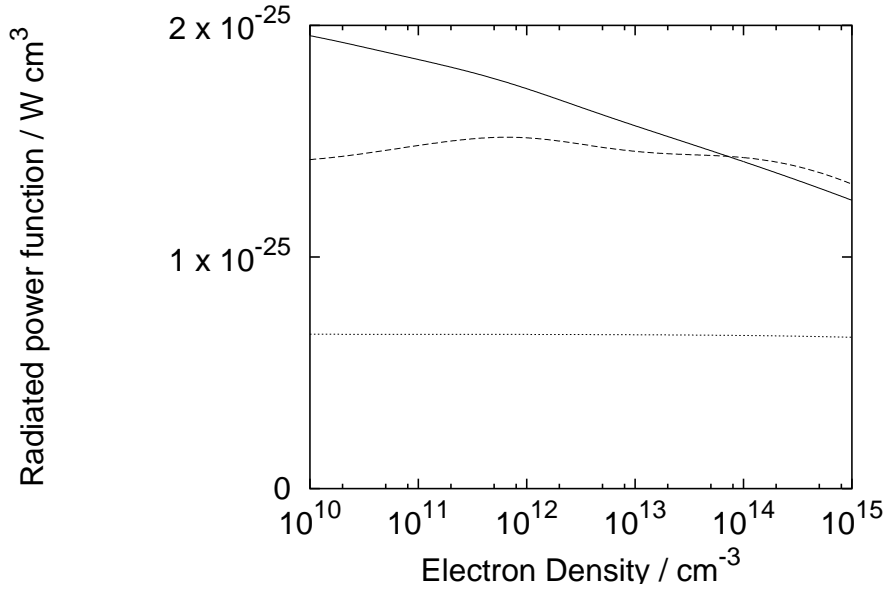


Figure 4.6: Radiated power for tungsten as a function of density. The solid curve denotes the present work at a temperature of $T_e = 35\text{eV}$, the dashed curve at a temperature of $T_e = 800\text{eV}$ and the dotted curve at a temperature of $T_e = 8\text{keV}$.

4.4 Impurity transport modelling

Impurity transport modelling has been key to the understanding of the behaviour of a tokamak. Two important tools in performing this analysis are STRAHL (Behringer 1987a) and SANCO (Lauro-Taroni *et al* 1994). Both of these packages work in a predictive sense, in that when they are supplied with plasma profiles (electron temperatures and densities), geometry information (e.g. position of flux surfaces), transport coefficients and an external source term (usually an influx from the plasma edge), then they will return impurity ion densities as a function of space and time. A brief overview of how these methods work is given below.

Assuming a cylindrical geometry, impurity transport can be described by (see also section 2.3.1.3)

$$\frac{\partial n_z}{\partial t} = -\frac{1}{r} \frac{\partial}{\partial r} (r\Gamma_z) + \text{Sources} - \text{Sinks} \quad (4.13)$$

where sources and sinks include:

- electron-impact ionisation from lower charge states,
- electron recombination from higher charge states,
- charge exchange recombination with neutrals.

The particle flux can be described by a diffusion coefficient, D , and a convection velocity, v ,

$$\Gamma_z = -D \frac{\partial n_z}{\partial r} + v n_z. \quad (4.14)$$

Substituting this into the equation 4.13 gives

$$\begin{aligned} \frac{\partial n_z}{\partial t} = & D \frac{\partial^2 n_z}{\partial r^2} + \left(\frac{D}{r} + \frac{\partial D}{\partial r} - \frac{v}{r} \right) \frac{\partial n_z}{\partial r} \\ & - \left(\frac{v}{r} + \frac{1}{r} \frac{\partial v}{\partial r} \right) n_z + \text{Sources} - \text{Sinks}. \end{aligned} \quad (4.15)$$

The sources and sinks are typically functions of electron temperature and density. From the solution of this equation set (a set of n_z as a function of space and time), diagnostics or other plasma quantities (e.g. total radiated power) can be simulated.

The application of this methodology can be found in numerous works with a variety of important findings. Dux *et al* (2003) studied impurity accumulation (including tungsten) in JET and ASDEX-U using STRAHL; Kubo *et al* (2003) also used STRAHL to look at the impurity behaviour in JT60-U, with particular attention being paid to radiation enhancement. SANCO has been used by O'Mullane *et al* (1996a, 1996b) to analyse the variation of transport coefficients on JET plasmas. Giroud *et al* (2001) used SANCO to study argon and neon in JET. SANCO has also been used with tritium (Zastrow *et al* 1998) to analyse the JET DTE experiments. We also note the tungsten transport simulations in ITER of Murakami *et al* (2003), which are relevant to the present work.

In this thesis we seek to address the quantitative nature of impurity transport. This is explored and analysed using an error propagation and least-squares fitting methodology, whose practical implementation is UTC (Whiteford and Zastrow, unpublished). UTC is an integral part of a number of current and recent studies such as Giroud *et al* (2001, 2004), Hender *et al* (2004), Stork *et al* (2004),

Whiteford *et al* (2004) and Zastrow *et al* (2002, 2004).

In section 4.5 we will discuss the measurement of transport coefficients from spectroscopic measurements, specifically charge exchange spectroscopy and VUV spectroscopy, and how much can be inferred from diagnostic data. Particular attention is given to covariances in the measured transport coefficients and how these covariances can be reduced by the availability of diagnostic data. In section 4.7 the transport of tritium and the modelling of neutron emission are discussed.

4.5 Measurement of transport coefficients from diagnostic data

4.5.1 The fitting and error analysis methodology

In order to fit a transport simulation (e.g. SANCO or STRAHL as described above) against experimental measurements, free and fixed parameters must be identified. For the purposes of this thesis, we will assume that the geometry and temperature/density profiles are fixed inputs to the model and that the transport coefficients and influx data are free parameters. This is a reasonable course to take for analysis of tokamak experiments since often the electron temperature and density are measured using a Thomson scattering system, while there is no direct measurement of transport coefficients.

4.5.1.1 Parameterisation of the transport

The transport coefficients are parameterised by a set of discrete points which specify D and v at a given spatial position of r/a and time, t . These points are interpolated temporally and spatially in order to generate the full transport coefficients. It is the values of D , v and r/a which are used as free parameters to the fit. Allowing r/a to be a free parameter allows, e.g., tracking the position of an internal transport barrier (ITB - see chapter 1) as it evolves in time.

4.5.1.2 The fitting algorithm

We use a variation of the Levenberg–Marquardt method (Marquardt 1963) to optimise the transport parameters.

First, a solution is evaluated for a given set of transport coefficients to find a discretised function f_n . Here, f_n can represent a number of different data including, but not limited to, soft x-ray emission, spectroscopic emission and impurity densities at a discrete number of points, indexed by n with total number of points, N . We label corresponding experimental data by y_n , each with a relative weight, w_n , based upon the error attributed to that particular data point according to

$$w_n = \frac{1}{\Delta y_n}. \quad (4.16)$$

The free parameters, p_i , are then varied by some amount δp_i , one at a time, and a similar set of solutions is found. From these solutions and the initial solution, partial derivatives can be found at each point, n , from

$$\frac{\partial f_n}{\partial p_i} = \frac{f'_n - f_n}{\delta p_i}. \quad (4.17)$$

A matrix and a vector are then assembled in order to perform the fit, as specified by Marquardt (1963), viz.

$$M_{ij} = \sum_{n=1}^N \frac{\partial f_n}{\partial p_i} \frac{\partial f_n}{\partial p_j} w_n, \quad (4.18)$$

$$b_i = \sum_{n=1}^N \frac{\partial f_n}{\partial p_i} (f_n - y_n) w_n. \quad (4.19)$$

An improvement on the free transport parameters can then be found by solving $M\Delta\mathbf{p} = \mathbf{b}$. Here, Δp_i are the suggested change in the initial parameters p_i ¹. Thus, our new (improved) parameters, p'_i , are given by $p'_i = p_i + \Delta p_i$.

A χ^2 merit function is introduced to grade the accuracy of a solution, defined

¹Note that Δp_i and δp_i are different.

as

$$\chi^2 = \sum_{n=1}^N w_n (y_n - f_n)^2. \quad (4.20)$$

This fitting process can then be repeated until χ^2 converges.

A slightly more advanced form of this method introduces a damping-factor in to the M matrix such that:

$$M'_{ii} = M_{ii} (1 + \lambda) \quad (4.21)$$

i.e. diagonal elements are multiplied by some factor, typically not much more than 1.2. This increases the speed of convergence. In practice, for each set of initial conditions and derivatives, we construct three different matrices, each with different damping factors. These three cases are processed and the χ^2 evaluated for each one allowing the best damping factor to be used.

Typically, a high value of λ will give a better set of Δp_i when the parameters are far from the optimal values and a small value of λ will give a better result when the parameters are close to the ‘final’ values.

4.5.1.3 Error propagation

We consider two types of error and their associated covariance with each other:

- Errors in the data (i.e. measurement errors) which we are fitting to where the error is given by σ_n for an error in data point n and the covariance between two data points (n and m) is given by $\rho_{n,m}$.
- Errors in fixed model parameters. These are parts of the model that are fixed (hence not varied in the fitting procedure) but which could still have an error in them. The error in the i th fixed parameter (p_i) is denoted by σ'_i and the covariance between two fixed parameters (p_i and p_j) is given by $\rho'_{i,j}$.

In order to take into account both types of errors, we define a new χ^2 merit function given by

$$\chi^2 = \sum_{n=1}^N \sum_{m=1}^N w_{n,m} (f_n - y_n) (f_m - y_m), \quad (4.22)$$

where w are the elements of the weighting matrix (W) given by

$$W = S^{-1}, \quad (4.23)$$

where S is given by

$$s_{n,m} = \rho_{n,m} \sigma_n \sigma_m + \sum_{i=1}^P \sum_{j=1}^P \rho'_{p,q} \sigma'_p \sigma'_q \frac{\partial f_n}{\partial p_i} \frac{\partial f_m}{\partial p_j}. \quad (4.24)$$

For the case of no correlated errors and no errors in the fit parameters, ρ (and hence ρ^{-1}) becomes the unit matrix and equation 4.22 reverts back to its previous form in equation 4.20.

In order to calculate the error in each fit parameter (and also the error in any modelled quantity) we need to construct a matrix, M , similar to that of equation 4.18,

$$M_{ij} = \sum_{m=1}^N \sum_{n=1}^N w_{n,m} \frac{\partial f_n}{\partial p_i} \frac{\partial f_m}{\partial p_j}. \quad (4.25)$$

Again, it is trivial to show that, for the case of W being the unit matrix, this equation is the same as equation 4.18.

In either case (with or without correlated errors), we construct a covariance matrix, C , by inverting M (from equation 4.18 or equation 4.25)

$$C = M^{-1}. \quad (4.26)$$

The diagonal elements of this matrix (C_{ii}) give the error in fit parameter i , and the off-diagonal elements ($C_{ij}, i \neq j$) the covariance between i and j .

In addition, this matrix can also be used to give an error in any modelled quantity, f_n , from

$$\Delta f_n = \sqrt{\sum_{i=1}^P \sum_{j=1}^P \frac{\partial f_n}{\partial p_i} \frac{\partial f_n}{\partial p_j} C_{ij}}, \quad (4.27)$$

where the partial derivatives come from equation 4.17.

Our treatment of the covariance matrix, and the derivation of the errors from it, implicitly assumes that all the statistical errors have Gaussian distribution. In

practice this will not be the case but saves on the computational time of Monte-Carlo simulations which imposes too great an overhead.

4.5.2 Constructing a model plasma

We consider a theoretical fusion plasma with specifications similar to those of JET; a model plasma is used so that key issues can be addressed without the complications of experimental details not relevant to the matter in hand.

Our approach is to take simulated diagnostics from our model plasma and then try to fit the same model back to the diagnostics (with parametric variation of transport and influx parameters). For the purposes of the fit, we assume a 10% (random) error in all simulated measurements. This approach has the implicit assumption that a 1D transport model is correct and will not highlight any errors or sources of ambiguity caused by the use of an incorrect model; this is a standard problem in most sensitivity tests of this type across all scientific disciplines.

We assume steady-state equilibrium, electron temperature and electron density profiles and allow only the transport parameter profiles to change in time. This will not be the case in a real situation since a change in transport may be accompanied by a change in electron temperature and density. We do not wish to model processes of this kind and are merely concerned with inferring the transport parameters from measured impurity densities.

For our model plasma, we take electron temperature and density profiles of the form:

$$T_e(r/a) = [6 \times 10^3 \text{eV}] (1 - (r/a)^2)^{0.4} + [30 \text{eV}], \quad r/a < 0.98, \quad (4.28)$$

$$T_e(r/a) = [30 \text{eV}] \exp\left(\frac{1 - (r/a)}{0.01}\right) + [1 \text{eV}], \quad r/a > 0.98, \quad (4.29)$$

$$N_e(r/a) = [3 \times 10^{19} \text{m}^{-3}] (1 - (r/a)^2)^{0.4} + [3 \times 10^{18} \text{m}^{-3}], \quad r/a < 0.98, \quad (4.30)$$

$$N_e(r/a) = [3 \times 10^{18} \text{m}^{-3}] \exp\left(\frac{1 - (r/a)}{0.01}\right) + [1 \times 10^{17} \text{m}^{-3}], \quad r/a > 0.98, \quad (4.31)$$

as shown in figure 4.7. We also take a steady state geometry typical of a quiescent

Index	r/a	D	v/D	v
1	0	0.5	0.0	0.0
2	0.25	0.5	0.0	0.0
3	0.5	0.5	0.0	0.0
4	0.75	1.3	-0.21	-0.273
5	0.9	1.3	-0.43	-0.559
6	0.91	0.17	0.0	0.0
7	1.00	0.17	0.0	0.0

Table 4.1: Transport parameters used in the reference case, these are used as free parameters in sections 4.5.3 and 4.5.4 to find errors and covariances respectively.

JET discharge.

We consider a model plasma where D and v are parameterised with linear interpolation between points. The model plasma transport parameters are given in table 4.1 and illustrated in figure 4.8.

We take an influx representative of a gas puff with recycling, as illustrated in figure 4.9. This influx is made up of two components: one to simulate the gas puff and another to simulate wall recycling. They are convoluted together but for the purposes of identifying covariances and fitting data, the scaling of these profiles will be treated independently. We shall denote these scaling parameters IM_1 and IM_2 .

From the above criteria we can run a transport simulation (in this case SANCO) to derive numerical densities as a function of space, time and ionisation stage and hence simulate what diagnostics would detect.

We simulate a CXRS system with radial points as given in table 4.2; points for the simulated system and also example points from the JET CXRS system are shown (for $t = 53.7s$ in shot 60933). It is noted that in a real charge exchange system, the position of the measurements change position (in r/a space) with time. For our purposes we will keep the positions constant in time. Since we are dealing with a non-transient reference plasma it is valid to do this since a will not change in time. We use a timebase of 250ms for our simulated CXRS system. Changing the resolution of this system (both temporally and spatially) is discussed in section 4.5.5.1.

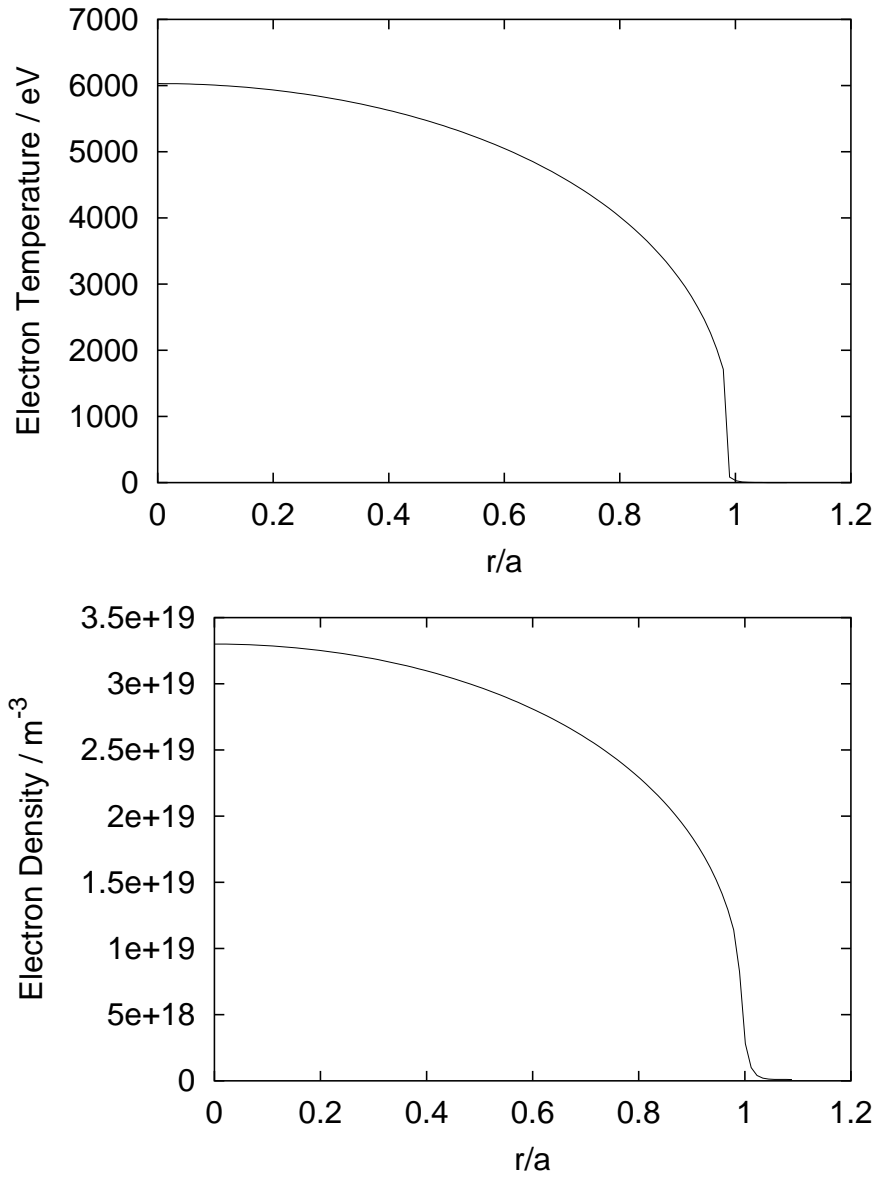


Figure 4.7: Electron temperature and density profiles for a simulated plasma, as specified in equations 4.28–4.31. The upper plot shows the electron temperature profile and the lower plot the electron density profile.

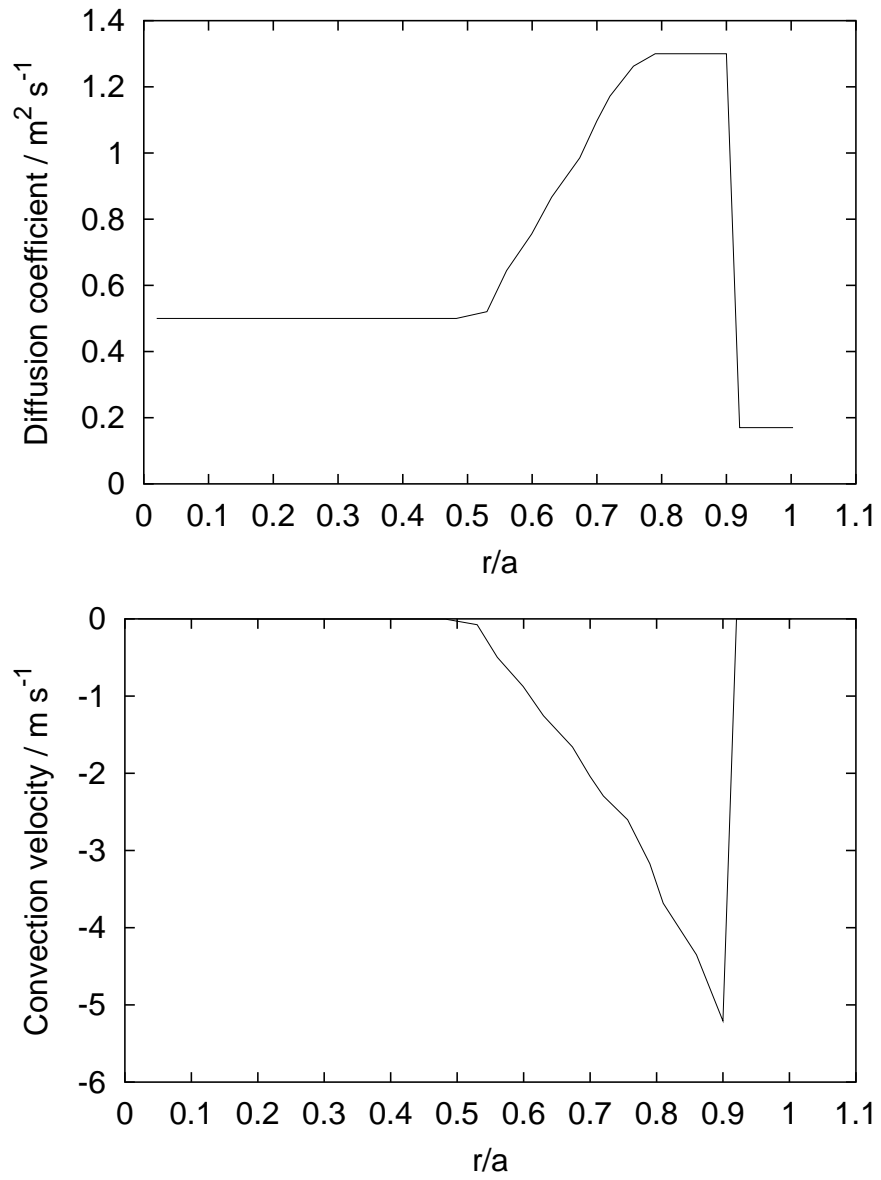


Figure 4.8: D and v profiles used in the reference case. These are typical profiles of those found in a JET discharge — see text for details.

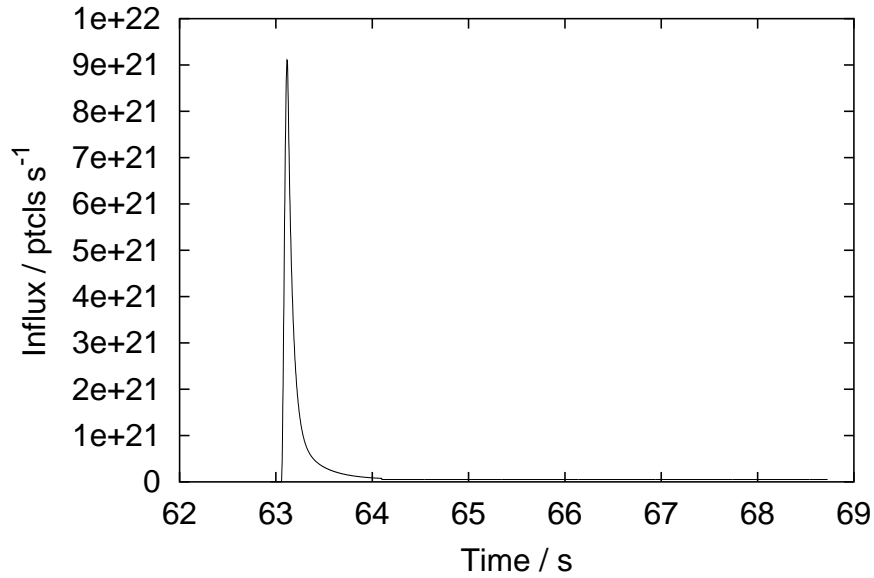


Figure 4.9: Influx of impurity used in the reference model.

Point	1	2	3	4	5	6	7	8	9
Simulated	0.020	0.220	0.320	0.430	0.530	0.630	0.720	0.810	0.900
JET	0.021	0.233	0.336	0.437	0.537	0.634	0.730	0.824	0.917

Table 4.2: Radial position of charge exchange measurements, for both the simulated reference model discussed here and an example of real positions of the JET CXRS system at $t = 53.7\text{s}$ for shot 60933.

Parameter	Value	Error
D_0	0.50	0.0096
D_3	1.30	0.0752
D_5	0.17	0.0232
v/D_1	-0.01	0.1802
v/D_2	-0.01	0.2545
v/D_3	-2.10	0.2307
v/D_4	-4.30	1.6743
v/D_5	-0.01	8.1956
v/D_6	-0.01	20.4484
IM_1	1.0	0.4749
IM_2	0.5	0.0266

Table 4.3: Uncertainties when the reference model is compared to itself.

4.5.3 Calculation of uncertainties in the free parameters

If the transport coefficients given in table 4.1 are taken to be free parameters² with a coupling scheme such that $D_1 = D_2 = D_3$, $D_4 = D_5$, $D_6 = D_7$ (i.e. the seven diffusion parameters are condensed down to only three free parameters) then we can calculate partial derivatives (equation 4.17) and hence a covariance matrix from equations 4.18 and 4.26. The diagonal of this matrix is then the uncertainty in each free parameter. These errors in the parameters are shown in table 4.3.

The largest percentage errors can be seen at the edge. This is a feature of trying to determine edge transport parameters using only core measurements. Very large covariances are also found between these parameters (see section 4.5.4). Reducing these errors via spectroscopic measurement in the VUV is discussed in section 4.5.5.2.

4.5.4 Identification of covariances

The covariances between free parameters can be found assuming the same treatment of free parameters as in section 4.3 and the same construction of the covariance matrix. Strong covariances are found between many of the parameters, the largest are given in table 4.4. These covariances show that even with a model that

² D and v/D are actually taken to be the free parameters.

Parameter 1	Parameter 2	Covariance
D_5	v/D_4	-0.72
D_5	v/D_5	0.77
D_5	v/D_6	-0.90
D_5	IM_1	-0.93
D_5	IM_2	-0.93
v/D_1	v/D_2	-0.73
v/D_2	v/D_3	-0.75
v/D_3	v/D_4	-0.74
v/D_4	v/D_5	-0.96
v/D_4	v/D_6	0.91
v/D_4	IM_1	0.87
v/D_4	IM_2	0.86
v/D_5	v/D_6	-0.96
v/D_5	IM_1	-0.92
v/D_5	IM_2	-0.91
v/D_6	IM_1	0.99
v/D_6	IM_2	0.99
IM_1	IM_2	1.00 ^a

^a Rounded to two significant figures, to three significant figures the value is 0.998

Table 4.4: Covariances in the reference model greater than 0.7

is correct (our model is implicitly correct here since we have used the same model to simulate the experimental data as we are using to describe it) we cannot measure D and v profiles without large covariances. In terms of formal statistics, the data reduction process does not retain all the information about the transport coefficients, when going from D and v profiles to discretised impurity concentrations (i.e. CXRS measurements).

A reduction of these covariances can be achieved in a number of ways, as given below:

- measurements other than CXS,
 - accurate measurement of influx,
 - VUV emission from the plasma edge (see section 4.5.5.2),
 - neutron emission in the case of tritium transport (see section 4.7),
- theoretical restrictions on the transport.

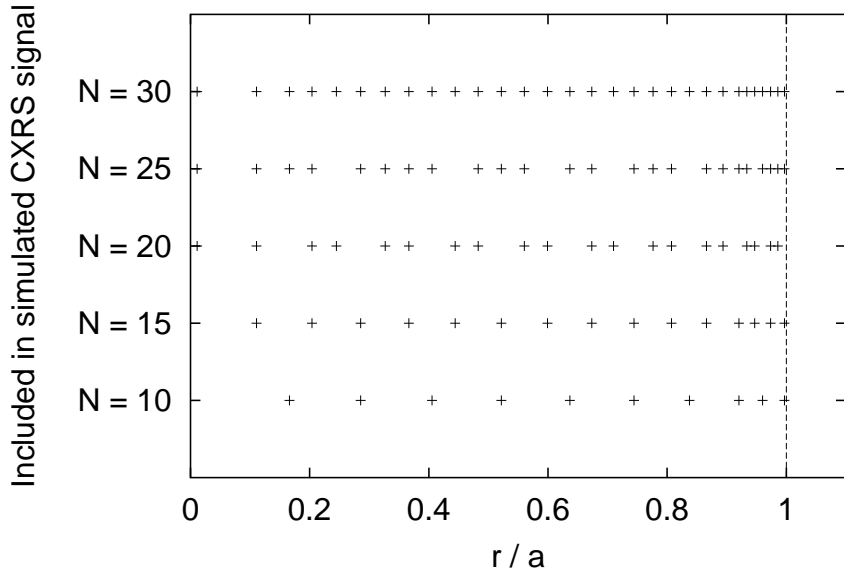


Figure 4.10: Chord positions of simulated CXRS system. Five cases are considered with 10, 15, 20, 25 and 30 data points. These different cases are represented by the vertical axis. The data here are shown in tabular form in table 4.5.

4.5.5 Diagnostic effects

In the previous section (4.5.4) when identifying covariances (i.e. how well transport coefficients could be measured) we only assumed that local impurity densities at nine points (table 4.2) were available. We now address how the available diagnostics affect the covariances and measurability of the impurity transport — namely more local impurity density measurements (i.e. more CXRS chords) in section 4.5.5.1 and the use of VUV spectroscopy at the edge in section 4.5.5.2.

4.5.5.1 Local density measurements

We consider a CXRS system with more (than the nine previously used) chords and look at how well this can retain information about the transport parameters. Consider a model system with 10, 15, 20, 25 and 30 chords at the positions shown in table 4.5 and in figure 4.10.

The propagated uncertainty in D_0 is shown in figure 4.11 along with a curve

Position	Present in				
	$N = 10$	$N = 15$	$N = 20$	$N = 25$	$N = 30$
0.0111				•	•
0.1108		•	•	•	•
0.1661	•		•	•	•
0.2038		•		•	•
0.2448			•		•
0.2857	•	•	•	•	•
0.3267				•	•
0.3666		•	•	•	•
0.4054	•		•	•	•
0.4441		•			•
0.4829			•	•	•
0.5216	•	•	•	•	•
0.5604				•	•
0.5992		•	•		•
0.6368	•		•	•	•
0.6734		•		•	•
0.7099			•		•
0.7443	•	•	•	•	•
0.7764				•	•
0.8074		•	•	•	•
0.8373	•		•		•
0.8661		•		•	•
0.8938			•	•	•
0.9204	•	•	•	•	•
0.9336				•	•
0.9469		•	•		•
0.9602	•		•	•	•
0.9735		•		•	•
0.9857			•	•	•
0.9970	•	•	•	•	•

Table 4.5: Chord positions of simulated CXRS system, five cases are considered with 10, 15, 20, 25 and 30 data points respectively. The values of r/a included for each case are shown here. Note that in all cases the last r/a is considered, these cases are shown graphically in figure 4.10.

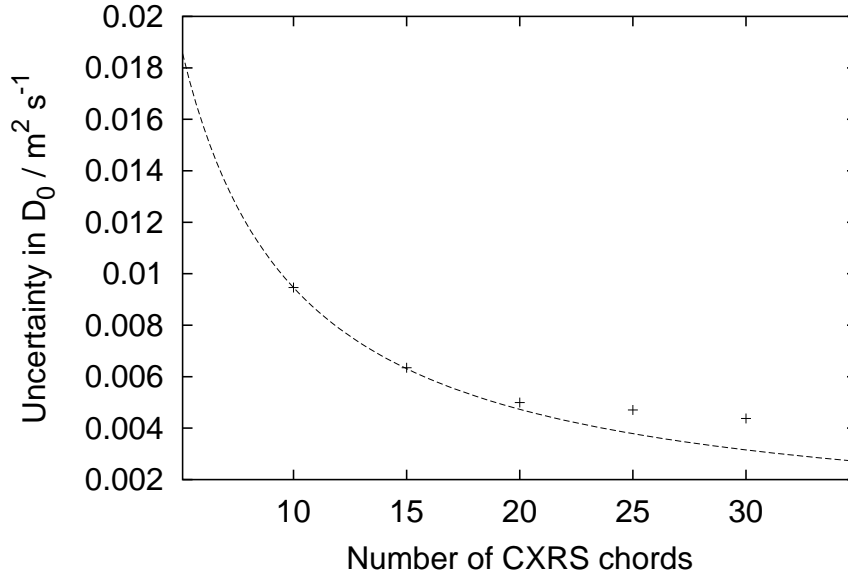


Figure 4.11: Propagated uncertainty in D_0 as a function of which charge exchange chords are included (see table 4.5 for details). The calculated points are shown as crosses and the dashed line is a curve showing $\sim 1/N$ behaviour — see text for details.

showing $\sim 1/N$ behaviour. To first order, and neglecting covariances³, this is how the error should scale because of the $1/N$ term in a crude error definition. It can be seen that significant deviation from this behaviour is found because of the covariances.

The calculated covariances between v/D_4 & v/D_6 and v/D_4 & IM_1 are shown in figures 4.12 and 4.13 respectively. These show that the covariances are quite insensitive to the number of CXRS points, especially so for the influx to edge transport covariance. A conclusion can be made here that measurement of core impurity densities alone cannot be used to determine uniquely (i.e. without covariance) edge transport parameters. VUV spectroscopy is shown to be useful in this determination in section 4.5.5.2.

We now consider our original CXRS system with the chords as given in table 4.2 but with varying time resolution. We consider a system with time points

³Specifically, the matrix inversion process in equation 4.26 is not the same as taking the reciprocal of each diagonal element.

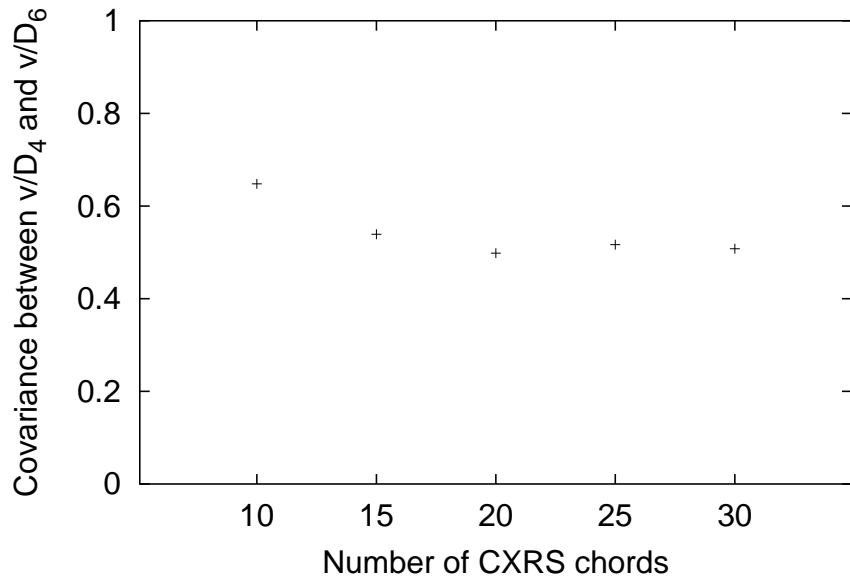


Figure 4.12: Covariance between v/D_4 and v/D_6 as a function of which charge exchange chords are included (see table 4.5 for details).

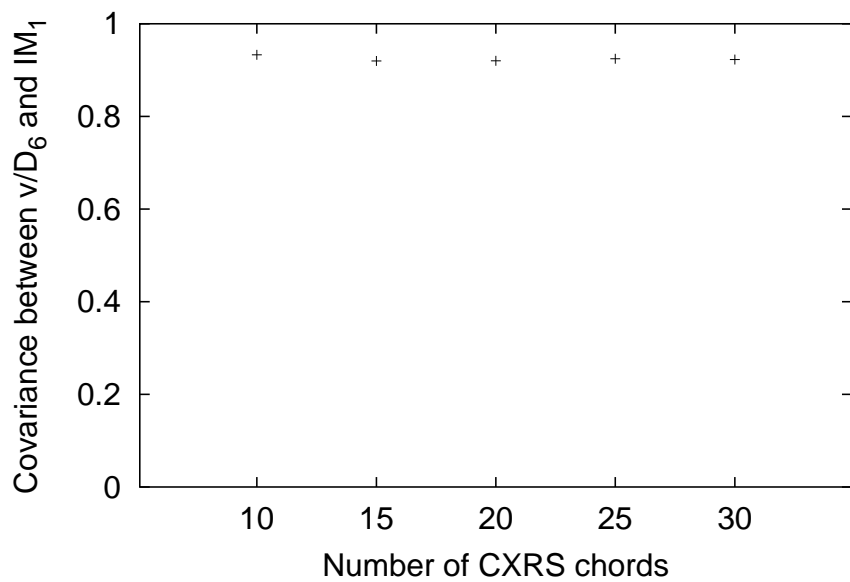


Figure 4.13: Covariance between v/D_6 and IM_1 as a function of which charge exchange chords are included (see table 4.5 for details).

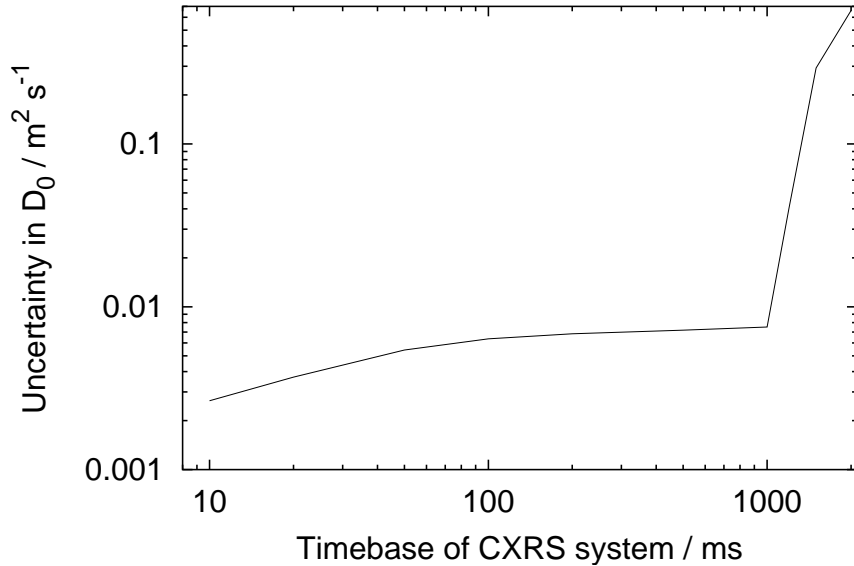


Figure 4.14: Error in D_0 as a function of the timebase of the simulated CXRS system. The inverse of the timebase (actually 5000ms over the timebase) is proportional to the number of points included in the error estimate.

of 2000ms, 1500ms, 1200ms, 1000ms, 500ms, 200ms, 100ms, 50ms, 20ms and 10ms, as opposed to our original system which had a 250ms time base. The covariances do not change significantly for the different time resolutions (as expected) and the increasing error as the timebase increases is expected since the total error, to first order, contains a N_{points}^{-1} term. The error in D_0 is shown in figure 4.14. For very low time resolution (i.e. high timebase) the error in D_0 increases sharply, this is because eventually we lose all information on what the plasma is doing — the statistical analysis shows this by increasing the uncertainty on D_0 , as expected.

4.5.5.2 Line integrated spectrometer measurements

VUV emission from the edge is often measured in tokamaks (see section 2.2.1). While the spatial VUV emission envelope is very small for many species (we take the example of neon here), it contains information about the edge transport and influx. We can construct a VUV emission profile for our model plasma. We take

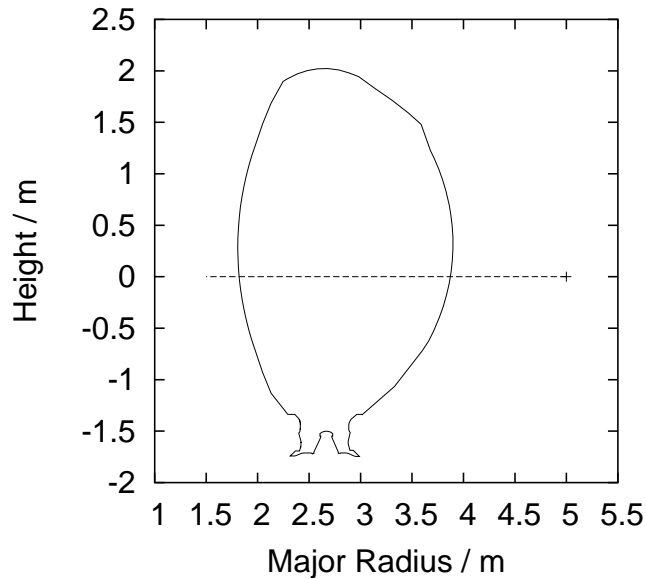


Figure 4.15: Line of sight of the simulated VUV instrument.

the $1s^2 2p \ ^2P - 1s^2 2s \ ^2S$ transition in Ne^{7+} for a simulated instrument using the line of sight of the JET KT2 instrument, as illustrated in figure 4.15. The modelled emission as a function of time is shown in figure 4.16. With the addition of these data, and allowing them to enter the transport and influx covariance calculation, the covariances and errors at the edge are reduced significantly: see tables 4.6 and 4.7 respectively. As expected, the covariances towards the centre of the plasma change less than the edge covariances since the VUV signal does not contain much information about the centre of the plasma.

4.5.5.3 Diagnostic design implications

The simulations performed here on a typical JET plasma, but with arbitrary diagnostic systems, can be used for diagnostic design. In particular, for designing diagnostics intended to give information about impurity transport and influx. Simulations of the type given in section 4.5.5.1 could be used to justify the temporal and spatial resolution of the proposed ITER CXRS system⁴ where the simulations

⁴It is noted that the primary use of the CXRS system on current machines is to measure ion temperatures, and not impurity concentrations but CXRS is the only diagnostic for ITER which

Parameter 1	Parameter 2	Old Covariance	New Covariance
D_5	v/D_4	-0.72	0.50
D_5	v/D_5	0.77	-0.68
D_5	v/D_6	-0.90	0.58
D_5	IM_1	-0.93	0.52
D_5	IM_2	-0.93	0.76
v/D_1	v/D_2	-0.73	-0.73
v/D_2	v/D_3	-0.75	-0.72
v/D_3	v/D_4	-0.74	-0.65
v/D_4	v/D_5	-0.96	-0.86
v/D_4	v/D_6	0.91	0.817
v/D_4	IM_1	0.87	0.497
v/D_4	IM_2	0.86	0.495
v/D_5	v/D_6	-0.96	-0.97
v/D_5	IM_1	-0.92	-0.66
v/D_5	IM_2	-0.91	-0.64
v/D_6	IM_1	0.99	0.71
v/D_6	IM_2	0.99	0.59
IM_1	IM_2	1.00	0.53

Table 4.6: Covariances from table 4.4 of section 4.5.4, but with the addition of VUV spectroscopy at the edge.

Parameter	Value	Old Error	New Error
D_0	0.50	0.0096	0.0096
D_3	1.30	0.0752	0.0659
D_5	0.17	0.0232	0.0074
v/D_1	-0.01	0.1802	0.1783
v/D_2	-0.01	0.2545	0.2402
v/D_3	-2.10	0.2307	0.1953
v/D_4	-4.30	1.6743	0.8641
v/D_5	-0.01	8.1956	3.3254
v/D_6	-0.01	20.4484	3.2547
IM_1	1.0	0.4749	0.0238
IM_2	0.5	0.0266	0.0009

Table 4.7: Uncertainties from table 4.3 of section 4.5.3, but with the addition of a VUV spectroscopy at the edge.

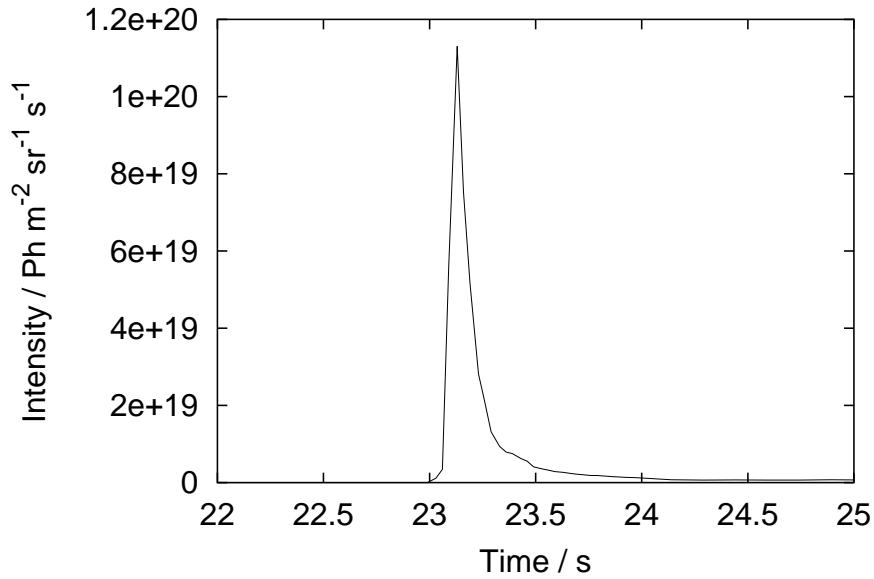


Figure 4.16: Modelled VUV emission of the $1s^2 2p \ ^2P - 1s^2 2s \ ^2S$ transition in Ne^{7+} .

given in section 4.5.5.2 can be used, along with appropriate atomic data, to simulate wavelength regions and discrimination levels necessary for a wide range of spectroscopic instruments. Such analysis is planned.

4.6 Application to heavy elements

The techniques presented in section 4.5 to measure the transport coefficients can be used alongside the work presented in chapter 3. Some additional work needs to be done. Firstly, the type of line integrated signals, as discussed in sections 2.2.1 and 4.5.5.2, formed from $\mathcal{P}\mathcal{E}\mathcal{C}$ s (section 2.3.1.1) must be replaced by more complicated line integrals to simulate spectra from $\mathcal{F}\text{-}\mathcal{P}\mathcal{E}\mathcal{C}$ s (section 3.2.1). The implementation of superstages (section 3.4) within transport modelling has also not yet been performed. For transport models as utilised here, the ion charge is simply a label. Modification of these implementations should, in principle, be simple. However, in more complex transport codes (e.g. the JETTO suite) the can track helium ash.

ionisation charge is used. Here, care would need to be taken over what is the ‘effective charge’ of a superstage.

We note again that Murakami *et al* (2003) studied tungsten transport for ITER and draw attention again to the extensive work of Neu (2003).

4.7 Tritium transport modelling and neutron emission

4.7.1 Background

An important part of the JET trace tritium campaign is the modelling of tritium transport. Knowledge of this transport process is key to understanding how a burning plasma will behave. Initial studies were done by Zastrow *et al* (1999) on the previous tritium campaign and the work here follows on from this. We use the methods and implementations discussed in this chapter (specifically sections 4.4 and 4.5) to quantify and fit the neutron transport coefficients. Here, we will discuss solely shot 61097 as an example. The discussion of the implications of this analysis and the application to other shots can be found in Stork *et al* (2004), Whiteford *et al* (2004) and Zastrow *et al* (2004).

4.7.2 Influx and plasma profiles

From the point of view of particle transport of tritium, where a set of transport coefficients are given or they are trying to be measured, the core electron temperature and density profiles are non-critical. The electron temperature and density will clearly affect the transport coefficients but will not affect the particle evolution given by these coefficients. Since we are trying to measure transport coefficients from the behaviour of the impurities, our core T_e and N_e are a weak input to the model (i.e. they do not affect the results significantly).

The influx is shown in figure 4.17. This was generated from valve measurements as the tritium is injected. In figures 4.18 the electron temperature profile at $t = 66\text{s}$ is shown and in figure 4.19 the electron density profile is shown at the same time. The data came from Thomson scattering measurements.

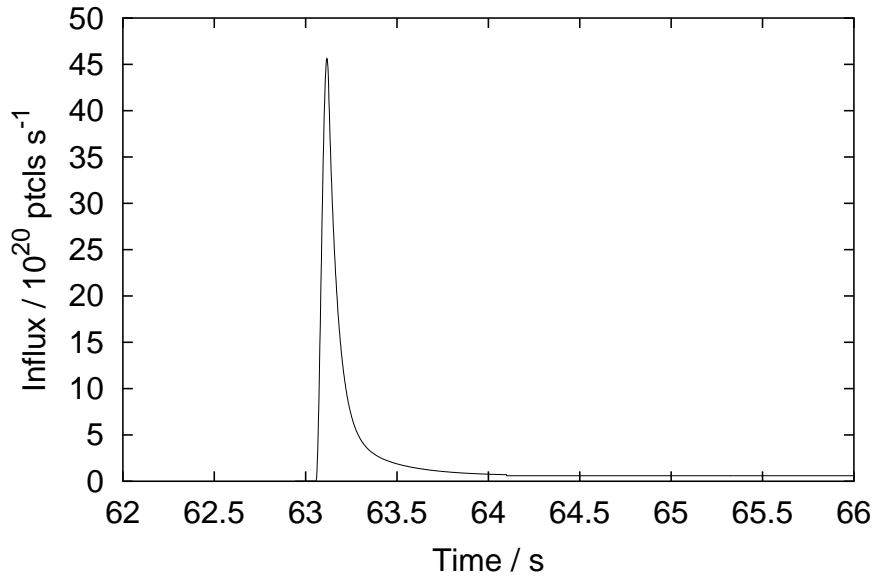


Figure 4.17: Tritium influx for shot 61097.

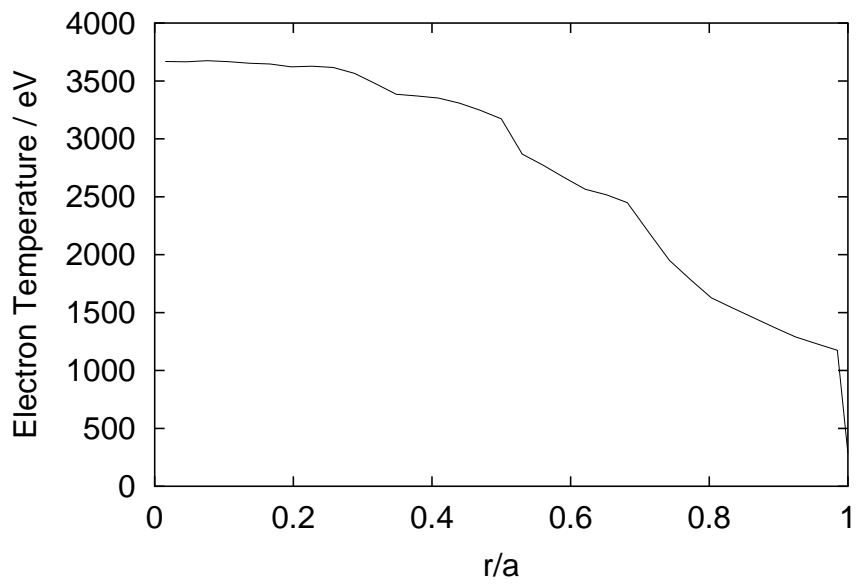


Figure 4.18: Electron temperature profile for shot 61097 at $t = 66s$.

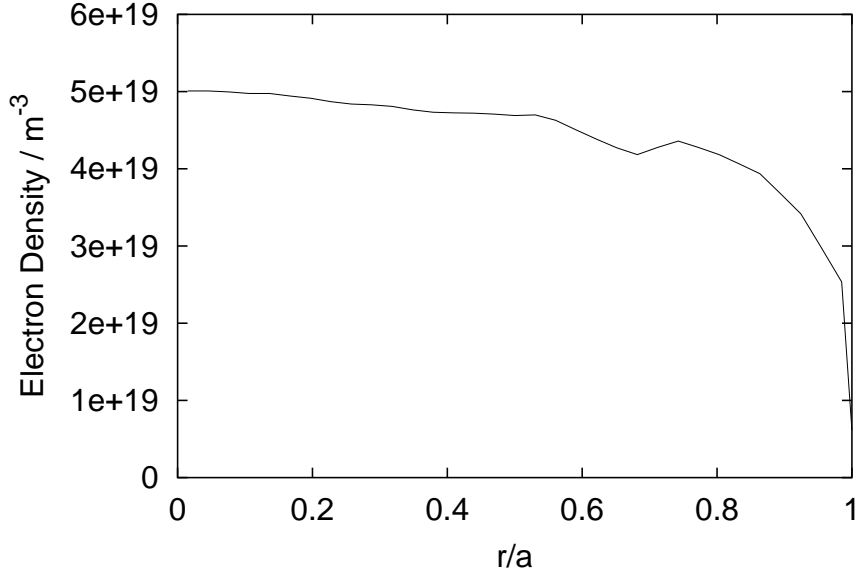


Figure 4.19: Electron density profile for shot 61097 at $t = 66\text{s}$.

The modelled part of the shot lasted from $t = 60\text{s}$ until $t = 66\text{s}$ and the fitting of the transport coefficients was between $t = 63\text{s}$ and $t = 66\text{s}$.

4.7.3 Modelling neutron emission

Modelling neutron emission along a line of sight is similar to modelling line emission (see section 2.3.1.1). The exception is that the emissivity, ϵ , can be one of the following:

$$\epsilon(T_e) = n_D n_T \langle v\sigma \rangle_{DT} \quad (4.32)$$

$$\epsilon(T_e) = n_D n_D \langle v\sigma \rangle_{DD}, \quad (4.33)$$

where equation 4.32 is for a D–T reaction (giving a 14MeV neutron) and equation 4.33 is for a D–D reaction (giving a 2.5MeV neutron). n_T and n_D are the tritium and deuterium densities respectively while $\langle v\sigma \rangle_{DT}$ and $\langle v\sigma \rangle_{DD}$ are the temperature-averaged D–T and D–D cross-sections (or reactivities) — see Bosch and Hale (1992).

The JET neutron profile monitor consists of a system of detectors that detect

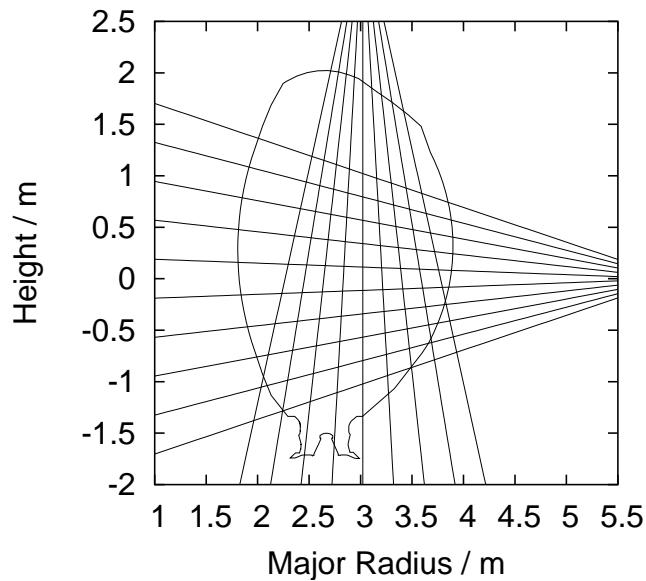


Figure 4.20: Lines of sight of the JET neutron profile monitor showing the 10 horizontal and 9 vertical channels.

both 2.5MeV and 14MeV neutrons along nineteen lines of sight — ten horizontal and nine vertical (see figure 4.20).

The global neutron yield can also be modelled from emissivity profiles by carrying out a volume integral over the whole plasma. Global neutron yields are recorded at JET using a silicon diodes for 14MeV neutrons and fission chambers for the totals (2.5MeV and 14MeV).

4.7.4 Forward modelling of the diagnostic system

A neutron that is emitted can be scattered inside the vessel and detector system. We define here two distinct types of scattering:

- forward scattering — where a neutron emitted along a particular line of sight is deflected to another detector,
- back scattering — where a neutron emitted in an arbitrary direction is reflected from the walls of the vessel into a detector.

In addition, due to the energy spectrum of a D–T neutron not being a δ -function at 14MeV, some D–T neutrons will register 2.5MeV counts and hence be counted as D–D neutrons.

All of the above effects can be forward modelled — an accurate model of the detector system is combined with modelled neutron emission along lines of sight and a global neutron yield (section 4.7.3).

We define $L_{2.5}$ to be a vector containing the emission of the neutrons along a particular line of sight, with the index of the vector corresponding to a given detector (as illustrated in figure 4.20) and $R_{2.5}$ to be the modelled ‘recorded’ counts of the detector (similarly for L_{14} and R_{14}). With $\Gamma_{2.5}$ and Γ_{14} being modelled global neutron yields we obtain:

$$\begin{bmatrix} \begin{bmatrix} R_{2.5} \\ R_{14} \end{bmatrix} \end{bmatrix} = \begin{bmatrix} \begin{bmatrix} A \\ C \end{bmatrix} \begin{bmatrix} B \\ D \end{bmatrix} \begin{bmatrix} E \\ G \end{bmatrix} \begin{bmatrix} F \\ H \end{bmatrix} \end{bmatrix} \begin{bmatrix} \begin{bmatrix} L_{2.5} \\ L_{14} \\ \Gamma_{2.5} \\ \Gamma_{14} \end{bmatrix} \end{bmatrix}, \quad (4.34)$$

where the sub-matrices A-D represent how the line of sight modelled quantities influence the detection, and the sub-vectors E-H influence how the modelled global neutron yield influences the detectors.

We use the following detection system data:

- S_{DD}^F — 19×19 matrix with data of how D–D neutrons in one line of sight scatter into the line of sight of another detector,
- S_{DT}^F — 19×19 matrix with data of how D–T neutrons in one line of sight scatter into the line of sight of another detector,
- S_{DD}^B — 19 element vector with data on how globally emitted D–D neutrons are back scattered in a detector,
- S_{DT}^B — 19 element vector with data on how globally emitted D–T neutrons are back scattered in a detector,
- $E_{DD \rightarrow DD}$ — Efficiency of a D–D neutron registering a 2.5MeV count,
- $E_{DD \rightarrow DT}$ — Efficiency of a D–D neutron registering a 14MeV count,

- $E_{DT \rightarrow DD}$ — Efficiency of a D–T neutron registering a 2.5MeV count,
- $E_{DT \rightarrow DT}$ — Efficiency of a D–T neutron registering a 14MeV count.

From these definitions the sub-matrices and vectors A-H in equation 4.34 are given by:

$$A(n, m) = S_{DD}^F(n, m) E_{DD \rightarrow DD}(n), \quad (4.35)$$

$$B(n, m) = S_{DT}^F(n, m) E_{DT \rightarrow DD}(n), \quad (4.36)$$

$$C(n, m) = S_{DT}^F(n, m) E_{DD \rightarrow DT}(n), \quad (4.37)$$

$$D(n, m) = S_{DT}^F(n, m) E_{DT \rightarrow DT}(n), \quad (4.38)$$

$$E(n) = S_{DD}^B(n) E_{DD \rightarrow DD}(n), \quad (4.39)$$

$$F(n) = S_{DT}^B(n) E_{DT \rightarrow DD}(n), \quad (4.40)$$

$$G(n) = S_{DD}^B(n) E_{DD \rightarrow DT}(n), \quad (4.41)$$

$$H(n) = S_{DT}^B(n) E_{DT \rightarrow DT}(n). \quad (4.42)$$

Applying the correction matrix in equation 4.34 allows the counts recorded by the detection system to be predicted from modelled physical quantities. For more details see Whiteford and Zastrow (2003).

4.7.5 Results

The fitting process described in section 4.5.1.2 was applied to the neutron profile monitor signals. Temporally constant solution for D and v were fitted, and are shown in figures 4.21 and 4.22. The total neutron yield is shown in figure 4.23, the D–D signals for channels four and seven are shown in figure 4.24, and the D–T signals for the same channels in figure 4.25. Note the enhancement to the D–D recorded and predicted D–D counts when the tritium is added to the plasma and the D–T neutrons start contributing to this signal. The χ^2 breakdown for the D–T counts is shown in table 4.8.

The free parameters and their propagated error are given in table 4.9 and strong covariances (greater than 0.6) in these parameters are shown in table 4.10.

The results given here are meant as an illustration of the method and are not supposed to explain the behaviour of the plasma or the tritium in any detailed way.

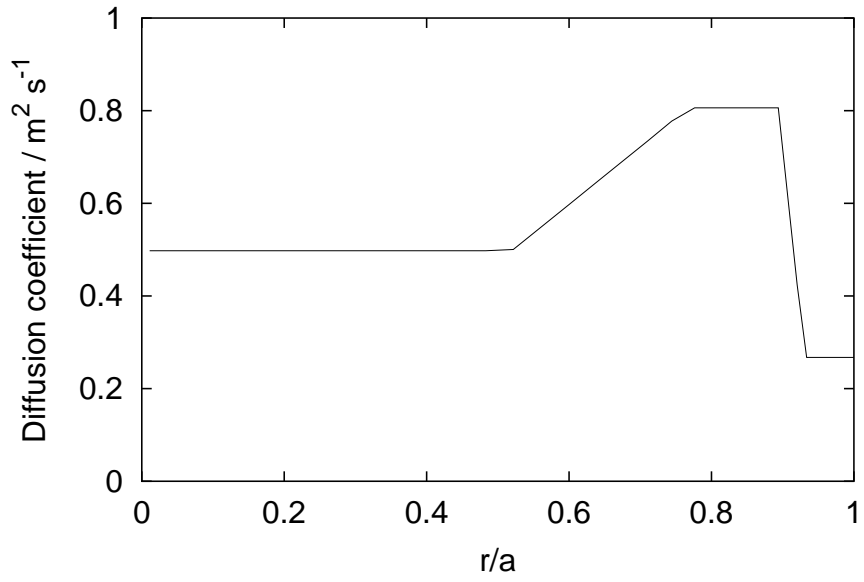


Figure 4.21: Final D profile for JET shot 61097 after fitting.

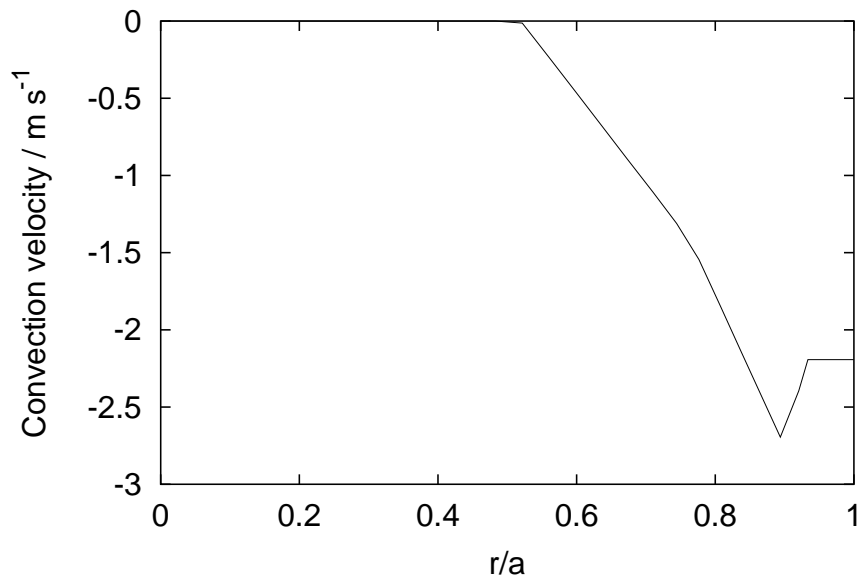


Figure 4.22: Final v profile for JET shot 61097 after fitting.

Quantity	χ^2
Neutron profile monitor channel 1	1.33
Neutron profile monitor channel 2	1.22
Neutron profile monitor channel 3	1.74
Neutron profile monitor channel 4	1.58
Neutron profile monitor channel 5	1.75
Neutron profile monitor channel 6	1.15
Neutron profile monitor channel 7	1.23
Neutron profile monitor channel 8	1.64
Neutron profile monitor channel 9	2.19
Neutron profile monitor channel 10	0.94
Neutron profile monitor channel 11	0.94
Neutron profile monitor channel 12	1.52
Neutron profile monitor channel 13	1.57
Neutron profile monitor channel 14	1.60
Neutron profile monitor channel 15	3.63
Neutron profile monitor channel 16	1.97
Neutron profile monitor channel 17	2.00
Neutron profile monitor channel 18	2.92
Neutron profile monitor channel 19	1.31
Total neutron yield	4.17
Global	1.82

Table 4.8: χ^2 breakdown for the fit to shot 61097. Shown are values for each neutron line of sight and the global neutron yield. Also shown is the global χ^2 value for the whole fit.

Parameter	Value	Error
$D(0.0)$	0.50	0.015
$D(0.5)$	0.79	0.044
$D(0.9)$	0.28	0.021
$v/D(0.5)$	-1.80	0.049
$v/D(0.9)$	-8.47	0.640
IM_1	0.05	0.001
IM_2	0.02	0.002

Table 4.9: Values and propagated errors in fit parameters for JET shot 61097.

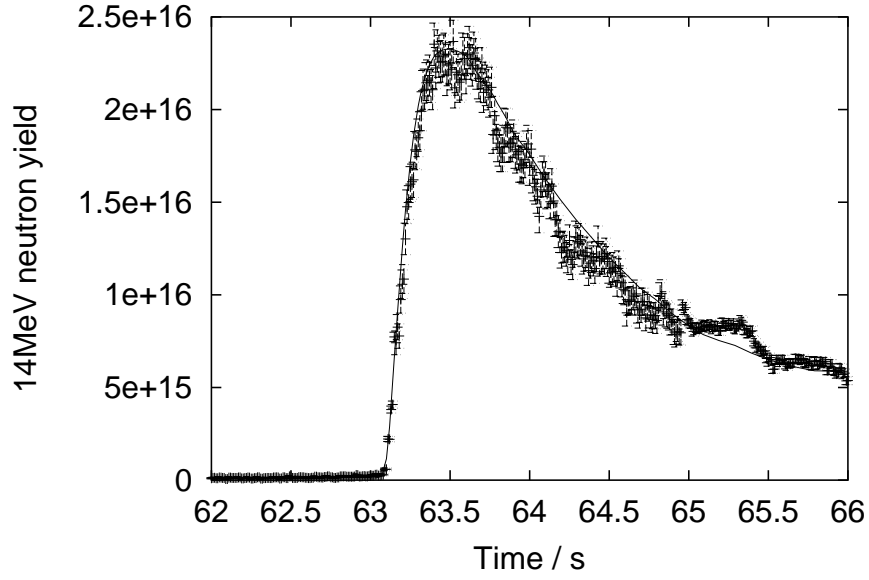


Figure 4.23: Global 14MeV neutron yield for JET shot 61097, the solid curve denotes the modelled emission and the points with error bars the measured emission.

Parameter 1	Parameter 2	Covariance
$D(0.0)$	$D(0.5)$	-0.73
$D(0.5)$	$D(0.9)$	-0.93
$D(0.9)$	$v/D(0.5)$	-0.60
$D(0.5)$	$v/D(0.9)$	0.92
$D(0.9)$	$v/D(0.9)$	-0.97

Table 4.10: Covariances in fit parameters for JET shot 61097.

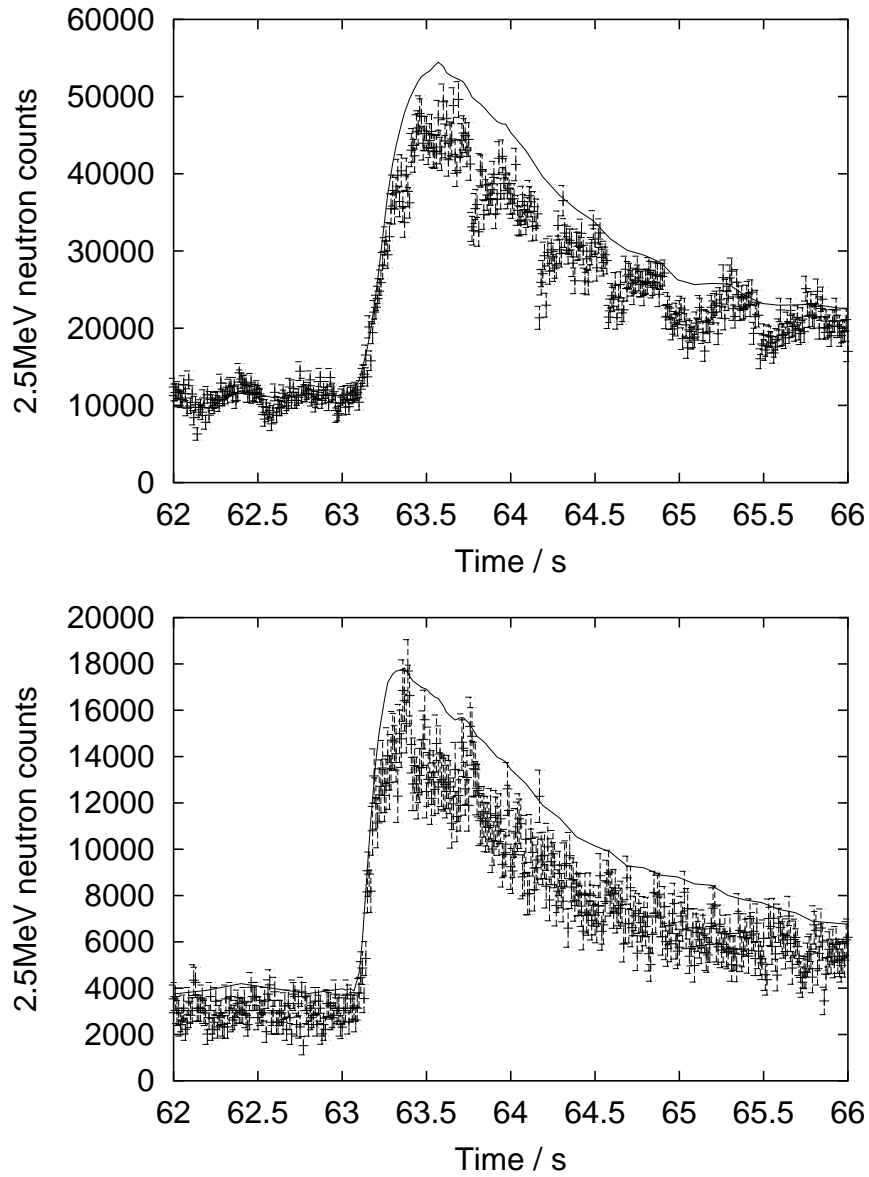


Figure 4.24: D–D neutron counts for JET shot 61097. The upper plot shows the predicted (solid line) and measured (points with error bars) data for channel four. The lower plot shows the same data for channel seven.

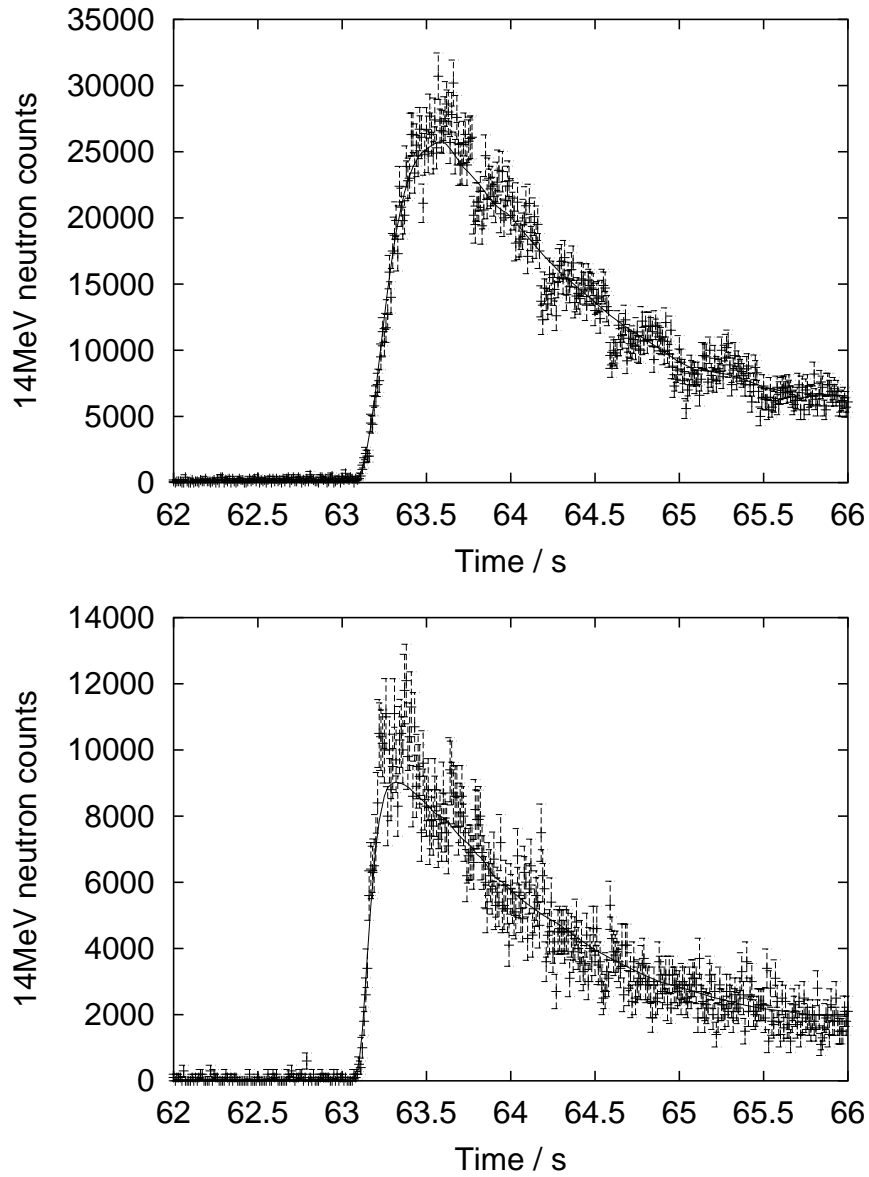


Figure 4.25: D-T neutron counts for JET shot 61097. The upper plot shows the predicted (solid line) and measured (points with error bars) data for channel four. The lower plot shows the same data for channel seven.

For such a discussion see Stork *et al* (2004), Whiteford *et al* (2004) and Zastrow *et al* (2004).

Chapter 5

Conclusions

The scientific conclusions of this thesis are varied but contain a common theme, namely the need for quantitative analysis of fusion plasmas with a perspective which spans from calculation of fundamental data through delivery of appropriate derived data to the confrontation of plasma models with experiment.

Particular attention is drawn to the following points regarding the appropriateness of atomic data:

- Figure 2.10 (page 34), where it is demonstrated that the fundamental atomic data on electron-impact excitation are best mapped and critically judged as collision strengths, effective collision strengths or C -plots rather than as cross-sections or excitation rate coefficients.
- Section 2.3.1 (page 18), where deliverable atomic data is identified and shown why it is useful as opposed to the discussion in section 1 of the collection of cross-sections at ‘atomic data centres’.
- The use of R -matrix calculations in section 2.5 (page 55) where they are warranted, i.e. high resolution spectroscopy where individual lines can be distinguished in contrast with the use of cruder Born approximations in section 3.5.1 (page 107) for very heavy species where the lines are blended into one another.
- The use of an isolated line emission model to interpret VUV spectra of the sort given in section 2.2.1 (page 13) in contrast to the use of special features

for many lines in section 3.2.1 (page 84) to model the emission from a quasi-continuum.

- The inclusion of finite density effects and the demonstration of why they are necessary, e.g., figure 4.6 (page 129).

Whilst no plasma analysis was presented in this work, it was very much the theme throughout — various atomic models were generated and developed, always with a view to providing useful deliverables. The application of these deliverables was discussed in detail in chapter 4 where some of the issues involved in applying atomic data, such as soft x-ray filters (section 4.3.3), were discussed. Particular attention was given to measuring transport coefficients using a parameterised transport model using the atomic data discussed primarily in section 2.3.1.

The thesis also established a framework for the handling of very heavy species (chapter 3) incorporating automated generation of atomic data, a flexible partitioning methodology in order that the derived data may be presented in a manageable way and the definition of the $\mathcal{F}\text{-}\mathcal{P}\mathcal{E}\mathcal{C}$ — a special feature.

The theme of the special feature was prominent in this work. Coming from the $\mathcal{P}\mathcal{E}\mathcal{C}$ as introduced in section 2.2.1 (page 13), the special feature was introduced in section 2.2.2 (page 15) as a way to model molecular emission, defined in detail in section 2.3.1.4 (page 23) then applied to helium-like spectra in section 2.4 (page 39), and then to the emission from very heavy species in sections 3.2.1 (page 84) and 3.5.5 (page 114).

Error and uncertainty analysis when applying atomic data to spectroscopic measurements were discussed. Attention is drawn to the results of table 4.6 (page 148), where it is shown that covariances of transport and influx coefficients at the edge of a fusion plasma approach unity when only core charge exchange measurements are considered. On a more atomic level, the results of table 2.6 (page 82) show the results of Monte-Carlo analysis on excited populations.

This thesis sits complete as a critical analysis of how atomic physics plays a part in the diagnosis of a fusion plasma. Problems in current practices and methods are highlighted, with solutions developed and demonstrated. The methodologies and principles of this thesis provide for us a roadmap which we believe to be fruitful and effective for the analysis of real fusion experiments.

References

- Aichele K, Arnold W, Hathiramani D, Scheuermann F, Salzborn E, Mitnik D M, Griffin D C, Colgan J and Pindzola M S 2001 *Phys. Rev. A* **64** 052706
- Badnell N R 1997 *J. Phys. B: At. Mol. Opt. Phys.* **30** 1
- Badnell N R and Griffin D C 2001 *J. Phys. B: At. Mol. Opt. Phys.* **34** 681
- Badnell N R and Pindzola M S 1993 *Phys. Rev. A* **47** 2937
- Badnell N R and Seaton M J 1999 *J. Phys. B: At. Mol. Opt. Phys.* **32** 3955
- Badnell N R, O'Mullane M G, Summers H P, Altun Z, Bautista M A, Colgan J, Gorczyca T W, Mitnik D M, Pindzola M S and Zatsarinny O 2003 *Astronomy and Astrophysics* **406** 1151
- Ballance C P, Badnell N R and Berrington K A 2001 *J. Phys. B: At. Mol. Opt. Phys.* **34** 3287
- Bar-Shalom A, Klapisch M and Oreg J 1988 *Phys. Rev. A* **38** 1773
- Bartschat K, Hudson E T, Scott M P, Burke P G and Burke V M 1996 *J. Phys. B: At. Mol. Opt. Phys.* **29** 115
- Bates D R, Kingston A E and McWhirter R W P 1962 *Proc. Roy. Soc.* **A267** 297
- Bautista M A, Mendoza C, Kallman T R and Palmeri P 2003 *Astronomy and Astrophysics* **403** 339
- Behringer K H 1987a *JET Joint Undertaking Report* JET-IR(87)08
- Behringer K H 1987b *J. Nucl. Mater.* **145–147** 145
- Behringer K H 1998 IPP-Report 10/11
- Behringer K H, Summers H P, Denne B, Forrest M and Stamp M 1989 *Plasma Phys. Control. Fusion* **31** 2059
- Berrington K A, Eissner W B and Norrington P H 1995 *Comput. Phys. Commun.* **92** 290

- Berrington K A and Tully J A 1997 *Astron. Astrophys. Suppl. Ser.* **126** 105
- Bhatia A K and Temkin A 1977 *J. Phys. B: At. Mol. Phys.* **10** 2893
- Bosch H S and Hale G 1992 *J. Nucl. Fusion* **32** 611
- Bray I and Stelbovics A T 1993 *Phys. Rev. Lett.* **70** 746
- Brooks D H 1997 *PhD Thesis, Univ. of Strathclyde*
- Brooks D H, Fischbacher G A, Fludra A, Harrison R A, Innes D E, Landi E, Landini M, Lang J, Lanzafame A C, Loch S D, McWhirter R W P and Summers H P 2000 *Astronomy and Astrophysics* 357 697
- Burgess A 1964 *Astrophys. J.* **139** 776
- Burgess A 1965 *Astrophys. J.* **141** 1588
- Burgess A 1974 *J. Phys. B: At. Mol. Phys.* **7** L364
- Burgess A and Chidichimo M C 1983 *Mon. Not. R. Astr. Soc.* **203** 1269
- Burgess A, Chidichimo M C and Tully J A 1995 *Astronomy and Astrophysics* **300** 627
- Burgess A, Chidichimo M C and Tully J A 1997 *J. Phys. B: At. Mol. Opt. Phys.* **30** 33
- Burgess A, Hummer D G and Tully J A 1970 *Phil. Trans. R. Soc. A* **266** 225
- Burgess A and Tully J A 1992 *Astronomy and Astrophysics* **254** 436
- Burgess A and Summers H P (1969) *Astrophys. J.* **157** 1007
- Burgess A and Summers H P (1976) *Mon. Not. R. Astr. Soc.* **174** 345
- Burgess A, Summers H P, Cochrane D M and McWhirter R W P 1977 *Mon. Not. R. Astr. Soc.* **179** 275
- Burke P G and Berrington K A 1993 *Atomic and molecular processes — an R-matrix approach* (Bristol: Institute of Physics Publishing)

- Burke V M, Burke P G and Scott N S 1992 *Comput. Phys. Commun.* **69** 76
- Colgan J, Mitnik D M and Pindzola M S 2001 *Phys. Rev. A* **63** 012712
- Colgan J, Pindzola M S, Whiteford A D and Badnell N R 2003 *Astronomy and Astrophysics* **412** 597
- Cordey J G 2001 *Private Communication*
- Cowan R D 1981 *The Theory of Atomic Structure and Spectra* (Berkeley: University of California Press)
- Chantrenne S, Beiersdorfer P, Cauble R and Schneider M B 1992 *Phys. Rev. Lett.* **69** 265
- Chen M H and Reed K J 1992 *Phys. Rev. A* **45** 4525
- Drake G W 1988 *Can. J. Phys.* **66** 586
- Dux R, Giroud C, Neu R, Peeters A G, Stober J, Zastrow K-D, Contributors to the EFDA-JET Workprogramme and the ASDEX Upgrade Team 2003 *J. Nucl. Mater.* **313–316** 1150
- Dyall K G, Grant I P, Johnson C T, Parpia F A and Plummer F P 1989 *Comput. Phys. Commun.* **55** 424
- Duxbury G, O'Mullane M G, Summers H P, Whiteford A D, Meigs A, Stamp M F, Behringer K H and Brezinsek S 2004 *Abstract for the 31st EPS Conf. on Contr. Fusion and Plasma Physics*
- Eckstein W, Carcía-Rosales C, Roth J and Ottenberger W 1993 IPP-Report 9/82 337
- Eissner W, Jones M and Nussbaumer H 1974 *Comput. Phys. Commun.* **4** 270
- Fischbacher G A, Loch S D and Summers H P 2000 *Astronomy and Astrophysics* **357** 767
- Fischbacher G A, Loch S D and Summers H P 2002 *Astronomy and Astrophysics* **389** 295

- Gabriel A H 1972 *Mon. Not. R. Astr. Soc.* **160** 99
- Geier A, Coster D P, Elder J D, Krieger K, Rugno R, Rohde V, Neu R and the ASDEX upgrade team 2003 *30th EPS Conf. on Contr. Fusion and Plasma Phys.* ECA **27A** P-1.156
- Gervids V I and Kogan V I 1975 *JETP Lett.* **21** 150
- Giroud C, Zastrow K-D, Dux R, O'Mullane M and Whiteford A D 2001 *28th EPS Conf. on Contr. Fusion and Plasma Phys.* ECA **25A** 549
- Giroud C, Barnsley R, Challis C D, Coffey I, Dux R, von Hellermann M, Joffrin E, Jupen C, Lawson K, Meigs A, O'Mullane M, Pericoli Ridolfini V, Sips A C C, Whiteford A D, Zastrow K-D and JET EFDA contributors 2004 *Abstract for the 31st EPS Conf. on Contr. Fusion and Plasma Physics*
- Goett S J and Sampson D H 1983 *Atomic Data and Nucl. Data Tables* **29** 535
- Goett S J, Sampson D H and Clark R E H 1984 *Astrophys. J. Suppl. Ser.* **54** 115
- Gorczyca T W and Badnell N R 1996 *J. Phys. B: At. Mol. Opt. Phys.* **29** L283
- Gorczyca T W and Badnell N R 1997 *J. Phys. B: At. Mol. Opt. Phys.* **30** 3897
- Gorczyca T W and Badnell N R 2000 *J. Phys. B: At. Mol. Opt. Phys.* **33** 2511
- Gorczyca T W and Robicheaux F 1999 *Phys. Rev. A* **60** 1216
- Gorczyca T W, Robicheaux F, Pindzola M S and Badnell N R 1995 *Phys. Rev. A* **52** 3852
- Gorczyca T W, Robicheaux F, Pindzola M S and Badnell N R 1996 *Phys. Rev. A* **54** 2107
- Griffin D C, Badnell N R and Pindzola M S 1998 *J. Phys. B: At. Mol. Opt. Phys.* **31** 3713
- Gu M F 2003 *Astrophys. J.* **582** 1241

Hathiramani D, Aichele K, Hofmann G, Steidl M, Stenke M, Volpel R, Salzborn E, Pindzola M S, Shaw J A, Griffin D C and Badnell N R 1996 *Phys. Rev. A* **54** 587

Hebb M H and Menzel D H 1940 *Astrophys. J.* **92** 408

Hender T C, Buttery R J, de la Luna E, Ferreira J S, Howell D F, Nave M F F, Strachan J and EFDA-JET contributors 2004 *Abstract for the 31st EPS Conf. on Contr. Fusion and Plasma Physics*

Henke B L, Gullikson E M and Davis J C 1993 *Atomic Data and Nucl. Data Tables* **54** 181

Herrmann A, Eich T, Rohde V, Fuchs J C, Neuhauser J and the ASDEX upgrade team 2003 *30th EPS Conf. on Contr. Fusion and Plasma Phys.* ECA **27A** P-1.155

Higashijima S, Asakura N, Kubo H, Miura Y, Nakano T, Konoshima S, Itami K, Sakurai S, Takenaga H, Tamai H and The JT-60 Team 2003 *J. Nucl. Mater.* **313–316** 1123

Hummer D G, Berrington K A, Eissner W, Pradhan A K, Saraph H E and Tully J A 1993 *Astronomy and Astrophysics* **279** 298

ITER Physics Basis Editors, ITER Physics Expert Group Chairs and Co-Chairs and ITER Joint Central Team and Physics Integration Unit 1999a *J. Nucl. Fusion* **39** 2137

ITER Physics Expert Group on Confinement and Transport, ITER Physics Expert Group on Confinement Modelling and Database and ITER Physics Basis Editors 1999b *J. Nucl. Fusion* **39** 2175

ITER Physics Expert Group on Divertor, ITER Physics Expert Group on Divertor Modelling and Database and ITER Physics Basis Editors 1999c *J. Nucl. Fusion* **39** 2391

ITER Physics Expert Group on Diagnostics and ITER Physics Basis Editors 1999d *J. Nucl. Fusion* **39** 2541

ITER Physics Expert Group on Disruptions, Plasma Control, and MHD, ITER Physics Expert Group on Energetic Particles, Heating and Current Drive, ITER Physics Expert Group on Diagnostics and ITER Physics Basis Editors 1999e *J. Nucl. Fusion* **39** 2577

ITER Physics Basis Editors, ITER Physics Expert Group Chairs and Co-Chairs and ITER Joint Central Team and Physics Integration Unit 1999f *J. Nucl. Fusion* **39** 2627

ITER Team 2000 *ITER Technical Basis G A0 FDR 1 00-07-13 R1.0 Plant Description Document*

Jones M 1974 *Mon. Not. R. Astr. Soc.* **169** 211

Jones M 1975 *Phil. Trans. R. Soc. A* **277** 587

Kelly R L 1987 *J. Phys. Chem. Ref. Data* **16** Suppl. 1 (*Atomic and Ionic Spectrum Lines below 2000 angstroms: Hydrogen through Krypton*)

Kim Y-K 2001 *Phys. Rev. A* **64** 032713

Kim Y-K and Rudd M E 1994 *Phys. Rev. A* **50** 3954

Kimura E, Nakazaki S, Berrington K A and Norrington P H 2000 *J. Phys. B: At. Mol. Opt. Phys.* **33** 3449

Kubo H, Sakurai S, Higashijima S, Takenaga H, Itami K, Konoshima S, Nakano T, Koide Y, Asakura N, Shimizu K, Fujita T and Hill K W 2003 *J. Nucl. Mater.* **313–316** 1197

Kukushkin A S, Pacher H D, Janeschitz G, Loarte A, Coster D P, Matthews G, Reiter D, Schneider R and Zhogolev V 2002 *J. Nucl. Fusion* **42** 187

Lackner K, Chodura R, Kaufmann M, Neuhasuer J, Rauh K G and Schneider W 1984 *Plasma Phys. Control. Fusion* **26** 105

Lanzafame A C, Tully J A, Berrington K A, Dufton P L, Byrne P B and Burgess A 1993 *Mon. Not. R. Astr. Soc.* **264** 402

Lauro-Taroni L, Alper B, Giannella R, Lawson K, Marcus F, Mattioli M, Smeulders P and von Hellermann M 1994 *21st EPS Conf. on Contr. Fusion and Plasma Phys.* ECA **18B** 102

Loch S D 2001 *PhD Thesis, Univ. of Strathclyde*

Loch S D, O'Mullane M G, Summers H P and Whiteford A D 2002a *UKAEA internal report* QS06915

Loch S D, Pindzola M S, Ballance C P, Griffin D C, Mitnik D M, Badnell N R, O'Mullane M G, Summers H P and Whiteford A D 2002b *Phys. Rev. A* **66** 052708

Loch S D 2003 *Private communication*

Lönnroth J-S, Parail V V, Corrigan G, Heading D, Huysmans G, Loarte A, Saarelma S, Saibene G, Sharapov S, Spence J and contributors to the EFDA-JET Workprogramme 2003 *Plasma Phys. Control. Fusion* **45** 1689–1711

Lotz W 1968 *Z Phys D* **216** 241

Maddison G P, Brix M, Budny R, Charlet M, Coffey I, Cordey J G, Dumortier P, Erents S K, Hawkes N C, von Hellermann M, Hillis D L, Hogan J, Horton L D, Ingesson L C, Jachmich S, Jackson G L, Kallenbach A, Koslowski H R, Lawson K D, Loarte A, Matthews G F, McDonald D, McKee G R, Meigs A, Messiaen A M, Milani F, Monier-Garbet P, Murakami M, Nave M F F, Ongena J, Puiatti M E, Rachlew E, Rapp J, Sharapov S, Staebler G M, Stamp M, Strachan J D, Suttrop W, Telesca G, Tokar M Z, Unterberg B, Valisa M, Zastrow K-D and EFDA-JET 2000 workprogramme contributors 2003 *J. Nucl. Fusion* **43** 49

Mandrekas J and Stacey W M Jr 1995 *J. Nucl. Fusion* **35** 843

Mandrekas J, Stacey W M and Kelly F 1996 *J. Nucl. Fusion* **36** 917

Mann J B 1983 *Atomic Data and Nucl. Data Tables* **29** 407

Marchuk O, Whiteford A, Fenzi-Bonizec C, Bertschinger G, Platz P and Summers H 2003 *DPG Conf. on Plasma Physics and Short Time-scale Physics* P7.4

- Marchuk O 2004 *PhD Thesis* FZ-Jülich
- Marquardt D W 1963 *J. of the Soc. for Ind. and App. Math.* **11** 431
- Mazzotta P, Mazzitell G, Colafrancesco S and Vittorio N 1998 *Astron. Astrophys. Suppl. Ser.* **133** 403
- Meigs A G 2003 *Private communication*
- Merts A L, Mann J B, Robb W D and Magee N H Jr 1980 *Los Alamos Report* LA-8267-MS
- Montague R G and Harrison M F A 1984 *J. Phys. B: At. Mol. Opt. Phys.* **17** 2707
- Murakami Y, Amano T, Shimizu K and Shimada M 2003 *J. Nucl. Mater.* **313–316** 1161
- Naujoks D, Asmussen K, Bessenrodt-Weberpals M, Deschka S, Dux R, Engelhardt W, Field A R, Fussmann G, Fuchs J C, Garcia-Rosales C, Hirsch S, Ignacz P, Lieder G, Mast K F, Neu R, Radtke R, Roth J and Wenzel U 1996 *J. Nucl. Fusion* **36** 671
- Neu R 2003 IPP-Report 10/25
- Neu R *et al* (133 authors) 1996 *Plasma Phys. Control. Fusion* **38** A165
- Neu R, Asmussen K, Deschka S, Thoma A, Bessenrodt-Weberpals M, Dux R, Engelhardt W, Fuchs J C, Gaffert J, García-Rosales C, Herrmann A, Krieger K, Mast F, Roth J, Rohde V, Weinlich M, Wenzel U, the ASDEX upgrade team and the ASDEX NI team 1997 *J. Nucl. Mater.* **241–243** 678
- Neu R, Rohde V, Geier A, Krieger K, Maier H, Bolshukhin D, Kallenbach A, Pugno R, Schmidtman K, Zarrabian M and the ASDEX upgrade team 2001 *J. Nucl. Mater.* **290–293** 206
- Neu R, Dux R, Geier A, Kallenbach A, Pugno R, Rohde V, Bolshukhin D, Fuchs J C, Gehre O, Gruber O, Hobirk J, Kaufmann M, Krieger K, Laux M, Maggi C, Murmann H, Neuhauser J, Ryter F, Sips A C C, Stäbler A, Stober J, Suttrop W,

Zohm H and the ASDEX upgrade team 2002 *Plasma Phys. Control. Fusion* **44** 811

Neu R, Dux R, Geier A, Greuner H, Krieger K, Maier H, Pugno R, Rgode V, Yoon S W and the ASDEX upgrade team 2003a *J. Nucl. Mater.* **313–316** 116

Neu R, Dux R, Geier A, Gruber H, Kallenbach K, Krieger K, Maier H, Pugno R, Rohde V, Schweizer S and the ASDEX upgrade team 2003b *Fusion Engineering and Design* **65** 367

Neuhauser J 1992 *Plasma Phys. Control. Fusion* **34** 2015

Norrington P H and Grant I P 1987 *J. Phys. B: At. Mol. Opt. Phys.* **20** 4869

NIST 2001 *Atomic spectra database*¹

Ohgo T, Wada M, Ohya K, Hirai T, Biel W, Tanabe T, Kondo K, Rapp J, Philipps V, Huber A, Sergienko G, Pospieszczyk A, Bertschinger G and Noda N 2003 *J. Nucl. Mater.* **313–316** 1156

O'Mullane M G, Chen H, Flewin C, Hawkes N C, von Hellermann M, Lauro-Taroni L and Peacock N J 1996a *JET Joint Undertaking Report* JET-IR(96)30

O'Mullane M G, Chen H, Flewin C, Hawkes N C, von Hellermann M, Lauro-Taroni L and Peacock N J 1996b *23rd EPS Conf. on Contr. Fusion and Plasma Phys.*

O'Mullane M G, Summers H P, Whiteford A D, Barnsley R, Coffey I H, Counsell G and Loch S D 2002 *Rev. Sci. Instr.* **74** 2080

Parail V V, Baranov Yu F, Challis C D, Cottrell G A, Fischer B, Gormezano C, Huysmans G T A, Litaudon X, Sips A C C, Söldner F X, Springmann E M, Taroni A and Ward D J 1999 *Plasma Phys. Control. Fusion* **39** 429–437

Parail 2003 *Private Communication*

¹<http://physics.nist.gov/>

- Peacock N, Barnsley R, Hawkes N, Lawson K and O'Mullane M 1996 *Diagnostics for Experimental Thermonuclear Fusion Reactors* Stott P, Gorinio G and Sidoni E (eds) (Plenum, New York) 291
- Pindzola M S, Griffin D C, and Bottcher C 1986a *Atomic Processes in Electron-ion and ion-ion Collisions*, NATO advanced study institute, series B: **145** Physics, ed Brouillard (Plenum, New York) 75
- Pindzola M S, Griffin D C, and Bottcher C 1986b *Phys. Rev. A* **33** 3787
- Pindzola M S, Badnell N R and Griffin D C 1992 *Phys. Rev. A* **46** 5725
- Pindzola M S, Griffin D C, Bottcher C, Younger S M and Hunter H T 1987 *Electron-impact ionization Data for the Fe Isonuclear Sequence*, Oak Ridge National Laboratory Report, ORNL/TM-10297
- Pindzola M S, Griffin D C, Bottcher C, Buie M J and Gregory D C 1991 *Physica Scripta* **T37** 35
- Pindzola M S and Robicheaux F 1996 *Phys. Rev. A* **54** 2142
- Pindzola M S and Griffin D C 1997 *Phys. Rev. A* **56** 1654
- Plante D R, Johnson W R and Sapirstein J 1994 *Phys. Rev. A* **49** 3519
- Post D E, Jenness R V, Tarter C B, Grasberger W H and Lokke W A 1977 *Atomic Data and Nucl. Data Tables* **20** 397
- Post D, Abdallah J, Clark R E H and Putvinskaya (1995) *Phys. Plasmas* **2** 2328
- Pradhan A K 1983a *Phys. Rev. A* **28** 2113
- Pradhan A K 1983b *Phys. Rev. A* **28** 2128
- Pradhan A K 1985 *Astrophys. J. Suppl. Ser.* **59** 183
- Pütterich T, Dux R, Gafret J, Kallenbach A, Neu R, Pugno R, Yoon S W and the ASDEX Upgrade Team 2003a *Plasma Phys. Control. Fusion* **45** 1873

- Pütterich T, Neu R, O'Mullane M, Whiteford A, Dux R and ASDEX Upgrade Team 2003b *DPG Conf. on Plasma Physics and Short Time-scale Physics* P17.21
- Radtke R, Biedermann C, Fuchs T, Fussmann G and Beiersdorfer P 1999 *Phys. Rev. E* **61** 1966
- Radtke R, Biedermann C, Schowb J L, Mandelbaum P and Doron R 2001 *Phys. Rev. A* **64** 012720
- Reiter D, Wiesen S and Born M 2002 *Plasma Phys. Control. Fusion* **44** 1723
- Robicheaux F, Gorczyca T W, Pindzola M S and Badnell N R 1995 *Phys. Rev. A* **52** 1319
- Rosmej F B, Reiter D, Lisitsa V S, Bitter M, Herzog O, Bertschinger G and Kunze H-J 1999 *Plasma Phys. Control. Fusion* **41** 191
- Sakimoto K, Terao M and Berrington K A 1990 *Phys. Rev. A* **42** 291
- Sampson D H 1986 *Phys. Rev. A* **34** 986
- Sampson D H, Goett S J and Clark R E H 1983 *Atomic Data and Nucl. Data Tables* **29** 467
- Sampson D H, Goett S J, Petrou G V, Zhang H and Clark R E H 1985a *Atomic Data and Nucl. Data Tables* **32** 343
- Sampson D H, Petrou G V, Goett S J and Clark R E H 1985b *Atomic Data and Nucl. Data Tables* **32** 403
- Seaton M J 1953a *Phil Trans. A* **245** 469
- Seaton M J 1953b *Proc. Roy. Soc. A* **218** 400
- Seaton M J 1955 *Proc. Roy. Soc. A* **231** 37
- Shaw J A, Pindzola M S, Steidl M, Aichele K, Hartenfeller U, Hathiramani D, Scheuermann F, Westermann M and Salzborn E 2001 *Phys. Rev. A* **63** 032709

- Stamp M F, Behringer K H, Forrest M J, Morgan P D and Summers H P 1987 *J. Nucl. Mater.* **145–147** 236
- Stenke M, Aichele K, Harthiramani D, Hofmann G, Steidl M, Völpel R and Salzborn E 1995 *J. Phys. B: At. Mol. Opt. Phys.* **28** 2711
- Stork D, Zastrow K-D, Adams M, Bertalot L, Brzozowski J H, Challis C D, Conroy S, de Baar M, de Vries P, Ericsson G, Garzotti L, Gorini G, Hawkes N C, Hender T C, Joffrin E, Kiptily V, Lamalle P, Loarte A, Lomas P J, Mailloux J, Mantsinen M, McDonald D C, Murari A, Neu R, Ongena J, Popovichev S, Saibene G, Santala M, Sharapov S, Stamp M, Stober J, Voitsekhovitch I, Weisen H, Whiteford A D, Yavorskij V, Zabolotsky A and JET EFDA contributors 2004 *Abstract for the IAEA 20th Fusion Energy Conference*
- Strömngren B 1932 *Z Astrophys* **4** 118
- Summers H P 1977 *Mon. Not. R. Astr. Soc.* **178** 101
- Summers H P, Behringer K and Wood L 1987 *Physica Scripta* **35** 303
- Summers H P 1994 *JET Joint Undertaking Report* JET-IR(94)06
- Summers H P 1999 *ADAS User manual Version 2.1*²
- Summers H P and Hooper M B 1983 *Plasma Physics* **25** 1311
- Summers H P and McWhirter R W P 1979 *J. Phys. B: At. Mol. Phys.* **12** 2387
- Tayal S S and Henry R J W 1991 *Phys. Rev. A* **44** 2955
- Tayal S S and Kingston A E 1984 *J. Phys. B: At. Mol. Phys.* **17** 1383
- Tayal S S and Kingston A E 1985 *J. Phys. B: At. Mol. Phys.* **18** 2983
- Thompson W T 1999 *CDS software note* **53**
- Tully J A 1973 *Can. J. Phys.* **51** 2047
- Van Regemorter H 1962 *Astrophys. J.* **136** 906

²<http://adas.phys.strath.ac.uk/>

Wilson R (1962) *JQSRT* **2** 477

Whiteford A D, Badnell N R, Ballance C P, O'Mullane M G, Summers H P and Thomas A L 2001 *J. Phys. B: At. Mol. Opt. Phys.* **34** 3179

Whiteford A D, Badnell N R, Ballance C P, Loch S D, O'Mullane M G and Summers H P 2002 *J. Phys. B: At. Mol. Opt. Phys.* **35** 3729

Whiteford A D, Zastrow K-D, Adams M, Bertalot L, Conroy S, O'Mullane M G, Popovichev S, Summers H P, Zabolotsky A and JET EFDA contributors 2004 *Abstract for the 31st EPS Conf. on Contr. Fusion and Plasma Physics*

Whiteford A D and Zastrow K-D 2003 EFDA-JET Internal Memo

Wong K L, Beiersdorfer P, Reed K J and Vogel D A 1995 *Phys. Rev. A* **51** 1214

Zastrow K-D, Andrew P, Basse N P, Breger P, Budny R, Core W G F, Ehrenberg J, von Hellermann M G, Jarvis O N, König R W T, Lauro-Taroni L, Loughlin M J, Marcus F B, Matthews G F, O'Mullane M G, Sadler G J, Strachan J D and Watkins N 1998 *ECA* **22C** 385

Zastrow K-D, Brix M, Dux R, Finken K-H, Giroud C, von Hellermann M G, Hillis D, Morgan P D, O'Mullane M G and Whiteford A D 2002 *29th EPS Conf. on Contr. Fusion and Plasma Phys.* *ECA* **26B** O-5.02

Zastrow K-D, Adams M, Bertalot L, Brzozowski J H, Challis C D, Conroy S, de Baar, de Vries P, Garzotti L, Joffrin E, Mailloux J, McDonald D C, Popovichev S, Stamp M, Stork D, Voitsekhovitch I, Weisen H, Whiteford A D, Zabolotsky A and JET EFDA contributors 2004 *Abstract for the 31st EPS Conf. on Contr. Fusion and Plasma Physics*

Zatsarinny O, Gorczyca T W, Korista K T, Badnell N. R, and Savin D W 2003 *Astronomy and Astrophysics* **412** 587

Zhang H L and Pradhan A K 1995 *J. Phys. B: At. Mol. Opt. Phys.* **28** L285

Zhang H L and Sampson D H 1987 *Astrophys. J. Suppl. Ser.* **63** 487

Zhang H L, Sampson D H and Clark R E H 1986 *Phys. Rev. A* **35** 267

Zhang H L, Sampson D H and Fontes C J 1990 *Atomic Data and Nucl. Data Tables* **44** 31

Appendix A

Fusion experiments

Several fusion experiments are mentioned in this thesis, brief overviews of some of them are given in the following paragraphs.

The Joint European Torus (JET) is currently the largest tokamak in the world, with a plasma volume of over 100m^3 , it has major radius of 2.96m and minor radii of 2.10/1.25m. The main concern of the JET program is studying physics and engineering issues relevant to reactor conditions and to contribute to the design and running of ITER (see below). A typical JET pulse lasts for over twenty seconds and currents of almost 5MA are possible. The main source of heating comes from neutral beams (up to 21MW) and radio frequency heating (up to 20MW).

The Axially Symmetric Divertor EXperiment (ASDEX-U) is, like JET, concerned with investigating physics issues under reactor like conditions. In recent years particular emphasis has been given to the investigation of tungsten as a first wall material, likely to be used in the divertor of ITER (see below). It is not as large as JET with a major radius of 1.6m and minor radii of 0.8/0.5m, the total vessel volume is around 14m^3 . A typical ASDEX-U pulse lasts for around ten seconds with a plasma current which can be in excess of 2MA. The plasma is predominantly heated with neutral beams (up to 20MW total power) but radio frequency and microwave heating systems also exist which can deliver around 6MW of additional heating.

The Tokamak EXperiment for Technology Oriented Research (TEXTOR) is a limiter machine (i.e. has no divertor) and is smaller than the tokamaks detailed

above with a major radius of 1.75m and a minor radius of 0.46m. The main scientific program is concentrated on plasma wall interaction and wall conditioning techniques (such as carbonisation and boronisation). A typical TEXTOR pulse is between seven and ten seconds long, the plasma current can go up to 700kA. The three main heating mechanisms are neutral beams, ICRH and ECRH with powers of order 3MW, 2MW and 0.5MW respectively.

The International Tokamak Experimental Reactor (ITER¹) is planned as the next large fusion experiment. The aim of the project is to produce a burning, energy-yielding plasma and hence investigate scientific, engineering and technical issues relevant for a fusion reactor. Some of the key aims of this research are superconducting magnetic field coils, tritium technology, exhaust of the thermal energy generated, and development of remotely replaceable components.

¹Also Latin for 'the way'.

Appendix B

Computational details

The computational implementation of the methods described in this thesis have not been discussed in the text to retain focus on atomic physics and transport issues.

The implementation comprises of approximately eighty to ninety thousand lines of source code and three to four gigabytes of archived, user-relevant data. The source code is principally in the IDL language with substantial amounts in FORTRAN (mainly core subroutines) and a modest amount of C (primarily for efficient linking). All codes have been written to the standards of the ADAS Project and archived data is formatted according to defined ADAS adf-specifications.

All of the codes and data are available through the ADAS Project with the exception of UTC which is available at JET. The latter was written to be portable to other machines and laboratories, and can be requested from JET. A brief overview of the computational details are given below, followed by some specific examples.

Computer hardware and operating systems

The computer systems used during this work were Intel-based systems running Linux, Sun systems running Solaris and SGI systems running IRIX. All of the heavy species calculations, as well as some of the R -matrix calculations, were performed on a 16CPU SGI Origin 300 cluster. A typical time for a complete lithium-like R -matrix calculations was of the order of one week. A similar timescale was required for calculating every ionisation stage of a heavy species.

For less intensive work, PC and Sun workstations were sufficient. Code development and debugging were also done on these smaller systems.

Programming languages

As mentioned above, the main programming languages used throughout this work were FORTRAN and IDL. FORTRAN was adopted primarily for computational demanding tasks and also for many of the fundamental atomic physics calculations. This choice was partly for efficiency and partly because a lot of existing legacy code was written in FORTRAN. IDL was used for data visualisation, the creation of graphical user interfaces, for smaller calculations and also for file processing. C interface codes were written to sit between IDL and FORTRAN allowing them to communicate efficiently via shared object libraries. These C routines were fairly simple but the compilation of shared object libraries on a number of different machine architectures and compilers can prove problematic. Perl was used for controlling FORTRAN code where IDL was not available. Perl was also the primarily language used for large scale file processing and batch control.

Parallelisation of heavy species calculations

The heavy species calculations took a simple, but effective approach to parallelisation. That is each independent (from the point of view of the bulk of the calculations) ionisation stage calculation was executed on a different processor. This is not true parallel programming in the academic sense but has immediate and significant advantages: complex codes remain serial, easier to debug; easy to implement; individual parts of the calculations can be easily isolated; no communication so near perfect scaling. The disadvantage of this approach is that of memory consumption. Rather than doing, say, a matrix operation to a single matrix using N processors, N matrix operations are done simultaneously to N matrices, requiring N times the memory.

Overview of UTC

UTC provides a graphical interface to an impurity transport code. The latter is, in principle, arbitrary but SANCO was used for the present work. UTC handles

reading of experimental diagnostic from the JET PPF system¹, creating electron temperature and density profiles and collating equilibrium information. The code will then either launch the underlying transport code and display the results or perform a least squares fit between diagnostic data and the outputs of the transport model. In most cases, the output of the transport model must be postprocessed by UTC in order to simulate the measurement of the various diagnostic systems. This system is proving quite versatile at JET and is becoming the method of choice for spectral analysts there.

¹While only JET data is currently read by UTC, the code is designed to be machine independent.